Department of Physics
University of Jyväskylä
JYFL Reserach Report 8/2008

Development and application of laser technologies at radioactive ion beam facilities

by
Thomas Kessler

Academic Dissertation
for the Degree of
Doctor of Philosophy

To be presented, by permission of the
Faculty of Mathematics and Natural Sciences
of the University of Jyväskylä,
for public examination in Auditorium FYS-1 of the
University of Jyväskylä on August 7, 2008
at 12 o'clock noon

Jyväskylä, Finland
August 2008

Impressions of a PhD thesis

The lab . . .

the boys . . .

the toys . . .

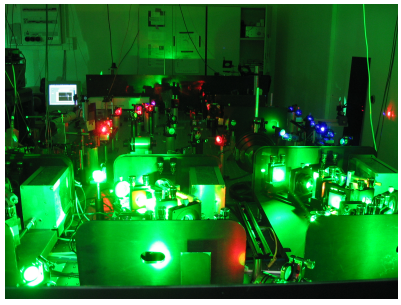

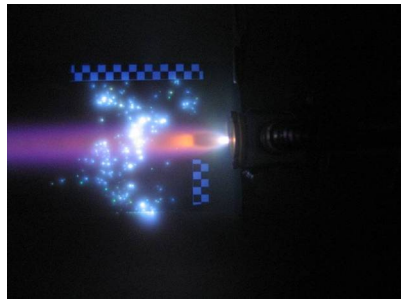

Acknowledgements

The work reported in this thesis was carried out during the years 2004-2008 at the Department of Physics of the University of Jyväskylä and the Department of Physics of the University of Mainz. I would like to thank the whole staff of both Departments for the pleasant working atmosphere.

I would like to thank my supervisors Professor Juha Äystö and Professor Klaus Wendt for the opportunity to carry out this work in an international environment and for their guidance and support.

I would like to thank the IGISOL group for their support, especially Dr. Ben Tordoff, MSc Mikael Reponen and MSc Viki Elomaa for fun with lasers and even more holes in my T-shirts. The JYFL Trap group members MSc Tommi Eronen and Dr. Ulrike Hager are acknowledged for support and patience in explaining the Trap data acquisition system. I would especially like to thank Dr. Iain Moore for four years of discussions, guidance, irresistible optimism and, last but not least, for the regular sunday night movie sessions in a small cinema in central Finland.

Part of this work was carried out at Mainz, and I would like to thank the Larissa working group for the lunch breaks on top and underneath the kicker table. Special thanks go to Dipl.Phys. Christoph Mattolat and Dr. Hideki Tomita (Nagoya University) for the combined effort in the laser development and to Dipl.Phys. Fabio Schwellnus for the evening entertainment. Sebastian Rothe is acknowledged for support of the IGISOL ice hockey team and the instructive introduction to geocaching in Finland.

My Ultimate club *Jyväskylä Sleepwalkers* is acknowledged for keeping *Count Deeku* in physical shape and spicing up the weekends.

I wish to thank my family for all the support and encouragement.
Finally, I thank Krissi for her endless understanding, support and love.

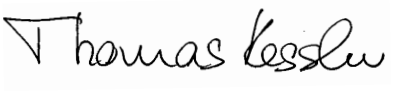

Jyväskylä, August 2008

Abstract

A laser ion source facility has been built and commissioned at the University of Jyväskylä, Finland. In addition to a conventional dye laser system an all-solid state laser system has been installed. To increase the spectral resolution of the solid-state system an injection-seeded high-repetition rate Ti:Sapphire laser has been built.

Excitation schemes for resonant laser ionization have been tested for a total of 14 elements and spectroscopic work on yttrium, technetium, nickel, gallium, aluminium and silver is presented in this thesis. High-resolution in-source laser spectroscopy experiments have been performed for bismuth and aluminium. Furthermore, optical manipulation of radioactive ions in an rf cooler buncher device has been realized.

The IGISOL front-end has been adapted to implement laser ionization techniques including the design of a new heavy-ion fusion evaporation laser ion guide. The gas jet leaving the ion guide has been visualized and characterized by photographing the optical emission from the discharged buffer gas in preparation for the IGISOL LIST approach. A hot cavity ion catcher device for the production of neutron-deficient silver isotopes has been developed and first tests have been successfully performed. Extensive off-line and on-line studies have been performed to understand the role of molecular formation and the effect of beam-produced plasma on the survival of laser-produced ions within the gas cell.

Preface

The work at ORNL has been sponsored by the Office of Nuclear Physics, U.S. Department of Energy, under contract DE-AC05-00OR22725 with UT-Battelle, LLC.

The work at Mainz has been sponsored by Bundesministerium für Bildung und Forschung (BMBF) of Germany under contract 06Mz197 and by the Ministry of Education, Culture, Sports, Science and Technology (MEXT) of Japan, a Grant-in-Aid for the 21st Century COE Program, "Isotopes for the Prosperous Future".

The work in Finland has been supported by the LASER Joint Research Activity project under the EU 6th Framework program "Integrating Infrastructure Initiative - Transnational Access", Contract number: 506065 (EURONS) and by the Academy of Finland under the Finnish centre of Excellence Program 2006-2011 (Nuclear and Accelerator Based Physics Program at JYFL). The work contained within this thesis satisfies the Joint Research Activities (JRA) of the LASER EURONS project.

Contents

List of Tables

List of Figures

1 Introduction

In the last ten years, laser resonance ionization has developed into a mature technique, playing a key role in the production of radioactive nuclides at on-line isotope separator (ISOL) facilities. In comparison to other ionization mechanisms utilized in the prepararation of radioactive ion beams, resonant laser ionization is sensitive to the number of protons in the nucleus and consequently provides isotopic selectivity when combined with a mass-selective device. Coupled with modern tunable laser systems an extraction efficiency in the order of 10% can be reached. The technique has advanced and developed to a point where it is the favoured production mechanism for hot cavity ion sources at on-line radioactive ion beam facilities such as ISOLDE (CERN). In order to implement resonant laser ionization into an IGISOL-type ion source, a careful systematic development both off-line and on-line has been achieved by the LISOL group of the University of Leuven. Both facilities rely on tunable dye lasers. More recently, however, a new solid state laser system has been successfully installed at the resonant laser ion source TRILIS, in TRIUMF.

During this thesis work a new laser ion source was installed and commissioned for the IGISOL facility of the University of Jyväskylä, Finland. The fast and universal resonant laser ion source (FURIOS) facility comprises both high-resolution Ti:Sapphire lasers and dye lasers, therefore providing an unparalleled universal coverage of ionization schemes throughout the periodic table. The challenge to prepare and manipulate pure samples of radioactive isotopes far from stability has required the development of new experimental techniques including optical pumping and in-source spectroscopy, both of which are treated in this thesis. The progress goes hand in hand with the demand for new laser technologies tailored to the specific application. This thesis introduces the laser system and presents the first results obtained from off-line and on-line experiments involving laser technologies at the IGISOL facility.

To provide a theoretical background to the process of laser ionization, the thesis begins with a description of the theory of atom-light interaction. Chapter 2 covers the basic solution of the Schrödinger equation for an atom in a coherent light-field. Additionally, different broadening mechanisms important for this thesis work are discussed and experimental examples are given. The theoretical part concludes with a short review on the technique of resonant laser ionization spectroscopy with focus on the ionization step.

The setup of the FURIOS laser system is discussed in chapter 3. Specifications to

both the dye laser system and the solid-state laser system are given. For applications requiring the highest spectroscopic resolution, a novel injection-seeded high-repetition rate Ti:Sapphire laser for high-resolution spectroscopy and trace analysis of rare isotopes has been built during this thesis work. The laser cavity and related locking electronics are described in Section 3.1.3. The description of the hardware present in the laser cabin is completed by a brief introduction to the control software written for the laser system and an atomic beam unit for off-line laser spectroscopy.

Chapter 4 describes the development and preparation of the IGISOL front-end for resonance ionization spectroscopy. Firstly, the IGISOL technique developed at Jyväskylä is introduced, followed by a discussion of the coupling of the FURIOS laser ion beams with the IGISOL source. The important theoretical concepts of stopping of ion beams in matter as well as the modeling of the gas flow are described. A new ion guide for heavy-ion fusion-evaporation reactions has been designed and built, incorporating the possibility of laser ionization. The gas jet has been visualized by photographing the fluorescence from discharged buffer gas and first conclusions towards an efficient coupling of the jet into a sextupole rf ion guide structure (SPIG) are drawn. A completely different approach, namely a hot cavity ion catcher device, has been tested in IGISOL to produce a beam of neutron-deficient silver isotopes by resonant laser ionization. Off-line testing has been completed and a first beam of laser-ionized stable silver was extracted from IGISOL.

To develop radioactive ion beams via resonant laser excitation and ionization, preparatory spectroscopic studies are needed. A total of 14 different elements have been studied during this thesis. A selection of highlights are provided in chapter 5 summarising the different techniques applied. The production of an ion beam of ^{99}Tc has been identified as a highlight by the LASER-EURONS community, as no stable isotope exists. Consequently special effort has to be given to careful sample preparation and detection. For the spectroscopy of yttrium by resonant laser ionization, both the dye laser system and the solid-state laser system have been used in parallel for the first time and new transitions applicable for laser ionization have been found. The possibility of Rydberg ionization has been studied in both a hot cavity ion source and IGISOL for the elements nickel and gallium, respectively. The enhancement in ionization efficiency compared to other techniques makes Rydberg ionization an attractive method in both sources for the production of radioactive ion beams. For stable beams a spectroscopic study of a high-lying Rydberg series reveals important atomic information and is discussed for the case of nickel in this thesis.

The relatively new technique of in-source spectroscopy is illustrated in section 5.5. It has been studied with a dye laser system on bismuth and with the newly designed seeded solid laser laser system on aluminium. The results indicate that in-source spectroscopy might indeed become a powerful tool to access nuclear moments and changes in mean-square charge radii of very short-lived, weakly-produced exotic isotopes by

high-resolution laser spectroscopy.

A new technique pioneered at the University of Jyväskylä is collinear laser spectroscopy assisted by optical pumping in an rf cooler-buncher device. The technique has been tested off-line and recently first on-line results have been obtained on the ionic systems of niobium and yttrium, presented in section 5.6.

For the coupling of FURIOS to IGISOL the competing processes in the gas cell need to be studied in detail. Chapter 6 is devoted to the studies of these effects. Simulation models were written in this thesis to cover the most important aspects, namely molecular formation and recombination in the beam-produced plasma. The influence on the laser ionization efficiency has been studied in experiments and compared to the simulation models for the case of yttrium and bismuth.

The important results of this thesis work are summarized in chapter 7 including an outlook on planned future activities at IGISOL.

The experimental work for this thesis was carried out at the IGISOL facility at the Accelerator Laboratory of the University of Jyväskylä (Finland), at the Institute of Physics of the University of Mainz (Germany) and the ISTF-2 facility of Oak Ridge National Laboratory (USA). The author of this work has been a main contributor to the commissioning and installation of the FURIOS laser ion source at Jyväskylä and the preparation of the IGISOL front-end. The author has been involved in the setup of all experiments at IGISOL described in this thesis and the analysis of the presented data. All simulation models described have been developed by the author. He has developed a seeded high-repetition rate Ti:Sapphire laser in collaboration with colleagues from the University of Mainz (Germany) and the University of Nagoya (Japan). The author has been in charge of the setup of the laser system at ORNL (USA) in preparation for a laser ion source for a future Rare Isotope Accelerator facility, and has carried out the analysis of the data.

This thesis is based on the following publications:

[1] **T. Kessler**, H. Tomita, C. Mattolat, S. Raeder, and K. Wendt. An injection-seeded high-repetition rate Ti:Sapphire laser for high-resolution spectroscopy and trace analysis of rare isotopes. *Las. Phys.*, 18(7):842–849, July 2008.

[2] **T. Kessler**, I. D. Moore, H. Penttilä, F. Quinquis, and J. Äystö. Towards on-line production of $N = Z$ ^{94}Ag at IGISOL. *Nucl. Instrum. Methods Phys. Res., Sect. B*, In Press, Accepted Manuscript:10.1016/j.nimb.2008.05.030, 2008.

[3] **T. Kessler**, T. Eronen, C. Mattolat, I. D. Moore, K. Peräjärvi, P. Ronkanen, P. Thörle, B. Tordoff, N. Trautmann, K. Wendt, K. Wies, and J. Äystö. Upgrade to the IGISOL laser ion source towards spectroscopy on Tc. *Hyperfine Interact.*, 171(1):121–126, July 2006.

[4] **T. Kessler**, K. Brück, C. Baktash, J. R. Beene, Ch. Geppert, C. C. Havener, H. F. Krause, Y. Liu, D. R. Schultz, D. W. Stracener, C. R. Vane, and K.Wendt. Three-step resonant photoionization spectroscopy of Ni and Ge: ionization potential and odd-parity Rydberg levels. *J. Phys. B*, 40(23):4413–4432, 2007.

[5] **T. Kessler**, I. D. Moore, Y. Kudryavtsev, K. Peräjärvi, A. Popov, P. Ronkanen, T. Sonoda, B. Tordoff, K. D. A. Wendt, and J. Äystö. Off-line studies of the laser ionization of yttrium at the IGISOL facility. *Nucl. Instrum. Methods Phys. Res., Sect. B*, 266(4):681–700, February 2008.

[6] I. D. Moore, **T. Kessler**, Yu. Kudryavstev, K. Peräjärvi, A. Popov, P. Ronkanen, T. Sonoda, B. Tordoff, K.D.A. Wendt, and J. Äystö. On-line studies with laser ionization and the first stopped primary beams at IGISOL. *Nucl. Instrum. Methods Phys. Res., Sect. B*, Manuscript in preparation, 2008.

2 Atom-light interaction

Any experiment utilizing laser spectroscopy is based on the interaction of light with matter. A theoretical understanding of the principles of the interaction is vital for the further discussion of the experimental laser techniques developed for the IGISOL facility. The theory of atom-light interaction is explained in detail in several text books [1, 2]. In the first section 2.1 of this chapter a theoretical description of the excitation of an atom by monochromatic laser light will be discussed in the framework of the Schrödinger equation. The density-matrix formalism, explained in the following section 2.2, allows one to take into account relaxation terms. In section 2.3 different broadening mechanisms arising from non-ideal experimental conditions are discussed. In each case comparison with experimental data is given to clarify the discussion. Finally a short review of the technique of resonant ionization spectroscopy (RIS) is given in section 2.4.

2.1 Solution of the Schrödinger equation for a 2-level atom

Before dealing with more complex situations it is important to describe the interaction of monochromatic laser light for the simple, but important case, of a 2-level atom as shown in figure 2.1(a).

The interaction of an atom with a laser beam is described by solving the Schrödinger equation in which the interaction is represented by a dipole term of the form

$$\begin{aligned} V &= -erE_0 \cos(\omega_L t) \\ &= -erE_0 \left(e^{i\omega_L t} + e^{-i\omega_L t}\right)/2 \,, \end{aligned} \tag{2.1}$$

where r is the, radial coordinate ω_L the laser frequency and e the electronic charge. The assumption is made that the atom is polarized towards the laser radiation and therefore

$$\vec{r}\vec{E_0} = rE_0 \,. \tag{2.2}$$

The electrodynamic field is approximated by a monochromatic wave. The time evolution of the wavefunction is described by the Schrödinger equation

$$i\hbar \frac{\partial}{\partial t}\Psi(r,t) = (H_0 + V)\Psi(r,t) \,. \tag{2.3}$$

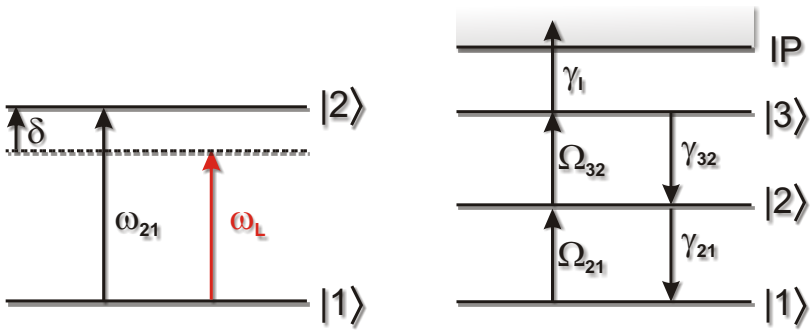

(a) 2-level atom

(b) 3-level atom with relaxation and ionization rates

Figure 2.1: Schematic drawing of the excitation of a 2-level system without a relaxation term and a 3-level system with relaxation terms.

In a 2-level system the problem is solved by the ansatz

$$\begin{aligned}\Psi(r,t) &= \langle\phi_1|\Psi\rangle\cdot|\phi_1\rangle + \langle\phi_2|\Psi\rangle\cdot|\phi_2\rangle \\ &= c_1(t)e^{i\omega_1 t}\phi_1(r) + c_2(t)e^{i\omega_2 t}\phi_2(r)\ ,\end{aligned} \tag{2.4}$$

where $c_1(t)$ and $c_2(t)$ describe the time-dependent amplitudes, $\phi_1(r)$ and $\phi_2(r)$ the stationary solutions of the unperturbed Schrödinger equation and $E_{1,2} = -\hbar\omega_{1,2}$ the corresponding binding energies. The resulting set of partial differential equations for the two amplitudes $c_{1,2}(t)$ yields

$$\dot{c}_1 = i\frac{\Omega_0}{2}\left(e^{-i(\omega_{21}+\omega_L)t} + e^{-i(\omega_{21}-\omega_L)t}\right)c_2 \tag{2.5a}$$

$$\dot{c}_2 = i\frac{\Omega_0}{2}\left(e^{i(\omega_{21}+\omega_L)t} + e^{i(\omega_{21}-\omega_L)t}\right)c_1 \tag{2.5b}$$

with the separation between the states $|1\rangle$ and $|2\rangle$

$$\omega_{21} = \omega_2 - \omega_1 \tag{2.6}$$

and the *resonant Rabi flopping frequency*

$$\Omega_0 = \frac{e\langle rE_0\rangle}{\hbar}\ . \tag{2.7}$$

The expressions in (2.5) can be further simplified by neglecting the fast oscillating

terms in the so-called *Rotating wave approximation*

$$\dot{c}_1 = \frac{i\Omega_0}{2} e^{-i(\omega_{21}-\omega_L)t} c_2 \tag{2.8a}$$

$$\dot{c}_2 = \frac{i\Omega_0}{2} e^{i(\omega_{21}-\omega_L)t} c_1 \ . \tag{2.8b}$$

The solution for the probabilities $|c_1|^2$ and $|c_2|^2$ to find the atom in state $|1\rangle$ or $|2\rangle$ is given by

$$|c_2|^2 = \frac{\Omega_0^2}{2\Omega_\delta^2}(1 - \cos\Omega_\delta t) \tag{2.9a}$$

$$|c_1|^2 = (1 - |c_2|^2) \ . \tag{2.9b}$$

These equations describe the well-known Rabi oscillations between state $|1\rangle$ and state $|2\rangle$ with the *non-resonant Rabi flopping frequency* Ω_δ, where

$$\Omega_\delta = \sqrt{\Omega_0^2 + \delta^2} \tag{2.10}$$

and δ is the detuning of the laser frequency from the atomic resonance frequency,

$$\delta = \omega_{21} - \omega_L \ . \tag{2.11}$$

An illustration of the impact of the detuning of the laser on the behaviour of the oscillations is shown in figure 2.2. If the laser is tuned into resonance with ω_{21}, i.e. $\delta = 0$, the probability $|c_2|^2$ to find the atom in the excited state oscillates between the values 0 and 1. As the detuning is increased, the amplitude of the oscillation decreases and the flopping frequency increases.

This oscillating solution lacks the important aspect of spontaneous emission which provides damping of the system and therefore leads to steady-state solutions. An approach for implementing these statistical processes will be described in the next section.

2.2 The density matrix formalism

The Schrödinger equation inherently describes the time evolution of pure (coherently mixed) states and therefore is not suitable for the description of mixing of the states due to statistical processes. A process is in general considered statistical when [3]

- it happens at a "random" time
- it is independent of the "history" of the atom.

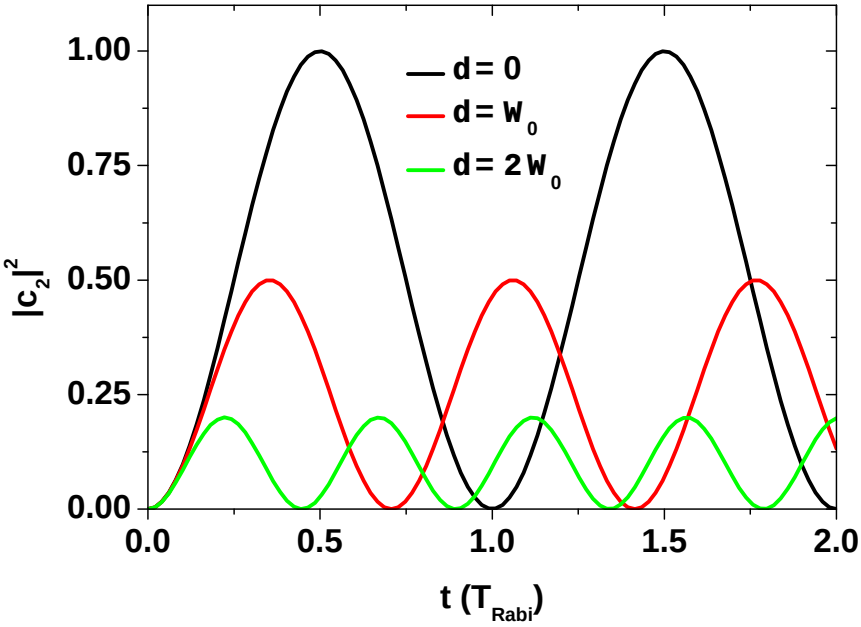

Figure 2.2: Illustration of Rabi oscillations.

The most important statistical process is the relaxation of the excited state by spontaneous emission which can not be described consistently by the Schrödinger equation. A concept which is capable of describing both statistically and coherently mixed states is the density matrix formalism [4].

The density operator ρ is defined as

$$\rho = \sum_n p_n |\psi_n\rangle\langle\psi_n| \tag{2.12}$$

where p_n is the probability to find the system in the statistically mixed state ψ_n.

In the case of spontaneous emission in an n-level scheme this is a single state which can be described with an ansatz of the form

$$\rho = |\psi\rangle\langle\psi| \; . \tag{2.13}$$

In the basis of the unperturbed atomic eigenstates of the Schrödinger equation one obtains

$$\rho_{mn}(t) = \langle\phi_m|\rho(t)|\phi_n\rangle = \langle\phi_m|\psi\rangle\langle\psi|\phi_n\rangle \; . \tag{2.14}$$

In this representation the diagonal matrix elements $\rho_{mm} = c_m c_m^*$ can be directly identified as the probability that the atom is to be found in the state $|\phi_m\rangle$. The non-diagonal matrix elements ρ_{mn} in turn contain the information about the coherence between the two states $|\phi_m\rangle$ and $|\phi_n\rangle$.

To describe the time evolution of the density matrix the Liouville equation

$$i\hbar\frac{\partial\rho(t)}{\partial t} = [H(t), \rho(t)] \tag{2.15}$$

can be derived from the Schrödinger equation. In the representation of the unperturbed normal basis $|\phi_m\rangle$ the equation can be written as

$$\begin{aligned} i\hbar\frac{\partial\rho_{mn}(t)}{\partial t} &= (E_m - E_n)\langle\phi_m|\rho(t)|\phi_n\rangle + \langle\phi_m|[V(t), \rho(t)]|\phi_n\rangle \\ &= (E_m - E_n)\rho_{mn} + \sum_k \left(\langle\phi_m|V|\phi_k\rangle\rho_{kn} - \rho_{mk}\langle\phi_k|V|\phi_n\rangle\right) \; . \end{aligned} \tag{2.16}$$

To obtain the Liouville equation for optical excitation the dipole operator of (2.1) has to be inserted as a perturbation V,

$$\begin{aligned} \frac{\partial\rho_{mn}(t)}{\partial t} &= -i(\omega_n - \omega_m)\rho_{mn} \\ &\quad + i\sum_k \left(\Omega_{mk}\rho_{kn} - \Omega_{kn}\rho_{mk}\right)\frac{1}{2}(e^{i\omega_L t} + e^{-i\omega_L t}) \; . \end{aligned} \tag{2.17}$$

The term Ω_{kn} describes the Rabi frequency linking the states $|k\rangle$ and $|n\rangle$ defined by equation (2.7). By the rotating wave approximation and the transformation

$$\rho_{mn} \rightarrow \rho_{mn} e^{i\omega_L t} \quad \forall m < n \tag{2.18}$$

the equations can be further simplified to

$$\frac{\partial \rho_{mm}(t)}{\partial t} = +\frac{i}{2} \sum_k (\Omega_{mk}\rho_{kn} - \Omega_{kn}\rho_{mk}) \tag{2.19a}$$

for the diagonal matrix elements (probabilities) and

$$\frac{\partial \rho^*_{nm}(t)}{\partial t} = \frac{\partial \rho_{mn}(t)}{\partial t} = i(\omega_m - \omega_n + \omega_L)\rho_{mn} + \frac{i}{2} \sum_k (\Omega_{mk}\rho_{kn} - \Omega_{kn}\rho_{mk}) \quad \forall m < n \tag{2.19b}$$

for the off-diagonal matrix elements (coherences).

At this stage decay losses can be introduced ad hoc into the partial differential equation system in the following manner [3, 5]:

$$\frac{\partial \rho_{mm}(t)}{\partial t} = \sum_{k \neq m} (\gamma_{km}\rho_{kk} - \gamma_{mk}\rho_{mm}) + \frac{i}{2} \sum_k (\Omega_{mk}\rho_{kn} - \Omega_{kn}\rho_{mk}) \tag{2.20a}$$

for the diagonal matrix elements (probabilities) and

$$\frac{\partial \rho_{mn}(t)}{\partial t} = -\frac{1}{2} \sum_k (\gamma_{mk} + \gamma_{nk})\rho_{mn} - i(\omega_n - \omega_m - \omega_L)\rho_{mn} + \frac{i}{2} \sum_{k \neq m,n} (\Omega_{mk}\rho_{kn} - \Omega_{kn}\rho_{mk}) \quad \forall m < n \tag{2.20b}$$

for the off-diagonal matrix elements (coherences). The meaning of the different terms can be illustrated by the example of a typical RIS application involving three bound atomic states as shown in figure 2.1(b). The first term in the equation for the diagonal matrix element ρ_{mm} represents the feeding into a given state $|\phi_m\rangle$ by a transition $|\phi_k\rangle \rightarrow |\phi_m\rangle$ with probability γ_{km}. The second term in turn represents decay losses from state $|\phi_m\rangle$ to state $|\phi_k\rangle$ with a rate γ_{mk}. Statistical processes not only shift the population of the states but also lead to a loss of coherence of the system. The coupling of different states driven by laser excitation are again implemented by the Rabi frequencies Ω_{km}. The coherences represented by the non-diagonal terms ρ_{mn} decay with half the decay rates $\gamma_{mk}/2$ and $\gamma_{nk}/2$.

The partial differential equations (2.20), known as the *Optical Bloch Equations* (OBE), describe the full dynamics of the system. If the laser radiation is fully specified and the transition strengths are well known they can be integrated. For RIS applications one typically adds an ionization rate γ_I to the system as shown in figure 2.1(b) describing a depopulation of the highest bound state. The ionization probability P_I then reads

$$P_I = 1 - \sum_k \rho_{kk} \; . \tag{2.21}$$

Excellent agreement between theory and experiment can be achieved as for example shown in [5, 6].

Unfortunately the transition rates are only known for a limited number of elements. In particular the ionization rate depends on the ionization mechanism and the element of choice, therefore has to be studied case by case. Additional complexity arises if the relaxation occurs via "dark" states which can not be immediately accessed by the laser. In these cases one has to rely on simplified models. If, for example, the ground state $|1\rangle$ is strongly coupled to the first excited state $|2\rangle$ by an excitation Ω_{12} and the depopulation of the state $|2\rangle$ is weak (Ω_{23} is not saturated) then the excitation from the ground state can be approximated by a 2-level scheme such as that in figure 2.1(a). Therefore the special case of the 2-level atom will be investigated again in the framework of the OBE in the following.

The OBE for a 2-level scheme with a spontaneous decay rate γ from state $|2\rangle$ to state $|1\rangle$ can be written

$$\begin{aligned}
\dot{\rho}_{11} &= \gamma\rho_{22} + \frac{i}{2}(\Omega_{12}\rho_{21} - \Omega_{21}\rho_{12}) \\
\dot{\rho}_{22} &= -\gamma\rho_{22} + \frac{i}{2}(\Omega_{21}\rho_{12} - \Omega_{12}\rho_{21}) \\
\dot{\rho}_{12} &= -\left(\frac{\gamma}{2} + i(\omega_2 - \omega_1 - \omega_L)\right)\rho_{12} + \frac{i}{2}(\Omega_{12}\rho_{22} - \Omega_{12}\rho_{11}) \\
\dot{\rho}_{21} &= -\left(\frac{\gamma}{2} - i(\omega_2 - \omega_1 - \omega_L)\right)\rho_{21} + \frac{i}{2}(\Omega_{21}\rho_{11} - \Omega_{21}\rho_{22}) \; ,
\end{aligned} \tag{2.22}$$

where $\Omega_{21} = \Omega_{12} = \Omega_0$ is the Rabi frequency from equation (2.7) and therefore the PDE system is simplified to

$$\begin{aligned}
\dot{\rho}_{11} &= \gamma\rho_{22} + \frac{i}{2}\Omega_0(\rho_{21} - \rho_{12}) \\
\dot{\rho}_{22} &= -\gamma\rho_{22} + \frac{i}{2}\Omega_0(\rho_{12} - \rho_{21}) \\
\dot{\rho}_{12} &= -\left(\frac{\gamma}{2} + i(\omega_2 - \omega_1 - \omega_L)\right)\rho_{12} + \frac{i}{2}\Omega_0(\rho_{22} - \rho_{11}) \\
\dot{\rho}_{21} &= -\left(\frac{\gamma}{2} - i(\omega_2 - \omega_1 - \omega_L)\right)\rho_{21} + \frac{i}{2}\Omega_0(\rho_{11} - \rho_{22}) \; .
\end{aligned} \tag{2.23}$$

By summing the first two equations we obtain the conservation of the total probability of the system

$$\dot{\rho}_{11} + \dot{\rho}_{22} = 0 \tag{2.24}$$

which follows from

$$\rho_{11} + \rho_{22} = 1 \; . \tag{2.25}$$

The OBE can be further simplified by defining the *inversion* w and the frequency detuning of the laser from resonance δ

$$\begin{aligned}
w &= \rho_{22} - \rho_{11} \\
\delta &= \omega_2 - \omega_1 - \omega_L \; .
\end{aligned} \tag{2.26}$$

The OBE then read

$$\begin{aligned}
\dot{w} &= -\gamma(w+1) - i\Omega_0(\rho_{21} - \rho_{12}) \\
\dot{\rho}_{21} &= -(\frac{\gamma}{2} - i\delta)\rho_{21} - \frac{i}{2}\Omega_0 w \; .
\end{aligned} \tag{2.27}$$

If the excitation time t of the system is longer than the damping time $1/\gamma$ a steady state can be reached. These steady state solutions can be calculated by setting $\dot{w} = \dot{\rho}_{21} = 0$. One obtains

$$\begin{aligned}
w &= -\frac{1}{1+S} \quad \text{and} \\
\rho_{21} &= \frac{i\Omega_0}{2(\gamma/2 - i\delta)(1+S)}
\end{aligned} \tag{2.28}$$

with the *saturation parameter* S

$$S = \frac{\Omega_0^2/2}{\delta^2 + \gamma^2/4} = \frac{S_0}{1 + 4\delta^2/\gamma^2} \quad \text{and} \quad S_0 = \frac{2\Omega_0^2}{\gamma^2} \; . \tag{2.29}$$

S_0 is called the *resonant saturation parameter* and describes the ratio between the Rabi frequency Ω_0 and the rate for spontaneous emission γ. The parameter S_0 can be converted to experimentally determinable properties by making use of the Einstein relation between spontaneous and stimulated processes [1, 7]. For the ratio of the factor for spontaneous emission A and for stimulated emission B,

$$\frac{A}{B} = \frac{\hbar\omega^3}{\pi^2 c^3} \tag{2.30}$$

one can obtain the expression

$$d^2 = \frac{3A\pi\epsilon_0\hbar c^3}{\omega^3} \tag{2.31}$$

for the electrical dipole moment d. Using the definition of the Rabi frequency from equation (2.7) and relating the electric field strength E_0 to the intensity I by

$$\Omega_0^2 = \frac{(dE_0)^2}{\hbar^2} \quad \text{and} \quad I = \frac{1}{2}\epsilon_0 c E_0^2 \tag{2.32}$$

one finally obtains

$$S_0 = \frac{I}{I_{sat}} \quad \text{with} \quad I_{sat} = \frac{\pi hc}{3\lambda^3\tau} \tag{2.33}$$

for an atom polarized to the polarization axis of the laser radiation, where τ describes the lifetime of the upper state and λ the laser wavelength.

In a RIS application we are interested in the probability of the excitation from the ground state $|1\rangle$ to the excited state $|2\rangle$. Therefore we calculate the probability of the atom to be in the excited state in static equilibrium

$$\begin{aligned} & \rho_{22} = w + \rho_{11} = w + 1 - \rho_{22} \\ \rightarrow \quad & \rho_{22} = (w+1)/2 \end{aligned} \tag{2.34}$$

and end up with the important results

$$\boxed{\rho_{22} = \frac{S}{2(S+1)}, \quad S = \frac{S_0}{1 + 4\delta^2/\gamma^2} \quad \text{and} \quad S_0 = \frac{I}{I_{sat}}\,.} \tag{2.35}$$

ρ_{22} represents a *Lorentzian* function with a full-width at half maximum γ',

$$\begin{aligned} \rho_{22} &= \frac{S_0/2}{1 + S_0 + 4\delta^2/\gamma^2} \\ &= \frac{S_0}{2(S_0+1)} \frac{1}{1 + 4\delta^2/\gamma'^2} \quad \text{with} \quad \gamma' = \sqrt{1+S_0}\,. \end{aligned} \tag{2.36}$$

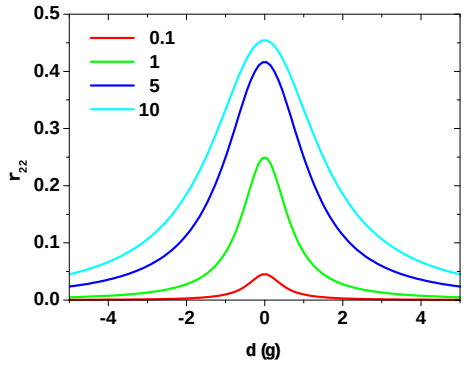

(a) ρ_{22} as a function of the laser frequency detuning δ for different values of S_0

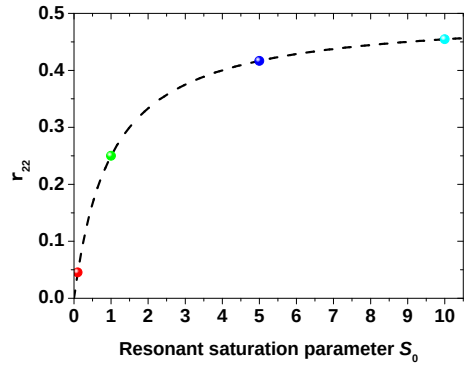

(b) ρ_{22} as a function of the resonant saturation parameter S_0

Figure 2.3: Plot of the function ρ_{22} for different levels of saturation. The levels of saturation indicated in (b) refer to the corresponding coloured Lorentzian function in (a).

The natural linewidth γ is broadened by the intensity of the laser light as illustrated in figure 2.3(a). This effect, called *power broadening*, depends on the saturation of the line. It should be clarified that the general shape of the spectrum does not change.

When the laser frequency is tuned onto resonance ($\delta = 0$) equation (2.36) simplifies to

$$\rho_{22} = \frac{S_0}{2(S_0 + 1)} = \frac{I/I_{sat}}{2(I/I_{sat} + 1)} \,. \tag{2.37}$$

This saturation curve describes the population of the upper state as a function of laser intensity and is illustrated in figure 2.3(b). For high intensities ($S_0 \to \infty$) the population converges towards its maximum, $\rho_{22} \to 1/2$. As a consequence, in a 2-level system the maximum population in the excited state is 50% and no inversion of the population can be achieved.

2.3 Broadening mechanisms

The natural linewidth of an atomic state is the lower limit of resolution for any spectroscopic application. However different mechanisms can broaden the observed linewidth of the transition. One of these mechanisms, power broadening, was explained in the previous section. In addition, when working with pulsed laser sources the frequency spectrum of the laser radiation is typically broader than the natural

linewidth of bound state resonances. Broadening effects may also arise because of non-ideal conditions in the atomic source. For in-source spectroscopy the major contributions come from collisional broadening and Doppler broadening. All these mechanisms will be discussed in the following section. Further information can be found in the literature [1, 2].

2.3.1 Laser linewidth

Thus far excitation by a monochromatic ideal laser has been discussed. However, in particular when working with pulsed lasers one has to take into account the spectral laser linewidth which is usually approximated by a Gaussian distribution of the form

$$I_L(\nu) = I_0 e^{-\frac{(\nu-\nu_L)^2}{2w_L^2}} \tag{2.38}$$

with a linewidth w_L and a centroid frequency ν_L. The situation for a broadband laser such as that of the pulsed laser radiation from the FURIOS laser system is indicated in figure 2.4. In the case of pulsed lasers the laser linewidth ($\sim$ 1 GHz) is usually considerably larger than the natural linewidth γ ($\sim$ 10 MHz). Consequently only the intensity of the laser spectrum at the maximum $\nu = \nu_0$ of the atomic transition can drive the excitation efficiently. The excitation probability ρ_{22} can therefore be approximated by

$$\begin{aligned} \rho_{22}(\nu_L) &\sim \frac{I_L(\nu_0)/I_{sat}}{2(I_L(\nu_0)/I_{sat}+1)} \\ &= \frac{S_L(\nu_0)}{2(S_L(\nu_0)+1)} \,. \end{aligned} \tag{2.39}$$

In conclusion, we can approximate the lineshape of an atomic resonance scanned by a broadband laser with a gaussian spectral distribution by a fit-function of the form

$$\boxed{\begin{aligned} y(\nu_L) &= y_0 + A\frac{S_L(\nu_0)}{2(S_L(\nu_0)+1)} \\ S_L(\nu_0) &= S_0 e^{-\frac{(\nu_0-\nu_L)^2}{2w_L^2}} \end{aligned}} \tag{2.40}$$

where y_0 and A are additional trivial fitting parameters to allow for a constant background and scaling of the overall amplitude of the fit-function. Note that the natural Lorentzian distribution of equation (2.35) has been replaced by the spectral profile of the laser. The FWHM of the spectral function $y(\nu_L)$ can be calculated as

$$\Delta_{FWHM} = 2\sqrt{2}w_L\sqrt{\ln(2+S_0)} \,. \tag{2.41}$$

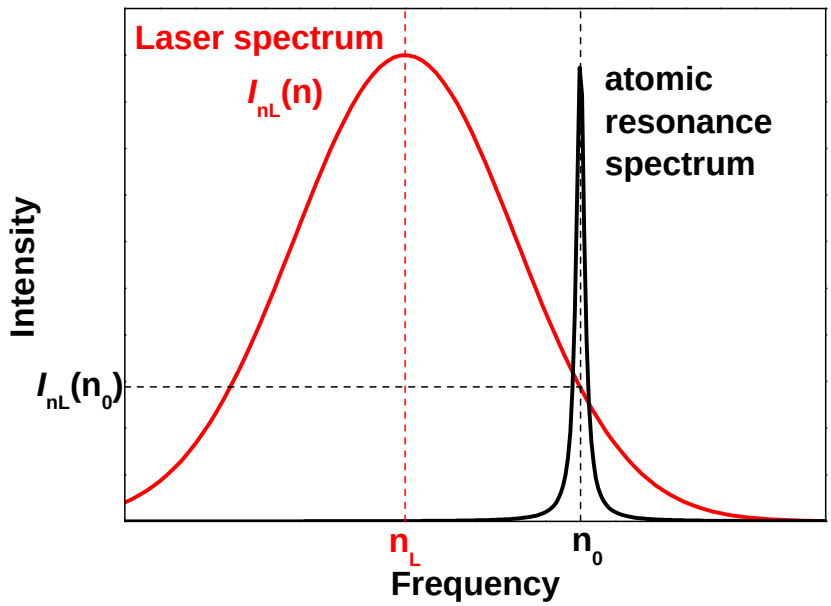

Figure 2.4: Convolution of the laser spectrum and the atomic resonance.

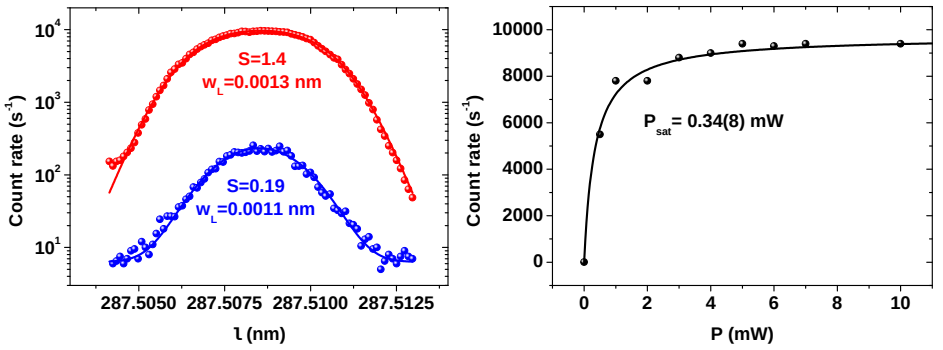

(a) Spectral dependence (b) Intensity dependence

Figure 2.5: Experimental determination of the saturation of the $[Ar]3d^{10}4s^2 4p\ ^2\mathrm{P}_{1/2} \rightarrow 4d\ ^2\mathrm{D}_{3/2}$ transition in gallium.

On resonance the dependence of the ionization signal to the laser power P_L can be calculated,

$$\boxed{\begin{aligned} y(P_L) &= y_0 + A\frac{P_L/P_{sat}}{2(P_L/P_{sat}+1)} \\ P_{sat} &= I_{sat}A_L \end{aligned}} \tag{2.42}$$

where A_L denotes the average area of the laser beam.

An example of an evaluation of experimental spectroscopic data using equations (2.40) and (2.42) is shown in figure 2.5. Figure 2.5(a) shows the result of a 2-step RIS experiment on gallium performed in the atomic beam unit utilizing a frequency-tripled Ti:Sapphire laser beam to drive the excitation from the $[Ar]3d^{10}4s^2 4p\ ^2\mathrm{P}_{1/2}$ ground state to the $4d\ ^2\mathrm{D}_{3/2}$ excited state and the CVL for non-resonant post-ionization. The saturation curve in figure 2.5(b) shows the count rate as function of the first step laser power, while the laser frequency was fixed on resonance. The data was fitted by the function in equation (2.42) and shows a good agreement with the theory. In this case the transition was fully saturated and a saturation power of $P_{sat} \sim 0.34$ mW was extracted. A laser scan was performed for maximum and minimum laser power, equivalent to high saturation and low saturation as shown in 2.5(a). The broadening of the transition at high laser power and the saturation effect of the count rate around the centroid frequency are clearly visible. The average spectral linewidth w_L of about 0.0012 nm from the two fits corresponds to 4 GHz, in agreement with the spectral linewidth of the laser radiation. A direct determination, however, of the saturation parameter from the spectral scan is not possible. At full laser power the fit gives a saturation parameter $S = 1.4$ which is not in agreement with the expected value of

$P/P_{sat} = 10/0.34 \sim 29$. While the shape of the spectral function can give a hint for saturation a precise value for P_{sat} can only be extracted from a saturation curve such as the one in figure 2.5(b).

2.3.2 Doppler broadening

Doppler broadening occurs when the atomic vapour under spectroscopic investigation is in a thermal equilibrium at a temperature T and therefore exhibits a velocity profile which is described by a Boltzmann distribution

$$\frac{dn}{dv} = n_0 e^{-mv^2/2k_BT} \tag{2.43}$$

where n is the density, m the atomic mass, k_B the Boltzmann constant and n_0 a constant. An atom moving with a velocity v away from (towards) the laser radiation sees the laser frequency shifted by the Doppler effect according to

$$\begin{aligned} \nu &= \frac{\nu_L}{1 \pm v/c} \sim \nu_L(1 \mp v/c) \\ v &\sim \pm \frac{\nu - \nu_L}{\nu_L} c \,. \end{aligned} \tag{2.44}$$

Inserting the expression for v into (2.43) yields

$$I(\nu) = I_0 e^{-\frac{mc^2}{2k_BT}\left(\frac{\nu-\nu_L}{\nu_L}\right)^2} \,. \tag{2.45}$$

for the line profile $I(\nu)$. If this effect is the dominant broadening mechanism the observed linewidth is calculated as

$$\Delta\nu_D = \nu_L \sqrt{\frac{8k_BT\ln 2}{mc^2}} \,. \tag{2.46}$$

For the previously mentioned case of gallium (m=69 amu) with a transition wavelength of $\sim$ 287.5 nm and at the typical temperature of the IGISOL buffer gas, 20°C, the Doppler broadening amounts to approximately 1.5 GHz and therefore exceeds the natural linewidth by far. However as it is in the same order of magnitude as the laser linewidth both effects contribute to the total spectrum and a convolution between the spectral function of the laser excitation and the velocity profile of the atomic vapour has to be carried out:

$$A(\nu) = \int_{-\infty}^{\infty} d\nu' I(\nu') N_D(\nu - \nu') \,. \tag{2.47}$$

The shape of the spectral function $I(\nu)$ depends on the laser specifications and can be

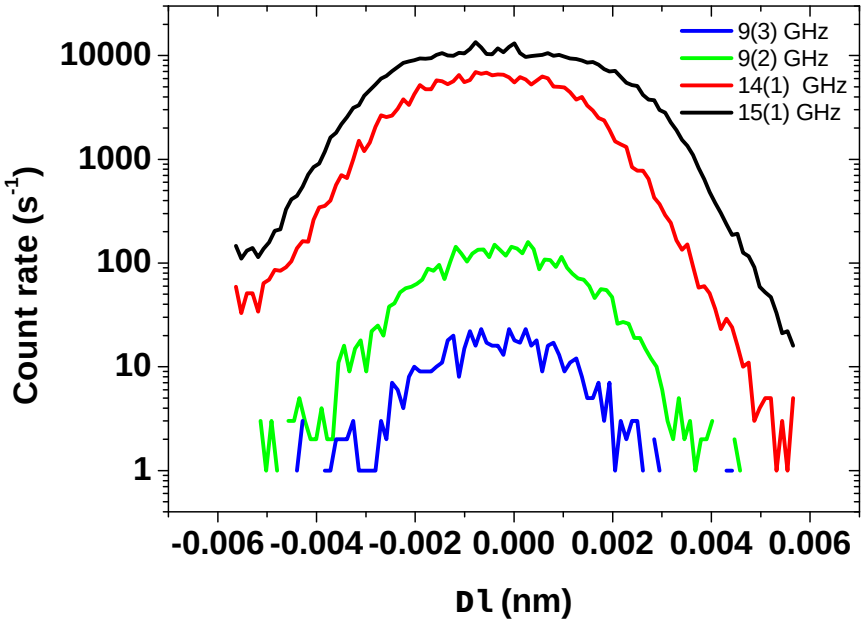

Figure 2.6: Effect of Doppler broadening on laser ionized silver in a hot-cavity ion source. By increasing the oven temperature the Doppler effect is increased.

1. saturated Lorentzian-type (see equation (2.35)) if the transition is power-broadened and the laser linewidth is negligible. The resulting convolution of Lorentzian and Gaussian-type profiles is called a *Voigt profile*.

2. Gaussian-type if the laser linewidth is dominant and the transition is not saturated. The resulting convolution of a Gaussian of width w_L with a Gaussian of width w_D yields a Gaussian function with a total width w

$$w = \frac{1}{\sqrt{\frac{1}{w_D^2} + \frac{1}{w_L^2}}} \,. \tag{2.48}$$

3. saturated Gaussian-type if the transition is broadened by both the laser linewidth and saturation.

An example of the effect of Doppler broadening is shown in figure 2.6. A sample of metallic silver was evaporated in a hot cavity oven described in detail in section 4.7. By increasing the current of the resistively heated oven the velocity distribution is

broadened. The signal saturates at the laser repetition rate of about 10 kHz because of the fast release (some microseconds) of the laser ions from the source. Note that the line was fully saturated and therefore only at a high oven current of about 12 A a significant broadening of the line up to 15 GHz was observed.

2.3.3 Collisional broadening and shift

IGISOL is operated on-line at pressures of $\gtrsim 100$ mbar. Therefore an atom experiences collisions in the vicinity of the buffer gas atoms. A phenomenological description of the theory of the effect of the collisions on the lineshape of the transition is given in [1] however a small overview will be given in this section.

One basically distinguishes between inelastic and elastic scattering processes. The former, so-called *quenching collisions*, lead to a depopulation of the excited state and therefore a line broadening by transferring energy from the collision into internal energy. The latter, so-called *phase-perturbing collisions*, give rise to both a broadening and a shift due to the modulation of the transition frequency by the perturbing gas atom B on the level structure of the atom of interest A.

The presence of a buffer gas leads to a broadening γ and a shift Δ of the line which is usually expressed by cross sections $\sigma_{s,b}$

$$\gamma = 2n_{gas}\langle(\sigma_{b,el} + \sigma_{b,inel})v\rangle \tag{2.49a}$$

$$\Delta = n_{gas}\langle\sigma_{s,el}v\rangle \ . \tag{2.49b}$$

Note that both terms are proportional to the the number density n_{gas} of the buffer gas. The relative velocity between A and the perturber B is denoted by v. The reaction rate $\langle\sigma v\rangle$ is usually averaged over a Boltzmann velocity distribution.

The broadening cross section is split into an elastic scattering cross section $\sigma_{b,el}$ and the depopulation cross section due to inelastic collisions $\sigma_{b,inel}$. Inelastic collisions primarily appear if a resonant energy transfer is achieved such as that in molecules exhibiting a huge number of rotational and vibrational states or in the case of self-broadening where an excited atom A^* collides with a ground state atom A of the same species. This process can be neglected in the gas cell enviroment as the density of the buffer gas exceeds the density of the atom of interest by far.

The cross sections for elastic scattering can be written as

$$\sigma_{b,el} = 2\pi \int_0^\infty (1 - \cos\eta(\rho))\rho \, d\rho \tag{2.50a}$$

$$\sigma_{s,el} = -2\pi \int_0^\infty sin(\eta(\rho))\rho \, d\rho \, , \tag{2.50b}$$

where ρ is the impact parameter and η the semi-classical phase shift due to the interaction potential V between the atom and the perturber. Assuming a straight line trajectory η can be calculated by

$$\eta(\rho) = -\frac{2}{v} \int_\rho^\infty \frac{V(r)}{\sqrt{1 - \rho^2/r^2}} \, dr \tag{2.51}$$

and is only dependent on the interaction potential. For a bound state one usually assumes a Lennard-Jones interaction potential of the form

$$V(r) = \frac{a}{r^{12}} - \frac{b}{r^6} \, , \tag{2.52}$$

where the parameters a and b describe the repulsive and attractive part of the interaction. Values for both broadening and shift in bound states typically reach about $\gamma \sim \Delta \sim \frac{10\,\mathrm{MHz}}{\mathrm{mbar}}$ in He gas at $T \sim 300$ K [1].

In the case of bound electrons in states of high principal quantum number n (Rydberg states, see also sections 2.4.3 and 5.3) the interaction can be simplified [8, 9] and a typical interaction potential can be described by

$$V(r) = -\frac{1}{2}\alpha E(r)^2 + 2\pi L \delta(r - \rho) \tag{2.53}$$

acknowledging the polarization α of the perturber by the electrostatic field E of the positive core and the Rydberg electron and a so-called Fermi contact interaction term proportional to the scattering length L. Kaulakys [9] has shown that only the normalisation and not the shape of the interaction potential defines the size of the effect. A closed form expression [10] for states $n > 30$ for broadening and shift of a Rydberg level includes the polarizibility α and the scattering length L,

$$\gamma = (K_{sc}^\gamma + K_{pol}^\gamma) n_{gas} \tag{2.54a}$$

$$\Delta = (K_{sc}^\Delta + K_{pol}^\Delta) n_{gas} \tag{2.54b}$$

	He	Ar
L	1.19	-1.7
α	1.383	11.08

Table 2.1: Scattering length L and polarizibility α of Ar and He in atomic units for high-lying Rydberg states [10, 11].

with

$$\begin{aligned} K_{sc}^{\Delta} &= 2\pi L \\ K_{sc}^{\gamma} &= \frac{8L^2}{n} \\ K_{pol}^{\Delta} &= -6.22(\alpha^2 v_{cm})^{1/3} \\ K_{pol}^{\gamma} &= 7.18(\alpha^2 v_{cm})^{1/3} \end{aligned} \tag{2.55}$$

where v_{cm} is the center of mass velocity. A list of typical values of L and α for Ar and He [10, 11] for large values of n is given in table 2.1. Both the broadening and shift are typically a few 100 MHz/mbar and therefore exceed the effects of the perturber on the low-lying bound states by an order of magnitude.

2.4 Resonance ionization spectroscopy

The technique of resonance ionization spectroscopy (RIS) [12, 13] was developed in the 1970s. It implies the resonant ionization of atoms by absorption of laser radiation. The excitation energies of the atomic levels provide a unique fingerprint of the atom of interest. Consequently, by applying resonant multi-photon excitation and subsequent ionization high selectivity and high efficiencies in the order of 10% can be achieved [14]. The development of RIS goes hand in hand with the development of powerful and high-resolution pulsed laser systems as described in chapter 3. In this section the general requirements for efficient resonant ionization will be given and thereafter a classification scheme of different types of excitations applying the RIS technique will be explained.

2.4.1 General requirements for RIS

The general task of a laser ion source is to provide an efficient and selective ionization mechanism.

The *selectivity* of the ionization process is defined as the ratio of the ionization produced with lasers on resonance compared to lasers off-resonance. Naturally the se-

lectivity increases by applying a multi-step excitation process involving a maximum number of resonant transitions. Note that the selectivity is not only improved by optimizing the ionization efficiency of the source but also by suppressing unwanted background ions.

The *efficiency* of the ionization process is experimentally hard to determine as it requires the full knowledge of all other related efficiencies of the system such as extraction efficiency and detection efficiency and of possible loss mechanisms. Off-line mass separators equipped with a hot-cavity ion source provide a simple and suitable tool to study the laser ionization efficiency as the sample can be evaporated completely and the produced ions are transported with low losses to the detector. Consequently a lower limit for laser ionization can be given by implanting a known amount of atoms into the source and integrating the total ion yield obtained from the source. Very high total efficiencies up to 40% have been demonstrated [15]. Details of a typical setup are described in [16]. However as these measurements are time consuming they can only be realized at dedicated off-line facilities. At on-line facilities one has to rely in general on the saturation of the transitions to estimate the ionization efficiency.

The density matrix formalism provides a full theoretical description of any atomic system excited by laser light and the according set of partial differential equations such as those in (2.20) can be solved numerically if all parameters (laser intensities, laser beam waists, transition strengths) are known. Outstanding agreement with experimental data [5, 6] can be obtained. Unfortunately, in the majority of experiments, not all parameters are known and therefore approximations have to be made to describe the minimal conditions for efficient resonant excitation in a multi-level scheme.

A general requirement for an efficient RIS scheme is that all resonant transitions should be saturated [12]

$$S_k \geq 1 \quad \forall k \; . \tag{2.56}$$

If all transitions are saturated the population of the different states is statistically determined by the degeneracy g_k of the state $|k\rangle$. The population of the final state in equilibrium is calculated by

$$n_f = g_f / \sum_k g_k \; . \tag{2.57}$$

Consequently an excitation scheme with the highest possible degeneracy of the final state g_f, and therefore a maximum quantum number of orbital angular momentum L gives the highest efficiencies. For example, in the case of a $L = 0$ ground state a scheme of type $S \rightarrow P \rightarrow D \ldots$ is preferred.

2.4.2 Classification of RIS schemes

In this section the different methods of laser excitation will be discussed. Ionization schemes can be classified by several characteristic features:

- the number of radiation frequencies (colours)
- the number of resonant excitation steps
- the type of ionization.

The standard notation introduced in [17] will be used for this thesis:

$$\text{Atom[Excitation steps,Ionization step]Positive Ion .}$$

The following list gives some frequently used examples:

- $A[\lambda_1,\lambda_2,\lambda_1 e^-]A^+$
  Two resonant steps and non-resonant ionization by λ_1
- $A[\lambda_1,\lambda_2,\lambda_3(\text{AI})e^-]A^+$
  Two resonant steps and autoionization by λ_3
- $A[\lambda_1,\lambda_2(\text{Ryd}),Be^-]A^+$
  Two resonant steps into a Rydberg state and collisional ionization by the catalyst B
- $A[\lambda_1,\lambda_2(\text{Ryd}),\text{IR}e^-]A^+$
  Two resonant steps into a Rydberg state and non-resonant ionization by IR laser radiation
- $A[\lambda_1\lambda_1,\lambda_2 e^-]A^+$
  Double-photon excitation by λ_1 and non-resonant photo-ionization by λ_2

The terms λ_k denote the wavelength of the corresponding laser step.

2.4.3 Ionization mechanisms

In this work three types of ionization have been investigated which are illustrated in figure 2.7, namely

(a) non-resonant ionization into the continuum

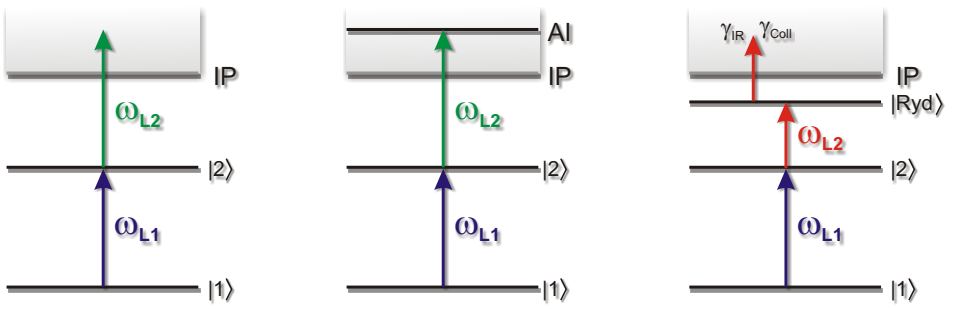

(a) non-resonant ionization (b) autoionization (c) Rydberg ionization

Figure 2.7: Ionization mechanisms used in this work.

(b) ionization via an autoionizing state in the continuum

(c) Rydberg ionization.

As the type of ionization is crucial for the efficiency of the ionization scheme the different mechanisms will be described in this section.

Non-resonant laser ionization

Non-resonant post-ionization is inherently a versatile technique. The drawback however is the relatively low ionization cross section of $\sigma_I \sim 10^{-17}$ cm^2 compared to the cross section for resonant excitation σ_R. The latter can be approximated [1, 7] by

$$\sigma_R \sim \frac{g_2}{g_1}\frac{\lambda^2}{8\pi}\frac{A_{ik}}{\Delta\nu} \sim 10^{-12}\ \text{cm}^2 \tag{2.58}$$

whre A_{ik} is the transition rate, λ the wavelength and $\Delta\nu$ the linewidth of the transition. The quantities g_2 and g_1 describe the degeneracy of the excited and the ground state, respectively. The ionization probability from the highest excited state P_I can be described by an exponential

$$P_I \sim (1 - e^{-\ln 2 P_L/P_{sat}}) \tag{2.59}$$

where P_L is the power of the laser driving the non-resonant transition and P_{sat} the power needed to reach an ionization efficiency of 50%. Figure 2.8 illustrates the non-resonant ionization of gallium of type Ga[287,511/578e^-]Ga$^+$, using the UV first step

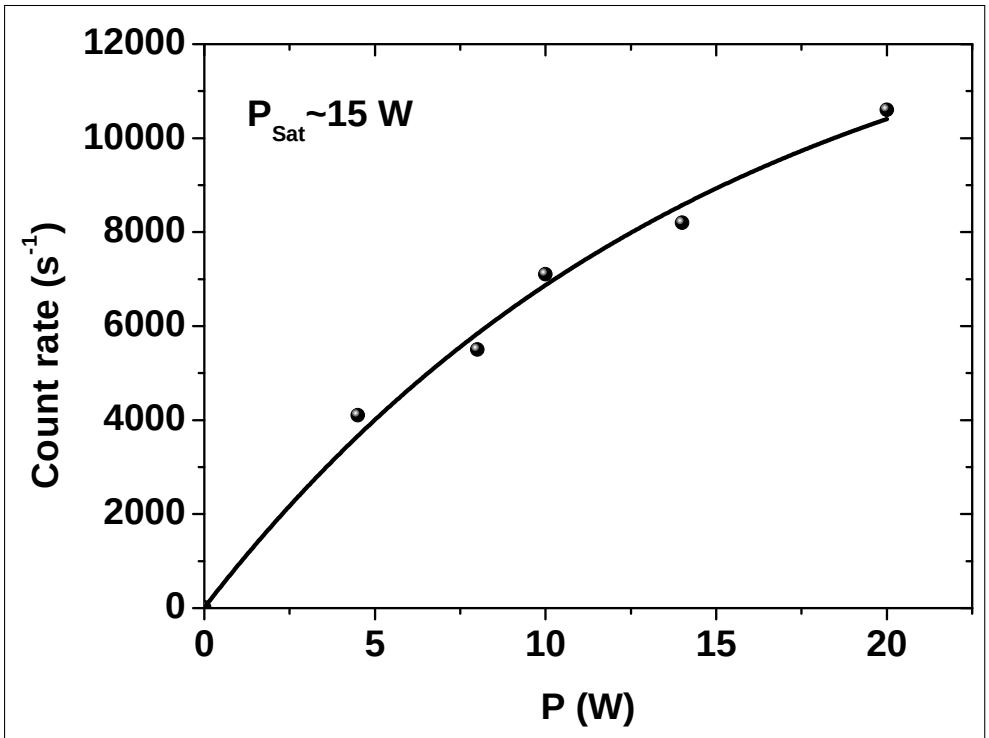

Figure 2.8: Saturation curve of a non-resonant ionization second step provided by the CVL laser beam for gallium. The first step was driven by a UV laser (see figure 2.5).

already shown in figure 2.5 and a CVL pump laser beam as a second step. Note the difference in saturation power of 0.34 mW for the first resonant step (figure 2.5) and for the second non-resonant step (15 W). For the latter case a maximum ionization probability of $P_I \sim 60\%$ can be reached according to equation (2.59), independent of the saturation level of the bound-state transitions.

From figure 2.8 it becomes clear that with the laser power available the ionization efficiency can only be enhanced if the ionization cross section can be increased. One possibility is via the excitation of an autoionizing state.

Autoionization

Autoionization (AI) is based on the excitation of a resonant state which lies energetically higher than the first ionization potential. By addressing this resonance with a laser beam, cross sections of $\sigma_I \sim 10^{-15}$ cm^2 can be obtained. As the cross section is proportional to the transition rate of the state the typical linewidth of an autoionizing resonance is typically one to two orders of magnitude higher than that of a bound state resonance.

Autoionizing configurations arise from multiple-electron excitation in the atom. Perhaps the most intuitive example of strong autoionization is that of the double-excitation in the He atom from the $(1s)^2\ ^1S$ ground state to the $(2s2p)^1P$ excited state. It was verified experimentally by Madden and Codling in the 1960s [18]. More information on the theoretical description of autoionizing resonances can be found in [19, 20]. A resonance scan and a saturation profile of a strong AI state observed by applying a three color excitation scheme in tin using Sn[286,812,824(AI)e^-]Sn^+ is shown in figure 2.9. Due to the fast ionization mechanism the resonance exhibits a huge full-width at half maximum value of 127(8) GHz which is completely dominated by the natural linewidth. Therefore the shape can be best described by a Lorentzian function. Compared to non-resonant ionization the laser ion signal was improved by more than two orders of magnitude.

The saturation profile shown in figure 2.9(b) was approximated by a combination of a resonant saturation function and a linear function

$$A(P) = y_0 + A_0 \frac{P/P_{sat}}{2(P/P_{sat}+1)} + m \cdot P \tag{2.60}$$

to acknowledge both the non-resonant ionization into the continuum and the autoionization process. A saturation power P_{sat} of about 60 mW and a slope m of 1.5 nA/W can be extracted from the data showing the full saturation of the AI step and only a slight contribution via the path of non-resonant ionization. Note the apparent difference in saturation power of the final step compared to the non-resonant saturation

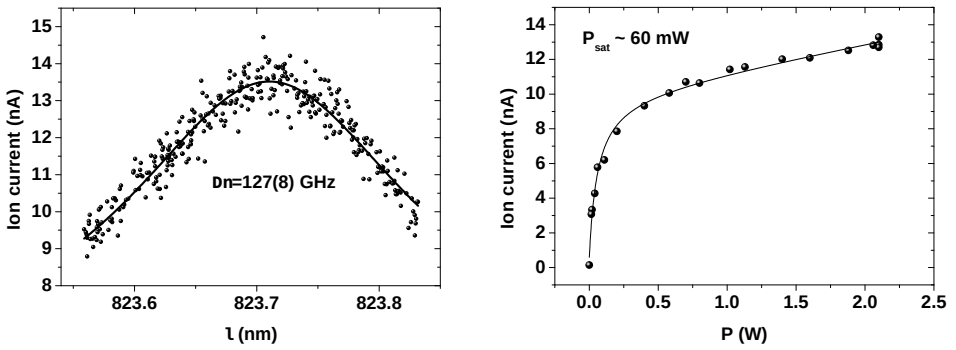

(a) Resonance scan (b) Saturation curve

Figure 2.9: Resonance ionization via an AI state in Sn.

shown in figure 2.8. The dataset in figure 2.9 has been recorded in a follow-up of an experiment at the Off-line mass separator of the Holyfield Radioactive Ion Beam Facility at ORNL (USA) using a hot-cavity ion source. More details on the experimental setup can be found in [16] and in section 5.3.

Rydberg ionization

A third ionization mechanism is that via a Rydberg state. Rydberg states are atomic levels with a high quantum number n energetically close to the ionization potential.

For Rydberg-states the binding potential of the electron can be described by a central potential modifed by the screening of the nuclear charge by the shell electrons and the corresponding binding energy by the Rydberg formula

$$E_n = E_{IP} - \frac{R_M}{(n - \delta(n,l))^2} \ , \tag{2.61}$$

where $\delta(n,l)$ denotes the quantum defect and R_M the Rydberg constant, given by

$$R_M = \frac{M}{m+M} R_\infty \ . \tag{2.62}$$

Here, m and M are the electron and nuclear masses, respectively. Ionization of these highly excited atoms can easily be achieved by electrostatic fields, IR radiation or collisions. These options will be described in the following paragraphs.

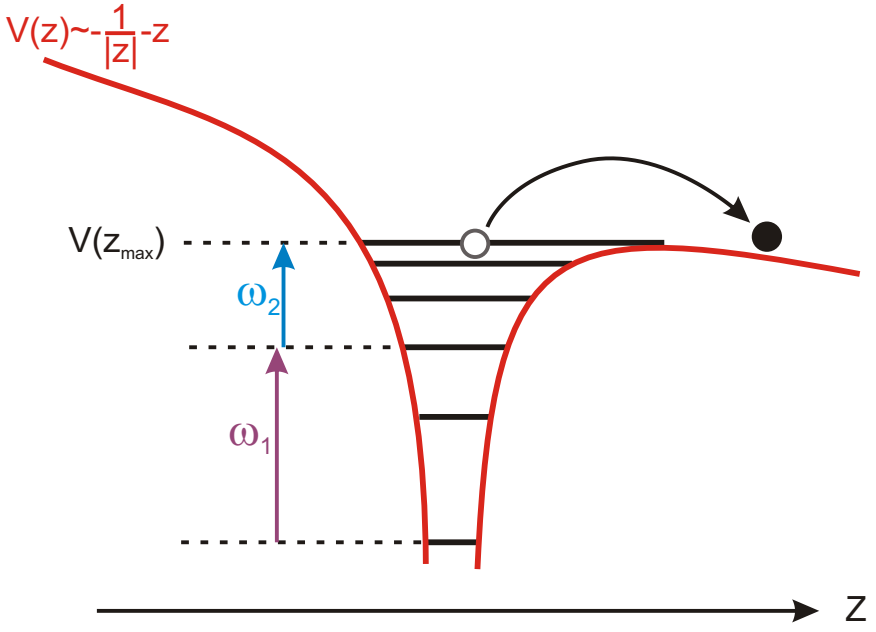

Figure 2.10: Illustration of Rydberg ionization by an electrostatic field.

Field ionization can be easily depicted by the classical saddle point approach [12]. In a strong electrostatic field aligned to the z-axis the potential of the bound electron can be described by

$$\begin{aligned} V(z) &= -\frac{e^2}{4\pi\epsilon_0 r} - Eez \\ &= -\frac{\alpha\hbar c}{r} - Eez \end{aligned} \tag{2.63}$$

as shown in figure 2.10. The local maximum of the potential lies along the z-axis at $z_{max} = \sqrt{\alpha\hbar c/(eE)}$ with a maximum value of

$$V(z_{max}) = -2\sqrt{eE \cdot \alpha\hbar c}\,. \tag{2.64}$$

The unperturbed energy levels of a Rydberg electron can be approximated by those of a hydrogen atom with an excitation energy of

$$E_n = -mc^2\alpha^2 \frac{1}{2n^2}. \tag{2.65}$$

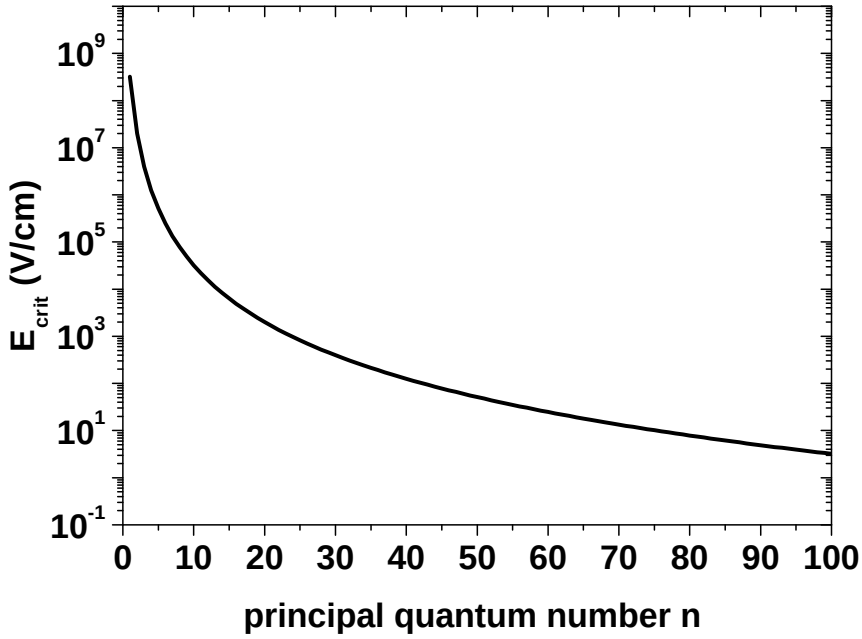

Figure 2.11: Critical electrostatic field needed to ionize a Rydberg atom in state n.

Comparing the binding energy E_n with the maximal binding energy of equation (2.64) we obtain the critical field needed to ionize an electron in state n

$$E_{crit} = \frac{(mc^2)^2\alpha^3}{\hbar ce}\frac{1}{16n^4} \,. \tag{2.66}$$

A plot of this function is shown in figure 2.11. An ionization experiment involving resonant excitation by lasers and subsequent pulsed field ionization is given in [21]. While no saturation of the ion signal could be obtained for non-resonant laser ionization an immediate full saturation was reached as soon as the field strength exceeded the critical value required for ionization.

In a similar experiment [22] $n = 31$ Rydberg atoms of sodium were ionized by a pulsed field at a voltage of approximately 460 V/cm. For a Rydberg level with $n = 40$ a field strength of $\sim$400 V/cm is needed to reach ionization. These field strengths are only available in the extraction region of the IGISOL, not in the buffer gas cell itself. Consequently field ionization can only be carried out in the buffer gas cell if an additional pulsed electrostatic field is applied. The ion guide introduced in section

4.5 is capable of providing an additional voltage and would be suitable to test field ionization in the buffer gas.

Photo-ionization can easily be accomplished by high power infrared laser radiation. The cross section for photo-ionization from a Rydberg state is [23]

$$\sigma_{ni} = \frac{64\pi}{3\sqrt{3}}\alpha \left(\frac{E_{IP}}{\hbar\omega}\right)^3 \frac{a_B^2}{n^5} \tag{2.67}$$

where E_{IP} is the ionization potential, α the fine-structure constant and a_B the Bohr radius. Naturally a minimal requirement for ionization is $\hbar\omega > E_{IP}/n^2$. The ionization cross section is inversely proportional to the laser frequency and reaches a maximum value at

$$\begin{aligned} \sigma_{ni}^{max} &= \frac{64\pi}{3\sqrt{3}}\alpha a_B^2 n \\ &\sim 10^{-17} n \text{ cm}^2 \, . \end{aligned} \tag{2.68}$$

Collisional ionization from an excited state in an atom A by collisions with buffer gas atoms of type B is based on the transfer reaction

$$A^* + B \rightarrow A^+ + B + e^- \, . \tag{2.69}$$

An extensive theoretical treatment of this process is given in [24, 25]. For highly excited electrons the problem can be treated in the basis of general scattering theory and the following expression can be obtained for the ionization cross section of a Rydberg atom in a state n

$$\begin{aligned} \sigma &= \frac{8}{3\pi}\frac{\sigma_{eB}^{el} n_{eff}}{v_B}\sqrt{\frac{2E}{\mu}}\left(1 - \frac{|E_n|}{E}\right)^{3/2} \quad \text{with} \\ v_B &= \alpha \cdot c \\ \sigma_{eB}^{el} &= 4\pi L^2 \\ E_n &= \frac{1}{2n_{eff}^2} m_e c^2 \alpha^2 \, . \end{aligned} \tag{2.70}$$

To obtain an average cross section the energy E of the atoms B can be approximated by the Boltzmann velocity

$$E = 3/2 k_B T \tag{2.71}$$

and the last term can be approximated by $|E_n|/E \sim 0$ for high-lying Rydberg states to obtain

$$\sigma = \frac{8}{\sqrt{3}\pi}\sigma_{eB}^{el} n_{eff}\sqrt{\frac{k_B T}{\mu v_B^2}} \,. \tag{2.72}$$

The cross section on its own is pressure independent. To obtain a reaction rate $\langle\sigma v\rangle$ the cross section has to be averaged over a thermal Boltzmann distribution as done in [24] and multiplied by the gas density $n_{gas} = P/(k_B T)$

$$A = \langle\sigma v\rangle n_{gas} = \frac{8}{\pi}\sigma_{eB}^{el} n_{eff}\frac{k_B T}{\mu v_B} e^{-E_n/(k_B T)} \cdot n_{gas} \tag{2.73}$$

$$= \frac{8}{\pi}\sigma_{eB}^{el} n_{eff}\frac{P}{\mu v_B} e^{-E_n/(k_B T)} \,. \tag{2.74}$$

Note that there is only a slight temperature dependence in the exponential which disappears for $E_n \ll k_B T$ and a linear pressure dependence. The formula is valid for high-lying Rydberg states obeying $l \ll n$. The term σ_{eB}^{el} is the total cross section for elastic scattering of the low-energy electron by buffer gas atoms and μ the reduced mass of the buffer gas and the atom of interest. The terms α, v_B and E_n denote the fine-structure constant, the Bohr velocity and the Bohr energy respectively. n_{eff} denotes the effective quantum number, defined by

$$n_{eff} = n - \delta \tag{2.75}$$

acknowledging for a shielding δ of the nuclear charge by core electrons. L represents the scattering length of the buffer gas and in the case of helium is calculated as

$$L_{He} = 1.19 \cdot a_B \sim 0.6 \text{ Å} \tag{2.76}$$

where $a_B = \hbar/(\alpha mc)$ is the Bohr radius. A graphical representation of the equations (2.72) and (2.74) for the example of an $A = 100$ atom in He gas is given in figure 2.12. IGISOL-type ion sources are operated at room temperature and therefore lower ionization cross sections are expected. However from experiments applying collisional Rydberg ionization of Rb and He atoms in noble gases [26–28] it could be shown that by increasing the buffer gas pressure in the cell signal saturation of the ion signal could be reached. A detailed description of the experiments dealing with Rydberg ionization in this thesis is given in section 5.3 and 5.4.

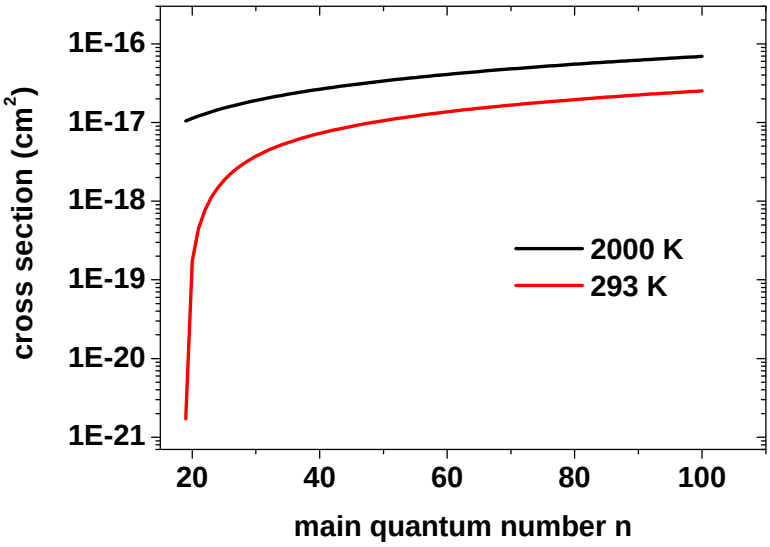

(a) cross section

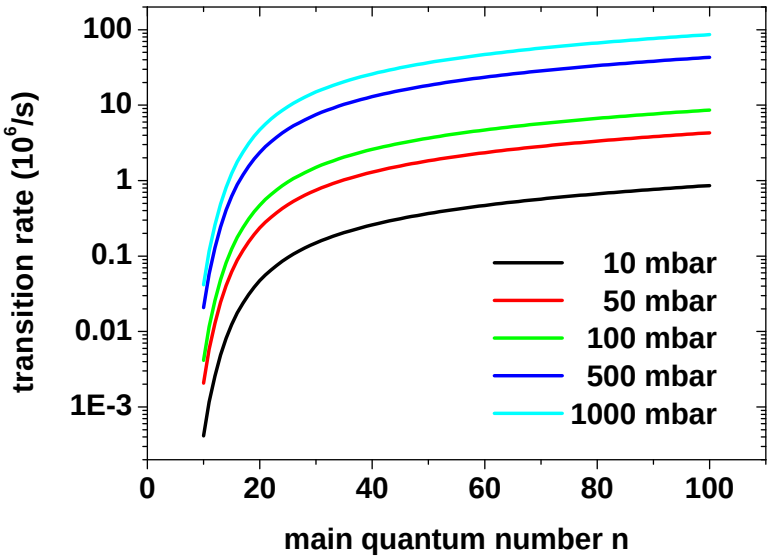

(b) transition rate

Figure 2.12: Theoretical cross section and transition rate for collisional ionization of an $m = 100$ amu atom in a He buffer gas.

3 Laser development

The Furios laser system is a unique system for resonance ionization as it employs both high-repetition rate pulsed Ti:Sapphire and Dye lasers. The typical linewidth for these lasers is ∼5 GHz and suitable for high-efficiency RIS. The wavelength range was further extended by the generation of higher harmonics. A full description of the laser system can be found in section 3.1. For applications requiring highest spectral resolution the linewidth of the system is not sufficient. In consequence a seeded pulsed Ti:Sapphire laser was developed and is described in section 3.1.3. The features of a LabView based control program for the laser system are introduced in section 3.2 followed by a description of a mechanical shutter system for the temporal control of the laser pulses in section 3.3. In the final section 3.4 an off-line atomic beam unit for resonance ionization spectroscopy of stable isotopes is described.

3.1 FURIOS laser system

The basic requirements of a laser system for a laser ion source are:

- high efficiency
- elemental selectivity
- universality.

A high laser ion source efficiency can be provided if saturation of all resonant transitions is achieved, which can only be fulfilled by pulsed laser radiation. To avoid large duty cycle losses, lasers with a relatively high repetition rate, typically between 100 Hz and 10 kHz are used. The elemental selectivity is provided by matching the spectral linewidth of the laser to the spectral width of the transitions investigated in the source, typically reaching values of about 1 GHz. In addition, by applying widely tunable laser radiation a maximum wavelength coverage can be reached. Finally, reliable long-term operation with negligible maintenance has to be demanded.

To fulfill all requirements a twin laser system was constructed at the University of Jyväskylä [29] consisting of a solid-state Ti:Sapphire laser system and a set of dye lasers, each with independent pump lasers. The lasers will both briefly be described in sections 3.1.1 and 3.1.2.

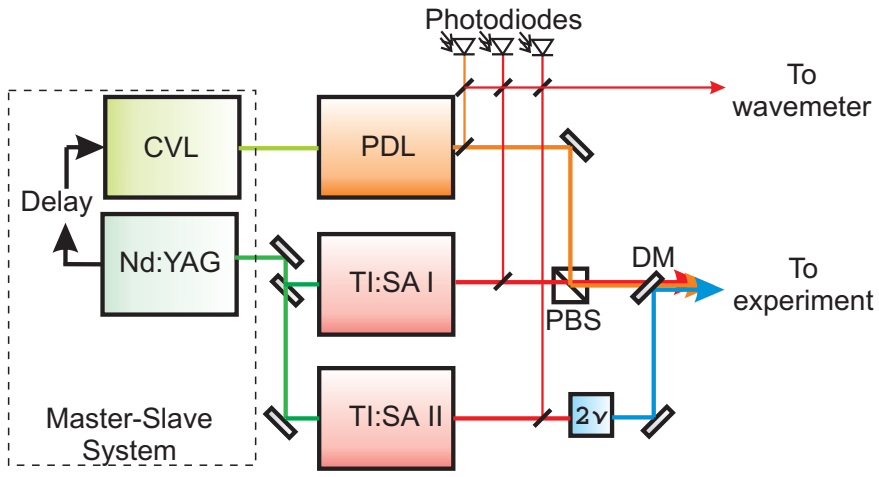

Figure 3.1: Typical setup of the lasersystem for a RIS application.

In a typical experiment involving resonant laser ionization at IGISOL, two or three laser beams have to be overlapped spatially and the different laser pulses need to be overlapped in time. A typical laser setup for a RIS experiment is shown in figure 3.1. The master clock of the system is provided by the Q-switch trigger of the Nd:YAG laser which is fed through a gate-and-delay unit to the copper vapour laser. After possible higher harmonic generation using non-linear optics the beams are overlapped in space either by using polarizing beam splitters or dichroic mirrors. For monitoring the wavelength and the temporal overlap of the laser pulses glassplates can be inserted into the beam-path of each laser reflecting about 1% of the radiation. The position of the glassplates can be remotely controlled by the shutter mechanism described in section 3.3. The temporal overlap is monitored using fast photodiodes[1] while the wavelength is measured using a commercial wavemeter[2]. The Ti:Sapphire lasers can be controlled and monitored remotely by a program written in LabView which is introduced in section 3.2.

3.1.1 Ti:Sapphire laser system

The first laser system, an all-solid-state system, has been developed in collaboration with the University of Mainz. A detailed description can be found in [30, 31]. The

[1] Roithner Laser-Technik SSO-PD-Q-0.25-5-SMD
[2] Wavestar High Finesse LM7

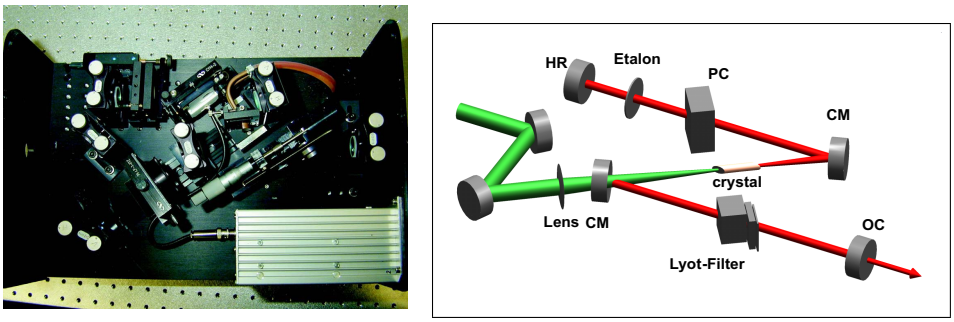

Figure 3.2: Picture and schematic diagram of the Ti:Sapphire cavity.

laser system consists of a high repetition rate (10 kHz) diode-pumped Nd:YAG laser[3] with up to 100 W average laser power in the second harmonic, pumping three tunable Ti:Sapphire lasers. Figure 3.2 shows a photograph and a schematic of the Ti:Sapphire cavity. The basic setup corresponds to an astigmatism-compensated Z-cavity, consisting of a planar high-reflector, two curved mirrors (radius of curvature 75 mm) and a wedged output coupler with a transmission of 70-80%. The pump beam is focussed by a lens with a focal length of 88 mm onto a brewster-cut Ti:Sapphire crystal positioned between the two curved mirrors. The absorption of the crystal to 532 nm laser radiation amounts to $\alpha = 1.5$ cm^{-1} with a figure of merit of 150. Each laser contains a Lyot filter (100 THz free spectral range) and an etalon (300 GHz free spectral range) for generation of narrow bandwidth laser radiation of $\sim$5 GHz. The laser pulses can be synchronised by inserting a pockels cell into the cavity serving as a Q-switch. It operates at a quarter-wave voltage of approximately 3.75 kV which is switched off with ns timing by two MOSFET switches being controlled via a standard TTL logic. A typical output power of $\sim$2 W can be achieved.

The wavelength tuning range can be extended by an appropriate choice of the coating of the cavity mirrors as shown in figure 3.3. Two mirror sets were purchased for the FURIOS laser system centered at 750 nm and 850 nm for the high reflector and the two curved mirrors. The wavelength coverage of each mirror set can be further extended by inserting an output coupler centered at the wavelength required as indicated in figure 3.3.

One of the Ti:Sapphire lasers was upgraded with a double-sided pumping technique as described in [32]. In this manner the crystal can be pumped at higher input powers without reaching the damage threshold of $\sim$1 J/cm^2 [33]. Figure 3.4(a) shows a schematic of the double-pumping principle. Figure 3.4(b) illustrates the conversion

[3] Lee Laser LDP-200MQG

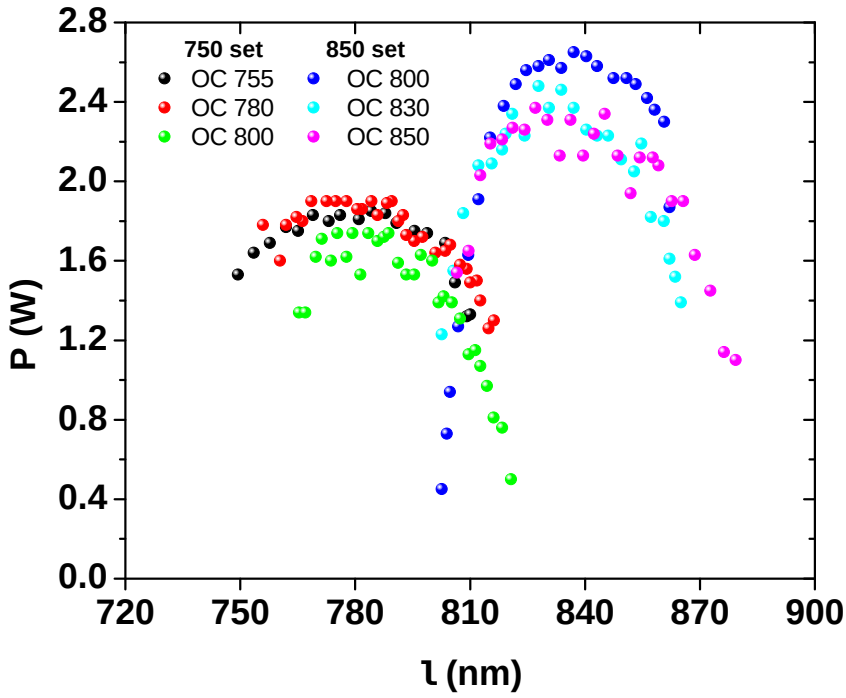

Figure 3.3: Overview of the wavelength tuning range of the FURIOS Ti:Sapphire lasers.

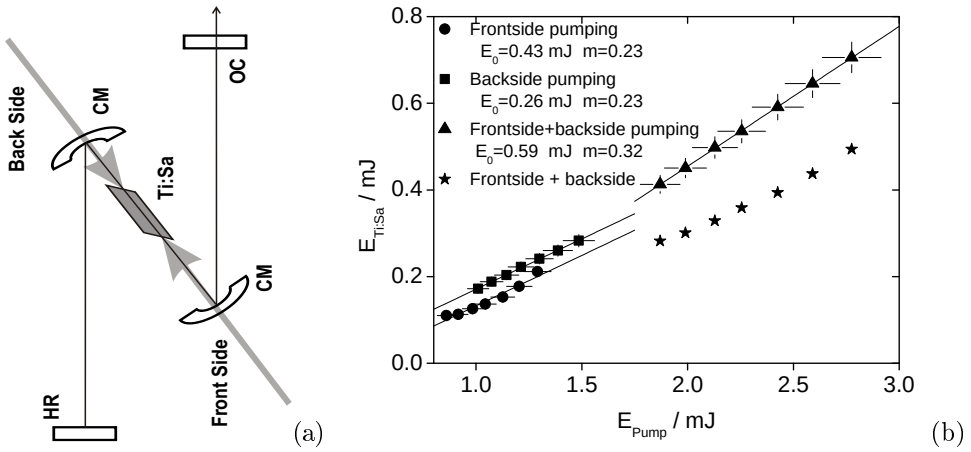

Figure 3.4: (a) The double-sided Ti:Sapphire laser. HR = high reflector, CM = curved mirror, Ti:Sa = Ti:Sapphire crystal, OC = output coupler. (b) Conversion efficiencies for the double-sided Ti:Sapphire laser.

efficiency for the double-sided pumping cavity compared to that of a standard single-sided laser. The energy of the pump laser was varied by adjusting the repetition rate from 7 to 10 kHz in steps of 0.5 kHz. The circles and squares correspond to the output energy obtained by pumping the crystal from the front and rear side respectively. The triangles correspond to the output pulse energy obtained when pumping both sides at the same time. A linear fit of the form

$$E_{out} = (E_{in} - E_0) \cdot m \tag{3.1}$$

was applied to the data, where m is denoted as the slope conversion efficiency and E_0 the lasing threshold. The extracted coefficients are shown in the figure.

The result of the fitting shows an increase in the conversion efficiency for the double-sided pumping with a maximum value for the output energy of 0.7 mJ/pulse. This value can not be obtained with single-sided pumping due to the damage threshold of the Ti:Sapphire crystal. The lasing threshold E_0 for the front-side pumping is higher than for the back-side since the overlap of the pump-beam with the laser-mode is optimized for this side.

A comparison between the double-sided pumped cavity with the sum of the two single-sided cavities (indicated by stars in figure 3.4(b)) suggests that the double-sided Ti:Sapphire laser is more efficient [6]. This can be explained by the fact that the same lasing threshold has to be surpassed for both the single-sided and the double-sided cavities. Consequently the inversion gain due to back-side pumping directly

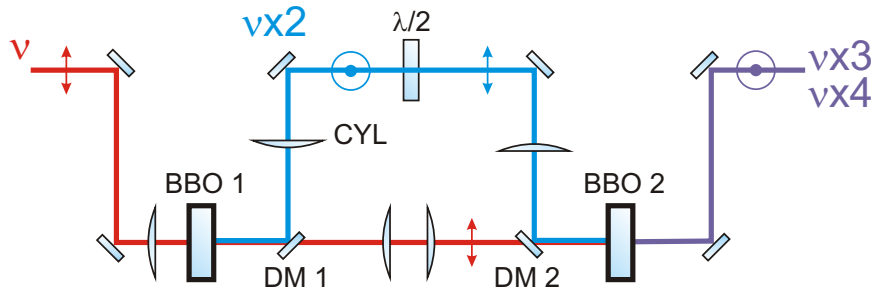

Figure 3.5: Schematic diagram of the frequency-mixing unit.

contributes to the laser process. During a high power test up to 5 W output power was obtained with a total input power of 28 W at a typical repetition rate of 10 kHz.

The range of the Ti:Sapphire laser is extended by higher harmonic generation, using non-linear crystals of type BBO and LBO[4]. For pulsed lasers the frequency conversion can be done in a simple single-pass configuration without the need for an enhancement cavity. For that purpose a unit for applying frequency-doubling/tripling and quadrupling techniques has been realized. A schematic diagram of the setup is shown in figure 3.5. The fundamental Ti:Sapphire laser beam is focussed onto the first BBO-type crystal (BBO1), producing typically 200 mW of frequency-doubled laser radiation in a wavelength range of ∼350-470 nm. The second harmonic beam is then split from the non-converted fundamental radiation by a dichroic mirror (DM1), reshaped subsequently by a cylindrical lens (CYL) and p-polarized by a $\lambda/2$ phase-retardation plate. Both the fundamental and the second harmonic beam are finally overlapped again by DM2 and focused onto a BBO-type crystal for sum-frequency generation of typically 30 mW of ultraviolet laser radiation in a wavelength range of ∼230-320 nm. Alternatively the second harmonic can be frequency-doubled in BBO2 to extend the coverage of the UV part of the optical spectrum down to 180 nm. The efficiency for this process is comparable to the third harmonic generation.

3.1.2 Dye laser system

A gap in the optical spectrum remains in the visible region between 500 and 700 nm. One possibility to fill this gap would be difference frequency-mixing of the second harmonic beam of a Ti:Sapphire laser with the fundamental beam of a Nd:YAG laser at 1064 nm, a technique currently under development at the University of Mainz. An

[4]Fujian Castech Crystals, Inc. See `http://www.castech-us.com/` for details

alternative approach utilized by the FURIOS project uses a pulsed dye laser system to deliver laser light in the visible region.

The first laser ion source for on-line production of radioactive nuclei was established at ISOLDE, CERN (Geneva) [34]. A system of dye lasers pumped by copper vapour lasers (CVL) has been the working horse since the early 1990s and has proven its reliability and versatility, delivering beams of close to 30 species [14, 35]. The RILIS laser ion source is the most often used ion source at ISOLDE delivering ion beams for ∼50% [36] of the approved beamtime.

A similar system has been installed at the IGISOL facility during this thesis work. Both a high repetition rate (10-15 kHz) 50 W copper vapour laser[5] and a low repetition rate (10-50 Hz) externally frequency doubled and post-amplified Nd:YAG laser[6] are used as pump lasers. The setup comprises a commercial pulsed dye laser (PDL)[7] and a pulsed dye amplifier (PDA)[8]. The PDL consists of an oscillator cavity tuned by a grating mounted in a Littrow configuration and a single-pass amplification stage installed after the cavity to increase the average output power of the dye laser to up to 500 mW on the peak of the dye tuning curve at an input power of typically 20 W. An increase in the conversion efficiency can be achieved by increasing the dye pumping speed as discussed in [37]. The laser can be scanned by a control software written in LabView.

For specific applications such as in-source laser spectroscopy a high spectral resolution combined with high laser intensities is a requirement. The PDA system primarily fulfills the first requirement by applying an external seeding technique. A narrow linewidth commercial continuous wave ring dye laser[9] was chosen as a seed laser, locked to an absorption peak of an iodine vapour, permitting long term stability with a linewidth of a few MHz. The seed beam is injected into a sequence of up to three dye cells in the PDA pumped by one of the pulsed pump lasers, therefore providing pulsed amplification of the continuous laser beam. The resulting spectral bandwidth of the pulses of typically 50 MHz provides access to the hyperfine structure and isotope shift of most of the elements on the periodic table.

3.1.3 Development of a seeded Ti:Sapphire laser

The technique of pulsed amplification of a continuous seeded laser beam with a narrow bandwidth in a single pass can only be realized for high-gain media such as dyes with an optical cross section for stimulated emission of $\sigma \sim 10^{-16}$ cm^2 [38]. Due to the long

[5] Oxford Lasers LM100X(KE)
[6] Spectron Laser Systems: SL801-50
[7] Spectra Physics Quanta-Ray PDL 1
[8] Spectra Physics Quanta-Ray PDA 1
[9] Spectra Physics 380D

lifetime of the Ti:Sapphire excited laser level and the resulting comparably low optical cross section for stimulated emission of $2.8 \cdot 10^{-19}\text{cm}^2$ [38] a single-pass amplification of the continuous laser beam is not suitable for this medium. For low repetition rates (1-100 Hz) seeded Ti:Sapphire multi-pass amplifiers, similar in design to the standard PDA layout described in section 3.1.2, have been developed [39]. For high repetition rates seeding of a pulsed Ti:sapphire laser with narrow bandwidth radiation from a continuous wave laser can be applied. The basic principle is that rather than introducing losses to unwanted modes by placing frequency-selective elements into the bare laser cavity as described in section 3.1.1, the number of photons of a wanted frequency is enhanced by injecting a single-mode continuous wave laser beam into the cavity. Seeding operation is obtained when the seeded mode wins the competition against the modes naturally occurring by spontaneous emission of the Ti:Sapphire crystal after the population-inversion has been obtained. Therefore not only is a suitable laser power of the master laser needed but a good overlap between the mode of the slave cavity and the injected beam and a mechanism to lock the cavity length of the slave laser to the injected laser beam are mandatory. A detailed review of the theory of the technique is given in [40].

For Ti:Sapphire lasers this approach has been demonstrated in various publications [41–45] again generally for low repetition rate systems well below 1 kHz. The operation at repetition rates as high as 10 kHz requires tight focussing of the laser mode to obtain a reasonable conversion efficiency of the slave laser system. Another requirement for the design of the seeded Ti:Sapphire laser for the FURIOS laser system was the capability to use the optics for the standard Ti:Sapphire cavity to save costs. The cavity needed to be redesigned into a ring laser to avoid spatial hole-burning [38]. A bow-tie cavity was chosen.

A detailed description of the cavity and its performance can be found in [46]. A schematic of the setup is shown in figure 3.6(a). The cavity is formed by an output coupler with a transmission of typically 20% (M1), two curved mirrors (M2 and M3) and a high-reflector (M4) mounted on a piezo actuator (P). The Ti:Sapphire crystal, with a length of 2 cm and an optical absorption coefficient of $\alpha = 1.5\ \text{cm}^{-1}$ is placed at a distance of 5 cm from M2 to achieve a mode matching with the pump laser beam. To ensure the stability of the cavity a mode calculation routine following the ABCD matrix formalism [47] was written in Mathematica [48]. The result of the calculation is shown in figure 3.6(b). The vertical lines mark the positions of the mirrors starting from M1. A solid (dashed) line represents the mode in the saggital (tangential) plane.

To maintain the rather compact design and reduce the costs of the laser setup a home-built external cavity diode laser (ECDL [49]) was chosen as the master laser. Laser diodes are commercially available for the complete infrared optical spectrum[10]. A disadvantage is the somewhat limited tuning range of a single laser diode (10 to 50

[10] see for example `http://www.roithner-laser.com/LP-laserdiodesIR.htm`

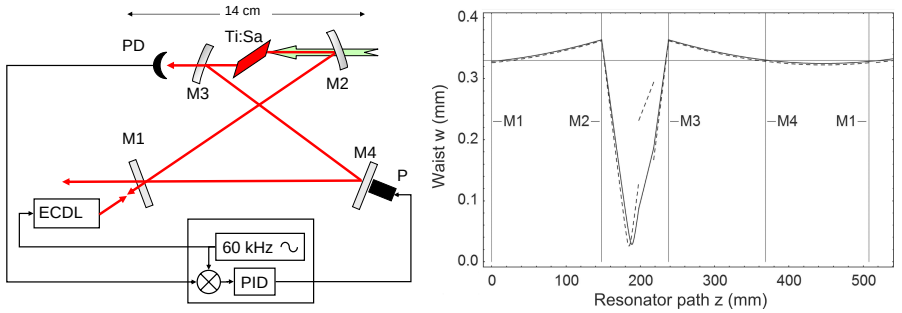

(a) Sketch of the setup (b) ABCD mode calculation

Figure 3.6: General design of the ring-cavity laser.

nm). This disadvantage can be circumvented by using a continuous wave Ti:Sapphire laser[11] as the master laser. In tests at the University of Mainz both systems gave a comparable performance, however in this work only the results obtained with an ECDL are shown.

The Ti:Sapphire cavity is locked to the diode laser frequency via a standard dither lock system [50] schematically shown in figure 3.6(a). The ECDL diode current is modulated by a frequency generator operating at 60 kHz, resulting in a modulation of the diode laser frequency of approximately 1 MHz. The same signal is fed into a phase-sensitive detector together with a photodiode signal (PD) detected from leakage behind mirror M3. The resulting feedback signal is fed through a PID controller into the piezo actuator, which regulates the cavity length to maximize the transmission of the seeding light onto the photodiode. To avoid saturation of the photodiode positioned behind mirror M3 by the high intensity light of the pulsed Ti:Sapphire laser an additional electronic circuit triggered by the pump laser clock was installed. During the duration of the Ti:Sapphire laser pulse the photodiode was shorted and the subsequent amplifier turned off. Both electricial circuits are described in more detail in appendix A.

The diode laser can be locked to an external frequency standard and scanned by tuning the grating mounted in a Littrow-configuration. Both a commercial locking system[12] and a fringe-offset locking technique [51] were applied. An overview of the performance of the laser system is given in table 3.1. The values were obtained without any additional frequency-selective element in the cavity with a laser diode[13] operating

[11] Coherent MBR-110
[12] TEM-Messtechnik: IScan. See `http://www.tem-messtechnik.de/en/products/iscan_en.htm`
[13] Eagleyard Photonics: EYP-RWL-0940-00100-1500-SOT02-0000.

Performance characteristic	Value
Seeding efficiency	∼90%
Mode	TEM_{00}
x/y beam waist (20 cm distance from cavity)	0.835(2)/0.909(2) mm
Pulse length	∼50 ns
Finesse of the cavity	6(1)
Laser efficiency (seeded)	18(2)%
Spectral linewidth	20 MHz

Table 3.1: Performance of the seeded Ti:Sapphire laser.

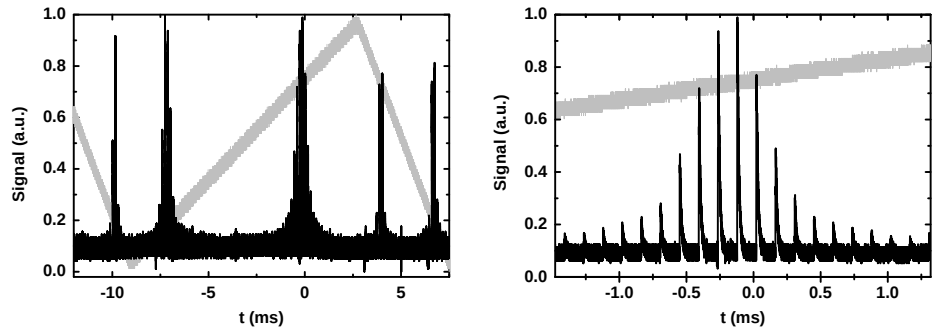

Figure 3.7: Oscilloscope trace of the seeded Ti:Sapphire laser in a 300 MHz FPI. The spectral linewidth is ∼20 MHz. The grey line shows the ramping signal of the piezo actuator of the FPI.

at an output power of approximately 1 mW. This power is needed to get a sufficient signal from the photodiode to obtain a stable lock. The general performance of the Ti:Sapphire laser is comparable to the standing wave system described in section 3.1.1. The striking difference is the spectral linewidth which was reduced by more than 3 orders of magnitude. Figure 3.7 shows an oscilloscope trace of the seeded ring laser in a Fabry-Perot interferometer (FPI) with a free spectral range of 300 MHz. The trace shows sharp resonance indicating the high resolution of the pulsed laser system. The more detailed view shows a single resonance. The sub-structure represents the single laser shots occurring at a repetition rate of 7 kHz. The full-width at half maximum (FWHM) corresponds to a linewidth of approximately 20 MHz. A review of the realization of the seeded Ti:Sapphire laser cavity for the application of in-source spectroscopy can be found in section 5.5.

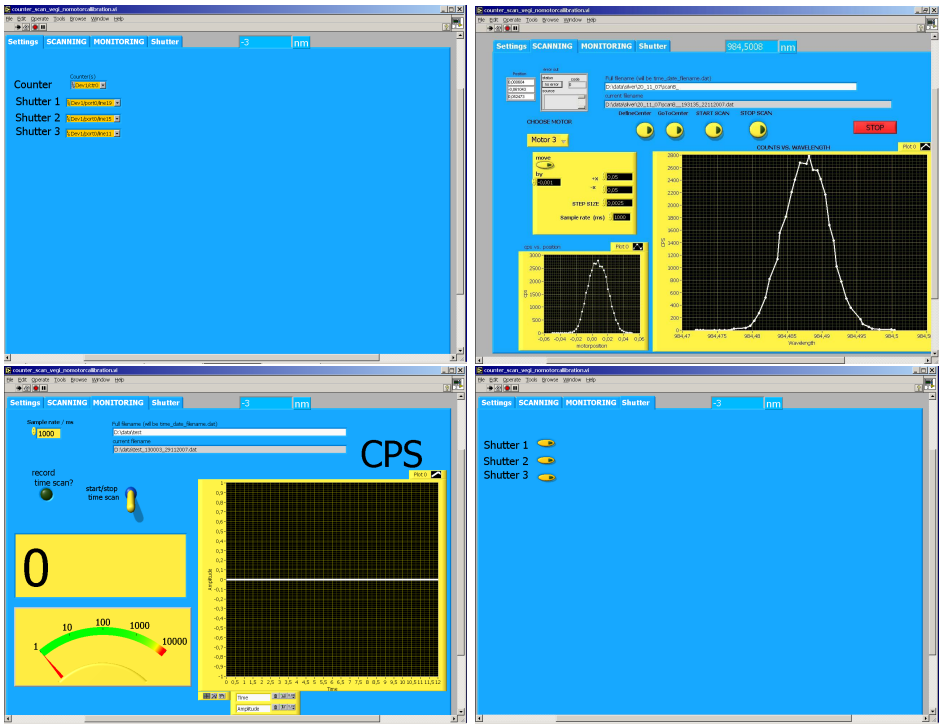

Figure 3.8: LabView control interface for the Ti:Sapphire laser system.

3.2 LabView monitoring program

Continuous remote monitoring of the wavelength and the temporal overlap of the laser pulses is a mandatory requirement as in on-line experiments stable running conditions are needed for the full duration of the experiment. For that purpose a LabView routine was written to monitor and adjust the wavelength of the lasers and to monitor the temporal overlap of the laser pulses. A standard PC equipped with a data aquisition card[14] with 32 digital I/O channels and four 32-bit counters was taken as a control interface. Figure 3.8 shows the front-end of the control interface. The program is split into four sub-panels. In the settings panel the different tasks of the program are assigned to the channels of the DAQ card. The scanning routine in turn provides a full control of the wavelengths of all three Ti:Sapphire lasers. The wavelength can be read from the server application provided by the wavemeter. The

[14] National Instruments PCI-6601

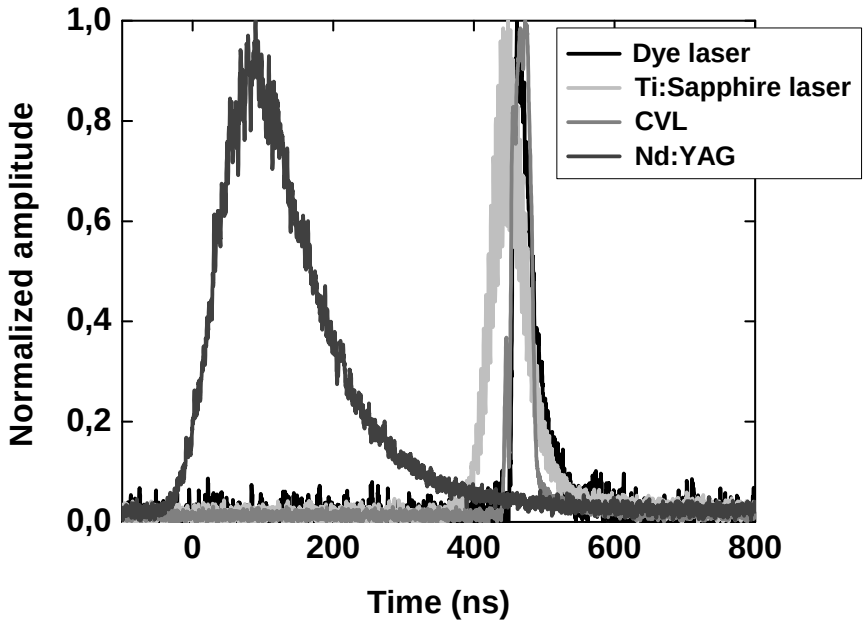

Figure 3.9: Temporal profiles of the two pump lasers, a single Ti:Sapphire laser and a pulsed dye laser.

position of the actuators[15] driving the etalons in the Ti:Sapphire laser cavities can be read out and changed remotely. Furthermore an automated frequency scan can be carried out, sequentially changing the frequency of one of the lasers while monitoring the count rate via a counter channel on the DAQ card. The monitoring panel acts as a simple digital ratemeter and can be used to monitor and save the rate of any signal fed into the system over time. Finally the shutter panel provides control over the glass plates illustrated in figure 3.1 to redirect a small fraction of the laser beams to the wavemeter and photodiodes for analysis of the laser frequency and the time delay. The temporal overlap can be simply monitored by inserting all glass plates into the laser beams and feeding the voltages from the photodiodes into an oscilloscope which can be read-out via a network connection based on http. An oscilloscope trace of the two high repetitition rate pump lasers, a Ti:Sapphire laser and a dye laser is shown in figure 3.9. The laser control pc can be operated as a vnc-server and all features can be accessed by a remote client computer in the IGISOL control area.

[15] Physik Instrumente: M-232.17. See `http://www.physikinstrumente.com/en/products/prdetail.php?sortnr=703600` for details.

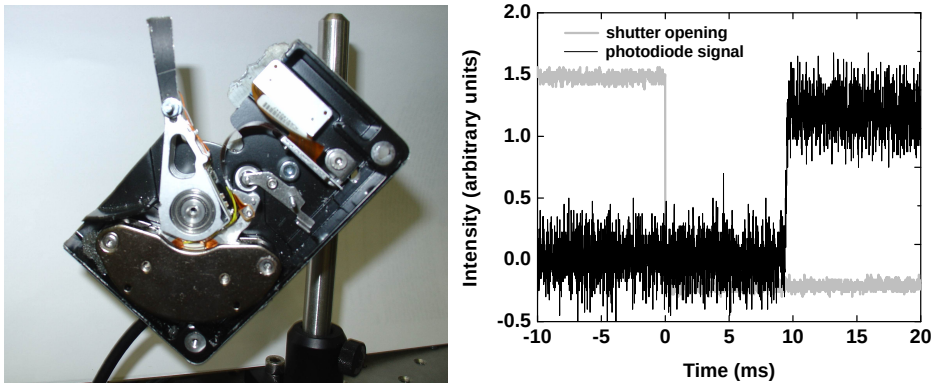

(a) Photograph of the single-arm shutter (b) Measurement of the delay time

Figure 3.10: A photograph of the modified hard disk with extended readout arm used for mechanical control of the laser arrival time at the ion guide is shown in (a). The delay between the TTL for the single-arm shutter and the detection of a helium-neon laser is illustrated in (b).

3.3 Mechanical shutter

The temporal control of the spatially overlapped lasers is mandatory for the investigation of the time evolution of a laser-related ion signal within the ion guide. For sources with an evacuation time faster than the laser repetition rate the signal can be triggered to the arrival of the laser pulse in the source. This technique has been applied for both high repetition rate lasers in hot-cavity ion sources [52, 53] and for low repetition rate lasers in an ion guide [54,55]. However in the case of the FURIOS laser ion source, this approach is not feasible as a high repetition rate laser system with a duty cycle of 100 μs is combined with the ion guide technique operating at ms timescales.

Therefore a fast shutter mechanism was designed to provide the required timing information. As the time resolution is restricted by the bin width of the data readout system ($\approx$ 0.5 ms) a mechanical solution is still feasible and preferred over a fast (ns) but rather expensive light switch in a typical polarizer/analyzer setup in combination with a pockels cell as proposed in [56]. In this experiment a modified version of the mechanical shutter design detailed in [57] was used. A conventional broken hard disk drive was dismantled and the readout arm of the disk was connected to an electrical switching circuit providing a shutter current of roughly 500 mA. The shutter arm was extended with a thin aluminium plate to decrease the shutter time (figure 3.10).

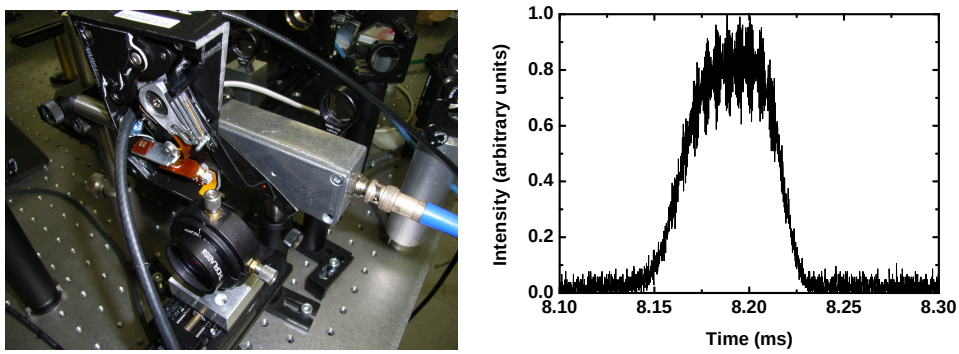

(a) Photograph of the double shutter setup

(b) Measured time resolution

Figure 3.11: A photograph of the test setup for the double shutter system. The control of the time resolution is of the order of 100 microseconds.

The direction of the feeding current can be switched by using standard TTL logic. The performance of the shutter was tested using a continuous wave helium-neon laser beam focused in the same manner as that of the Ti:Sapphire laser beams. The light was detected by a fast photodiode behind the shutter. A typical delay time of 5-14 ms between the TTL signal and the shutter mechanism was observed depending on the alignment of the shutter with the laser beam, with an overall jitter of 50 microseconds. A shutter time of roughly 20 microseconds was achieved. The long delay of the shutter does not allow for laser "on" timescales of less than 15 ms. Therefore, to reach the single laser shot level for a high repetition rate laser system (100 μs) a double shutter system was designed. In this approach two shutters were introduced in series into the laser beam so that shutter 1 opens the laser path and shutter 2 blocks the path. The damping of the movement of the shutters was improved to reduce the jitter of the shutter mechanism. By choosing an appropriate TTL logic a pulse of laser radiation of 100 microseconds was achieved as illustrated in figure 3.11.

Before applying the shutter technique for resonant ionization laser spectroscopy in IGISOL the functionality and reliability was tested in a RIS application in the atomic beam unit (ABU) described in section 3.4. The ABU provides an ideal test as the flight time of the ions from the interaction region to the detector is about 10 μs with a jitter of < 1 μs (see section 5.4). Therefore the additional delay of the extraction of the ions from IGISOL can be neglected. Calcium was chosen as a test element due to its easy access by RIS as for example shown in [5, 58]. The experimental setup was equivalent to the one shown in figure 3.13. The RIS scheme of $\mathrm{Ca}[422.79, 827.81, 422.79e^{-}]\mathrm{Ca}^{+}$ involves two excitation steps, provided by a fre-

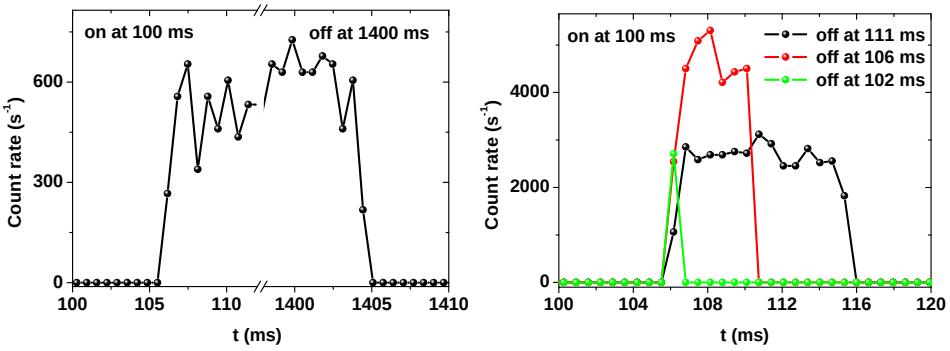

Figure 3.12: Performance of the double-shutter system in a RIS application on Ca in the ABU.

quency doubled and a fundamental Ti:Sapphire laser. The first excitation step is pivotal and therefore the double shutter was set up to block the relevant laser beam. The shutters were placed in front of the frequency doubling crystal in the gradual focus of the fundamental laser beam in order to maximize the blocking speed. The DAQ system of JYFLTRAP [59] was used to control the TTL pulses for the shutters and to read out the ion signal from the ABU.

The results obtained with the described setup are shown in figure 3.12. Figure 3.12(a) shows a time scan applying the same timing scheme used for the off-line tests in IGISOL on stable yttrium (see section 6.1), where the laser radiation was turned on after 100 ms and turned off after 1.4 s. The ion signal follows the laser radiation with a typical shutter delay of 5 ms and has a rise time of approximately 1 ms. Figure 3.12(b) shows a second experiment where the delay of shutter 2, responsible for the closing of the laser beam, was repeatedly reduced until the full ion signal was accumulated in one bin of width 0.65536 ms of the DAQ system. This result provides a proof-of-principle for using the shutter system to achieve a time resolution to study the processes in a gas cell with an evacuation time of typically 100 ms.

3.4 Atomic beam unit

The experimental setup in the laser cabin is completed by an atomic beam unit for off-line calibration and tests of laser excitation and ionization schemes. The vacuum chamber was provided by the University of Birmingham, originally used for fluorescence laser spectroscopy using photomultiplier tubes (PMT) as detectors in a crossed-beams setup. To perform RIS applications the unit had to be modified for

efficient ion collection and counting. The current setup of the unit is shown in figure 3.13.

The sample (grains, powders or solutions) of material is evaporated from an electrothermally heated tantalum tube with a length of 50 mm, an outer diameter of 2 mm and a thickness of 0.5 mm mounted in the lower chamber. Alternatively a rotating target can replace the oven. In this setup refractory material is ablated by a 20 Hz Nd:YAG laser[16] at 1064 nm focussed onto the target through a quartz window on the top of the upper chamber. The atomic plume enters the interaction region in the upper chamber after having been collimated by a slit system. The laser radiation enters the unit from the side, perpendicular to the atomic beam. A simple electrostatic lens system has been designed to efficiently extract the ions created by the laser radiation and direct them to an electron multiplier tube[17]. At a typical operating potential of -2 kV the multiplier gain is specified to approximately $3 \cdot 10^7$. The ions are focussed onto the detector cathode by a deflector-lens system on electrostatic potentials of about 1000 V and 900 V respectively as depicted in figure 3.13(b). The diameter of the deflector is 80 mm and the open aperture of the lens 50 mm. The deflector is placed at a distance of 90 mm from the detector and 20 mm from the lens.

The geometry was optimized by an electrostatic field simulation using the software package COMSOL [60]. The field is simulated by solving the Laplace equation in a finite element method. To save computing power the first simulations were done in a radial geometry as shown in figure 3.14(a). The density and contour plot indicate the field calculated with the geometry. Tracks of ions of mass 100 starting within the laser interaction region in the center the lens and the deflector at radii from 0 to 20 mm are indicated by the coloured lines. The colour coding shows the time of flight of the ions of approximately 6 μs. Due to the focussing of the system all ions hit the detector with an active area of 8x8mm^2. A second simulation in three dimensions confirmed the result. Figure 3.14(b) shows a typical extraction time distribution of 1000 ions of mass 100. The ion starting distribution was created by a random number generator in the interaction region. Note the excellent time resolution of below 1 μs which is mandatory for a precise gating of the ion signal.

The full setup is mounted on four threaded rods on a single flange for easy access and modification as shown in figure 3.15. The input voltages as well as the signal from the EMT are fed through the flange. The signal processing by standard NIM electronics is illustrated in figure 3.16. The signal is processed by a fast amplifier unit and subsequently brought into coincidence with a delayed gate of the high-repetition rate Nd:YAG pump laser to overlap with the ion arrival time after the ionization process. If ablation is applied an additional coincidence with a gate provided by the 20 Hz ablation laser can be required, therefore discarding spurious signals produced

[16] Spectron Laser Systems: Mini-Q
[17] ETP Electron Multipliers, Model AF150H

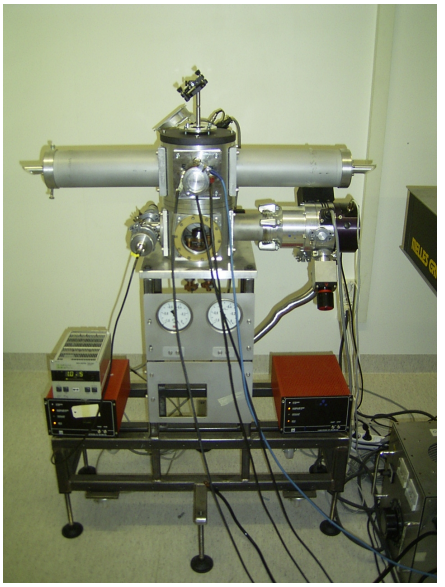

(a) Photograph of the atomic beam unit.

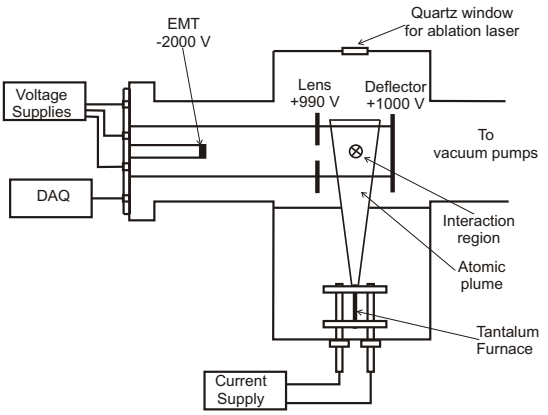

(b) Schematic drawing.

Figure 3.13: Photograph and schematic diagram of the atomic beam unit (ABU). See text for detailed description of the setup.

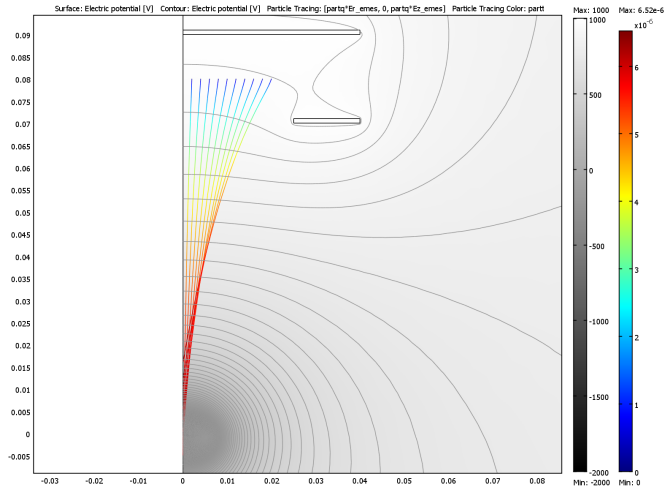

(a) Field simulation in radial coordinates

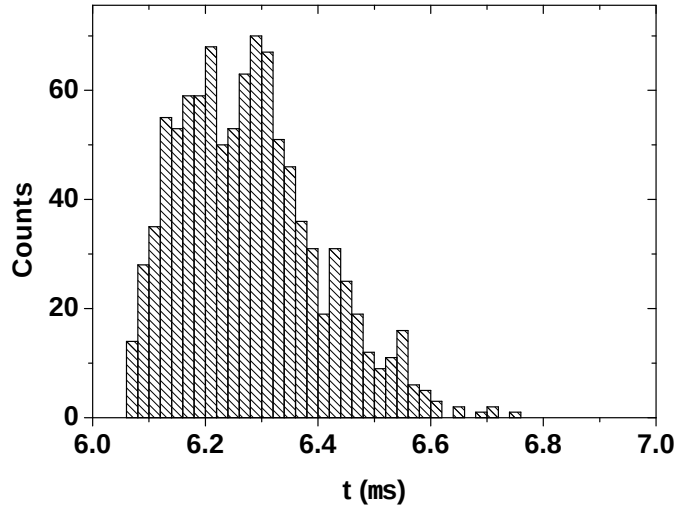

(b) Extraction time

Figure 3.14: (a) FEM simulation of the electrostatic field and tracks of mass 100 ions in the ABU for a deflector voltage of 1000 V and a lens voltage of 900 V. (b) Simulated extraction time distribution for 1000 ions of mass 100.

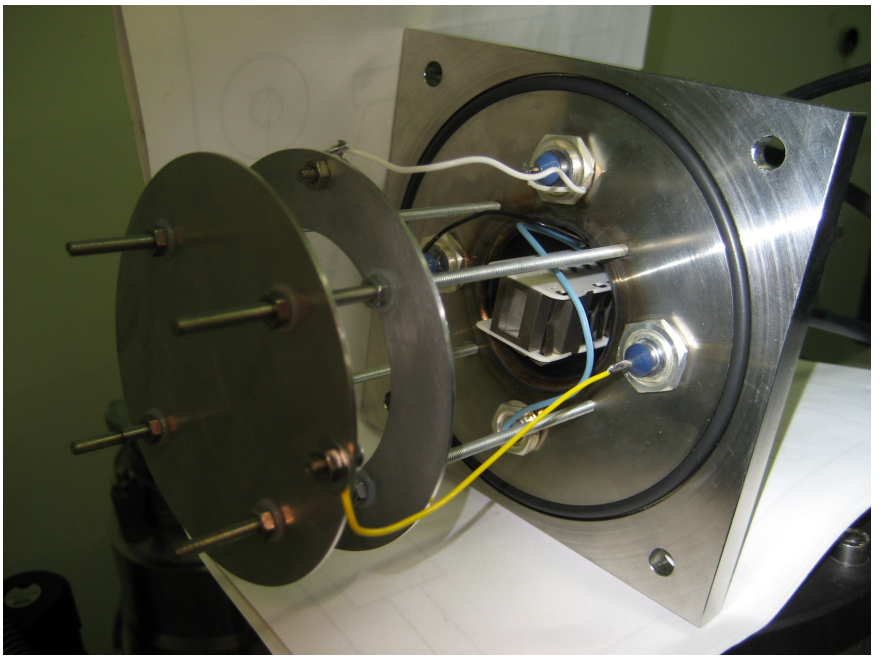

Figure 3.15: Ion collection region of the ABU.

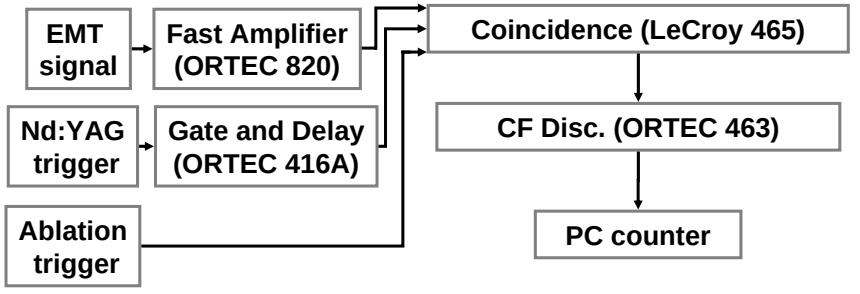

Figure 3.16: Scheme of signal processing for the ABU.

by electrical noise such as that from the Q-switches of the pulsed laser system. Before being fed to a counter card the linear output of the coincidence unit is discriminated by a constant fraction discriminator device (CFD).

4 Preparation of the IGISOL front-end for RIS applications

This chapter deals with the development of hardware for the IGISOL front-end and the required preparation of IGISOL for the operation of the FURIOS laser ion source. In section 4.1 an introduction to the IGISOL technique is given, followed by the discussion of the coupling of the laser ion source to the IGISOL in section 4.2. The important theoretical models of stopping of ions in matter and the gas flow are treated in sections 4.3 and 4.4.

The description of a new ion guide for heavy-ion fusion-evaporation reactions in section 4.5 is followed by studies to improve the transport of radioactive atoms from the ion guide to the sextupole. The transport efficiency is linked to the shape of the supersonic jet after the exit nozzle of the ion guide. Both a theoretical treatment and an improved setup to photograph the gas jet in real-time are described in section 4.6. The chapter closes with a discussion of a hot-cavity ion source for the production of neutron-deficient silver isotopes. Both the source as well as the development of an efficient laser ionization scheme for silver are described in this section.

4.1 Ion guide isotope separator on-line

In the early 1980's the ion guide technique was developed in Jyväskylä in order to overcome limitations related to the standard ISOL technique, namely the inability to produce refractory elements and a need for complicated ion source-target combinations. A full description of the IGISOL technique may be found in [61, 62] and references therein, however it will be briefly described here. A projectile beam impinges on a thin target and the reaction product nuclei recoil out into a chamber filled with a buffer gas, usually helium. The highly-charged ions slow down, thermalize in the gas, and continuously change their charge state until a significant fraction, 1-10%, reach a 1^+ charge state. This fraction is transported, along with all other species, out of the ion guide with the gas flow and is guided through a radiofrequency sextupole ion guide (SPIG) [63] before being injected into the mass separator. The key advantage of the IGISOL technique is the short evacuation time of radioactive nuclei ($\approx$ ms timescales) resulting in a chemical insensitivity of the ion guide.

However, there are two inherent deficiencies in the IGISOL method, namely the lack

of Z-selectivity and, for certain reactions, a poor efficiency. These drawbacks become more important in fission reactions involving the light-ion bombardment of heavy actinide targets. The plasma generated from the passing of the fission fragments through the stopping gas can lead to severe recombination losses. This deteriorates the ion guide efficiency.

Heavy-ion fusion-evaporation reactions can be used to produce nuclei close to the $N = Z$ line in regions that play a special role in nuclear astrophysics since the rapid-proton (rp) capture process passes right through them. The properties of these neutron-deficient nuclei, in particular the masses and beta decay half-lives, are needed as input parameters for rp-process nuclear reaction network calculations. The production yields using heavy-ion reactions at IGISOL are relatively low. In consequence, the FURIOS laser ion source project aims to improve the yield of the nuclei of interest.

4.2 Coupling of FURIOS to IGISOL

In order to overcome the deficiencies arising from the effect of plasma and to provide Z-selectivity an alternative approach to the IGISOL technique has been pioneered by the LISOL group at the University of Leuven [64, 65]. By allowing the recoiling product nuclei to neutralize a selective re-ionization process is achieved using lasers. This work has demonstrated the feasibility of combining high-power low-duty cycle lasers with the ion storage capability of a high pressure gas cell. By employing a pulsed primary beam with a time structure that is optimized for the evacuation time of the ion guide total efficiencies in the order of 1-10% have been reached for Ni [66,67] and several other refractory elements, such as Co, Rh and Ru [68]. The presence of only weakly-ionized plasma means that the gas flow rates to transport ions out of the ion guide can be significantly lower than in the standard IGISOL system. This permits heavier stopping gases to be used such as Ar, leading to a better stopping efficiency for recoiling nuclei. In comparison to the standard IGISOL however, the laser ion guides of the LISOL laser ion source at Leuven suffer from delay times of several 100 ms.

At the IGISOL facility, a similar project is underway to combine the selectivity and efficiency of a laser ion source with the fast (sub-millisecond) evacuation, and chemical non-selectivity of the ion guide technique [29]. Two approaches of coupling the laser beams to IGISOL are employed and depicted in figure 4.1. One is similar to that pioneered by the Leuven group as discussed above. A second technique, developed in order to provide the highest selectivity, will ionize the neutral atoms after extraction from the gas cell, within a sextupole ion guide (SPIG) [69]. The technical development of the LIST (Laser Ion Source Trap, see [70]) approach will be discussed in section 4.6. The results of laser ionization experiments involving both, the "LIST-mode" and

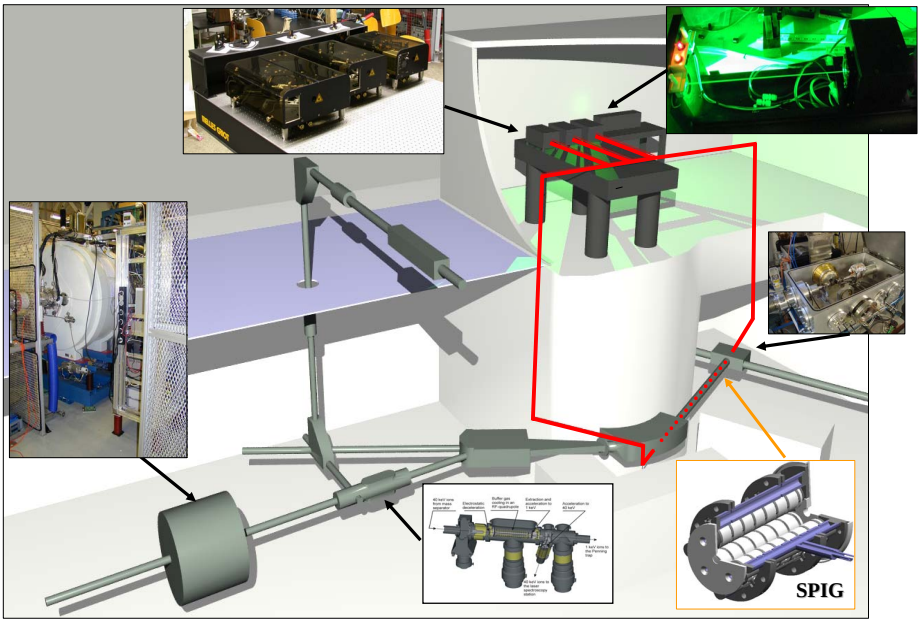

Figure 4.1: Coupling of the FURIOS laser beams to the IGISOL front-end.

the "Ion guide mode" will be discussed in chapter 5.

4.3 Stopping of ions in matter

To estimate the extraction efficiency of any IGISOL ion guide it is important to be able to simulate the stopping process of the recoil ions in the buffer gas environment. Three mechanisms define the stopping of ions in matter, namely

- Electronic stopping
  Energy loss of the projectile by Coulomb interaction with the shell electrons of the target atoms.
- Nuclear stopping
  Energy loss of the projectile by Coulomb interaction with the screened nuclear charge.
- Charge exchange between the projectile and the atom.

A detailed review of the topic can be found in [71]. The well-established Bethe-Bloch equation [72, 73] for the stopping power S which was later refined to its modern form [74] can be written

$$S = \frac{4\pi a_B^2 m_e c^2}{\beta^2} Z_2 Z_1^2 \left(\ln \frac{2m_e v^2}{\langle I \rangle} - \ln(1-\beta^2) - \beta^2 - \frac{C}{Z_2} - \frac{\delta}{2} \right) \tag{4.1}$$

where Z_1 and Z_2 are the atomic numbers of the projectile and the target, $\langle I \rangle$ the average excitation potential per electron, a_B the Bohr radius, $\beta = v/c$ and the last two terms corrections to the low and the high energy limits of the traditional Bethe-Bloch equation. The Bethe-Bloch formula models the stopping of particles with charge Z_1 which is not a realistic experimental condition as charge exchange between the projectile and target atoms during the stopping process needs to be taken into account [75]. The charge state distribution as a function of energy can be studied with the help of computer codes such as LISE [76]. An estimate for the statistical net charge Z_1^* based on the assumption that all electrons with a Bohr velocity v_B less than the projectile velocity v are stripped [71] is given by

$$\frac{Z_1^*}{Z_1} = 1 - e^{-v/\left(v_B Z_1^{2/3}\right)}. \tag{4.2}$$

Nowadays computer codes are available to simulate the stopping of ions in matter. For this thesis the SRIM code [77] was used. The accuracy of the code is estimated to be 5%[1].

[1] see: `http://www.srim.org/SRIM/SRIM2008.htm`

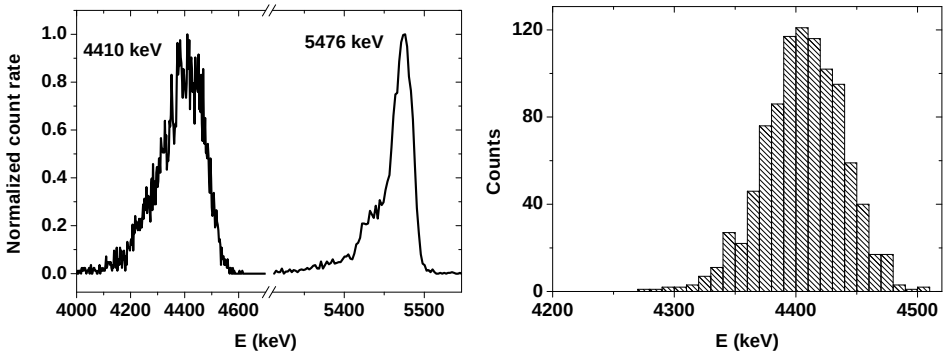

(a) Experimental data (b) Simulation

Figure 4.2: Comparison of a SRIM simulation and experimental data of the degrading of a 5476 keV α beam by a 2.5 μm nickel window.

Compared to a metal foil, the buffer gas only contributes a small amount to the total stopping process in the ion guide. This is particularly true for the case of helium which has a low atomic number. Consequently a good knowledge of the thickness of the metallic materials in both the primary beam and recoil ion path is compulsory in order to obtain efficient stopping in the IGISOL buffer gas cell.

The thickness of a foil can be accurately determined by measuring the energy loss through the foil of an α particle emitted from a radioactive recoil source. The results of such an experiment are illustrated in figure 4.2(a). In this case a ^{241}Am source emitting α particles at energies of 5486.6 keV (84.5%) and 5442.8 keV (13.0%) [78] was used. A nickel foil was placed in front of the source and a degraded energy to $\sim$4.4 MeV was measured with a silicon detector. The result was cross-checked with a SRIM simulation shown in figure 4.2(b). By matching the degraded energy of the simulation a foil thickness of 2.6(1) μm could be extracted in agreement with the specifications of the manufacturer.

Once all relevant foils are characterized a full SRIM simulation can be run to optimize the stopping process including the buffer gas. A typical full simulation is illustrated in figure 4.3 in preparation for an experiment in which a ^{40}Ca beam at an energy of 200 MeV was stopped with help from a novel degrader system in the HIGISOL ion guide described in section 4.5. Nickel was chosen as the material for the degrader foil (12.5 μm) and the ion guide entrance window (2.5 μm). Free parameters for optimization were the degrader angle and the helium gas pressure in the guide. A flat-top shaped mono-energetic ion distribution with a diameter of 3 mm was taken as the incoming beam. A sample of 1000 ions was simulated to pass the degrader set at an angle of 23°

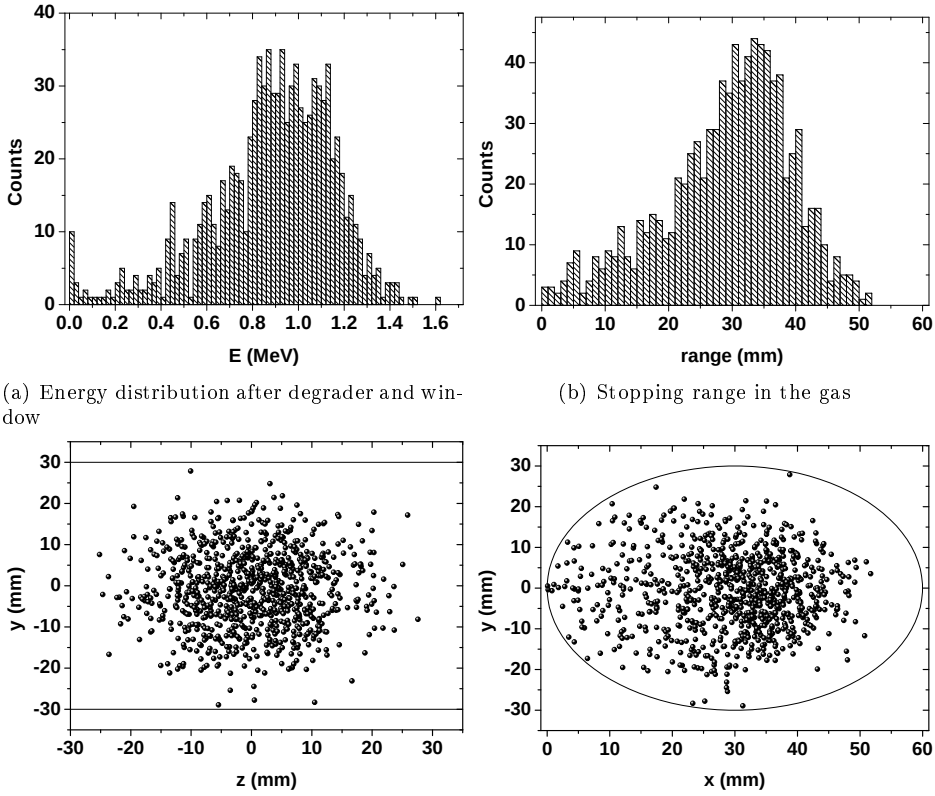

(a) Energy distribution after degrader and window

(b) Stopping range in the gas

(c) Ion distribution in the cell from the beam side

(d) Ion distribution in the cell from the back

Figure 4.3: Simulation of the stopping of a 200 MeV Ca beam in the HIGISOL ion guide.

and the nickel window. The path of the ions is then extrapolated through vacuum until they reach the entrance window of the guide. The average energy after the degrader and window is 0.88(27) MeV (figure 4.3(a)). In figure 4.3(b) the stopping range of the ions in 300 mbar helium buffer gas is shown with an average range of 29(10) mm. Note that the total size of the guide is 60 mm in diameter. Finally, to obtain a stopping efficiency the spatial distribution of the stopped ions is compared to the ion guide geometry as illustrated in figures 4.3(c) and (d) for a beam-side view and a back-view into the ion guide respectively. A total of 89.8% was stopped in the guide, the major losses coming from ions stopped in the window. In summary, the simulation code combined with an accurate measurement of the foil thickness good estimates for all relevant parameters can be given to ensure an efficient stopping in the gas cell. Fine tuning can be done on-line by optimizing the gas pressure and the degrader angle.

4.4 Gas flow simulation studies

An important parameter of any IGISOL-type system is the study of the gas flow in the ion guide which defines the evacuation time of the cell and the transport efficiency. The underlying Navier-Stokes equation for uncompressible flow is written

$$\begin{aligned} \rho\left(\frac{\partial\vec{v}}{\partial t} + (\vec{v}\cdot\nabla)\vec{v}\right) &= -\nabla P + \mu\Delta\vec{v} \\ \nabla\cdot\vec{v} &= 0 \end{aligned} \tag{4.3}$$

where ρ is the density, μ the viscosity and P the pressure of the gas. As the equation is non-linear in the velocity field v the problem can only be treated numerically. A numerical solution to the partial differential equation can be calculated by the Finite-Element approach. Simulation codes following this method are commercially available. The problem of the high computing power required for these kind of calculations can be significantly reduced by using cylindrical coordinates, suitable for the geometry of the ion guide. The COMSOL software package [60] provides an option for the use of cylindrical coordinates and therefore was chosen for the simulations in this thesis.

The partial differential equation can only be solved when suitable boundary conditions are applied to obtain physically realistic solutions. The walls of the ion guide are easily treated by no-slip conditions, demanding that the radial velocity v_r is equal to zero. The boundary at the exit nozzle and the input to the ion guide is fixed by the experimental conditions, given by the massflow rate through a choked nozzle and the static pressure in the guide respectively. For a detailed theoretical description the reader is referred to text books [79] however the basic equations will be given here.

The governing velocity in a gas jet is the speed of sound, also known as the Mach velocity v_M, which is calculated by

$$v_M = \sqrt{\frac{\gamma k_B T}{m}} \tag{4.4}$$

where m and T are the mass and the temperature of the gas respectively. The term γ defines the ratio of specific heats which can be expressed in terms of degrees of freedom f

$$\gamma = \frac{f+2}{f} \tag{4.5}$$

of the buffer gas atoms. Note that for mono-atomic gases such as He and Ar, γ equals 5/3. As the nozzle can be assumed to be "choked" a velocity of 1 Mach is reached in the nozzle area and a supersonic jet is formed after the nozzle (see section 4.6.3). The conductance of a choked exit nozzle with a diameter d is given by

$$C = \frac{\pi}{4} v_M \sqrt{\left(\frac{2}{\gamma+1}\right)^{\frac{\gamma+1}{\gamma-1}}} d^2 \, . \tag{4.6}$$

For typical IGISOL operational conditions ($T = 293.15$ K) one obtains

$$\begin{aligned} C_{\mathrm{He}}[l/s] &= 0.45 \cdot \; d[mm]^2 \quad \text{for He and} \\ C_{\mathrm{Ar}}[l/s] &= 0.14 \cdot \; d[mm]^2 \quad \text{for Ar.} \end{aligned} \tag{4.7}$$

The evacuation time t_{evac} of a volume V can be estimated by

$$t_{evac} = \frac{V}{C} \, . \tag{4.8}$$

The mass flow rate is calculated by using the ideal gas law

$$\frac{dm}{dt} = C \cdot \rho_m = C \frac{P}{k_B T} m \, . \tag{4.9}$$

This rate is maintained throughout the guide and therefore can provide a boundary condition on the input velocity $v_{in}(r)$. The flow regime is typically described by a so-called *Reynolds number* Re [80] defined by the ratio of dynamic pressure and shearing stress as

$$Re = \frac{2 R_{max} \rho_m \bar{v}}{\eta} \tag{4.10}$$

where ρ_m is the mass density and η the dynamic viscosity of the medium. The gas velocity can be estimated to $\bar{v} \sim 1$ m/s in the gas feeding channel with a typical

radius of $R_{max} = 5$ mm. For 100 mbar helium at room temperature with a viscosity of $\eta_{He} \sim 19 \cdot 10^{-6}$ Pa s [81,82] a value of $Re \sim 9$ is reached which is far below the critical value of turbulent flow $Re_{crit} \sim 1000$ [83]. Thus, a Newton-type laminar flow with a parabolic velocity profile of the form

$$v_{in}(r) = v_{max}\left(1 - \left(\frac{r}{R_{max}}\right)^2\right) \tag{4.11}$$

can be assumed, where v_{max} is the maximum gas velocity reached at $r = 0$. The maximum velocity can be calculated using

$$v_{max}[m/s] = \frac{8C[l/s]}{1000\pi d^2[mm]} \tag{4.12}$$

by demanding

$$C_{nozzle} = 2\pi \int_0^{R_{max}} v_{in}(r) r dr \; . \tag{4.13}$$

The remaining undefined boundary at the nozzle is conventially fixed to a pressure P_{nozzle} which has to be adapted to match the experimentally determined total static pressure in the ion guide. A flow pattern obtained by following this procedure in radial symmetry for the case of an ion guide borrowed from the LISOL facility (IKS LEUVEN) is shown in figure 4.4. Note that the maximum velocity reached in the center of the exit area is overestimated by the model. The theory predicts a limit of 1 Mach for a choked flow which corresponds to ∼1000 m/s for He according to equation (4.4) for a quasi one-dimensional flow. However as the massflow rate is conserved and inserted as a boundary condition of the system the bulk features of the evacuation from the guide can still be modelled by this type of simulation. A more detailed study of the treatment of the transition from subsonic to sonic flow and the impact on the evacuation time is given in [84].

The flow of atoms in the gas is governed by the macroscopic motion of the gas flow. Additionally a microscopic random diffusion can be taken into account according to the model described in [84, 85]. During a time step Δt the particle travels a distance of

$$\Delta x = \vec{v}(\vec{x})\Delta t + \vec{x}_D \tag{4.14}$$

where $\vec{v}$ denotes the macroscopic gas velocity and $\vec{x}_D$ a random diffusion step. A velocity map containing the coordinate pair (r, z) and the velocity vector (v_r, v_z) in cylindrical coordinates was exported from the software package. With the known velocity profile equation (4.14) can be numerically integrated from any starting point

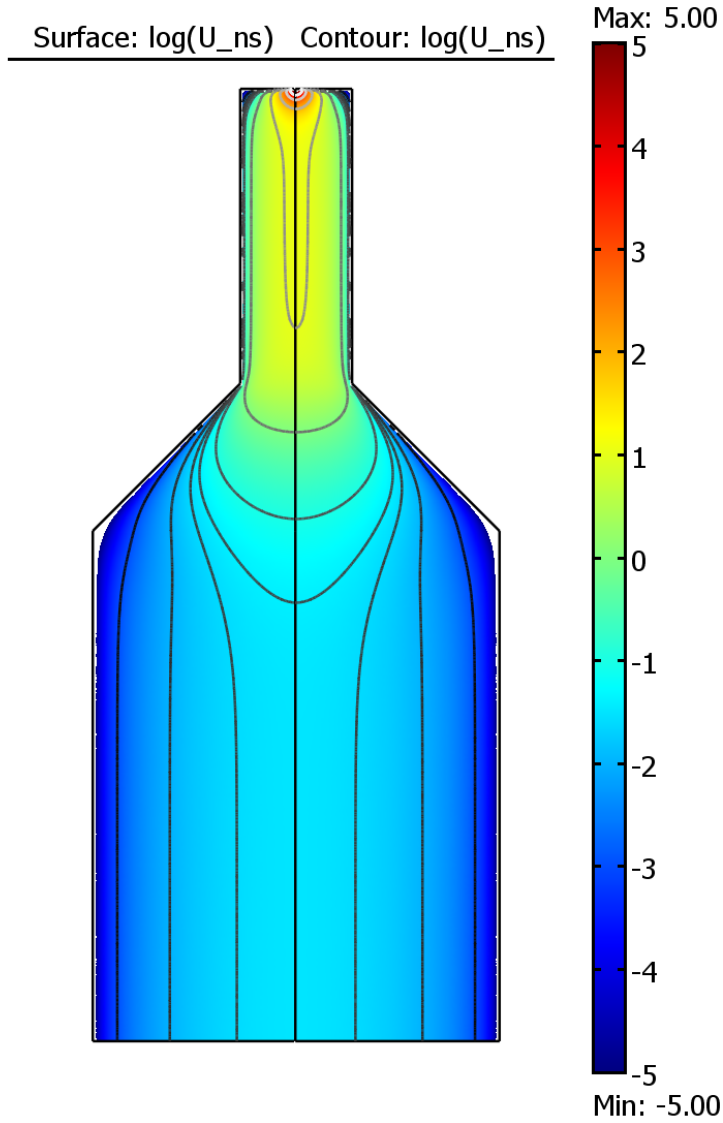

Figure 4.4: Velocity flow pattern for the LISOL ion guide with an exit nozzle diameter of $d = 0.5$ mm and a pressure of 150 mbar in He in logarithmic scale. The lines indicate regions of constant velocity.

inside the guide to monitor the track of a single ion, using a routine written in *Mathematica* [48]. As the typical evacuation time of the Leuven ion guide is ∼100 ms and the simulation a rather moderate integration time of $\Delta t = 10$ μs was chosen based on the needed simulation time on a standard pc.

The diffusion step $\vec{x}_D$ is calculated with standard diffusion theory. The mean free path λ in a gas mixture is defined as

$$\lambda = \frac{4k_B T}{\pi P(\xi_{ion} + \xi_{gas})^2 \sqrt{1 + m_{ion}/m_{gas}}} \tag{4.15}$$

with a collision time of

$$t_c = \frac{\lambda^2}{2D} \, . \tag{4.16}$$

The quantities ξ denote the atomic radii of the buffer gas and the ion of interest. Typical values are $\xi_{He} = 31$ pm and $\xi_Y = 212$ pm for helium and yttrium, respectively [86]. Under the assumption that the diffusion constant D remains constant one obtains a rescaled value for one diffusion step of

$$\begin{aligned} D &= \frac{\lambda_{ab}^2}{2t_c} = \frac{x_D^2}{2\Delta t} \\ \rightarrow \quad x_D &= \sqrt{\frac{\Delta t}{t_c}} \lambda_{ab} \, . \end{aligned} \tag{4.17}$$

Figure 4.5(a) shows a single ion track in the Leuven ion guide without diffusion (blue solid line) and with diffusion (red solid line) added to the model. While the ion track without diffusion simply follows the stream line of the velocity field, the track with diffusion is distorted and shows an initial tendency to decrease in radius. The radial diffusion process is governing for small gas flow velocities in the main body while the gas flow is dominant towards the exit nozzle. The effect of the diffusion on the evacuation time is shown in figure 4.5(b) where the evacuation time of the ion is plotted as function of the starting position z in the axial direction. A position of 0 mm corresponds to the back of the ion guide and 85 mm corresponds to the position of the nozzle. The ions are allowed to start along the symmetry axis of the ion guide, equivalent to laser ionization along the axis. Taking into account the diffusion process, the evacuation time smears out with a tendency towards longer evacuation times especially for ions starting in the back of the ion guide, where the movement by the gas velocity is small compared to the diffusion time. The kink in the plot refers to the transition from the main body to the exit channel at about $z \sim 60$ mm.

The problem of the definition of an appropriate starting distribution naturally depends on the ion production mechanism. In case of an on-line reaction a realistic

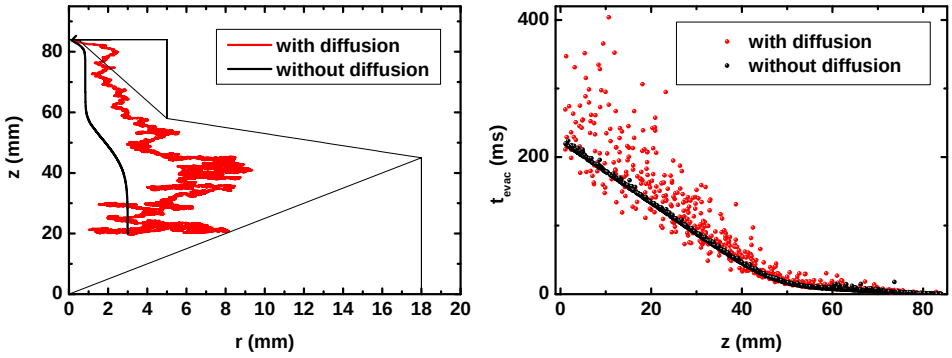

(a) Single ion track (b) Evacuation time

Figure 4.5: Comparison between a gas flow with and without diffusion for the evacuation of laser-produced ions along the central axis of the ion guide.

starting distribution can be calculated with the SRIM code. For laser ionization alone the ion creation region is restricted to the laser interaction region. Consequently for this thesis the ionization from a laser channel is simulated by a random starting distribution along the z-axis of the ion guide and a Gaussian probability distribution

$$A(r) \sim e^{-2(r/w)^2} \tag{4.18}$$

along the r-axis with a laser beam waist w of 3 mm. The distribution was limited to $r = 1.6\ w$. Figure 4.6(a) shows a typical laser ion starting distribution in the ion guide. The color coding refers to the ions which reach the exit nozzle of the guide (red) and those which hit the walls of the guide and therefore are counted as lost (blue). In this simulation an evacuation efficiency of ∼79% can be estimated for a total of 1000 simulated ions. Figure 4.6(b) shows the evacuation time pattern obtained from the ions reaching the exit of the ion guide. The division of the ion guide into a fast extraction channel and the main body leads to a time focus at small evacuation times. Because of the diffusion losses from ions starting of the back of the chamber the evacuation time profile reduces towards high values of t.

With a high repetition rate laser system it is impossible to probe the evolution of a single laser shot, and consequently, it is not straight forward to compare the simulated evacuation time profile with experimental data. This is particularly true, when the ions created in the guide experience loss mechanisms such as charge exchange and molecular formation, discussed in section 6.1 and 6.2. In the case of molecular formation the atomic ion is converted to a molecular form but can still be detected following mass separation. A new procedure to obtain the single shot evacuation profile from

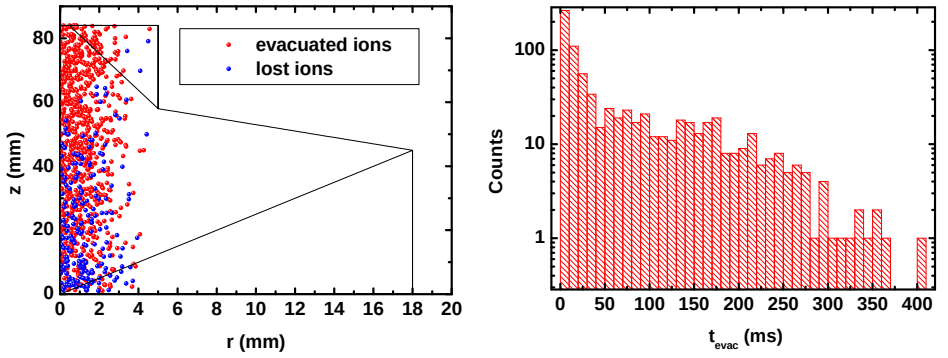

(a) Starting distribution (b) Evacuation time profile

Figure 4.6: Typical starting distribution and evacuation time profile for a laser ion channel. The red dots mark the ions which reach the exit nozzle. The trajectories of the blue dots collide with the walls of the ion guide and are lost.

experimental data is described in [87]. In a closed system, in which the total output current remains constant the full ion signal can be reconstructed. An example of this procedure using real experimental data obtained by laser ionization of yttrium in the Leuven ion guide is shown in figure 4.7. The experimental details of the setup are described in sections 6.1 and 6.2.2. In figure 4.7(a) the laser was turned on at $t = 0$ ms and the mass-separated yield of yttrium and related molecules was recorded. The total ion signal profile is then obtained by simply summing the individual profiles as shown in figure 4.7(b). The summed data can be fitted with a combination of two exponential functions with time constants of 9(1) and 112(2) ms respectively. The faster exponential contributes to about 20% of the total ion signal. The derivative of the fitted function is equivalent to the evacuation time profile of the laser channel and is shown in figure 4.7(c) together with the histogram of the simulated evacuation time profile from figure 4.6. The simulation is in good agreement with the fit to the experimental data. Both datasets feature a fast and a slow componenent arising from evacuation of the converging part of the ion guide and the main body (compare figure 4.4).

4.5 A new ion guide for heavy-ion fusion-evaporation reactions

To investigate laser ionization under IGISOL on-line and off-line conditions a versatile ion guide had to be built. The basic requirements were to grant access to laser radiation from the back of the guide and the front of the guide. The evacuation

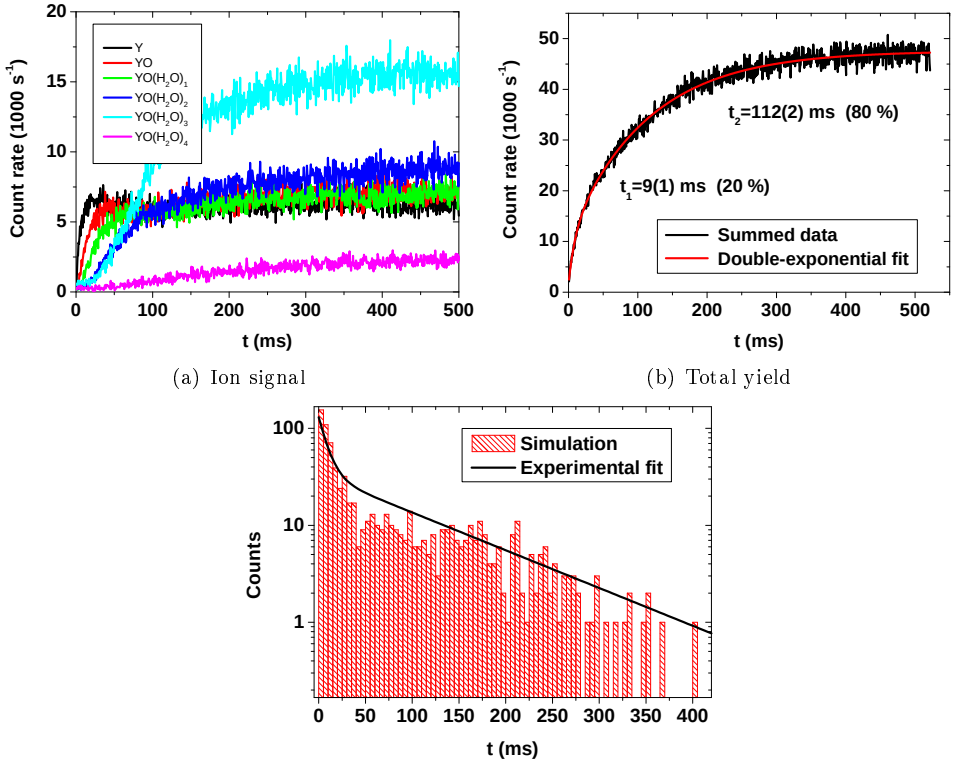

(a) Ion signal

(b) Total yield

(c) Differentiated total yield compared with simulation

Figure 4.7: Extraction of the evacuation profile of the laser channel from experimental data.

time should be rather large to allow the reaction products to neutralize and for the plasma introduced by the primary beam to decay. These basic considerations led to the choice of a heavy-ion fusion-evaporation ion guide, also known as the "HIGISOL" ion guide [88, 89]. Recoils produced by a heavy-ion fusion-evaporation reaction are emitted in a cone centered along the beam direction where the ratio of angular half-widths α_p/α_r of the projectile and the recoil scales as [88]

$$\frac{\alpha_p}{\alpha_r} \sim \frac{Z_p}{Z_r}\frac{A_p}{A_r} \,. \tag{4.19}$$

Consequently in a standard HIGISOL reaction neutralization by the primary beam plasma can be minimized by preventing the primary beam from entering the gas cell with a suitably sized beam stop. The following additional requirements had to be taken into consideration for the design:

- Efficient evacuation
  - Efficient gas flow transport in the guide
  - Optimized nozzle design
- Mechanical requirements
  - Compatibility with the IGISOL vacuum chamber
  - Cooling and heating capability
  - Modular design to add filaments and DC fields.
- Efficient stopping of the reaction products

The recoil distribution requires a rather large stopping volume and efficient evacuation of the cell becomes of critical importance. Consequently gas flow simulation studies had to be carried out and the results are presented in section 4.5.1. The realized design which takes into account all mechanical requirements is described in 4.5.2 followed by the introduction of a new degrader system for IGISOL, discussed in section 4.5.3.

4.5.1 Gas flow design studies

The standard HIGISOL ion guide has been continuously developed over several years for on-line applications however the use of lasers has made it compulsory to redesign the main body of the stopping cell, including the optimization of the gas-flow. A complete description of the gas flow simulation model used in this thesis can be found in section 4.4. In the following, only the basic results of the design-study will be illustrated. A gas flow simulation for the standard HIGISOL ion guide shown in figure

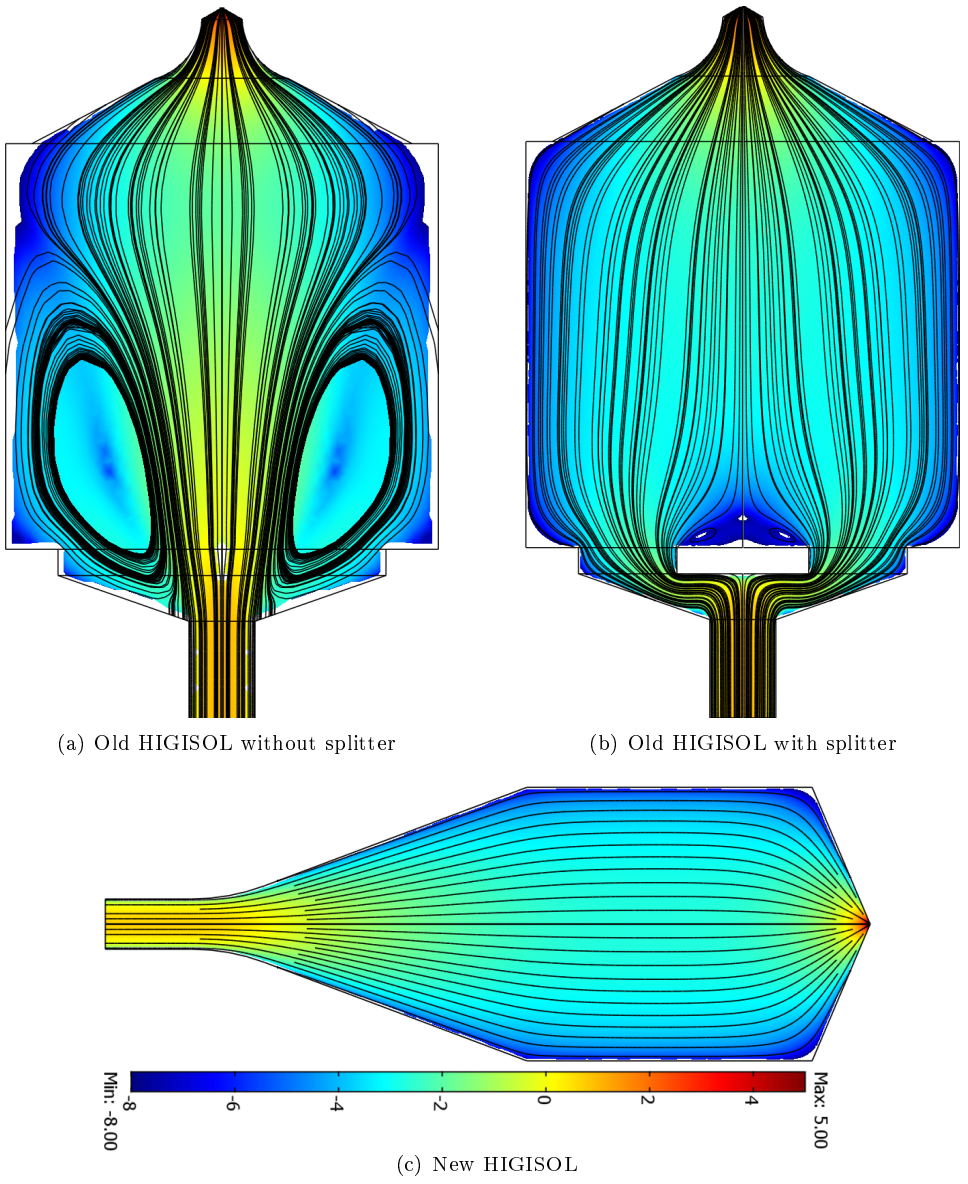

(a) Old HIGISOL without splitter

(b) Old HIGISOL with splitter

(c) New HIGISOL

Figure 4.8: Comparison of the gas flow of the old and the new HIGISOL ion guide for a static He gas pressure of 200 mbar and a 0.5 mm exit hole. The color coding represents the gas velocity in logarithmic scale.

4.8(a) clarifies the problem. The gas is not able to expand quick enough in the guide and therefore forms a fast channel in the center and vortices in the outer region. This was previously circumvented by adding a gas splitter into the ion guide as illustrated in figure 4.8(b). However this leads to a build-up of a vortex immediately behind the splitter which acts to deteriorate the gas flow along the symmetry axis. This effect becomes more apparent for larger exit-nozzle diameters. Additional complications were encountered during laser ionization tests as a window had to be inserted into the splitter to allow the laser beams to enter the ion guide. The window was coated by the sample evaporated from a filament placed inside the ion guide. Therefore higher off-line yields were actually achieved without the splitter even though the gas flow was not optimized. The new design for the heavy-ion fusion ion guide is shown in figure 4.8(c). It features an extended input side which smoothly diverges allowing the gas to expand. The design does not show any formation of vortices up to 500 mbar and therefore a splitter is not required.

To estimate the evacuation time of the guide the model of section 4.4 was applied. Two possible scenarios were calculated. In the first scenario the ions are created in a 3 mm wide channel centered along the beam axis corresponding to the typical size of a primary beam. In the second scenario the start distribution is expanded to a 48 mm wide channel along the beam axis, corresponding to the open aperture of the entrance window, respectively. The resulting time profiles are shown in figure 4.9 for a pressure of 150 mbar He. The time profiles are in reasonable agreement with the value of the maximum evacuation time of $\sim$ 909 ms from the beam axis to the 0.5 mm diameter nozzle, estimated from the conductance via equation (4.7). The reduced number of counts with an evacuation time of more than 500 ms can be explained by increased diffusion losses of the ions produced at high radii of $\sim$ 16-33 mm.

4.5.2 Technical realization

The mechanical design of the buffer gas cell needs to be compatible to the existing IGISOL infrastructure which reduces the maximum possible outer diameter of the cell to 90 mm. The realized design is illustrated in figure 4.10. The cell consists of a gas feeding part, a main body and a removable exit nozzle. The number of components was reduced compared to the old design to minimize the open surfaces in the ion guide. For the same reason indium foil was used as a sealing material. The back part feeds the buffer gas to the main body and was designed according to the simulation described in the previous section. The main body features the mandatory windows for the beam with an open aperture of 48 mm and the beam dump. Additional slots can be inserted into the side of the ion guide, if for example a DC collector plate or a base housing two high current feed-throughs for either a filament or an atom oven are required. The cooling water jackets are mounted onto to the side of the

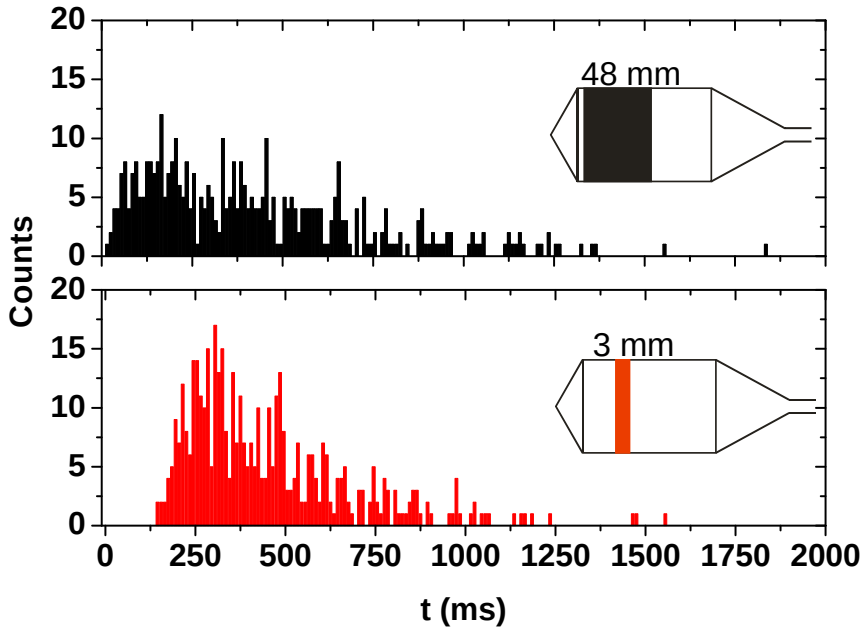

Figure 4.9: Simulated evacution time profile from a plasma channel in the new HIGISOL ion guide for a 0.5 mm exit hole in 150 mbar He.

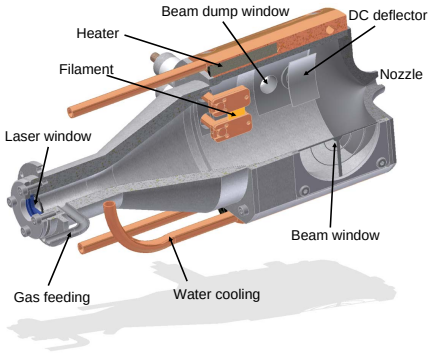

(a) ACAD design

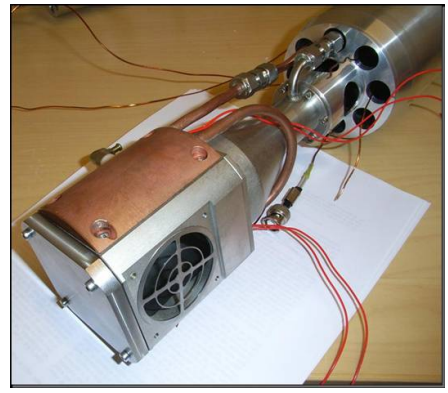

(b) Photograph

Figure 4.10: Design and realization of the new HIGISOL ion guide.

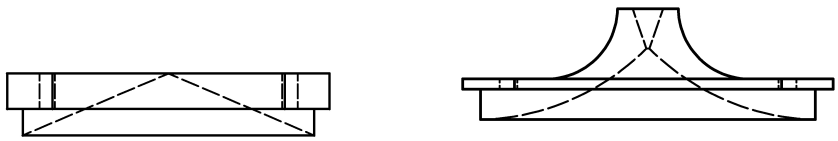

(a) Exit hole (b) De Laval nozzle

Figure 4.11: Different nozzle designs for the new HIGISOL ion guide.

main body. Heating cartridges are inserted into the copper blocks to allow for baking of the guide. The design of the cooling water jackets allows for quick access to the nozzle, not possible with the previous design. Apart from the standard exit hole, a de Laval nozzle was adapted for the ion guide from a gas catcher designed for the SHIPTRAP experiment [90]. It has been introduced to enhance the collimation of the gas jet. A technical drawing of the design of both nozzle types is shown in figure 4.11. A discussion of the development work on the nozzle design can be found in section 4.6.3.

4.5.3 Development of a beam degrader setup for IGISOL

A relatively straightforward way of estimating the total efficiency of an ion guide is to stop and extract a stable beam devlivered by the cyclotron. Because of the low density of the buffer gas and the smaller Z compared to a metallic degrader (see equation (4.1)) the buffer gas contributes only a small amount to the total energy loss and stopping of the beam. Consequently a good knowledge of the thickness of any metal foils placed into the beam as well as the beam energy is required. In order to provide a variable foil thickness a degrader setup was realized. The setup can as well be used for any on-line reaction to degrade the energy of the incoming beam and optimize the energy on target for a maximum production yield. As no energy degrading mechanism is provided after the ion acceleration and a change of the beam acceleration energy is rather time consuming a degrader setup has been requested for a variety of experiments carried out at IGISOL. The design and a photograph of the setup is shown in figure 4.12. A stepper motor[2] is mounted on a platform which is fully adjustable in three dimensions to the beam axis and the geometry of the guide. The degrader foil has a size of 42x15 mm^2. The angular resolution of the motor is equal to 1.8 degrees per step and is controlled by a LabView computer program.

[2]MAE HY200. See `http://www.ametektip.com/index.php?option=com_content&task=view&id=169&Itemid=90`

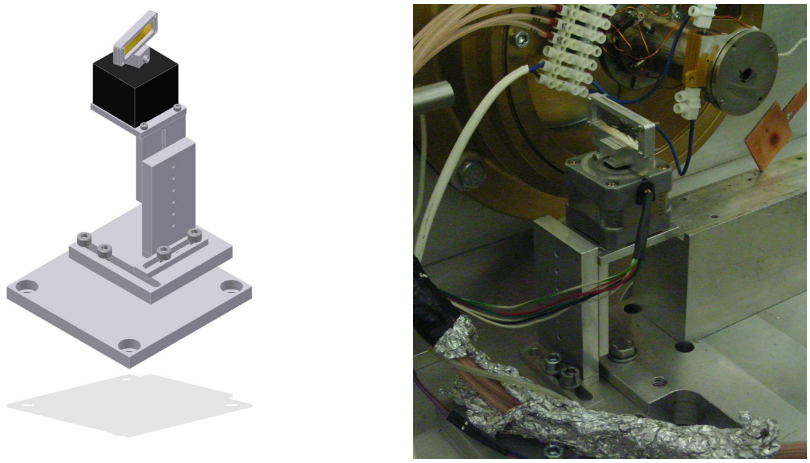

(a) ACAD drawing (b) Photograph

Figure 4.12: Design and realization of a degrader device for IGISOL. The photograph shows the installation of the degrader in the IGISOL vacuum chamber. The sexutopole ion beam guide can be seen in the background.

The degrader setup was tested in combination with the new ion guide by stopping a 280 enA $^{40}Ca^{8+}$ beam of energy 183-200 MeV with a 12.5 μm nickel degrader and a 2.5 μm nickel window. The preparatory SRIM studies to obtain an estimate for the required degrader thickness are described in section 4.3. Some results of this experiment are shown in figure 4.13. In the first part of the experiment the energy of the Ca beam was tuned to 183 MeV and the mass-separated ion current extracted from the ion guide was measured for different buffer gas pressures and degrader angles. In figure 4.13(a) the degrader angle was fixed to 0° and the pressure of the buffer gas (Ar and He) was changed. As expected less pressure is needed in the case of argon to maximize the signal as the stopping power of argon is approximately nine times higher than helium. For the maximum pressure of 300 mbar He the degrader angle was detuned (figure 4.13(b)). Any deviation from 0 degrees led to a decrease of the stopped fraction in the gas indicating that higher primary beam energy is required to penetrate the degrader efficiently. Figure 4.13(c) shows the graph for stopping in He at a degrader angle of 27 degrees for a 200 MeV beam. The curve is comparable to the one in figure 4.13(a) for a beam energy of 183 MeV and 0 degrees. At a fixed pressure of 200 mbar a tuning of the degrader angle for a pressure of 200 mbar in He gave a clear maximum, as shown in figure 4.13(d), in rough agreement with the SRIM estimates from section 4.3.

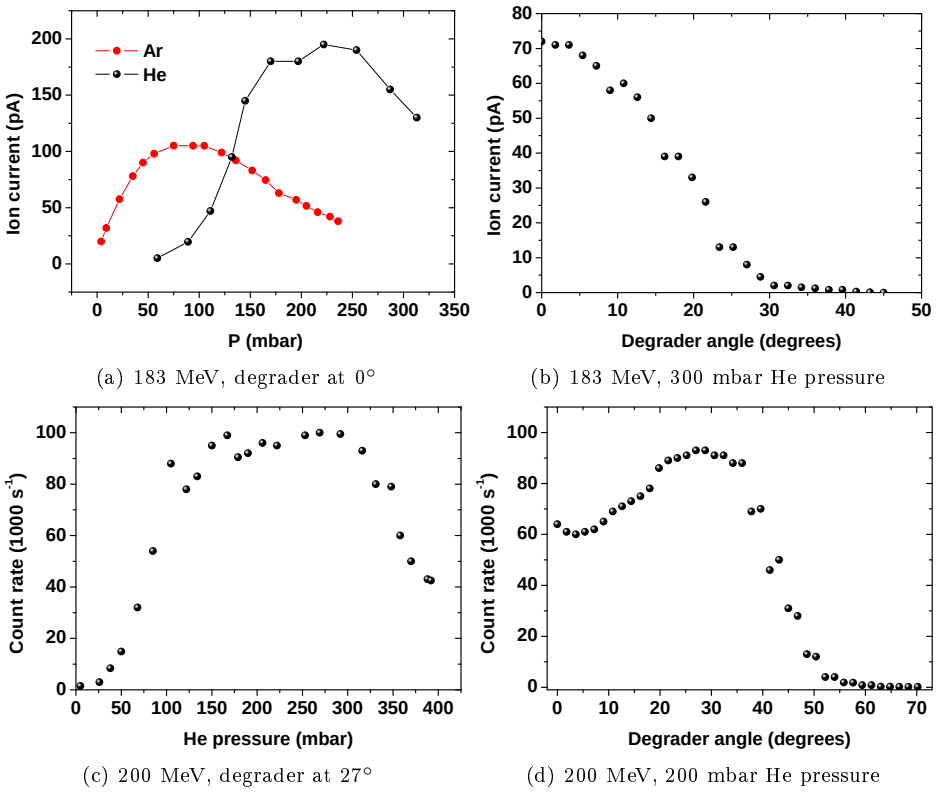

(a) 183 MeV, degrader at 0°

(b) 183 MeV, 300 mbar He pressure

(c) 200 MeV, degrader at 27°

(d) 200 MeV, 200 mbar He pressure

Figure 4.13: Test of the beam degrader for the stopping of a Ca beam.

4.6 Preparations for the IGISOL LIST approach

The SPIG (sextupole ion beam guide) has recently replaced the skimmer system used in the traditional IGISOL approach [61]. It is superior to the skimmer in transmission efficiency and in producing higher quality ion beams [63]. In section 4.6.1 some technical details of the SPIG will be given. With the development of the SPIG and in particular the possibility of laser ionization in the LIST approach an increasing interest in the properties of the gas jet leaving the ion guide is pertinent. While a good understanding of the gas flow in the nozzle area has been established [84] only a few studies have been carried out so far to study the behaviour of the gas jet evolving outside of the ion guide [91]. To understand the underlying concept a small introduction into the theory of supersonic flow is given in section 4.6.2. The shape of the gas jet has been studied by photographing the discharged gas leaving the gas cell. The results of these observations are discussed in section 4.6.3. Results of laser ionization in the SPIG in the manner of the LIST [70] approach are detailed in section 5.1 for the case of technetium and in [37] for the case of bismuth.

4.6.1 Specifications of the SPIG

A complete description of the SPIG and its specifications can be found in [63, 92]. An illustration of the current design is shown in figure 4.14. The SPIG has been constructed in two segments. The first has an enclosed structure around the parallel rods in order to keep the background pressure high enough to collimate the gas jet [91]. The second SPIG is kept "open" and any remaining buffer gas or neutral fraction can be efficiently pumped away through the gaps between the rods. An adjustable stainless steel iris separates the two segments, added to control the pressure in a coarse way in the first segment. The sextupole structure has an inner diameter of 10 mm. The full length of the device is approximately 165 mm. Additional DC voltages can be applied to two electrodes on the front and the back of the device. For the operation of a laser ion source additional selectivity can be attained by ionizing the species of interest in the SPIG while repelling unwanted ions from the source with a positive electrostatic potential on the first electrode [70]. The effect of the repelling potential is illustrated in figure 4.15 via the detection of positrons from the β decay of the isotope ^{58}Cu ($t_{1/2}$=3.20 s) produced in the light-ion fusion-evaporation reaction ^{58}Ni(p,n)^{58}Cu. A remarkably low voltage of $\sim$ +1 V is sufficient to repel the ions from entering the SPIG and a full suppression of the radioactive yield is observed. The β count rate of approximately 1/s for a positive repeller voltage is attributed to detector noise. When the SPIG is used in a standard ion transport mode, the voltages on the electrodes are optimized in such a way that the repeller electrode is set to a small negative potential to focus the ions into the SPIG structure.

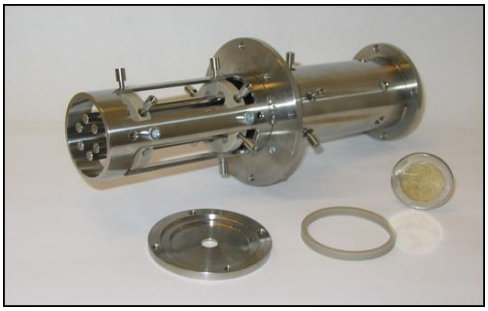

(a) Photograph

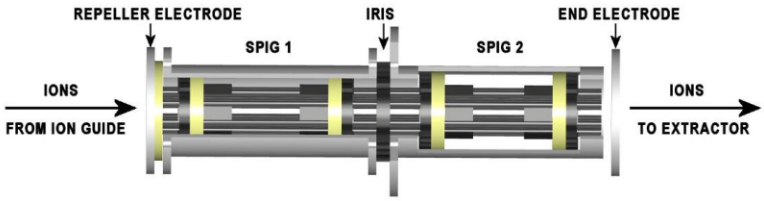

(b) Schematic

Figure 4.14: Photograph and schematic of the SPIG in ion transport mode.

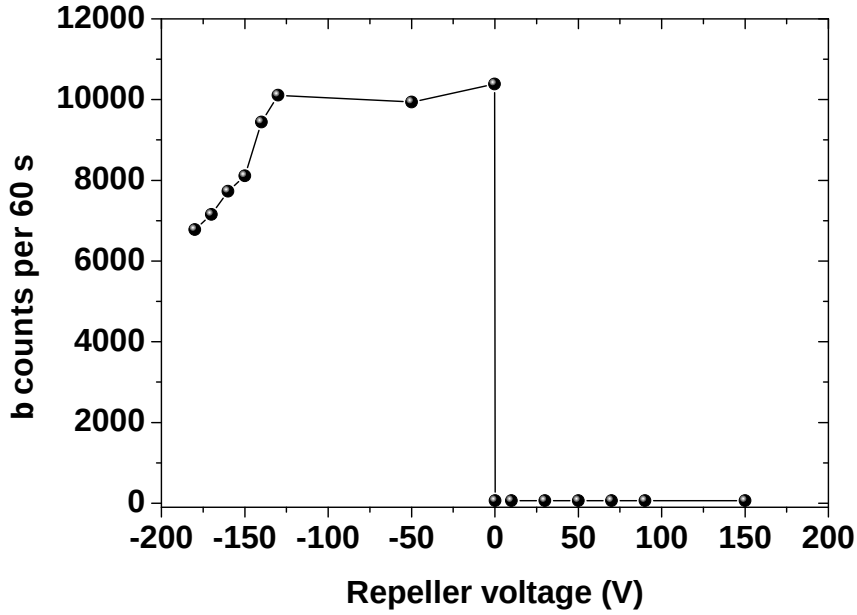

Figure 4.15: Effect of the voltage of the repeller electrode on the ion signal.

4.6.2 Theory of supersonic gas flow

The behaviour of the gas flow inside the ion guide is basically fixed as soon as the nozzle is "choked" and a maximum mass flow rate set by the conductance (equation (4.7)) is reached. In contrast, the properties of the gas jet after the ion guide depend strongly on the shape of the nozzle itself and the pressure boundaries. The theory of gas jet expansion is treated in detail in [79,93] and a collection of the most important theoretical formulas will be given in the following paragraphs.

The main features of the transition from subsonic to supersonic flow in a converging-diverging nozzle is usually described in a quasi-one dimensional symmetry, assuming a constant velocity perpendicular to the symmetry axis of the boundaries. In the case of an adiabatic flow, the change in velocity in terms of a Mach number M is described by the so-called *area-velocity relation*

$$\frac{dA}{A} = (M^2 - 1)\frac{du}{u} \tag{4.20}$$

where A is the cross-sectional area of the enclosing structure and u the gas velocity. The equation states that the speed of the gas is completely determined by the shape of the boundary surface. One immediate result from equation (4.20) is that the speed of sound ($M = 1$) can only be reached in the throat of the nozzle where $dA = 0$. Inside the guide the gas accelerates as the area is decreased until a velocity of Mach 1 is reached at the minimal radius. As $dA > 0$ after the nozzle the gas accelerates during the expansion phase and a super-sonic flow pattern is reached. For a calorically perfect gas equation (4.20) can be solved explicitly to obtain the *Area Mach number relation*

$$\left(\frac{A}{A_n}\right)^2 = \frac{1}{M^2}\left[\frac{2}{\gamma+1}\left(1 + \frac{\gamma-1}{2}M^2\right)\right]^{(\gamma+1)/(\gamma-1)} \tag{4.21}$$

where $A_n < A$ is the area of the nozzle throat and γ the ratio of specific heats. Note that for every value of A two solutions of M fulfill equation (4.21), the subsonic and the supersonic solutions which are illustrated in figure 4.16(a). Once the velocity is known, related parameters such as the temperature, density and pressure can be calculated for a calorically perfect isentropic gas. The pressure in the jet P is calculated by

$$\frac{P}{P_{in}} = \left(1 + \frac{\gamma-1}{2}M^2\right)^{-\gamma/(\gamma-1)} \tag{4.22}$$

where P_{in} is the static pressure for $M = 0$. Equations (4.21) and (4.22) can be combined to obtain an expression for the pressure ratio as a function of the area ratio, illustrated in figure 4.16(b) for the case of monoatomic gases where γ equals 5/3. The behaviour of the isentropic solution for a supersonic jet depicted in figure

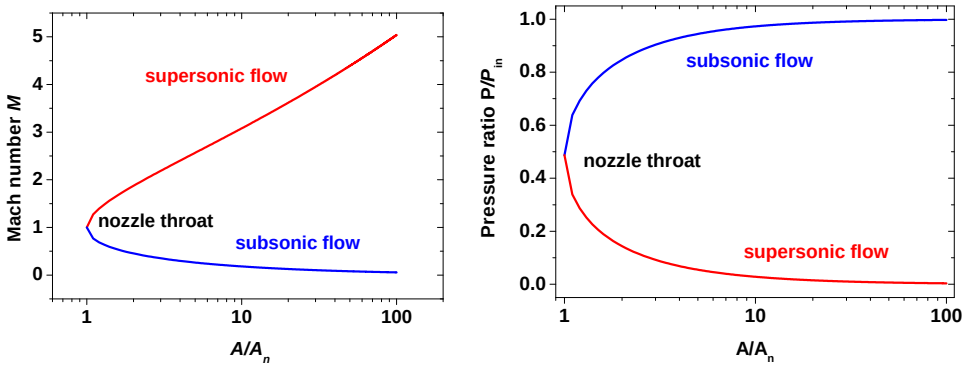

(a) Velocity profile (b) Pressure profile

Figure 4.16: Velocity and pressure in a transition from a subsonic to a supersonic gas jet.

4.16 is usually referred to as the *design condition*. At the nozzle throat a value of $M = 1$ is reached and equation (4.22) reduces to

$$\left.\frac{P}{P_{in}}\right|_{\text{throat}} = \left(\frac{2}{\gamma+1}\right)^{\gamma/(\gamma-1)} . \tag{4.23}$$

For monoatomic gases such as He and Ar a value of ~ 0.487 is reached.

In realistic experimental conditions the gas jet does not follow the isentropic design solution as it is forced to a fixed pressure boundary at the nozzle exit given by the pumping capacity. As an example of the dependence of the behaviour of the gas under different boundaries one may take a standard IGISOL ion guide with a simple exit hole such as that depicted in figure 4.11(a). If no pressure difference is applied between the gas cell and the vacuum chamber naturally no flow occurs. Only if the background pressure P_{bg} in the IGISOL chamber is decreased to a value of $P_{bg}/P_{in} < 0.487$ a supersonic flow condition is obtained. When this critical pressure ratio at the throat of the nozzle is reached the nozzle is said to become *choked* and the subsonic flow part is fixed.

A mismatch between the given pressure boundary at the nozzle exit and the pressure of the jet is compensated by shock structures in the jet. The impact of the background pressure on the behaviour of the gas jet in a converging-diverging nozzle is depicted in figure 4.17(a). The subsonic and supersonic isentropic design solutions are indicated as guidelines. Let us first consider the situation for a background pressure $P_{bg} = P_1$. At this pressure the nozzle is choked, however the pressure P_1 given at the exit is

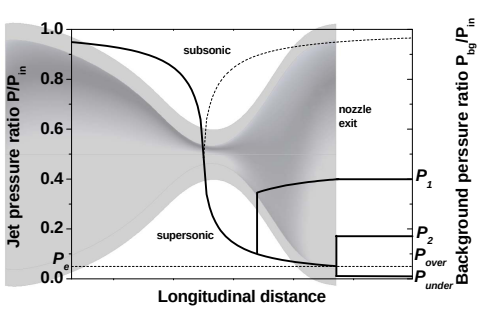

(a) Pressure dependence in a Laval nozzle

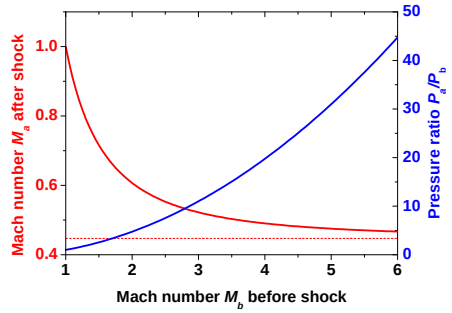

(b) Shock relations

Figure 4.17: (a) Behaviour of the gas pressure ratio in a Laval nozzle for different exit pressures. (b) Comparison of pressure and velocity before and after a normal Mach shock.

higher than the pressure P_e calculated from the isentropic solution for the freely expanding jet. The only way to fulfill the required higher pressure boundary is to form a normal shock in the nozzle as indicated by the vertical line in figure 4.17(a). The velocity M_a and pressure P_a after the shock are only dependent on the Mach number M_b and pressure P_b in front of the shock and are given by

$$M_a = \sqrt{\frac{1 + \left(\frac{\gamma-1}{2}\right) M_b^2}{\gamma M_b^2 - (\gamma-1)/2}} \tag{4.24a}$$

$$\frac{P_a}{P_b} = 1 + \frac{2\gamma}{\gamma+1}\left(M_b^2 - 1\right) \ . \tag{4.24b}$$

A plot of both functions for $\gamma = 5/3$ is shown in figure 4.17(b). Consequently after a normal shock an immediate increase in pressure is seen in the nozzle. The flow becomes subsonic and the pressure continuously increases during the expansion phase to converge to the given pressure boundary P_1 at the exit as indicated in figure 4.17(a).

By decreasing the background pressure P_{bg} further, the shock disc moves towards the exit of the nozzle. At a pressure of $P_{bg} = P_2$ the shock is positioned at the nozzle exit. At this point the jet is supersonic throughout the whole volume of the nozzle. If the background pressure P_{bg} is further reduced to a value $P_e < P_{bg} = P_{over} < P_2$ an oblique shock occurs outside of the nozzle area which increases the pressure towards the boundary condition leading to a spatial compression of the jet. In this case the nozzle is said to be *overexpanded*. If the pressure P_{bg} is reduced to below the isentropic value at the exit, $P_{bg} = P_{under} < P_e$, the jet can only reduce its pressure by forming an expansion wave. In this instance the nozzle is said to be *underexpanded*. In both overexpanded and underexpanded nozzle configurations complex shock patterns occur

(a) 1 mm exit hole, 300 mbar He (b) 1 mm exit hole, 210 mbar Ar

Figure 4.18: Photographs of the gas jet for a simple exit hole in helium and argon.

downstream from the nozzle which are characteristic for the reflection of the jet on the free pressure boundary.

4.6.3 Studies of the gas jet confinement at IGISOL

The gas jet can be easily visualized by creating a DC discharge in an ion guide and observing the optical fluorescence emitted with strong components in the visible part of the optical spectrum[3] as described in [94]. This work has continued in [91] to investigate the influence of the background pressure on the gas jet. However the picture quality was limited by the light intensity and exposure times of several minutes were needed to obtain a picture of the jet. In the present study an optimization of the discharge geometry resulted in a much higher brightness such that the gas jet can now be observed by the naked eye. A variety of different nozzle types were tested [95] however only the results of a Laval-type nozzle (throat diameter 1.45 mm, exit diameter 4 mm) and a simple exit hole (diameter 1 mm) will be presented in this thesis.

The behaviour of the gas jet passing through a simple exit hole is illustrated in figure 4.18(a) for helium and in figure 4.18(b) for argon. The position of the first shock disc from the exit nozzle can be estimated according to [94] by

$$x \sim 0.88d\sqrt{\frac{P_{in}}{P_{bg}}} \tag{4.25}$$

where d is the diameter of the nozzle throat. The position is difficult to determine by the naked eye. Therefore a program was written in Matlab [96], together with a graduate student, which evaluates the light intensity of the photograph along the jet and determines the positions of maximum intensity corresponding to the shock discs as well as the diameter of the jet [95]. An illustration of the program is given in figure 4.19. From a distance of approximately 10 mm to the first shock a pressure ratio of $\sim 1\%$ can be extracted from equation (4.25). However the design pressure ratio for

[3] see: `http://astro.u-strasbg.fr/~koppen/discharge/`

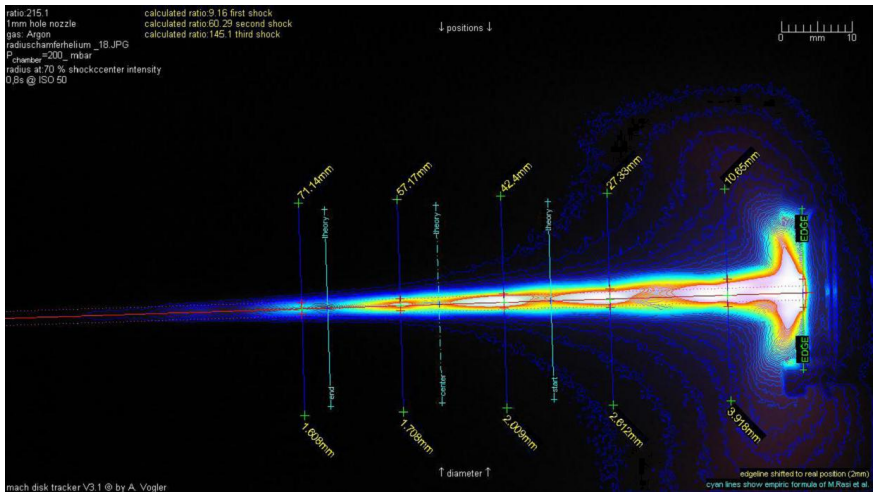

Figure 4.19: Picture of the gas jet analysis program.

the exit hole is ∼0.487 and consequently the exit hole is highly underexpanded. This behaviour is illustrated by a very strong Mach shock and subsequent supersonic flow. A discussion of this scenario is given for example in [97].

Naturally, a nozzle operating at the design condition is preferred to a highly underexpanded nozzle. In previous studies [91] it has been shown that by increasing the background pressure a significant improvement of the collimation of the gas jet was achieved, leading to the current design of the "enclosed" sextupole, described in section 4.6.1. However, unforeseen problems have been recently revealed in the operation of the SPIG with Ar gas. Strong discharging was observed in the standard operational conditions.

This observation can be explained by Paschen's law [98] which essentially states that the breakdown voltage is a function of the product of the gas density and the distance d between the electrodes. The breakdown voltage V_{Br} is parametrized as described in [99] and can be written

$$V_{Br} = B\frac{Pd}{\ln(APd) - \ln\left(\ln\left(1 + 1/\gamma\right)\right)} \,. \tag{4.26}$$

Typical values for the Townsend discharge parameters A, B and γ are extracted from experimental data and can be found in textbooks [100]. These are listed in table 4.1 for completeness. Figure 4.20(a) shows the dependence of the breakdown voltage as a function of the product of pressure P and distance d of the electrodes for Ar and He

Gas type	A (Pa/m)	B (V/(Pa m))	γ
He	2.10	25.50	0.263
Ar	10.20	176.27	0.095

Table 4.1: Parameters for the Paschen curve for Ar and He [100].

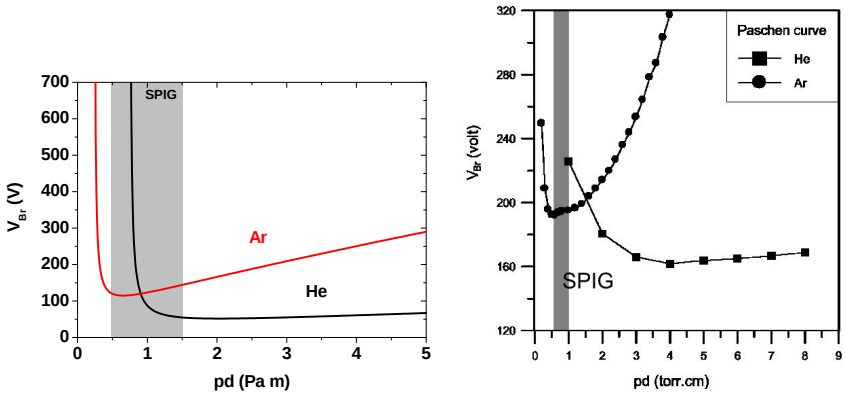

(a) Theoretical Paschen curve (b) Experimental data from [101]

Figure 4.20: Illustration of the Paschen curve for He and Ar. The grey band illustrates the typical operating regime of the JYFL rf sextupole.

according to equation (4.26). For comparison an experimentally determined Paschen curve [101] is plotted in figure 4.20(b). The theoretical data deviates slightly from the experimental data, however it needs to be stated that equation (4.26) is empirical and that the actual shape of the curve is dependent on the uniformity of the electric field and the electrode geometries and materials used, as for example pointed out in [102]. Therefore results from different setups are rather difficult to compare. The typical value Pd for the IGISOL SPIG system can be estimated to be 1 Pa m and the according region of interest is indicated by the gray boxes in the graphs in figure 4.20. The graphs indicate that the SPIG operates in the minimum of the Paschen curve for Ar and consequently a voltage of approximately 100-200 V is sufficient to create a discharge which is a typical RF operating voltage applied to SPIG for radial confinement of the ions. The appearance of a discharge in Ar but not in He might indicate that a value of $Pd \sim 0.5$ Pm is reached in the vicinity of the sextupole rods.

The discharge problem can be reduced by decreasing the pressure in the first sextupole. This can be achieved by removing the enclosure around the first SPIG structure. For a LIST experiment, one then has to rely on a good preparation of the gas jet by

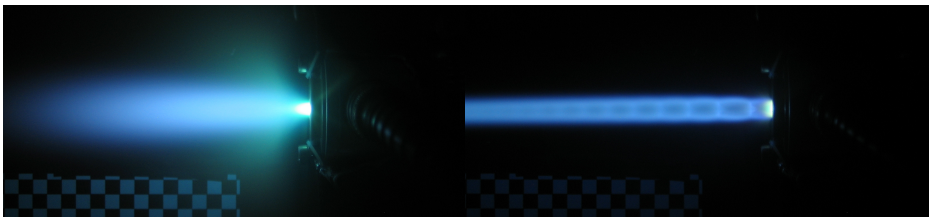

(a) 1.45 mm Laval nozzle, 30 mbar (left) and 230 mbar (right) Helium

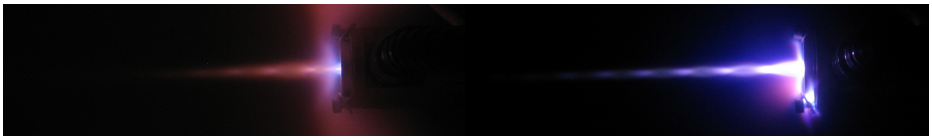

(b) 1.45 Laval nozzle, 70 mbar (left) and 500 mbar (right) Argon

Figure 4.21: Photographs of the gas jet for a Laval nozzle in helium and argon.

a suitable nozzle geometry to avoid a blow-up of the jet in the SPIG. The decreased pressure needs to be compensated by a larger diameter of the exit of the nozzle to maintain the design condition of $P_e \sim P_{bg}$ (see figure 4.17(a)).

The Laval-type nozzle tested in this work had a throat diameter of 1.45 mm and a diameter of 4 mm at the outlet resulting in a design Mach number of ∼4.5 at the exit and a critical pressure ratio of ∼0.006 to achieve the design condition according to equations (4.21) and (4.22). This pressure ratio is to be compared to the design ratio of ∼0.487 for a simple hole with $M = 1$ at the exit. The Laval nozzle starts to be choked at a pressure of approximately 100 mbar. Below this value no jet structure appears as indicated in the pictures on the left of figure 4.21(a) and 4.21(b). At high pressure ratios the gas jet shows a pattern of equidistant normal shock waves, typical for a "slightly underexpanded" jet as for example illustrated in [103].

The typical distance between the nozzle and the first shock is 10 mm for both argon and helium. Using equation (4.25) this can be converted to a pressure ratio of ∼2%, which is indeed rather close to the design pressure ratio of ∼ 0.6%. Consequently in contrast to the simple exit hole, the Laval nozzle operates close to the ideal design conditions. The numbers might suggest an overexpansion of the nozzle, in contradiction to what has been stated before. However, it has to be pointed out that equation (4.25) only provides a rough estimate of the background pressure ratio. Typical distances between neighbouring shocks for choked flow at IGISOL operational pressures are ∼ 9 mm for He and 17 mm in the case of Ar. For high pressures the gas jet diameter reduces to approximately 10 mm for He and to 4 mm for Ar. The jet diam-

eter remains constant over the whole length of the sextupole and consequently a good overlap with the counter-propagating laser radiation in LIST mode can be provided. The values for both the diameter of the jet and the static pressure in the chamber are in reasonable agreement with earlier experimental observations discussed in [104].

When coupling to the SPIG structure the shape of the gas jet is particularly important. The main hurdle is the entrance to the SPIG which is currently restricted by the repeller electrode aperture of 6 mm. In a normal IGISOL experiment the SPIG structure is placed at a small distance of some millimeters from the ion guide and consequently a sonic jet has built up in front of the entrance electrode. If the aperture is not considerably larger than the jet diameter the gas jet experiences a normal shock [94] and becomes subsonic after the nozzle leading to an almost spherical distribution of the gas. The only way to prevent the shock is to guide the gas from the nozzle structure directly to the SPIG by matching the exit diameter of the nozzle with the entrance aperture of the SPIG. To obtain the design flow conditions outside of the nozzle at a pressure ratio of approximately 1%, a Mach number of $\sim$4 is required at the exit. From the area-velocity relation the ratio of the exit diameter to the nozzle diameter can be estimated to be $\sim$2.3. The SPIG entrance electrode would represent the nozzle exit and a fully sonic jet would enter the sextupole structure. The gap between the SPIG and the ion guide can only be bridged by a highly insulating material to still enable a voltage difference between the devices. First successful tests have been carried out with a spacer made out of boron nitride. However to ensure a smooth change of the radius and obstacle-free expansion of the jet more effort has to be put into the axial alignment of the system. A suitable voltage of a few volts on the repeller can help to focus the ions transported by the jet into the ion guide. Such a focussing electrostatic device, a so-called squeezer, has been tested successfully for a skimmer system [104].

As becomes obvious from the discussion of this section further investigations are needed to be carried out to provide an optimized coupling from the ion guide to the SPIG. It is mandatory to build an off-line test bench as at the IGISOL front-end on-line studies are a higher priority. A simple rig is currently being installed. It features a quick ion guide mounting system compatible with the IGISOL front-end to allow for conditioning of ion guides for on-line use. A skimmer system separates the front-end chamber from the high-vacuum chamber where a radio-frequency quadrupole mass filter device and ion detectors are placed. The new chamber has large view ports and will provide much better accessibility than the IGISOL front-end, making it an ideal tool for optical observation of the gas jet.

The imaging method described in this section provides pictures of high intensity. The drawback of the method however is the sensitivity of the discharge in respect to the material of the electrodes and the pressure in the cell, making it a rather unreliable approach. An artistic impression of a failed discharge can be found in the front cover

of this thesis. An alternative approach could be imaging by the well-established and cost-effective Schlieren method [105, 106]. To test the impact of the SPIG structure on the gas jet it is planned to construct a plexiglas version of the structure. The velocity of the jet itself can be probed via a direct measurement of the Doppler shift of laser light scattered by the gas jet as discussed in [107].

The theoretical treatment of three-dimensional supersonic flow is difficult to treat in a closed form [93]. Nowadays, however, the problem can be approached by numerical simulation codes. To simulate and optimize the nozzle design based on the general design criteria described in this section a collaboration with a group based in Warsaw University [108,109], specialized in the simulation of supersonic flow, has been established and a first simulation is underway. Together with the experimental results from the off-line rig all the tools and the methods described here are available to complete the understanding of the gas jet in IGISOL.

4.7 Development of an ion beam of ^{94}Ag

The study of radioactive neutron-deficient silver isotopes in the region of the $N{=}Z$ line has been of considerable interest within the nuclear physics community for several years. In particular the isotopes of ^{94}Ag [110–112] and ^{96}Ag [113] have been extensively studied. The recently observed (21^+) isomeric state with a half-life of 0.39(4) s in the odd-odd $N = Z$ nucleus ^{94}Ag [114] has been identified as a nuclear spin trap having the highest spin ever observed for β-decaying nuclei. The properties of this isomer are unprecedented in the entire known Segré chart. Its decay can proceed via five pathways; β-delayed γ-ray, proton and two-proton emission as well as direct proton and two-proton radioactivity. In particular, the direct emission of one-proton and two-protons from the same long-lived nuclear state is a unique phenomenon, with the hindered rate of the former and the enhanced probability of the latter decay mode as well as the indication of a strong deformation of the parent state needing verification [115,116]. It is a challenge to future experiments to obtain proton-proton correlations with high resolution and better statistics, and furthermore to directly determine the shape of the (21^+) isomer via measurements of the nuclear quadrupole moment.

A program to produce a neutron-deficient silver ion beam has been started at IGISOL involving laser ionization of the radioactive species previously stopped and evaporated from a hot graphite catcher. An ionization efficiency of 14% has been reported by the ISOLDE RILIS laser ion source facility [117] using non-resonant post-ionization. Off-line tests have been carried out in the ABU to develop an efficient ionization scheme for Ag using the FURIOS laser ion source. The two different schemes sketched in figure 4.22(a) have been investigated. The first excitation step can be realized by a

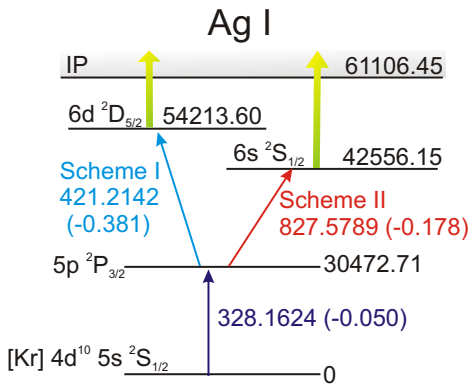

(a) Laser ionization schemes for silver

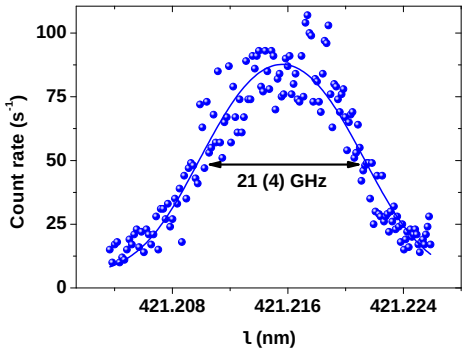

(b) Frequency scan of the blue second excitation step

Figure 4.22: Ionization scheme for silver and a frequency scan of the most efficient second excitation step.

frequency-doubled dye laser or a frequency-tripled Ti:Sapphire laser. As considerably more power in the UV was achieved with the Ti:Sapphire laser and the CVL beam which has been used to pump the dye laser was needed for post-ionization, it was decided to drive all resonant steps with the solid-state laser system. In this experiment the 511 nm component of the CVL radiation was used for ionization. A frequency scan of the second excitation step of scheme 1 is illustrated in figure 4.22(b). The width of the resonance indicates that full saturation of this step can be expected. A comparison of the saturation levels for the two schemes is shown in figure 4.23. The saturation data has been plotted as a function of the fraction of the maximum laser power available in each step. Full saturation was achieved in the resonant steps for both schemes. The saturation of the first step was corrected for the signal arising from non-resonant UV-UV ionization indicated in the figure. For the scheme with the second step transition in the blue (Scheme 1) a considerably better saturation of the non-resonant step into the continuum was achieved compared to the excitation step involving an infrared step (Scheme 2). This is despite the lower power available for the second step in the case of scheme 1 and the seemingly lower value of the oscillator strength indicated in figure 4.22(a). The low saturation power required for the second step in scheme 2 of 24(19) mW points towards the non-resonant step as the bottleneck of this scheme resulting in a lower ionization efficiency. Consequently for all subsequent tests described in the following, scheme 1 was chosen.

The design of the ion source was adapted from the GSI FEBIAD ion source described in detail in [118]. A technical drawing and a photograph of the catcher device are

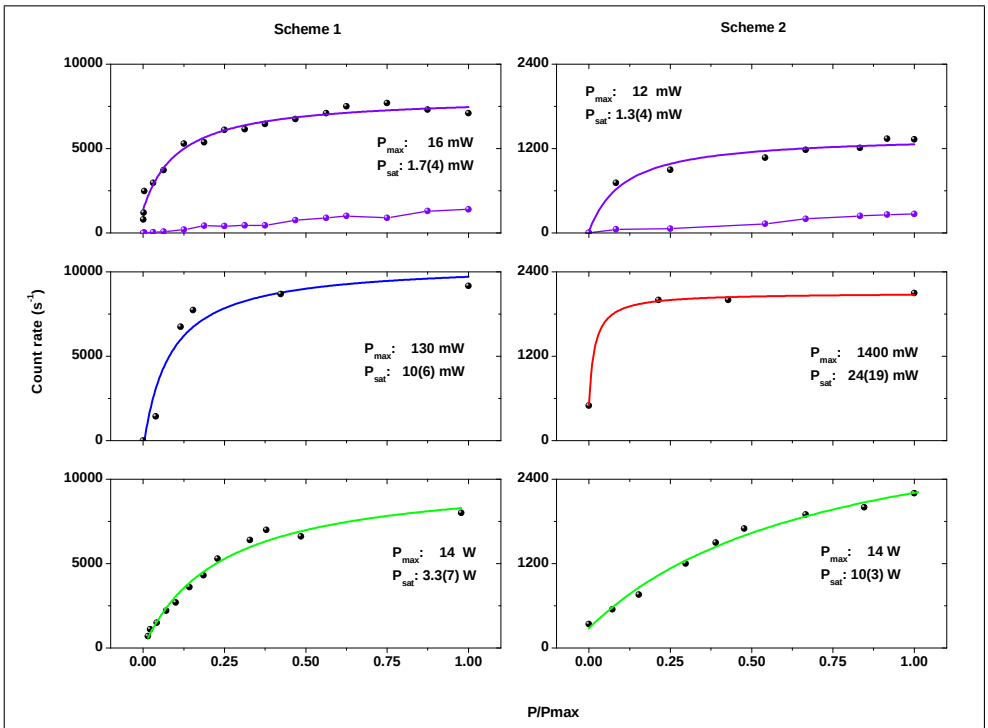

Figure 4.23: Comparison of the saturation of two different laser ionization schemes in silver.

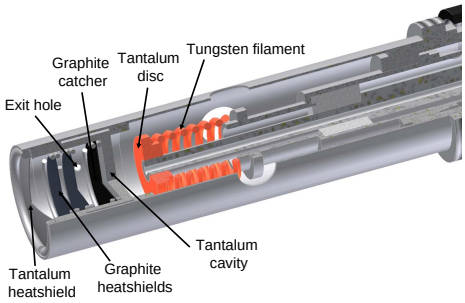

(a) CAD drawing

(b) Photograph

Figure 4.24: CAD drawing and photograph of the hot cavity ion source.

shown in figure 4.24. One disc of sintered graphite[4] with a thickness of 100 μ thickness was used in this work as a catcher material. The catcher is placed into a tantalum body which is externally heated by electron bombardment. The electrons are provided by a tantalum disc placed on top of a tungsten filament which is electrothermally heated by a current of ∼25 A. A second supply provides an acceleration voltage of ∼200 V between the filament and the catcher main body. Typical specifications of the cathode can be found in [119]. Additional shielding can be added to retain the heat in the main body. Typically up to 6 layers of 15 μm tantalum foil are wrapped around the device. The cold spot of the setup remains the beam window side. Three layers of graphite foil (30 μg/cm^2) and a tantalum shield of 1.8 mg/cm^2 can be stacked in front of the catcher device as described in [118]. The ions leave the catcher through an exit hole with a diameter of 1 mm placed towards the extraction side.

Two characteristics, namely the extraction efficiency of silver and the corresponding delay time make this type of source suitable for the project. In bunched release tests from the source [120,121] and simulations [122] a fast extraction in the order of 10 ms was observed for silver which is sufficient for the production of an ion beam of the ^{94}Ag 21^+ isomer which has a half-life of ∼0.39(4) s. An extraction efficiency of up to 40% was reached in the case of silver with a FEBIAD-type ion source configuration [122]. Whether a similar efficiency can be obtained with a laser ion source is yet to be seen. For efficient diffusion in the catcher material a temperature of ∼2000°C has to be reached. Off-line heating tests are currently underway to optimize the shielding of the cavity and a lower temperature limit of 1700°C has been measured so far without additional shielding of the beam window.

[4]Grade 5890PT by Le Carbone-Lorraine

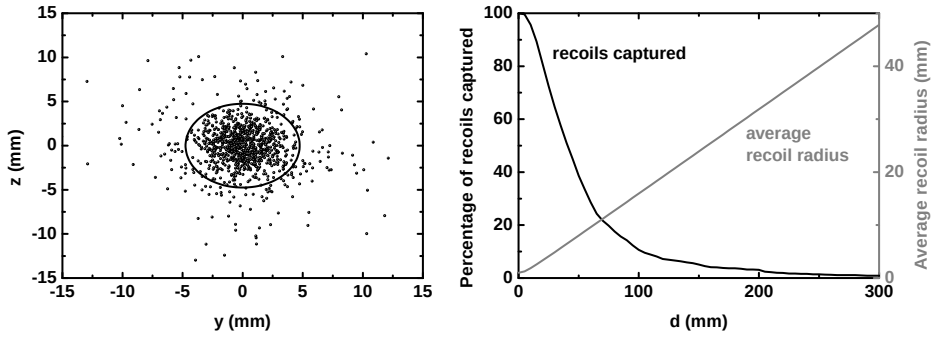

(a) Recoil distribution 20 mm after the target. The solid line defines the entrance to the graphite catcher.

(b) Number of ions captured as a function of distance d to the target.

Figure 4.25: Simulation of the recoil distribution in a ^{58}Ni(^{40}Ca,p3n)^{94}Ag reaction.

A primary beam intensity of at least 300 pnA of ^{40}Ca at approximately 5 MeV/u impinging on a 4 μm thick ^{58}Ni target is expected to drive the fusion-evaporation reaction of ^{58}Ni(^{40}Ca,p3n)^{94}Ag. In the earlier work at the ISOL facility of GSI, Darmstadt, the beam intensity was 75 pnA and with a separator efficiency of 30% the ^{94}Ag isomers were produced with an intensity of 2 atoms/s [115]. In the IGISOL setup a nickel target, segmented into four pieces, is mounted on a rotating wheel which is placed in front of the catcher device. To estimate the losses due to the scattering of the recoils leaving the target a simulation program was written. The details of the program are discussed in [123]. An estimate of the losses as a function of distance between the target and the catcher is illustrated in figure 4.25. Figure 4.25(a) shows the transversal recoil distribution 20 mm downstream from the target. At this typical distance for the experimental setup approximately 81% of the recoils are stopped. Figure 4.25(b) illustrates the captured fraction of recoils as a function of distance d from the target. Additionally for each distance the average transversal radius of the recoils was calculated. At a distance of about 30 mm from the target the average diameter of the recoil distribution is equivalent to the diameter of the catcher. At this distance approximately 65% of the recoils can be stopped.

A first test of the setup has been performed in IGISOL. In this experiment the CVL was not available and consequently a Ti:Sapphire laser was used for non-resonant laser ionization with an average output power of ~1.6 W. A sample of metallic silver was placed into the main body and evaporated by applying a heating current of 15 A to the filament. The bomdardment voltage was turned off. Laser ionization was performed in a counter-propagating or in a perpendicular geometry depending on whether the

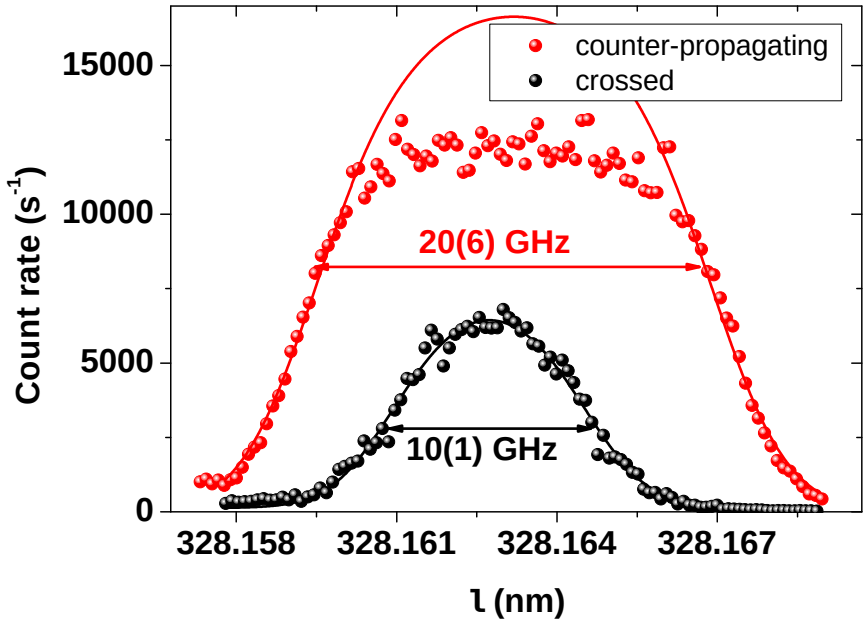

Figure 4.26: Laser scans of the first step for a crossed and an counter-propagating geometry in silver.

lasers beams were aligned through the magnet window or enter the interaction region through a window on top of the IGISOL vacuum chamber, respectively. A comparison of two laser frequency scans for the first excitation step is shown in figure 4.26. Unfortunately the ion count rate was saturated at the laser repetition rate at 12 kHz. Therefore a direct comparison of the ionization efficiency between the two geometries is not possible. To estimate the shape of the spectrum for the counter-propagating geometry a fit was attempted where only the wings of the structure having a count rate of less then 10000/s were taken into account. A gain of a factor of 2 in the efficiency can be deduced with laser radiation entering from the front rather than from the side of the extraction axis. On the other hand, a factor of 2 can be gained in the spectral resolution by entering from the top of the IGISOL chamber which can be ascribed to a reduction of the Doppler width of the transition.

A similar trend can be observed in a scan of the magnetic field of the dipole magnet of the IGISOL separator as shown in figure 4.27(a). In a crossed-beams geometry a mass resolving power (MRP) of $M/\Delta M \sim 180$ was achieved. Two different dipole mass scans are shown for the counter-propagating geometry. If the exit hole of the catcher is carefully aligned with the laser beams and the separator symmetry axis a

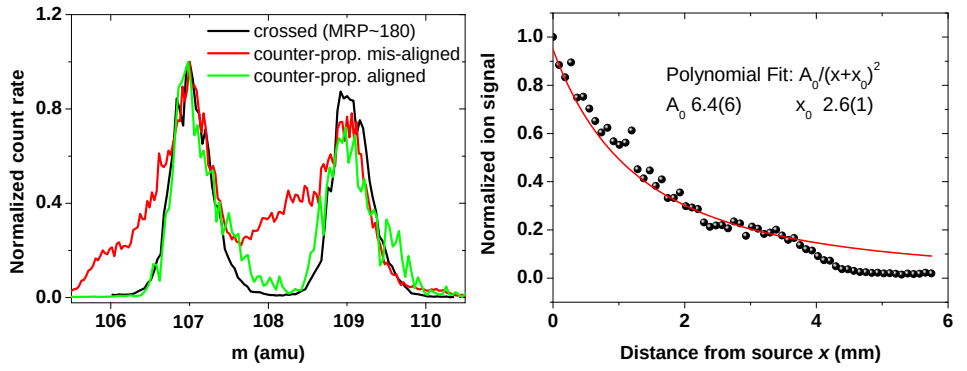

(a) Mass scan (b) Distribution of ions

Figure 4.27: Mass scans of a silver laser ion beam for different laser alignments and a calculated distribution of ions in front of the source.

comparable mass resolution can be achieved. By translating the laser beams off-axis a tail towards lower masses can be observed which can be explained by the ionization of atoms outside of the catcher along the separator axis at different extraction potentials. The distance x from the source for a particle with mass M_0 observed at a mass M in the mass scan is calculated by

$$x(M) = \left(1 - \left(\frac{M}{M_0}\right)^2\right) \frac{U_{acc}}{U_{ex}} x_{ex} \tag{4.27}$$

where U_{acc}/U_{ex} is the ratio between the acceleration voltage and the extractor voltage and x_{ex} the distance between the source and the extractor. A plot of the ion distribution in front of the source calculated from the broad mass distribution in figure 4.27(a) obtained under misaligned running conditions is shown in figure 4.27(b). The smaller number of atoms at higher distances from the source can be explained by the increase in the divergence of the atomic beam. The laser ion signal at any distance from the source can be estimated via the ratio of the area covered by the laser radiation and the area of the atomic beam at this distance. A linear increase in the atomic beam diameter with distance from the source corresponds to a parabolic increase in area and consequently the fraction of the atoms being illuminated by the laser radiation scales with $1/x^2$. A fit of this type, plotted in figure 4.27(b), gives a reasonable agreement with the data. In this model at a distance of approximately 2.5 mm from the exit hole the atomic beam has reached a diameter twice as large as the laser radiation.

One can conclude that for efficient laser ionization the counter-propagating alignment

would be preferred. The alignment of the laser and the source on the separator axis has to be done with extreme care to obtain a sufficient mass resolving power. As a manual steering of the beam did not prove to be sufficient, a piezo-driven remote-controlled mirror was installed close to the IGISOL user area. Experiments in need of good spectral resolution can benefit from an alignment of the laser beams in a perpendicular doppler-reduced geometry.

5 Development of laser techniques for IGISOL

In this chapter a variety of laser techniques developed during this thesis for the IGISOL facility will be introduced. An important aspect of the spectroscopic work at a laser ion source facility is the development and test of ionization schemes for RIS applications. A total of 14 different elements have been studied. An overview of the different laser ion beams developed in this work is given in table 5.1. The

Element		1st step	2nd step	3rd step	Comment
Z	Name	(nm)	(nm)	(nm)	and reference
13	Al	308.3048			residual blue [46]
28	Ni	274.7553	786.5936	821.97	Rydberg [16, 124, 125]
29	Cu	218.2405	828.36	761.23	AI
		217.9632	832.238	798.76	AI
		217.9632	832.380	761.23	AI [53, 125–128]
30	Ca	422.7918	413.9058		residual red [129, 130]
		422.7918	732.8163		[58]
31	Ga	403.4116			non-resonant [129, 130]
		417.3215			non-resonant
		287.5078			CVL, Rydberg
32	Ge	253.3991	909.8451	780.82	AI [16, 124, 125]
37	Rb	420.2972			non-resonant [129, 130]
39	Y	441.400	813.712	648.43	two second steps / AI [87]
43	Tc	429.827	395.15	841.72	AI [32, 127]
46	Pd	244.8652	715.0938		non-resonant [127, 128]
		244.8652	706.2252		non-resonant [127, 128]
47	Ag	328.1624	421.2142		CVL [123]
50	Sn	286.4158	811.629	823.723	AI [6, 125, 131]
83	Bi	306.861	382		YAG, AI [37, 132, 133]
90	Th	410.250	751.491	629.420	AI [134–136]

Table 5.1: RIS schemes applied in this thesis.

comments in the last column of the table give some information on the realization of the ionization step. The possible ionization mechanisms include auto-ionization (AI), ionization from a Rydberg state (Rydberg) or non-resonant ionization using a copper vapour laser (CVL), an Nd:YAG laser (YAG), residual light from higher harmonic generation (residual) or simple non-resonant ionization by one of the laser beams tuned to bound-state resonances (non-resonant).

The elements calcium, rubidium and gallium have been used as test cases for resonant ionization spectroscopy as they have low vapour pressures and atomic structure that can be easily accessed by the FURIOS laser system.

The ionization schemes for nickel, germanium, palladium, tin and copper were developed in collaboration with the University of Mainz and the Oak Ridge National Laboratory (ORNL) as test cases in preparation for a laser ion source for a future RIA-like facility. A summary of the results obtained so far is given in [125]. For efficient laser ionization of copper, a wavelength of 218.2 nm was needed for the first excitation step. The light was produced by generation of the fourth harmonic of a Ti:Sapphire laser operated at ∼873 nm.

For the case of yttrium a rather unusual ionization scheme with two second step excitations was applied. The ionization scheme for thorium was developed to improve the efficiency of a new ion guide for extraction of a beam of $^{229}Th^{g,m}$ produced from the α decay of ^{233}U. This scheme can also be used to perform resonance ionization spectroscopy within the ion guide in order to gain nuclear structure information from the hyperfine structure of ^{229}Th.

Aluminium was chosen as a test element for high-resolution in-source spectroscopy in a hot cavity using the seeded Ti:Sapphire laser described in section 3.1.3. Bismuth was taken as a test case for exploring the possibility of in-source spectroscopy in the buffer gas cell.

Detailed information on the schemes applied and the physics motivation can be found in the citations given in table 5.1 and references therein. In this chapter selected highlights of the spectroscopic work carried out during this thesis will be presented.

In the first section of this chapter the development of a laser ion beam of technetium will be discussed, which is particularly hard to develop as no stable isotope exists and therefore only trace sample sizes can be probed. The laser ionization scheme for yttrium, detailed in section 5.2, was used to study the role of impurities in the buffer gas arising from the strong reaction of Y^+ ions with oxygen. Another area of interest was the investigation of the possibility of Rydberg ionization in a hot-cavity and in IGISOL. High-resolution spectroscopy of Rydberg states in nickel was tested at the ISTF-2 separator of the HRIBF facility at ORNL (USA) as discussed in section 5.3. The results of Rydberg ionization on gallium at IGISOL are detailed in section 5.4.

A relatively new technique of high-resolution in-source spectroscopy with a huge potential especially for the investigation of short-lived radioactive nuclei is discussed in section 5.5. This technique goes hand-in-hand with the development of high-resolution pulsed laser systems performed in collaboration with the University of Mainz. In-source resonance ionization spectroscopy has been tested for the case of bismuth at IGISOL, detailed in section 5.5.1. The results of an off-line test applying the same technique for a hot-cavity ion source on aluminium are discussed in section

5.5.2. Finally, a novel technique developed at the IGISOL facility, namely the optical pumping of ions stored in an RF cooler device coupled to subsequent collinear laser spectroscopy is described in section 5.6.

5.1 Development of a laser ion beam of technetium

From a physics point of view, there is a three-fold motivation to study the isotopes of technetium: nuclear astrophysics, weak interaction physics and nuclear structure physics. For example, according to the conserved vector current hypothesis (CVC), the matrix elements of the superallowed Fermi transitions between the 0^+ isobaric analog states (IAS) should all be equal, independent of nuclear structure apart from small radiative and isospin-symmetry breaking terms. These latter terms become increasingly important with increasing Z of the nucleus, and uncertainties between different theoretical calculations dominate the uncertainty of the isospin correction [137, 138]. At IGISOL measurements of the Q-values of various superallowed β emitters have been carried out recently [139, 140]. A measurement of the Q-value and half-life of the $N = Z$ nucleus ^{86}Tc, would provide important experimental input to this field.

In addition, nuclei close to the $N = Z$ line play a special role in nuclear astrophysics since the rapid-proton (rp) capture process passes right through them. On the neutron-rich side of the valley of stability, extending the ability to produce even more exotic Tc isotopes will benefit the studies of nuclear structure in this region, and also provide input for calculations dealing with the astrophysical r-process.

The ion guide used for the laser ionization of Tc is described in detail in [87]. It is equipped with a mount for an electrothermally heated filament. The filament was prepared at the nuclear chemistry department of the University of Mainz using an electrodeposition technique as described in [141]. The filament substrate is made from rhenium and is cut into a 20x4 mm^2 foil, with a thickness of 25 μm. A sample of 10^{14} atoms of ^{99}Tc with a half-life $T_{1/2} = 2.111 \cdot 10^5$ years [142], is deposited onto the foil and can be evaporated with temperatures of up to 1500 °C under vacuum. A picture of the filament mounted on the back flange of the ion guide is shown in figure 5.1(a) with a corresponding heating curve in 5.1(b). The temperature was determined with an optical pyrometer. A temperature of about 1500°C was needed to efficiently evaporate technetium atoms from the filament.

The laser radiation enters the ion guide on-axis via an entrance window in the rear. A helium gas flow at a pressure of 60 mbar extracts the resonant ions through the exit nozzle of the ion guide. The ions are subsequently guided through the radiofrequency sextupole device (SPIG) before being accelerated to 30 kV and mass separated. The final detection is done with a set of microchannel plates (MCP) downstream from the

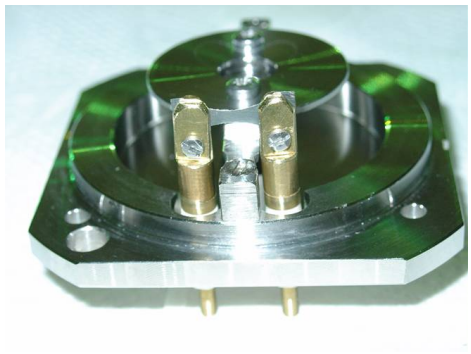

(a) Picture of the filament placed into the ion guide

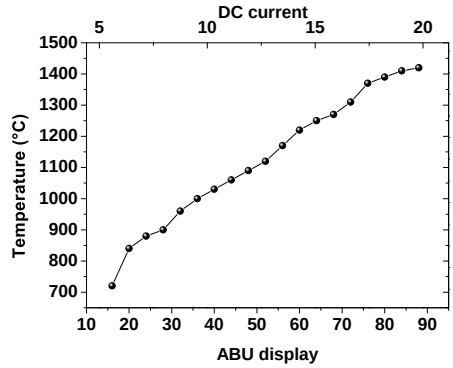

(b) Temperature calibration

Figure 5.1: Heating tests for the rhenium filament.

IGISOL focal plane.

The excitation of the first and second steps at 429.8 nm [143] and 395.2 nm [144] respectively, was achieved using two BBO crystals (2ν) to generate the second harmonic frequency. The laser powers measured at the entrance window of the ion guide were as follows: 70 mW for the first step; 130 mW for the second step; 1.4 W for the autoionization step at 841.72 nm. The power available for the first two steps exceeds that needed to saturate the transitions [127]. As no spectroscopic investigations have been carried out for the third step it is unknown as to whether this step is saturated.

Following the alignment of the lasers into the ion guide the filament was continuously heated to provide an atomic vapour of Tc. At a current of 18 A corresponding to a filament temperature of ∼1400 °C, a first Tc laser ion signal was observed. A maximum count rate of 180,000 counts/s was obtained after optimizing the laser wavelengths, spatial overlap and IGISOL ion beam tuning. Figure 5.2 shows a mass scan in the range of 84 to 100 amu. A key parameter for a laser ion source is the selectivity, determined by measuring the ratio of laser ions to non-resonant ions. In this work a selectivity of ∼ 56 was observed. Non-resonant surface ions were observed in the mass scan due to the high temperature needed to evaporate the Tc sample from the Re substrate. As expected, the alkali metal isotopes ^{23}Na, ^{39}K, ^{41}K, ^{85}Rb and ^{87}Rb were all observed. The non-resonant signals observed at masses of 92-101 amu most likely arise from molecular contaminants formed from impurities in the buffer gas.

Additionally to the ionization in the buffer gas cell, the possibility of ionizing Tc in

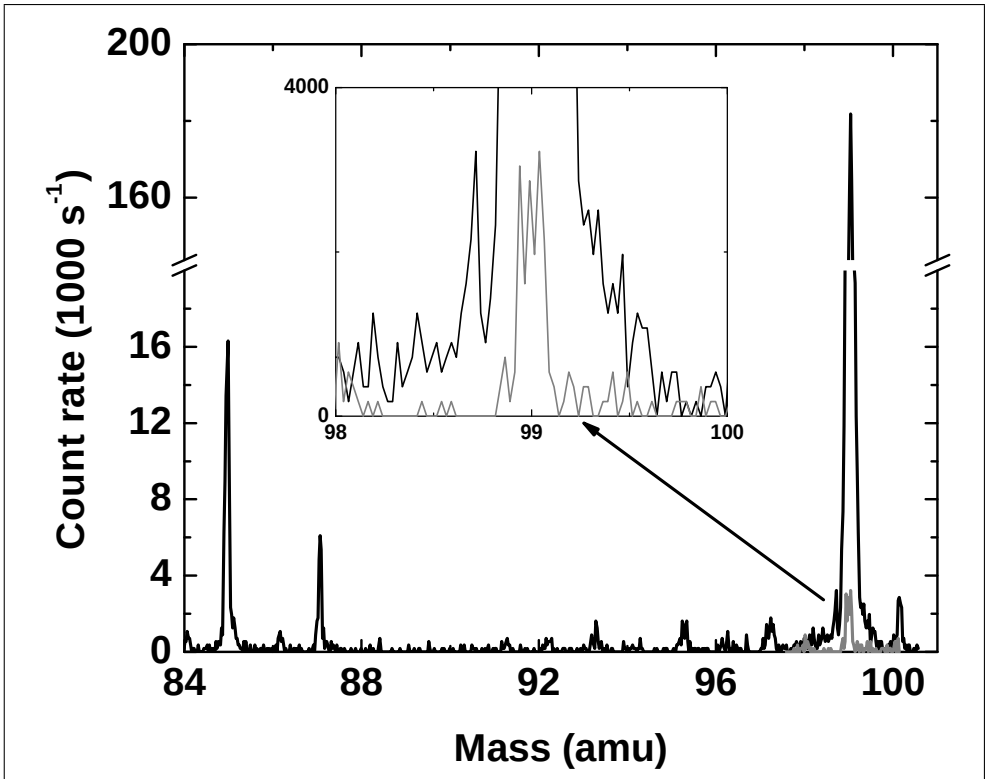

Figure 5.2: Mass scan from 84 to 100 amu. The surface ionised isotopes ^{85}Rb and ^{87}Rb as well as the laser ionised ^{99}Tc appear in the spectrum. The insert shows the mass scan in the region of 99 amu with lasers off. Note the y-axis break.

the SPIG was investigated. The gas jet has a considerably higher velocity (1000 m/s) compared to the velocity in the main body of the gas cell. With a repetition rate of 10 kHz, the FURIOS laser system can efficiently ionize the atoms within the gas jet over the length of the SPIG system. The repeller electrode of the SPIG was switched from -13 V to +13 V with respect to the ion guide to separate those ions created in the guide from ions created in the SPIG. In the same experiment the path of the laser radiation could be switched to the frontside (figure 4.1) by using flipper mirrors. A summary of the count rates observed is given in table 5.2. Note that the filament temperature

	repeller (V)	laser on	laser off	selectivity
backside	-13	10000	1800	5.6
	+13	900	5	180
frontside	-13	1700	1300	1.3
	+13	130	5	26

Table 5.2: Comparison of yields for laser ionization within the rf sextupole and the ion guide.

has been reduced for this experiment to provide constant running conditions. When the laser radiation is coupled into the back of the ion guide and the repeller voltage is switched from -13 V to 13 V the resonant ion signal is reduced by about one order of magnitude. The selectivity, listed in the last column of table 5.2, is significantly increased from 5.6 to 130 indicating the improvement which can be obtained with the LIST approach. When coupling the lasers into the front of IGISOL the resultant signal drops by about one order of magnitude. It was later discovered that the laser radiation experiences high losses at the entrance window of the dipole magnet which can only be accessed during a longer shutdown period for example in the IGISOL 4 upgrade phase. Therefore the numbers in table 5.2 have to be handled with care and comparisons between the yields obtained from within the SPIG and ion guide cannot be readily made. However it is clear that for the front side again an increase in selectivity can be observed by switching the repeller voltage to +13 V.

5.2 Development of a laser ionization scheme for yttrium

The first element studied with the laser ion source was yttrium. The element was initially chosen based on a need to extend a rich programme of ground state nuclear structure studies in the refractory region [145–147]. Yttrium is very sensitive to impurities in the buffer gas and therefore can be used to probe the impact of molecular formation on the efficiency of the source as discussed in section 6.1.

The search for an appropriate resonant ionization scheme is of crucial importance

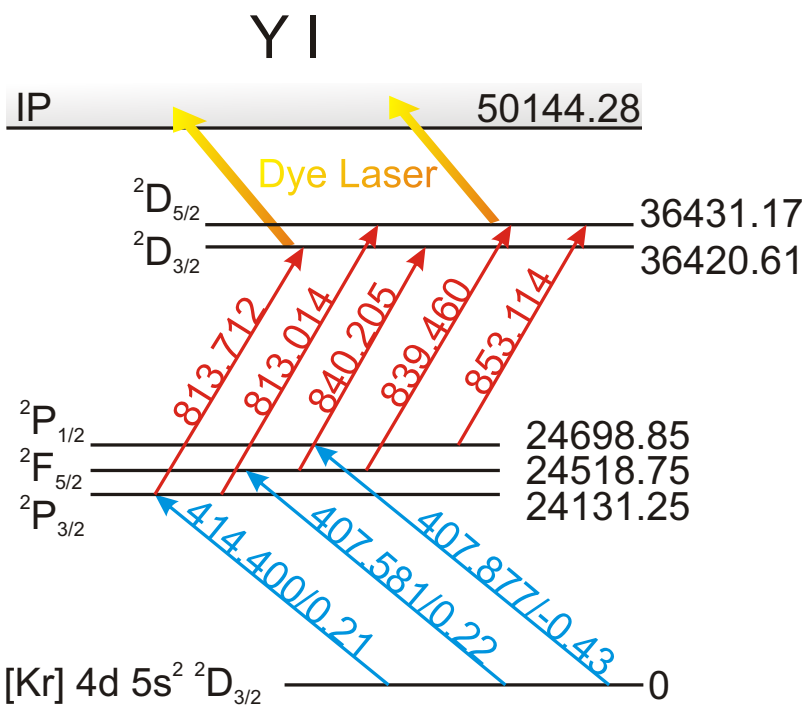

Figure 5.3: Relevant atomic energy levels in yttrium and the transitions investigated in this work.

prior to working with a laser ion source. The motivation for these spectroscopic studies was the comparison of the efficiencies of different ionization schemes. An atomic energy level scheme showing the transitions investigated in this work is shown in figure 5.3. The atomic excitation energy of the levels labeled on the right of the figure is given in units of cm^{-1}. The energy levels are identified on the left side and are given in the Russel-Saunders-Coupling notation with the atomic structure labeled as $^{2S+1}L_J$, where S is the total spin, L the total orbital angular momentum and J the quantum number of the spin-orbit interaction. The wavelengths of the transitions between the levels are denoted in units of nm and are given as wavelength in vacuum. Next to the wavelength, the log-gf (transition strength) is listed if known from literature [129,148].

The first resonant transition step was realized using a frequency-doubled Ti:Sapphire laser, while the second resonant step was driven by the fundamental output of a

second Ti:Sapphire laser. A non-resonant ionization step was achieved by exciting the atoms across the ionization potential (IP), 50144.275 cm^{-1}, with the frequency doubled light from the first transition.

The dye laser was used to scan across the IP to search for the existence of possible auto-ionizing levels. Two wavelength scans were made over the range of the available dye (DCM, 610-660 nm) starting from the excitation levels populated by the two second step Ti:Sapphire transitions at 36420.611 cm^{-1} and 36431.165 cm^{-1}. A summary of the final choice of lasers used for the different transitions and the laser powers measured at the entrance to the atomic beam unit is shown in table 5.3. Figure 5.4 shows the resultant dye laser spectrum starting from the excitation levels

Step	λ (nm)	Power at abu (mW)	Laser
1	414.40	240	Ti:Sa 2^{nd} harmonic
2	813.71	750	Ti:Sa
2	813.01	1050	Ti:Sa
3	619-655	200-400	Dye (DCM)

Table 5.3: The mixed Ti:Sapphire - dye transitions and laser powers obtained at the entrance to the atomic beam unit for RIS on yttrium.

of 36431.165 cm^{-1} (black line, left scale) and 36420.611 cm^{-1} (red line, right scale), respectively. A spectrum of resonances of differing intensities and widths was observed. The numerous broad structures were identified as auto-ionizing states. This was confirmed by blocking the second excitation step. If the signal drops to the background level then the second step is needed to perform the triple resonant ionization process. Three narrow resonances were also identified in both third step dye laser scans overlapping at exactly the same wavelength. These are labeled as 1, 2 and 3 in the more detailed view of the dye laser spectrum shown in the bottom figure of figure 5.4. It was concluded after further investigation that these resonances correspond to the dye laser driving a second step transition from 24131.250 cm^{-1} to levels at 39686.0 cm^{-1}, 39565.1 cm^{-1} and 39553.0 cm^{-1} (resonances 1, 2 and 3 respectively), not shown in figure 5.3. The atomic levels at 39686.0 cm^{-1} and 39565.1 cm^{-1} are previously known, while the level at 39553.0 cm^{-1} is newly discovered.

To evaluate the autoionizing spectrum of figure 5.4 the two wavelength scans from the $J = 3/2$ and the $J = 5/2$ states are plotted as function of the sum frequency of all three excitation steps as shown in figure 5.5. Overlapping lines such as the one at 52110 cm^{-1} represent autoionizing states which can be driven by both a $J = 5/2$ or a $J = 3/2$ lower step. For autoionizing resonances appearing in only one of the two panels a spin assignment can be attempted. The resonance marked with a star in the lower panel can only lead to a $J = 7/2$ autoionizing state while those marked with a summation sign in the upper panel can be linked to $J = 1/2$ states according to the

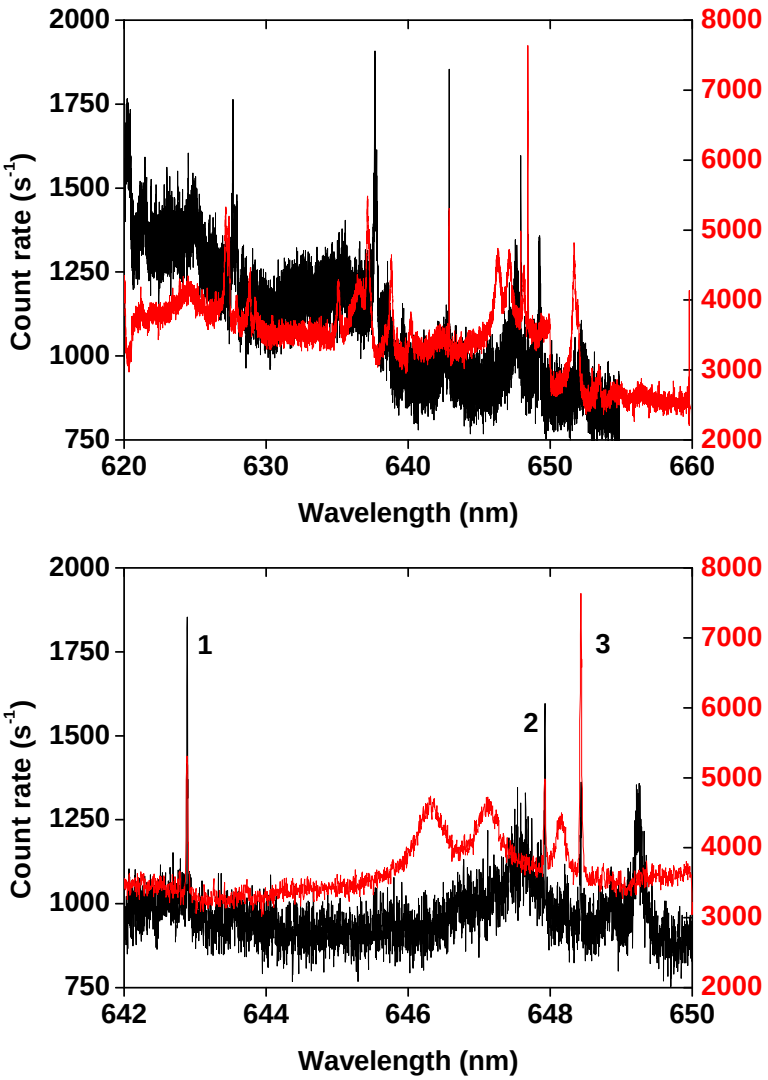

Figure 5.4: Dye laser spectrum starting from excitation levels of 36431.165 cm^{-1} (black line, left scale) and 36420.611 cm^{-1} (red line, right scale), respectively. The top figure shows the full dye laser scan, while the spectrum on the bottom is a magnified part highlighting the three narrow resonances of interest (see text for discussion).

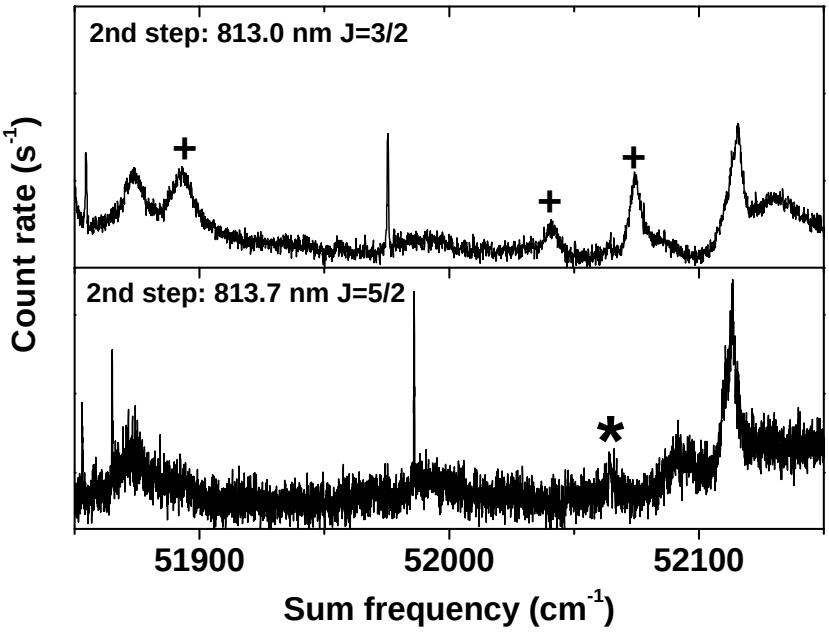

Figure 5.5: Detail of a full wavelength scan of the third step for two different second steps as a function of total frequency. See text for details.

dipole selection rules for atomic transitions.

Table 5.4 details the effects of blocking the different laser transitions, using the dye laser driving the new second step transition from the atomic level at 24131.250 cm^{-1} to the level at 39553.0 cm^{-1}. It is clear that the first step in the scheme is pivotal.

	Ti:Sa I 1st step blocked	Ti:Sa I 1st step only	Ti:Sa II 2nd step blocked	Dye 2nd step blocked	All lasers available
Count rate (ions/s)	0	10	600	1200	1800

Table 5.4: The effect of blocking Ti:Sa I (414.40 nm), Ti:Sa II (813.71 nm) and the dye laser (648.43 nm) on the ion count rate.

When this transition is blocked the ion signal disappears. If only the blue transition is used it is possible to have a double-blue non-resonant transition after the first step, though this is very weak, only 0.5% of the total count rate. By reducing the temperature of the oven this signal disappears and so these ions are indeed created via interaction with the laser beam. By including the second resonant Ti:Sapphire transition approximately 2/3 of the total ion signal is achieved. The main ionization pathway used in this case is then blue-IR-blue, where the final blue step is non-resonant. If the dye laser is used alone to drive a second step transition then approximately 1/3 of the total signal, 600 ions/s, is reached. In this scenario the possible ionization schemes are blue-red-blue and blue-red-red. When all three lasers are allowed to interact with the yttrium atoms, additional blue-IR-red and blue-red-IR pathways are possible, resulting in a total ion signal of 1800 ions/s.

The reason for the different rates depending on which second step laser is blocked may be due to different transition strengths, or to any efficiency differences in pumping using a dye or Ti:Sapphire laser. Future investigations on the latter possibility are needed and an atomic system will have to be found that enables the same transition wavelength to be used. In this manner the intrinsic differences between the laser systems, such as the pulse length (10 ns for a dye laser, 50 ns for a Ti:Sapphire laser) may be studied as a function of the ionization efficiency. However, for the purpose of a laser ion source, the high peak ion count rate achieved with this mixed dye-Ti:Sapphire scheme has led to the use of the twin laser system in the RIS experiments described in sections 6.1 and 6.2.2.

5.3 Rydberg spectroscopy on nickel in a hot cavity ion source

In the preparation towards realization of the RIA (Rare Isotope Accelerator) facility [149] an advanced laser ion source is needed to generate RIBs of high purity and

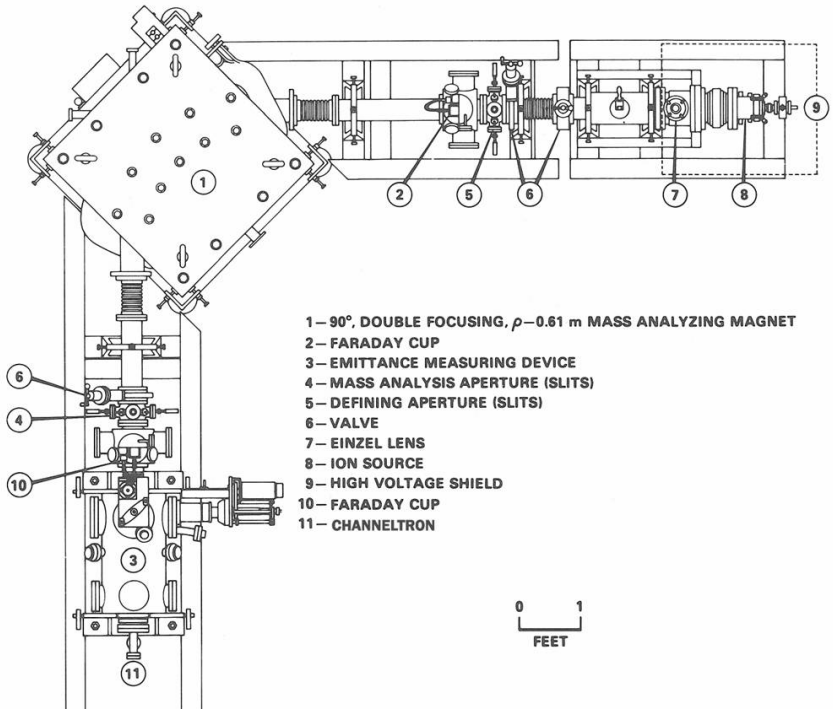

Figure 5.6: Setup of the ORNL off-line mass separator.

intensity [150]. Therefore at the HRIB facility of the Oak Ridge National Laboratory, (ORNL), USA, an off-line mass separator (ISTF-2) has been built. To test the hot cavity ion source coupled with laser ionization, the Mainz Ti:Sapphire laser system was shipped and installed at ISTF-2. Nickel, germanium and tin were chosen as test cases. The source was characterized with respect to efficiency, selectivity, time structure and emittance [16,53,124,125]. Hot-cavity atom sources coupled to a mass separator provide a unique tool to obtain high quality and intense stable beams for atomic in-source spectroscopy. In the following, studies of Rydberg ionization on stable nickel are presented.

A schematic illustration of the ISTF-2 ion source and mass separator at ORNL is shown in figure 5.6. The neutral atom and ion source assembly is mounted on a high voltage platform that is typically operated at a potential of 20 kV. The extracted ion beam is directed towards a 90° dipole sector magnet for mass separation (radius $\sim$ 0.61 m). The separated ion beam travels another 2 meters in vacuum before

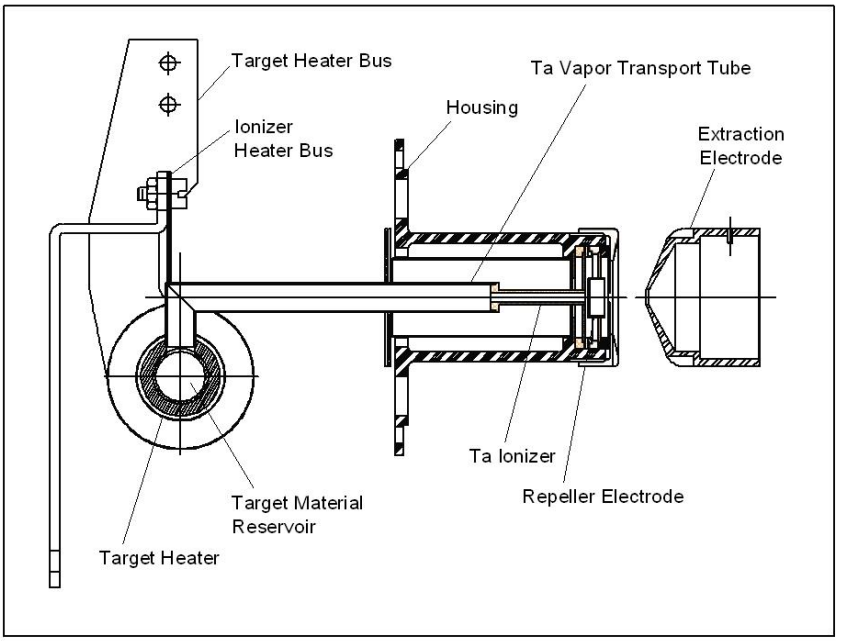

Figure 5.7: Schematic of the modified ion source for laser ionization at ISTF-2.

reaching various ion beam diagnostics, including a Faraday cup, a channeltron and an emittance meter. Various ion sources can be installed and operated at ISTF-2 for test use before on-line deployment at the HRIBF. For laser ion source development, a standard high-temperature surface ionization ion source and target material reservoir assembly was adapted for optimum neutral atom production. The design of the source is shown in figure 5.7. The species of interest is introduced into the heated reservoir in solid form and evaporated at temperatures around 1000°C. The atomic vapour effuses into an independently heated tantalum transfer tube and ionizer assembly. The dimensions of the transfer tube are 8.5 mm inner diameter and 100 mm length, while the ionizer tube is 30 mm long and 3 mm in diameter.

A photograph of the laser setup at ORNL is shown in figure 5.8. A commercial Nd:YAG laser[1] (1) was leased as a pump laser delivering up to 100 W of input power for the three Ti:Sapphire lasers (2). A unit for generation of the 2nd, 3rd and 4th harmonic was placed behind one of the Ti:Sapphire lasers (3). After being focused and overlapped in space (4) the laser beams are transported to the entrance window

[1] Photonics Industries Prototype

of the dipole magnet (5).

Three-step resonance excitation and ionization of Ni via a Rydberg state was demonstrated earlier by Ishikawa using dye lasers [151]. For the Ti:Sapphire laser system used here, an alternative excitation scheme had to be established which is shown in figure 5.9. Rydberg spectroscopy was performed by applying a Ni[275,787,814-837(Ryd),IRe^-]Ni^+ scheme [124]. The level assignments were taken from the NIST tables [130]. The first excitation step, in the ultraviolet spectral range around 276 nm, starts either from the low-lying $J = 3$ (204.787 cm^{-1}) or $J = 2$ (879.816 cm^{-1}) fine structure sub-levels of the $3d^9$ (^{2}D) 4s ^3D_J multiplet. At a typical atomizer temperature of 1700 °C these sub-levels have populations of 26.7% and 11.7%, respectively. The 786.59 nm transition was used in the second excitation step. For the third step, different ionization pathways were investigated that involve the population of either high-lying Rydberg levels or autoionizing levels, located near and above the first ionization potential (IP) respectively. The ionization from the Rydberg state is most-likely driven by black-body radiation as discussed later in this section. The highest ionization rate was obtained at a wavelength of 822.0 nm from a Rydberg state with a principal quantum number of $n = 30$.

For the Rydberg spectroscopy the laser frequencies for the first and second excitation step were fixed on resonance while the third laser frequency was scanned below the ionization potential. The resulting scan of the final step transition is shown in figure 5.10. Figure 5.10(a) shows a frequency scan of the laser driving the excitation into the Rydberg states. The numbers in the plot annotate the principal quantum number n. An increase in the laser ion yield by about 2 orders of magnitude can be observed for the strongest Rydberg states compared to non-resonant laser ionization. Figure 5.10(b) shows the same scan in the range of high n ranging from 49 to 72 indiciting a limit in spectral resolution of ∼10 GHz. In figure 5.10(c) the centroid frequencies of all resonances were plotted as a function of n. The theoretical function of equation (2.61) fitted to the data is indicated by the solid line together with the residual deviations shown in the bottom of the figure. The term $\delta(n)$ in equation (2.61) is approximated to second order in $1/(n - A)$ by a so-called Ritz expansion [152–154]

$$\delta(n) = A + \frac{B}{(n - A)^2} \tag{5.1}$$

where A is a constant offset and B defines the strength of the n-dependence in the form of an inverse parabola. Both terms account for the shielding of the Coulomb potential of the nucleus by the core electrons.

Apart from exploring the efficiency of ionization by different Rydberg states important spectroscopic information can be extracted from the fit. In this work for example, the precision of the ionization potential of nickel was improved by more than one order of magnitude to a value of 61619.77(14) cm^{-1} and a determination of the quantum-

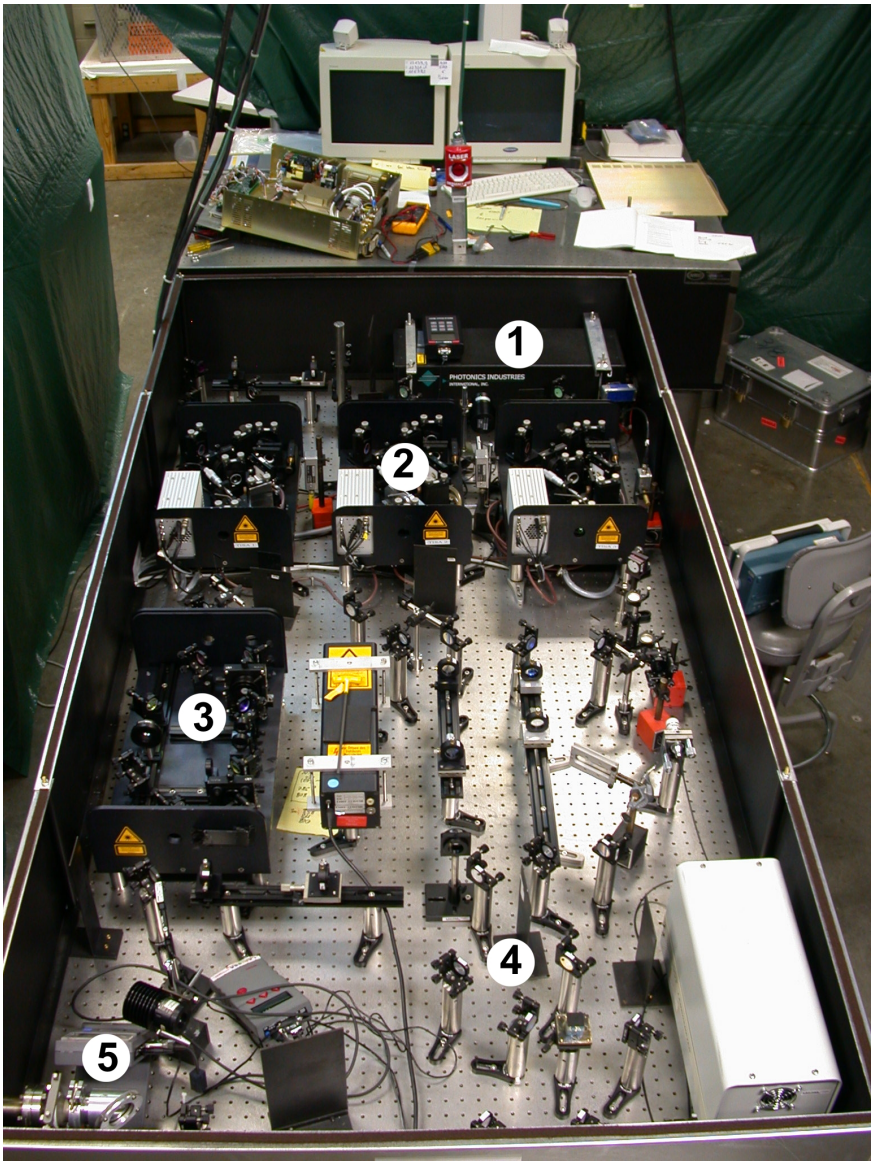

Figure 5.8: Laser setup at ORNL. For details see text.

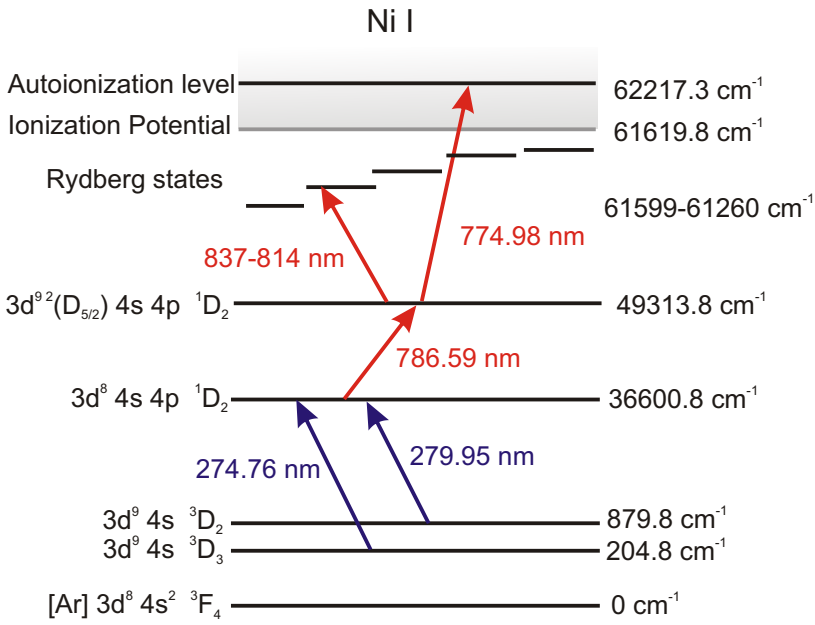

Figure 5.9: Ionization scheme for Rydberg spectroscopy in nickel.

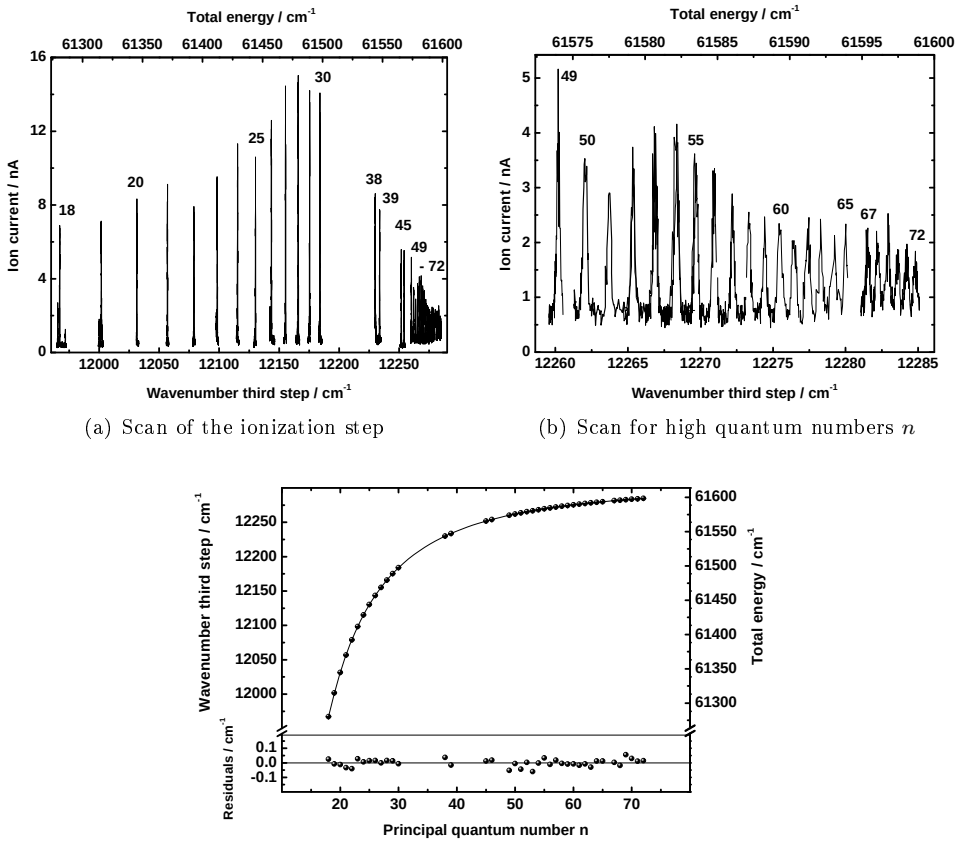

(a) Scan of the ionization step

(b) Scan for high quantum numbers n

(c) Rydberg level energies as function of n

Figure 5.10: Laser frequency scan of the third excitation step into Rydberg states in nickel.

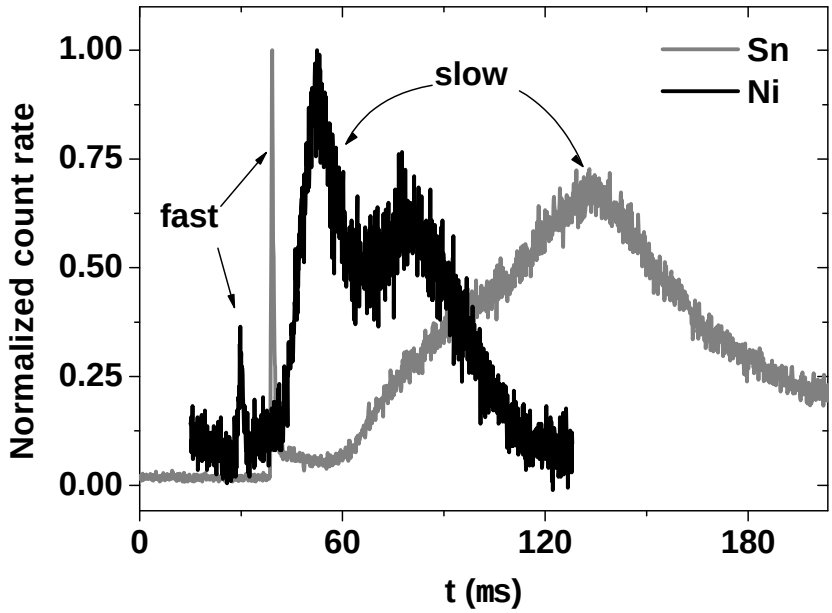

Figure 5.11: Time structure of a laser ion bunch of nickel and tin extracted from a hot cavity ion source.

defect of the Rydberg series to $A = 0.006(1)$ and $B = -0.006(9)$ by linking the series to well-known lower lying states in the degenerate $3d^9$ ($^2D_{5/2}$) nf $^2[7/2]^o_{3,4}$ or $^2[9/2]^o_4$ series. For more details the reader is referred to [124, 127].

The time structure of a laser ion bunch can reveal important information on the ion release properties of the source (see section 4.6) and on the laser ionization mechanism. A comparison of two time structures for the extraction of the elements tin and nickel is shown in figure 5.11. The general shape of the peak structure is dependent on various parameters, for example the choice of the element and the source material, ionizer and target temperatures, extraction fields and the source geometry. A detailed analysis of these structures can be found in [53]. The structure of the Sn laser ion bunch is split into a fast component and a slow component arising from direct laser ionization in the extraction field in front of the source and in the low field region inside the cavity. The nickel data shows a very small fraction for the fast and a pronounced interesting double structure for the slow component. This double structure is formed by ions produced in the ionizer and in the transfer tube (see figure 5.7). The reduced fast structure in the nickel data indicates that the prepared Rydberg state can only be ionized inside the source region and not in the extraction field, most likely by

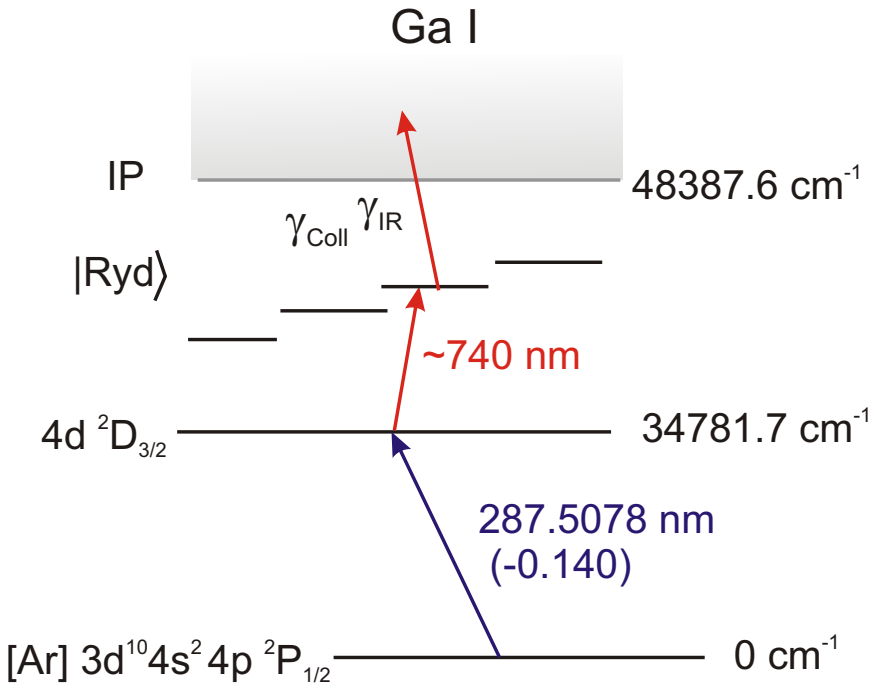

Figure 5.12: Ionization scheme for gallium.

infrared black-body radiation.

5.4 Rydberg spectroscopy on gallium at IGISOL

While the possibility of Rydberg ionization is reasonably well established for hot cavity ion sources, ionization from high-lying states has not yet been studied for IGISOL systems. However efficient ionization from high-lying states in pressurized cells has been observed [26, 27, 155] mainly for alkaline and alkaline earth samples in a noble gas environment. In the following the first studies on resonance ionization spectroscopy utilizing Rydberg states in the IGISOL buffer gas cell are presented for the test case of gallium.

Initially, tests were carried out in the atomic beam unit (ABU) (see section 3.4). A sketch of the ionization scheme is shown in figure 5.12. The first step was fixed on resonance and the second step scanned. The resulting ion yield as a function of

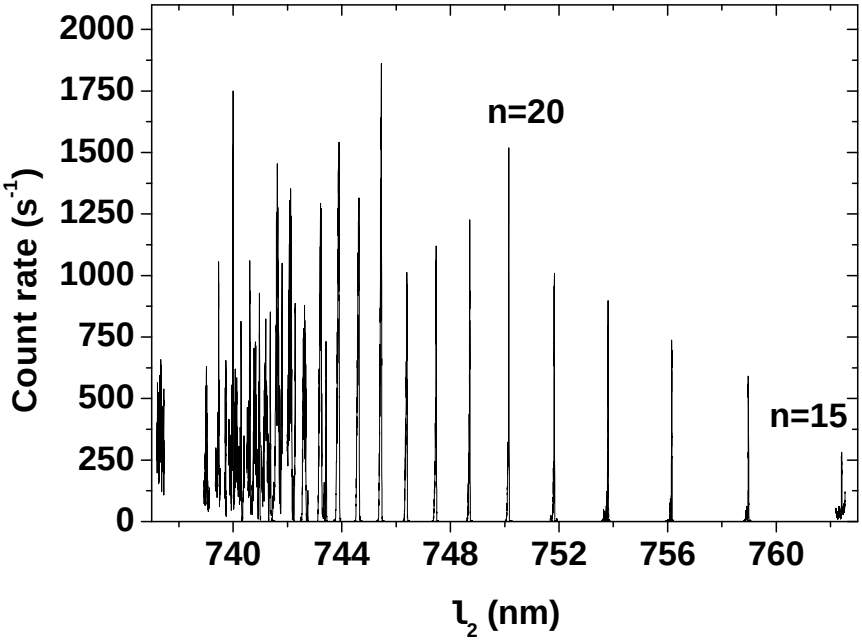

Figure 5.13: Laser scan across Rydberg levels from $n \sim 15 - 40$ in gallium in the ABU. The number in the graph indicates tentative values for n.

the laser wavelength λ_2 is shown in figure 5.13. The numbers in the graph indicate values for n tentatively assigned from the expected transition frequency assuming unperturbed hydrogenic Rydberg levels using equation (2.61) with $\delta(n) = 0$. A signal increase by about one order of magnitude compared to the non-resonant ionization process can be observed.

A striking difference compared with the series in figure 5.10(a) and 5.10(b) is the lower resolution of the gallium data where Rydberg levels only up to $n = 30$ could be resolved. This can be attributed to the fact that in a hot cavity the Rydberg atoms are ionized in a field-free source region while in the ABU the Rydberg atoms are ionized in the presence of a DC field and therefore the atomic levels experience a Stark splitting. This effect was first derived theoretically by Epstein [156] using the Bohr-Sommerfeld model of the atom and analytical mechanics. Schrödinger [157] reformulated the problem in first order perturbation theory. Both theories obtain the same splitting in the binding energy ΔE of

$$\Delta E = \frac{3}{2} n \cdot (n_1 - n_2) a_B e F \tag{5.2}$$

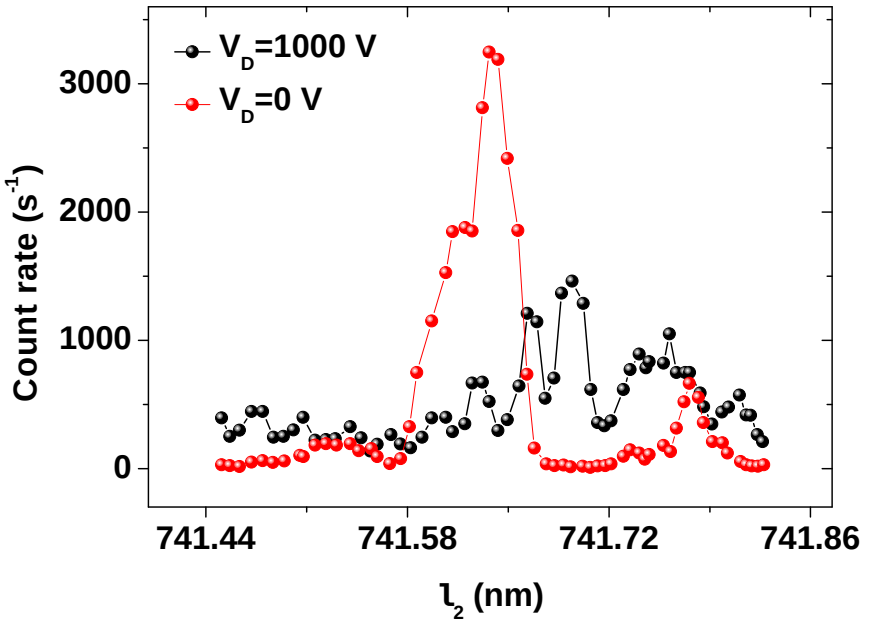

Figure 5.14: Resonance scan of the $n = 30$ Rydberg state for a high and low electrostatic potential V_D on the deflector.

for a state of main quantum number n in a hydrogen atom in an electrostatic field F. a_B and e denote the Bohr radius and the elementary charge. The so-called elliptical quantum numbers n_1 and n_2 fulfill the condition

$$n = n_1 + n_2 + |m| + 1 \tag{5.3}$$

and range from 0 to $n-1$, giving a splitting in $2n-1$ sub-states. A modern theoretical description can be found in [158]. Examples of the Stark effect in high-lying Rydberg states are given in [159–163].

The observation of the Stark effect for a Rydberg state of $n = 30$ is depicted in figure 5.14. While at a low electrostatic field the resonance is nicely resolved, a considerable Stark splitting can be observed in the high field configuration. According to the field simulations for the ABU extraction region the high (low) field settings correspond to ∼30 V/cm (15 V/cm) in the interaction region. From equation (5.2) a maximum splitting of approximately 50 (25) GHz can be expected for $n = 30$ in fairly good agreement with the observation. By reducing the extraction field, Rydberg levels up to $n = 30 - 40$ could be resolved as shown in figure 5.15.

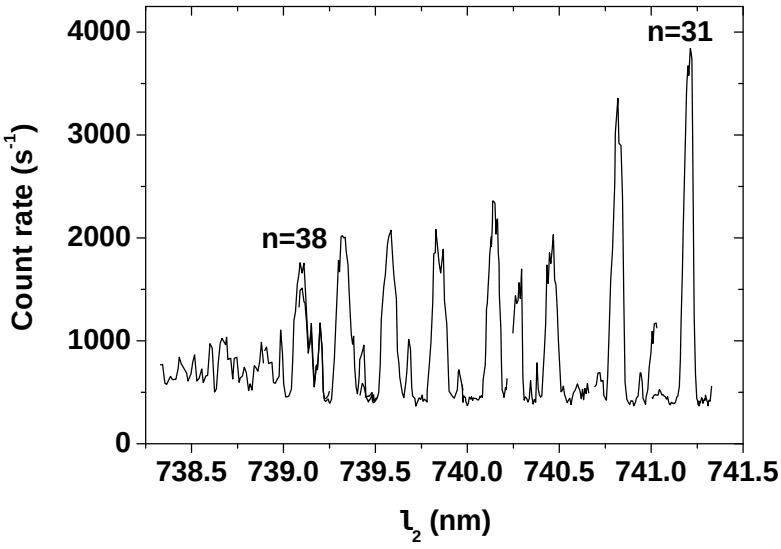

Figure 5.15: Scan across Rydberg states between $n = 30 - 40$ with a low extraction field in the atomic beam unit.

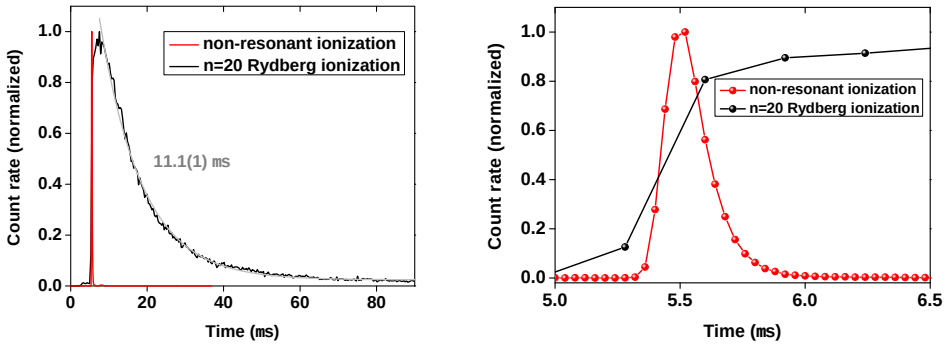

(a) Decay of the Rydberg state

(b) Detailed view of the non-resonant ion signal

Figure 5.16: Time profile of the laser ion signal triggered on the main clock of the master laser for Rydberg ($n = 20$) ionization (black curve) and non-resonant ionization (red curve).

Another interesting aspect is the ionization mechanism of the Rydberg states in the ABU. Different methods of ionization can be investigated by probing the time structure of the ion arrival triggered onto the incoming laser pulse as shown in figure 5.16. The time structure was recorded with the JYFLTRAP data aquisition program utilizing a multi-channel-analyzer triggered by the master clock of the laser system. Two profiles were recorded for a Rydberg state at $n = 20$ and non-resonant ionization by tuning the laser across the ionization potential. Figure 5.16(a) shows a clear difference between the non-resonant laser ionization process and the Rydberg ionization. In the case of non-resonant ionization (see also figure 5.16(b)) the ions are extracted in a small time window of less than 1 μs. The delay of $\sim 5.5\mu$s arises from the extraction of the ions from the interaction region towards the EMT, in good agreement with the simulation results illustrated in figure 3.14. In the case of the Rydberg state an exponential decay is observed with a maximum count rate at the time corresponding to the non-resonant signal indicating a continuous ionization of the decaying Rydberg level. An exponential decay of $\sim 11\mu$s was extracted from the data. Theoretical predictions for the lifetime of Rydberg states in alkaline metals [164] and experimental data [165] show rather good agreement with the estimate of the unshielded Coulomb potential. The typical life time of a Rydberg state scales with $\sim n^3$ and is $1.5 \cdot 10^{-4}$ s for $n = 50$ [1]. Therefore for $n = 20$ a life time of

$$\tau_{20} \sim \left(\frac{20}{50}\right)^3 \cdot 1.5 \cdot 10^{-4} \sim 10\ \mu\text{s} \tag{5.4}$$

can be expected in good agreement with the data in this work.

The critical voltage for field ionization can be calculated by following the arguments of section 2.4.3. For $n = 30$ one obtains $\sim$400 V/cm, which is considerably higher than the expected maximum field strength in the interaction region of 30 V/cm. Consequently field ionization can be excluded as an ionization mechanism.

The Rydberg laser scans were repeated in IGISOL utilizing the laser ion guide which is described in section 4.5. A tantalum oven containing a metallic gallium sample was electrothermally heated in the ion-guide to produce an atomic vapour. The laser radiation was coupled through a laser window at the back into the guide. A He pressure of 100 mbar was applied. The first laser scan across atomic Rydberg levels in IGISOL is shown in figure 5.17. The pressure of the buffer gas in the ion guide does not deteriorate the resolution of the lines and consequently states up to $n \sim 60$ can be observed.

As already discussed in section 2.3.3 collisions of the gallium atoms with the buffer gas lead to a broadening and a shift of the Rydberg levels. This behaviour was investigated for two different buffer gases, namely He and Ar, for Rydberg levels of two different series at $n = 30$. Laser scans as a function of pressure in Ar and He are shown in figure 5.18. No clear effect of the gas pressure on the linewidth of the

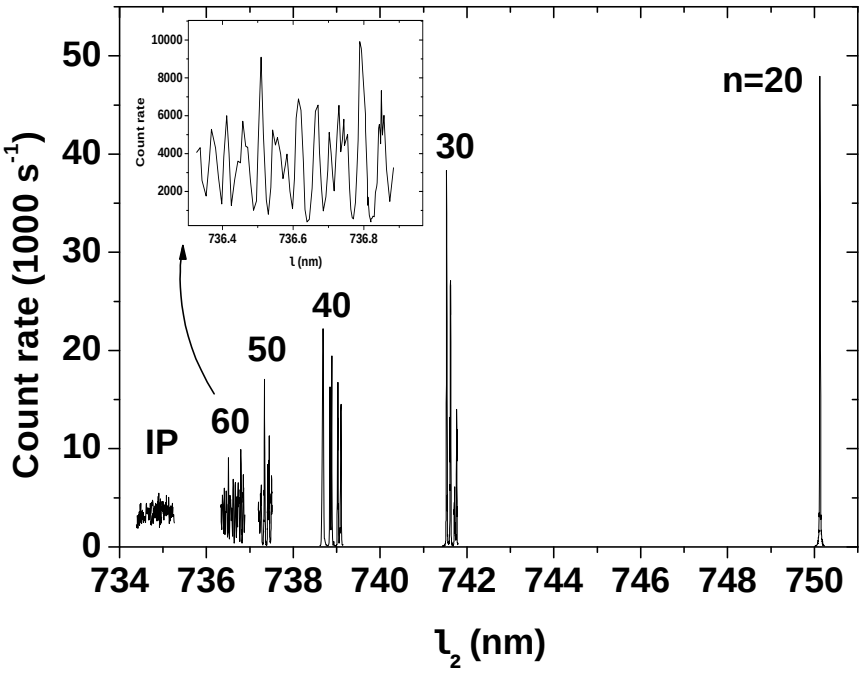

Figure 5.17: First Rydberg series measured in a He buffer gas cell at IGISOL. The inset shows the region of $n = 60$.

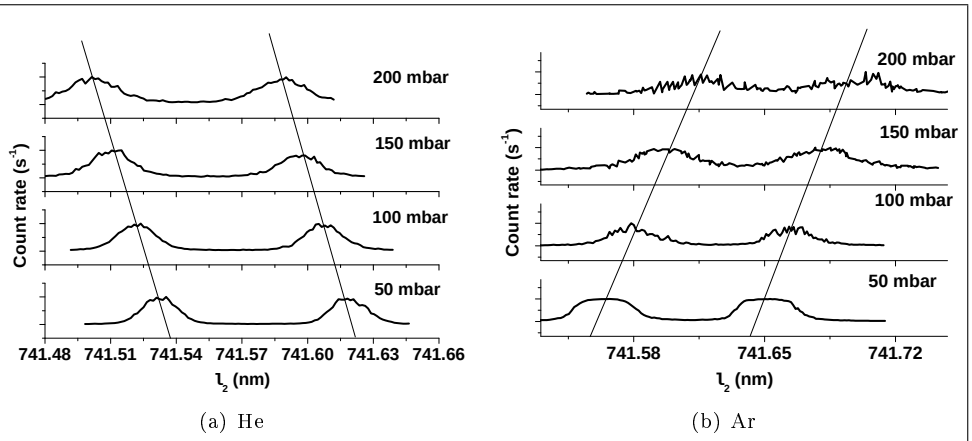

(a) He (b) Ar

Figure 5.18: Collisional shift of $n = 30$ Rydberg states in He and Ar as a function of pressure. The lines are drawn to guide the eye.

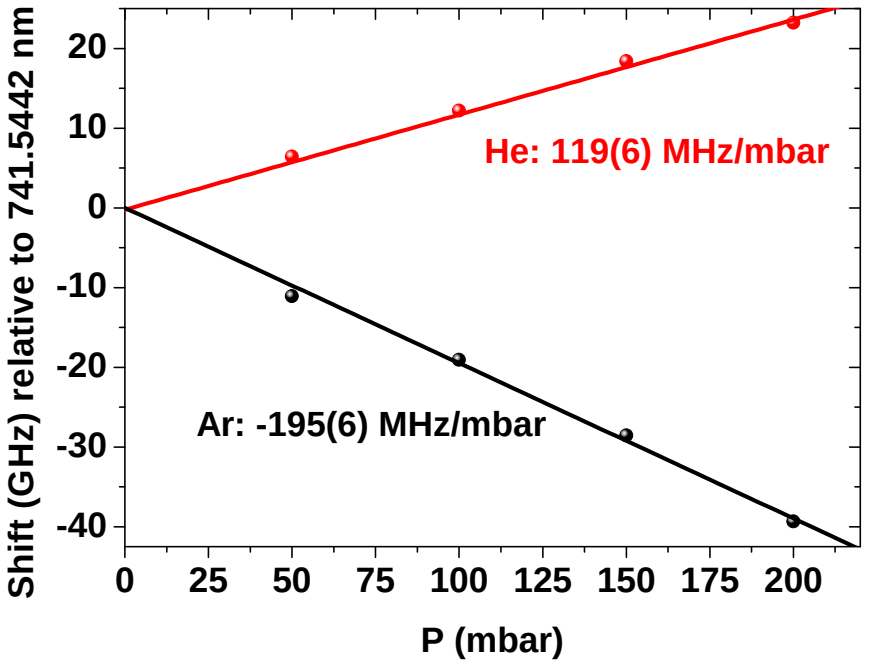

Figure 5.19: Experimentally determined pressure shifts for gallium in Ar and He buffer gas.

laser scans could be observed. In contrast a pronounced trend can be seen in the shift of the centroids for the different buffer gases. In He an increase in pressure leads to a blue-shift in the centroid, while in Ar a red-shift can be observed. Following the theory introduced in section 2.3.3 and equation (2.54) this trend is expected as the major contribution to the shift and comes from the scattering of the electron with the buffer gas atom. The scattering length of He and Ar have different signs (see table 2.1) and consequently the pressure shifts are opposite in sign. By plotting the centroid frequencies of the lower frequency resonance in figure 5.18 as a function of pressure an experimental value for the pressure shift in the ion guide can be extracted. Linear fits to the data shown in figure 5.19 were applied with an additional requirement that both lines intersect at a pressure of 0 mbar.

The extrapolated value for the unperturbed Rydberg transition frequency is estimated to be 741.5442 nm. This value is in reasonable agreement with the wavelength expected from the simple hydrogenic Rydberg model for an $n = 30$ state yielding $\sim$741.61 nm assuming a negligible contribution from the quantum defect $\delta(n) \rightarrow 0$.

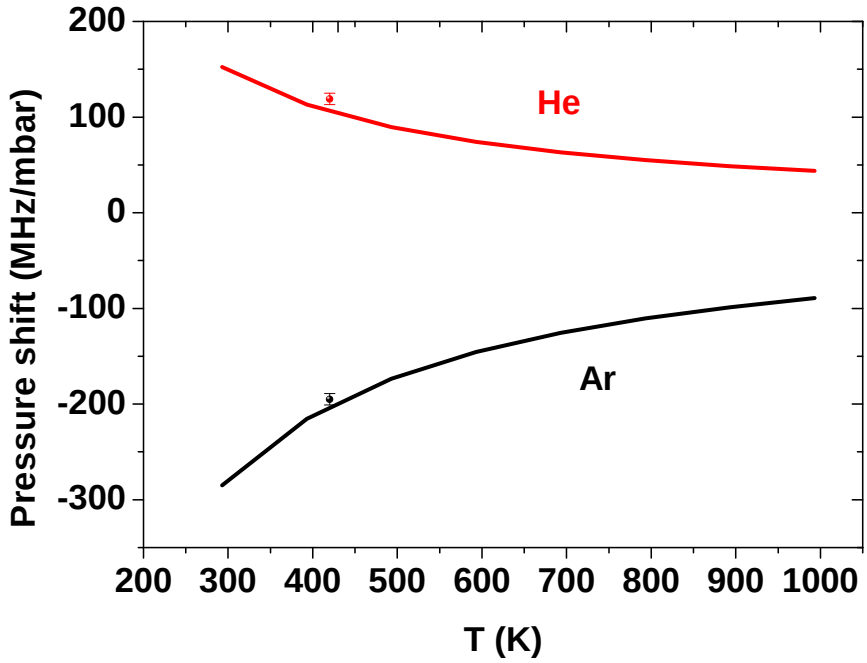

Figure 5.20: Theoretically determined pressure shifts for gallium in Ar and He buffer gas. The two points indicate the experimentally determined values.

From the gradient of the linear fits, pressure shifts of 119(6) MHz/mbar and -195(6) MHz/mbar for He and Ar respectively can be extracted. A rough comparison to the theory introduced in section 2.3.3 can be made by inserting known values for $n = 35$ from [10] for the Rydberg ionization of Sr in noble gases into equation (2.54). The only remaining unknown is the temperature in the ion-guide dominated by the heat radiated from the atomic oven. Therefore the theoretical shift is plotted as a function of temperature T in figure 5.20. Rather good agreement with the experimental data can be obtained for a temperature of 420 K, which is a reasonable temperature for the evaporation of gallium with a melting point of 302.91 K [86].

5.5 In-source spectroscopy

For the majority of analytical studies involving high resolution laser spectroscopy, not only is elemental selectivity required but also high isotopic selectivity. For this

purpose narrow bandwidth (∼1 MHz) continuous wave (CW) laser systems must be used, delivering only low power yet permitting the resolving of isotope shifts and hyperfine structure throughout chains of isotopes. For ensuring the highest sensitivity in trace detection, or alternatively high efficiency of an on-line resonance ionization laser ion source, sufficiently high laser power is imperative in order to saturate each individual excitation step. Therefore, powerful pulsed laser systems, usually operating in a high repetition rate mode (∼ kHz regime) with small duty cycle losses, are most suitable to minimize ionization efficiency losses.

The spectral linewidth of these laser systems is typically of the order of a few GHz. On the one hand this is by far sufficient to select an element, however on the other hand this value most often does not permit the resolution of isotope shifts or hyperfine structure in optical transitions. In pulsed laser RIMS, isotope selection is thus usually only provided through the different isotopic mass in the subsequent mass-selective ion detection system, e.g. a magnetic sector field of a high transmission mass separator or a quadrupole mass spectrometer.

Direct laser spectroscopy in an on-line ion source has recently been demonstrated at ISOLDE, CERN, where the different transition frequencies of individual hyperfine structure components of the nuclear ground and isomeric states in $^{68}\mathrm{Cu}^{g,m}$ and $^{70}\mathrm{Cu}^{g,m_1,m_2}$ were used to determine the magnetic moments of both nuclei [166]. In this case conventional pulsed dye lasers were used to separate the lines with a spectral resolution of about 4 GHz. Higher spectral resolution can only be obtained by using seeded pulsed laser systems such as the pulsed dye amplifier introduced in section 3.1.2 or the seeded Ti:Sapphire laser described in section 3.1.1. Both laser systems were applied for high-resolution in-source laser spectroscopy discussed in the following subsections.

5.5.1 In-source spectroscopy at IGISOL on bismuth

The first high-resolution laser spectroscopy in the IGISOL was performed on the hyperfine structure of stable bismuth (^{209}Bi, $I = 9/2^-$). The experimental details are given in [132]. The excitation scheme is shown in figure 5.21. Two different schemes were tested, both using a single mode frequency doubled CW dye laser (Spectra Physics 380D) at a power of 1 mW for the first excitation step. A pulsed laser source was chosen for the second step to provide efficient ionization. The first scheme used a non-resonant ionization step to the continuum with 355 nm from the frequency tripled 50 Hz Nd:YAG laser, and the second to a known autoionizing level [133] using a 10 kHz frequency doubled Ti:Sapphire laser operating at ∼ 382 nm.

The first laser ionization tests were performed in the ABU (see section 3.4) applying the autoionizing excitation scheme. A power of 400 mW was available to saturate

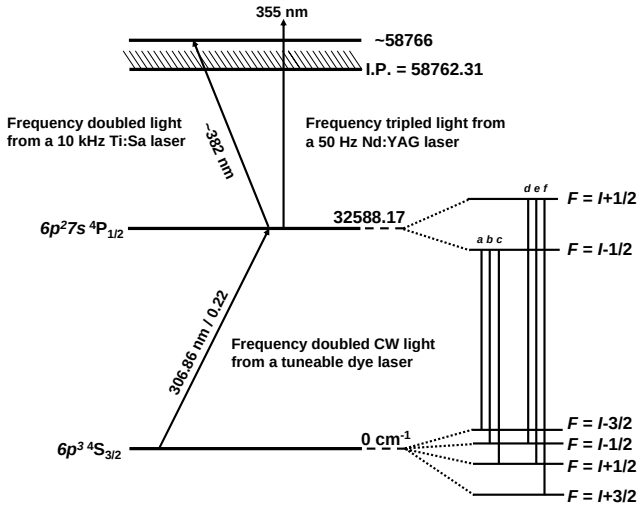

Figure 5.21: Excitation scheme for in-source spectroscopy on bismuth.

the autoionization step to ∼70%. The according frequency scan of the first step CW dye laser is shown in figure 5.22. The hyperfine structure of bismuth can be easily resolved in the crossed-beams setup of the ABU, basically only limited by the natural linewidth of the transition of ∼94 MHz [129].

To test the viability of in-source spectroscopy and compare the two possible ionization schemes the same experiment was repeated in IGISOL, evaporating atoms of ^{209}Bi sputtered onto a resistively heated Ta filament. The first scan used the frequency tripled light from the 50 Hz Nd:YAG as a non-resonant ionization step. On success, the frequency doubled Ti:Sapphire was then spatially overlapped with the CW laser beam and was used to reach the auto-ionizing level. Results from both scans are depicted in figure 5.23.

The Doppler width can be estimated to be ∼ 800 MHz according to equation (2.46). The pressure broadening for a bound state resonance is ∼10 MHz/mbar (see section 2.3.3) and therefore about ∼500 MHz in this experiment. Consequently the total spectral resolution is limited to approximately 1 GHz. The increase in count rate by approximately a factor of 60 on the largest peak is almost certainly due to the higher probability of ionizing when using an auto-ionizing level compared to a non-resonant transition. In addition, spectra were taken at differing ion guide pressures to provide information about pressure broadening effects [37]. The resolution achieved in figure 5.23 is clearly adequate to resolve the hyperfine structure. The apparent variation

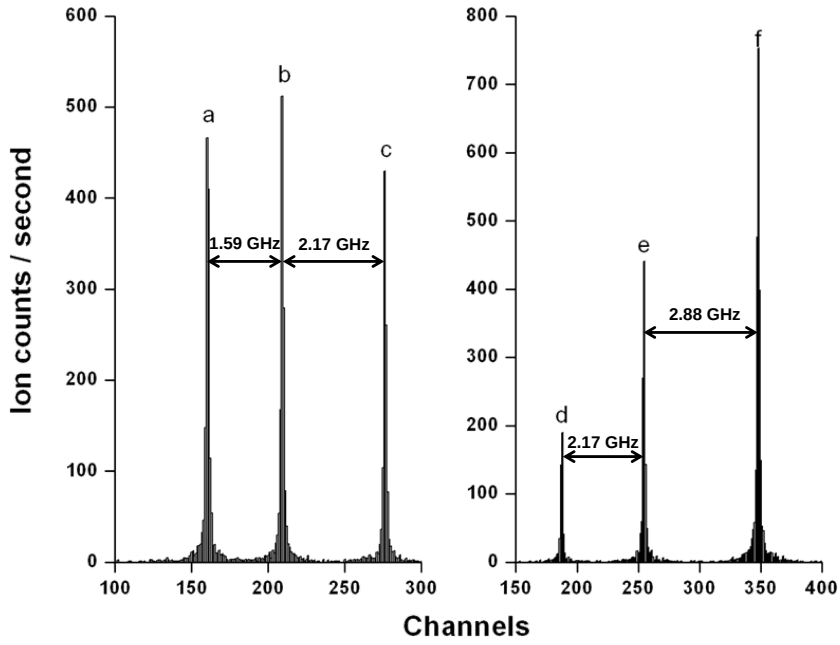

Figure 5.22: A dye laser wavelength scan over the lower frequency triplet of hyperfine states in ^{209}Bi (left) and the upper frequency triplet (right). The peaks are labeled using the notation shown in figure 5.21.

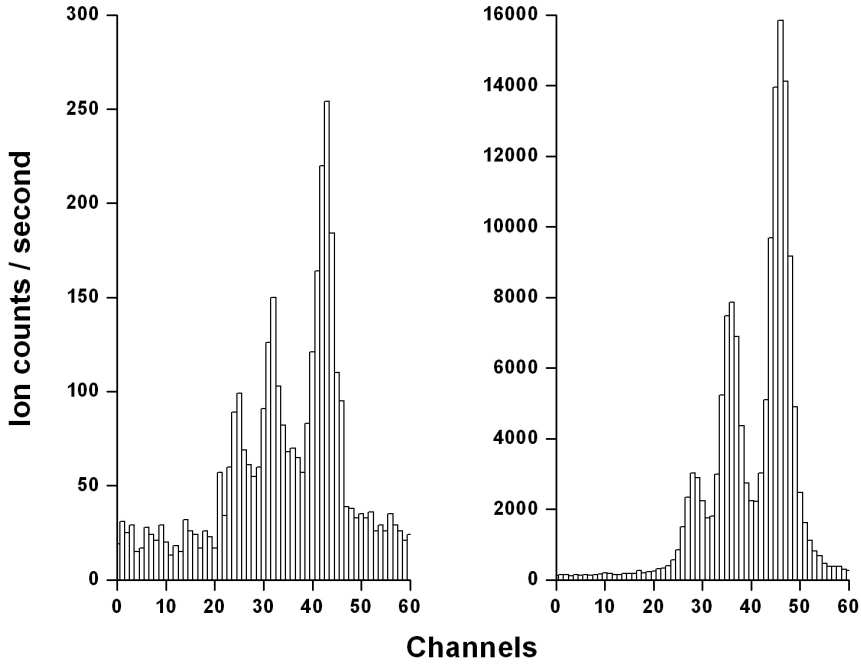

Figure 5.23: Resonance ionization spectroscopy in the ion guide at 50 mbar He pressure. The CW dye laser was scanned over the upper hyperfine peaks. The left figure shows results obtained using the non-resonant 355 nm ionization step, while the Ti:Sapphire was used to reach the auto-ionizing state in the figure shown on the right.

in the intensity of the hyperfine components of the upper peaks between figures 5.23 and 5.22 can be explained in terms of a rate equation model which includes optical pumping of the hyperfine levels and relaxation into dark states as shown in [37].

With the current setup the technique is limited in both the spectral resolution due to Doppler and collisional broadening in the source and the laser power available for the high-resolution CW laser. The former problem becomes apparent for nuclei with smaller Z which exhibit a smaller hyperfine structure in the order of $\sim$ 10-100 MHz. A possible solution might be the ionization of the atomic species in the gas jet after the ion guide in a crossed beams setup. This approach has been tested off-line in the case of a hot-cavity ion-source on aluminium discussed in section 5.5.2 and in the IGISOL in tests of a novel source for the production of radioactive silver isotopes. Some results of these measurements are discussed in section 4.7. The latter issue can be addressed by using seeded high-repetition rate pulsed lasers. Apart from a considerably higher laser intensity these laser systems exceed the wavelength coverage of the CW laser system by far as higher harmonic generation can be easily carried out by a single-pass through a non-linear crystal. First experimental results with the seeded Ti:Sapphire system developed during this thesis (see section 3.1.3) are described in the following section.

5.5.2 Hyperfine structure of ^{27}Al

To demonstrate the suitability of the seeded Ti:Sapphire laser for high-resolution spectroscopic applications the well-known hyperfine structure of the stable isotope of aluminium, ^{27}Al, was investigated [167]. The strong D_2 transition from the $3s^2 3p\ ^2P_{1/2}$ atomic ground state to the $3s^2 3d\ ^2D_{3/2}$ excited level at 32435 cm^{-1} was chosen as a benchmark test case, exhibiting a relatively small splitting of the hyperfine structure ($\sim$300 MHz). Laser ionization was performed using the residual blue laser light from the frequency tripling process at 462 nm for the ionization step. The seeded Ti:sapphire laser was scanned over the hyperfine structure and the photo-ions were detected as a function of the laser wavelength. The excitation scheme for the RIS experiment is shown in figure 5.24(a). The required laser radiation of 308 nm was achieved by sequential frequency doubling and tripling the fundamental light ($\sim$924 nm) of the seeded Ti:Sapphire laser using standard non-linear optics. With an output power of approximately 1.5 W in the fundamental, $\sim$150 mW of second harmonic light was produced and $\sim$10 mW in the third harmonic was available for spectroscopy. To avoid saturation and resulting power broadening of the resonance transition, the power of the UV radiation was reduced to $\sim$0.3 mW. The remaining non-converted second harmonic laser radiation was available for efficient non-resonant post-ionization as indicated in figure 5.24(a).

Measurements were performed in a crossed-beams geometry with an additional mass-

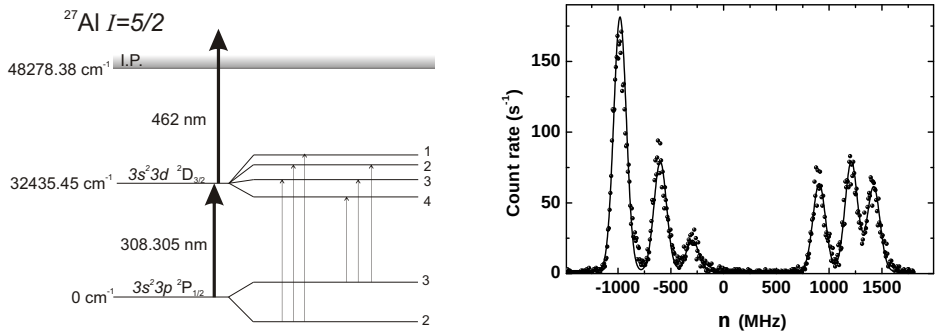

(a) Hyperfine structure of ^{27}Al

(b) Scan of the hyperfine structure

Figure 5.24: Resonant ionization spectrum for ^{27}Al and the hyperfine splitting of the ground and excited atomic states.

selection stage by a quadrupole-mass-filter as shown in figure 5.25. The seeding laser was locked and scanned in reference to a frequency-stabilized He-Ne laser as described in detail in [51]. The resulting laser scan over the hyperfine structure of ^{27}Al is shown in figure 5.24(b).

A standard χ^2 minimization routine was applied to the data as indicated by the solid line in figure 5.24(b). The fit function

$$y = y_0 + A\sum_{i=1}^{6} A_i \mathrm{e}^{-\frac{\nu-\nu_0-\nu_i}{w/(2\sqrt{\ln(2)})}^2} \tag{5.5}$$

was defined as a sum of six Gaussian functions of identical width w representing the individual hyperfine structure components. The relative intensities A_i of each individual component were calculated via the $6j$ symbols of the transition and were kept fixed, as was the expected shift in frequency between the hyperfine components. The four remaining fit parameters therefore are the background level y_0, an overall shift in frequency ν_0, a scaling amplitude A and the full-width at half-maximum (FWHM) of the transitions w. The spacing between the components was calculated by inserting the known ^{27}Al A and B hyperfine factors which are related to the magnetic dipole moment and electric quadrupole moment respectively into the well-known Casimir-formula [168]

$$\Delta E = \frac{A}{2}C + \frac{B}{4}\frac{\frac{3}{2}C(C+1) - 2I(I+1)J(J+1)}{I(2I-1)J(2J-1)} \tag{5.6a}$$

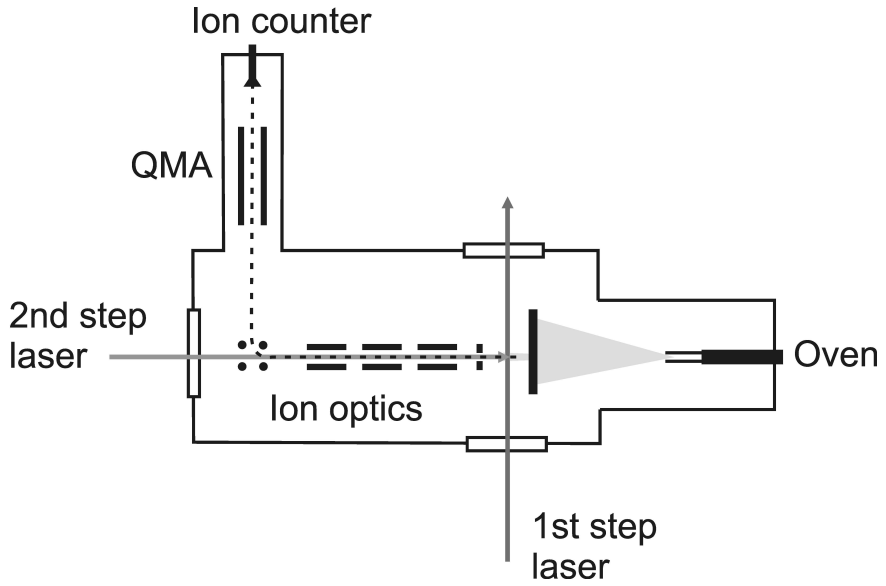

Figure 5.25: Crossed beams setup to measure the hyperfine structure of ^{27}Al.

with the so called Casimir-Factor

$$C = F(F+1) - I(I+1) - J(J+1)\ . \tag{5.6b}$$

The variables I, J and F denote the nuclear spin, the total angular momentum of the electronic shell and the coupled angular moment vector $F = I + J$ respectively. The factors A and B were measured for ^{27}Al by Cooper et al. [167] for the $^2P_{1/2}$ ground state (A=502.0336(5) MHz) and the $^2D_{3/2}$ excited state (A=-98.87(12) MHz, B=17.5(8) MHz). The resulting values for the free parameters after applying the fitting routine are shown in table 5.5 The experimental FWHM w = 145(1) MHz of the hyperfine components can be explained using a combination of power broadening and residual Doppler broadening. The good agreement for Gaussian-type fit functions with the data supports the dominance of Doppler broadening which can by approximated to be 100 MHz in the experimental setup.

5.6 Optical pumping of ions in a cooler buncher

Collinear laser spectroscopy at an ISOL facility possesses the speed and sensitivity to measure nuclear moments and mean-square charge radii of radioactive nuclei [169,

variable	value
y_0	1.6(3) cps
ν_0	8.3(6) MHz
A	166(1) cps
w	145(1) MHz

Table 5.5: Results of the fitting routine for the hyperfine structure of ^{27}Al according to equation (5.5).

170]. In the technique an atomic or ionic beam is overlapped collinearly with co- or counter-propagating laser light and, for fluorescence observation, a length of the overlap region is imaged onto a photomultiplier.

The information about the deformation and size of the nucleus is extracted from optical hyperfine structure and isotope shift measurements. In a simple deformed droplet-model the mean-square charge radius is expressed as

$$\langle r^2 \rangle = \langle r_0^2 \rangle \left(1 + \frac{5}{4\pi} \langle \beta_2^2 \rangle \right) \tag{5.7}$$

leading to a change in mean-square charge radius of the form

$$\delta \langle r^2 \rangle = \langle r_0^2 \rangle \frac{5}{4\pi} \delta \langle \beta_2^2 \rangle \ . \tag{5.8}$$

where $\langle r_0^2 \rangle$ is the mean-square charge radius for a spherical nucleus [169]. Consequently a sudden change in the deformation, as for example that observed around $N = 60$ in the yttrium system [171], can lead to a sudden increase in the mean-square charge radius. Deviations between $\delta \langle \beta_2^2 \rangle$ obtained from the isotope shift and the static deformation $\delta \langle \beta_2 \rangle^2$ from the hyperfine structure additionally provide information about a possible dynamic contribution to the change in mean-square charge radius by deformation.

The technique of laser spectroscopy has been further improved at the IGISOL facility by pulsing the release of the ions from an RF cooler device [172, 173] located in the IGISOL beam line (see figure 4.1). The well-defined time structure of the ions allows gating of the PMT signal on the passage of the bunch through the interaction region, thus reducing the background from the continuous scattering of laser light. Axial confinement of the slowly traveling cooled ions at the end of the RF cooler provides an opportunity to efficiently excite optical transitions and redistribute the electronic level populations. This can be done using the broadband Ti:Sapphire lasers of the FURIOS laser ion source project, whose high powers readily permit the production of higher harmonic frequencies and thus a broad range of wavelengths. Manipulation of state population in such a way extends the number of transitions available for study

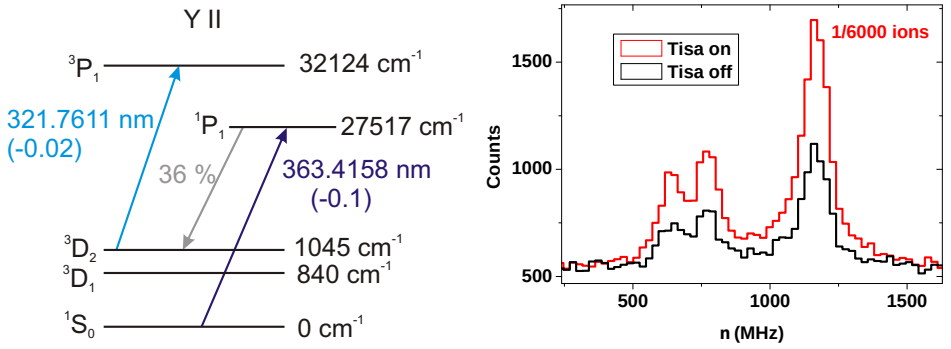

(a) Pumping scheme (b) Observed Effect

Figure 5.26: Pumping scheme for Y^+ and the effect of pumping on the spectroscopic 321.8 nm transition in $^{89}Y^+$.

by collinear techniques which is required when the ground state transition alone can not provide the full information on the deformation and change in mean-square charge radii.

The technique of optical pumping has been successfully tested for niobium, tantalum and yttrium during the course of this thesis work. Here some important results of the optical pumping experiments on the yttrium system are presented, the first case to be demonstrated on-line in 2007 [174], followed by a discussion of the optical pumping of neutron-deficient niobium isotopes which was performed in 2008.

5.6.1 Optical pumping of yttrium

High resolution spectra of the $5s^2\ ^1S_0$ (ground state)$\rightarrow$ $4d5p\ ^1P_1$ (27516.691 cm^{-1}) ionic transition were obtained for the $^{86-90,92-102}$Y ground states and isomeric states of $^{87-90,93,96,97,98}$Y [171] by classical collinear laser spectroscopy. For each isotope where the nuclear spin, I, is greater than $1/2$, the upper level is split into three hyperfine components, yielding the nuclear magnetic dipole and electric quadrupole moments and the change in nuclear mean-square charge radius between the isotopes. However, the values determined for these quantities depend on the nuclear spin assignments which are unconfirmed for the ^{98m}Y, ^{100}Y and ^{102}Y isotopes. All other transitions from the $J = 0$ ground state will be limited to $J = 0 \rightarrow J = 1$ transitions and likewise restricted.

By optical pumping into a metastable state however, the spectroscopy can be done from a $J = 2$ state as indicated by the pumping scheme in figure 5.26(a). The $^3D_2$

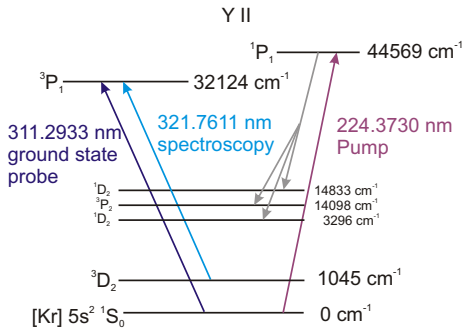

(a) Scheme for probing the depopulation of the ground state

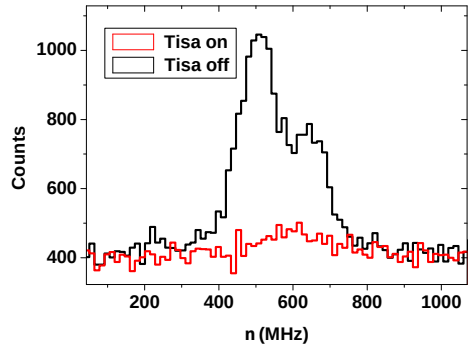

(b) Depopulation of the ground state

Figure 5.27: Depopulation of the ground state of $^{89}Y^+$ by optical pumping.

metastable state population can be maintained by illuminating the central axis of the cooler with 30 mW of frequency doubled 363.4 nm light from one of the FURIOS Ti:Sapphire lasers. The branching into the $^3D_2$ state can be estimated to be 36% in thermal equilibruum. The spectroscopic efficiency of 1 photon per 6000 ions obtained from the excitation of the metastable state is comparable to that of the transition in standard collinear spectroscopy in the yttrium system [171] from the ground state. Figure 5.26(b) shows the first signal enhancement observed in IGISOL by applying optical pumping of stable yttrium in the cooler. A signal increase of a factor of 2 was obtained compared to the thermal population.

The spectra obtained by collinear spectroscopy from the metastable state can be compared to calculated spectra for each possible nuclear spin assignment. In this manner, the spin of one of the isotopes in question, namely the ^{100}Y nucleus, could be unambiguously established as $I = 4$ [175]. More beam time has already been approved for the determination of the nuclear spins of the ^{98m}Y and ^{102}Y isotopes.

An alternative pumping scheme using 224 nm frequency quadrupled light from a Ti:Sapphire laser has also been investigated. Figure 5.27(a) shows the excitation scheme. The effect on the ground state population due to the 224nm pumping was probed by setting the dye laser on the 311 nm excitation frequency from the ground state and measuring the fluorescence from the $^3P_1$ state at 32124 cm^{-1}. A strong reduction of the counts in the 311.3 nm spectrum and therefore depletion of the ground state population is seen, as shown in figure 5.27(b). According to [129], only the three states indicated in figure 5.27(a) should be populated from the decay of the 44569 cm^{-1} level. Nevertheless, spectroscopy of the 321.8 nm line shows a population

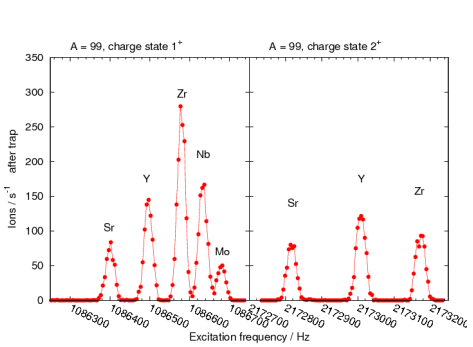

(a) Purified mass distribution in a fission reaction

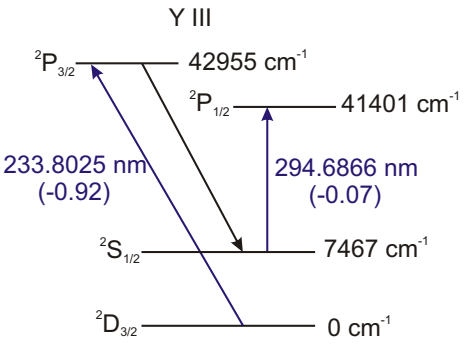

(b) Excitation scheme (see [148])

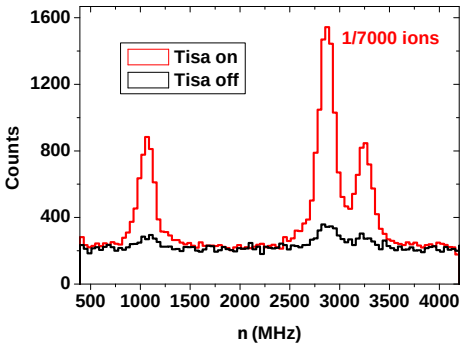

(c) Pumping effect

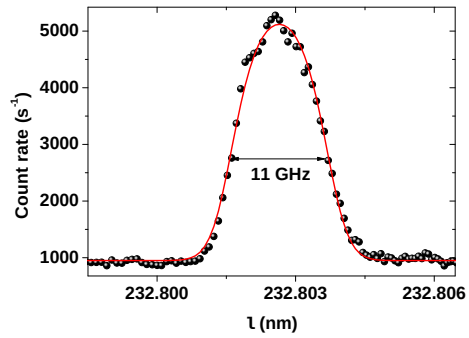

(d) Frequency scan of the pumping laser

Figure 5.28: Optical pumping of doubly-charged yttrium.

enhancement of the 1045 cm^{-1} level, again indicating a thermal distribution of the metastable atomic states and possible relaxation from higher states.

A new pumping scheme for doubly-charged yttrium was recently tested off-line. The availability of higher charge states than 1^+ is unique for the IGISOL ion source and opens access to a complete new set of atomic transitions suitable for collinear laser spectroscopy. The charge state distribution of neutron-rich isotopes produced by proton-induced fission of uranium has been investigated by the JYFLTRAP group. For the ^{99}Y isotope a ratio of ∼1:1 has been measured, as shown in figure 5.28(a).

The excitation scheme is shown in figure 5.28(b). The efficiency of the spectroscopic transition benefits from the intensity being split over fewer hyperfine components for $I > 1/2$ states due to the low values of atomic spin. When the Ti:Sapphire laser is

turned on an immediate signal increase by a factor of 9 was observed, attributed to an enhancement of the metastable population as shown in figure 5.28(c). A frequency scan of the pumping Ti:Sapphire laser shown in figure 5.28(d) was fitted with a saturated Gaussian function (see equation (2.40)) and a saturation parameter $S = 3.0(4)$ was obtained. The observed power-broadened linewidth of 11 GHz confirms the full saturation of the pumping transition. Additional broadening from collisions with the buffer gas can be neglected as the typical operational pressure in the cooler is ~ 0.1 mbar [172].

5.6.2 Optical pumping of niobium

Niobium has been recently investigated with the optical pumping technique on-line. This element cannot easily be studied with standard collinear spectroscopy because of the low probabilities for transitions from the ionic $[\mathrm{Kr}]4d^4\ {}^5\mathrm{D}_0$ ground state ($\log gf < -1$) and the difficulty to produce the required wavelength of $\sim$270 nm with the dye laser system. A second drawback of spectroscopy from the ground-state would be, as in the case of yttrium, the limitation to $J = 0 \rightarrow 1$ transitions. For these reasons optical pumping in the cooler was considered. The pumping scheme applied is shown in figure 5.29(a). The wavelength of 286.6452 nm required to depopulate the ground state can easily be produced by a frequency tripled Ti:Sapphire laser with an average power of up to 16 mW. The transition was tested off-line for the stable isotope ^{93}Nb and was completely saturated as shown in figure 5.29(b). A saturation power of 2.5(9) mW was extracted from the data applying equation (2.42).

The resulting effect of the pumping on the strongest hyperfine component of the radioactive ^{90}Nb isotope is shown in figure 5.29(c). The two datasets were taken in a sequence of 600 scans with a dwell time of 200 ms. A single scan consists of 25 channels with a step size of about 27 MHz per channel. With these settings the recording of a complete dataset therefore took approximately 50 minutes. While the hyperfine structure component could be clearly resolved in this scan, without optical pumping no significant signal was produced. The spectroscopic data obtained during this on-line run is currently under analysis by the collinear laser spectroscopy group.

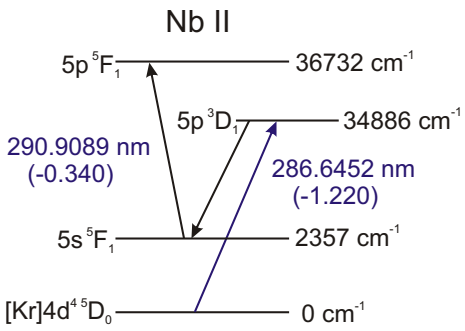

(a) Pumping scheme

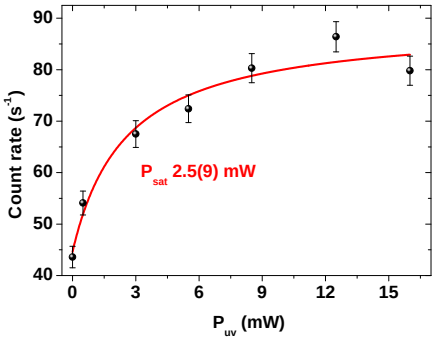

(b) Saturation curve

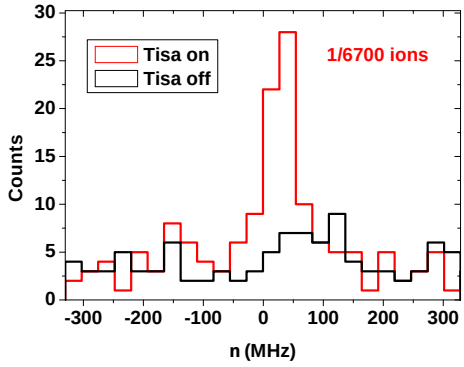

(c) Collinear laser signal of a hyperfine component of ^{90}Nb

Figure 5.29: Optical pumping scheme for niobium and signal obtained by collinear laser spectroscopy from the metastable state.

6 Studies of the processes in the gas cell

The development of laser ionization at IGISOL goes hand-in-hand with the progress and innovations carried out at the IGISOL front-end. For a description of the ion guide technique the reader is referred to section 4.1. Two major aspects can influence the efficiency for the extraction of radioactive ions from a gas cell, namely the interaction with impurities in the gas and with the plasma produced by the stopping process of recoils and the primary beam. The experiments carried out to study the impact of both effects on laser ionization in the cell will be described in this section.

6.1 Studies of the role of impurities

The role of impurities in the gas cell is a primary concern as, depending on the ion of interest and the buffer gas purity the formation of molecules can deteriorate the efficiency of the ion of interest. As the thermalized atom or ion moves through the guide towards the exit nozzle it collides many times with buffer gas atoms and impurity molecules. This can result in chemical bond formation or trapping in a metastable state which both lead to losses as the laser scheme excites only from the atomic ground state. Detailed studies of the role of impurities in a buffer gas cell have been carried out by the LISOL group [54, 55]. Because of the strong reaction rate of the 1^+ charge state with oxygen yttrium provides a benchmark test for the gas purity within the ion guide and the purity of the vacuum system. As atomic yttrium is rather robust against molecular formation laser ionization can be used to "trigger" the chemical reaction.

The details of this experiment are given in [87]. The preparatory studies to find an efficient ionization scheme are described in section 5.2. In order to control the arrival time of the lasers such that evacuation and molecular formation within the ion guide may be studied, the mechanical shutter system described in section 3.3 was used. For a realistic study of laser ionization of yttrium a laser ion guide was borrowed from the LISOL group at Leuven and installed in the IGISOL vacuum chamber as shown in figure 6.1. The conductance of the exit hole of 0.5 mm diameter in helium gas is equal to 0.112 l/s. An evacuation time for the whole guide of 480 ms can be estimated using equation (4.8). Compared to the ion guides used in JYFL these extraction times are considerably longer due to the smaller exit hole, however an increase in time is necessary in order to achieve neutralization of the recoiling nuclei. Atoms of different

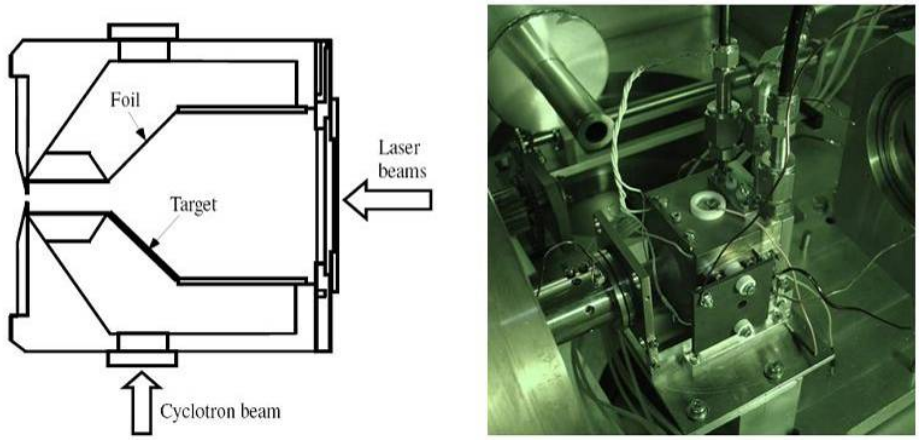

Figure 6.1: Schematic view of the laser ion guide loaned by the LISOL group at Leuven (left) and a picture of it installed in the IGISOL chamber (right). In the picture the lasers enter from the right, and the SPIG is seen directly in front of the ion guide exit hole. The beam pipe towards the beam dump can be seen in the top of the picture.

elements are evaporated inside the cell by the resistive heating of a corresponding filament.

The main loss mechanism in off-line conditions is the formation of molecules via reactions between an atom X or ion X^+ with a ligand molecule M in the presence of the buffer gas (in this case helium),

$$\begin{aligned} X^{(+)} + M &\leftrightarrow X^{(+)}M^* \\ X^{(+)}M^* + He &\rightarrow XM^{(+)} + He\ . \end{aligned} \tag{6.1}$$

The time evolution of the process of atoms or ions converting to molecules may be described by a reaction rate coefficient k (cm^3s^{-1}) and the rate equation

$$\frac{dn}{dt} = -nk\,[M] \tag{6.2}$$

where n is the number of atoms or ions, and $[M]$ the ligand molecular concentration. A corresponding time constant for the formation of the molecular ion can be defined as

$$\tau = 1/k\,[M]\ . \tag{6.3}$$

It is known that yttrium ions have a strong affinity towards binding with oxygen [176]. The main residual impurities in the buffer gas are oxygen and water. Therefore the formation of YO^+ can either happen directly

$$Y^+ + O_2 \rightarrow YO^+ + O \tag{6.4}$$

or via the dehydrogenation reaction

$$Y^+ + \text{H-O-H} \rightarrow \text{H-}Y^+\text{-O-H} \rightarrow H_2Y\text{-}O^+ \rightarrow YO^+ + H_2\ . \tag{6.5}$$

This has been discussed more thoroughly in [55] for the case of titanium.

Two experiments were carried out to study the purity conditions of the gas. In the first experiment two problems were discovered after analysis of the data. The first was a possible leak in the final part of the gas feeding line going directly to the ion guide, while the second was a leak in the venting valve attached to the IGISOL vacuum chamber which led to a pressure of $\approx 10^{-2}$ mbar (measured directly on the chamber) without helium gas flowing through the ion guide. In the preparation of the second experiment these leaks were fixed and a baseline chamber pressure of $1.3 \cdot 10^{-4}$ mbar was measured, representing a more typical value for IGISOL operation conditions. For this latter experiment a low impurity level was expected.

In order to study the evacuation time of the ions and corresponding molecules the ion signal from the channel plates, was fed into a multi-channel analyzer (MCA), triggered by the JYFLTRAP labview control program [59] . The time resolution was 655.36 μs per bin. The results of both experiments are shown for comparison in figure 6.2. In the first experiment the laser radiation was pulsed on for the first 90 milliseconds of a full cycle of about four seconds. This was accomplished by triggering the mechanical shutter device discussed in section 3.3 with a delayed TTL signal from the JYFLTRAP control program. It can be seen from figure 6.2(a) that the laser-produced Y^+ ions reach a saturation level before the lasers are turned off. The characteristic time to reach saturation can be related to a combination of the survival time of Y^+ against losses due to molecular formation (equation (6.3)) and evacuation from the ion guide. The bare atomic fraction of yttrium amounted to 10% of the sum of the full ion yield. An exponential growth curve fitted to the $^{89}Y^+$ data resulted in a value of $\tau = 5.1(4)$ ms. As the evacuation time from the ion guide as a whole is far longer than this timescale, this saturation time is indicative of the survival time of yttrium ions during evacuation against molecular formation.

The most striking difference between the data of figure 6.2(a) and that of figure 6.2(b) is that in the case of pure conditions yttrium is the dominant species over the next most abundant molecule extracted from the ion guide, yttrium oxide, by a factor of ≈ 20. No subsequent addition of hydrates could be observed at the expected mass numbers. Exponential fits to the rise time of the yttrium and the yttrium oxide data

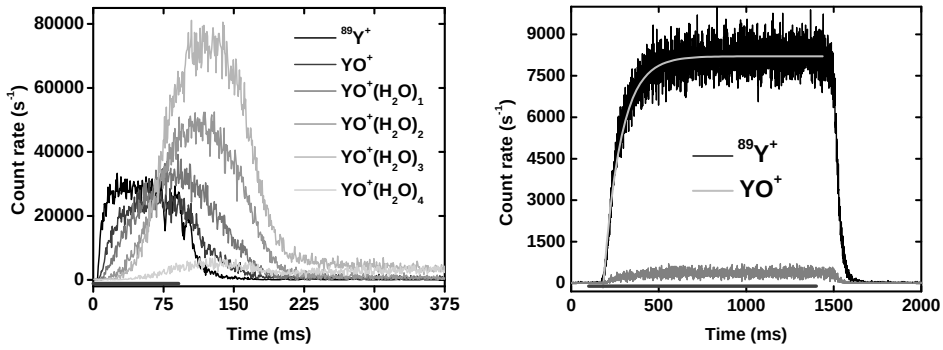

(a) Time-of-flight profiles of yttrium laser ions and corresponding molecules.

(b) Evacuation time profiles of Y^+ and YO^+. The grey line shows an exponential fit to the yttrium data.

Figure 6.2: Time distribution profiles of yttrium laser ions and subsequent molecules in low (a) and high (b) gas purity conditions. The black horizontal bar along the time axis represents the period the lasers were on.

yielded values of 96(10) ms and 135(7) ms respectively. The rise time for yttrium of 96(10) ms can be directly compared with the rise time of 5.1(4) ms fitted in the first experiment. With this new rise time and the ratio between yttrium and yttrium oxide, the primary effect dominating the saturation time scale is now the evacuation of the ion guide.

It can be seen from figure 6.2(a) that the formation of YO^+ ions is delayed with respect to the Y^+ ions, and each subsequent addition of a hydrate to the YO^+ molecule is delayed even further. The time behaviour indicates the following sequence of hydration of YO^+ ions:

$$YO^+ + H_2O \rightarrow YO^+(H_2O) \qquad (A = 123) \qquad (6.6a)$$

$$YO^+(H_2O) + H_2O \rightarrow YO^+(H_2O)_2 \qquad (A = 141) \qquad (6.6b)$$

$$YO^+(H_2O)_2 + H_2O \rightarrow YO^+(H_2O)_3 \qquad (A = 159) \qquad (6.6c)$$

$$YO^+(H_2O)_3 + H_2O \rightarrow YO^+(H_2O)_4 \qquad (A = 177)\ . \qquad (6.6d)$$

The relative intensities, the saturation time of the Y^+ signal and the delay times of the subsequent molecules illustrated in figure 6.2(a) can provide information about specific impurity concentrations in an environment where the impurity level can be controlled.

To determine the source of contamination and the corresponding molecular formation time the evacuation time of the ion guide has to be disentangled from the molecular

formation process. A simulation model was developed to describe the time evolution of the data and to extract reaction times for all chemical bonding reactions involved. It is based on the deconvolution of the total ion yield to a single laser shot, combined with a rate equation model for the molecular formation process. In ideal conditions this model, along with the experimental time profiles, could be used to extract individual impurity concentrations within the gas cell. This removes the need for complicated gas flow simulations which would be required if the evacuation time of the ions within the laser path was to be accurately described and then deconvoluted from the experimental time-of-flight profile in order to separate the effect due to chemistry. The details of this single-shot model are described in [87].

Figure 6.3 shows the individual experimental time-of-flight profiles of figure 6.2 compared to the reintegrated single shot profiles obtained by the model. Both data sets are reproduced fairly well. The time constants for molecular formation extracted from the reaction rate parameters that provide the optimum fits in figure 6.3 are given in table 6.1. In the simulation for the low impurity data the higher order reaction rate

	$\tau_1 = 1/k_1\,[M]$	$\tau_2 = 1/k_2\,[M']$	$\tau_3 = 1/k_3\,[M']$	$\tau_4 = 1/k_4\,[M']$	$\tau_5 = 1/k_5\,[M']$
high impurity	9	14	19	31	400
low impurity	2300	0	0	0	0

Table 6.1: The molecular formation time (ms) extracted from the fitted reaction rates in yttrium. τ_1 refers to the formation of oxide according to equation (6.4), τ_{2-5} to the formation of hydrates according to equation (6.6).

coefficients are assumed to be zero, reflecting the experimental data. Note the two orders of magnitude difference between the reaction time for the formation of the oxide molecule in high and low impurity conditions. The fitted exponential rise time for the low impurity data of 96(10) ms is much shorter than the time $\tau_1 = 2.3$ seconds obtained from the simulation model. This can be explained by the domination of the evacuation of the ions to the time profile of figure 6.2(b). This observation illustrates that the single shot model is a powerful tool to directly probe the level of impurities in a system dominated by the evacuation time, where simply fitting the rise time of the atomic species can only provide an upper limit. A more thorough explanation can be found in [87].

The saturation time extracted from the experimental results can be combined with equation (6.3) to obtain estimates for the impurity levels of water and oxygen. Within the literature one may find a reaction rate constant $k = 4.1 \cdot 10^{-10}$ cm^{3}s^{-1} [176,177] for the molecular formation described by equation (6.4) and a reaction rate of $k = 1.9 \cdot 10^{-10}$ cm^{3}s^{-1} [178] for the subsequent pickup of water as described by equation (6.6). The extracted impurity levels for water and oxygen are summarised in table

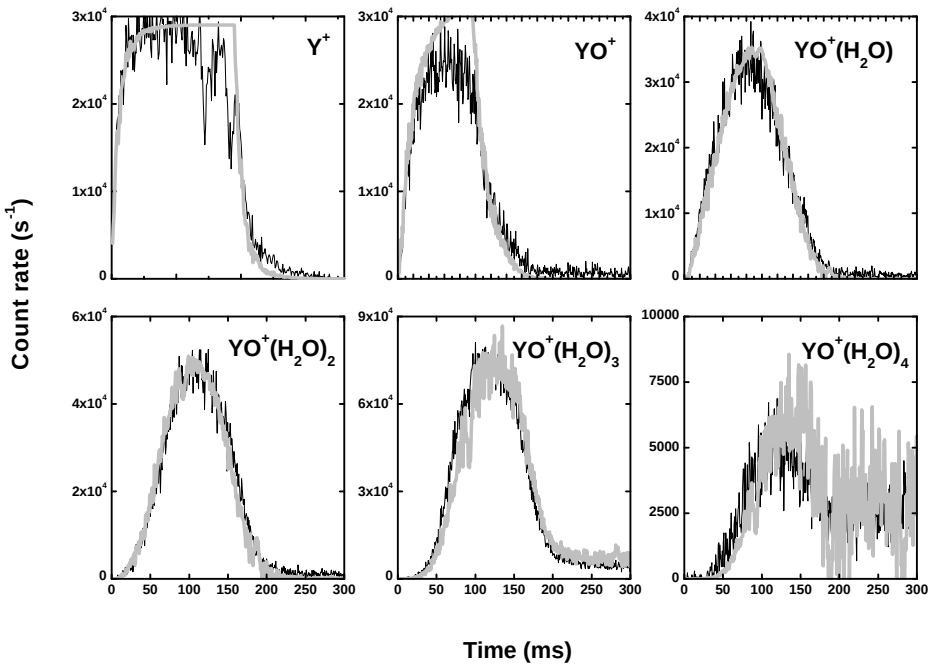

(a) High impurity conditions

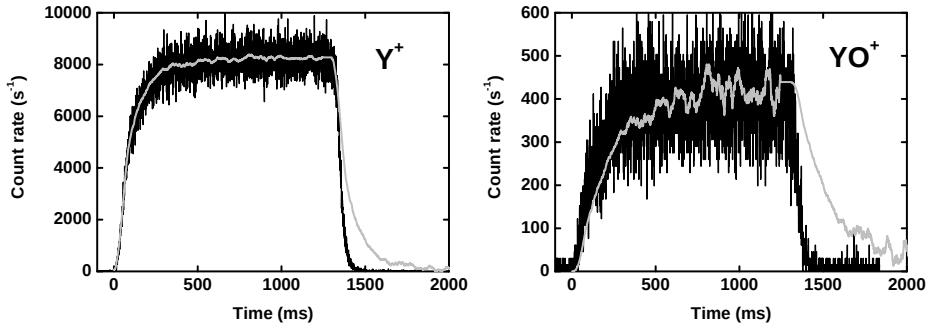

(b) Low impurity conditions

Figure 6.3: Comparison between the simulated time profiles laser ionized yttrium (grey line) and the experimental data (black line).

6.2.

	high impurity level	low impurity level
oxygen	73	0.29
water	101	0

Table 6.2: Estimates for the impurity levels for high and low impurity conditions in ppb.

In order to understand the importance of the baseline vacuum chamber pressure in a controlled fashion, a needle valve was attached directly to the IGISOL vacuum chamber and a leak was introduced. The count rates of yttrium and related molecules were monitored as a function of chamber pressure. By applying the simulation model it could be shown from the experimental data that in this instance the molecular formation was happening outside of the ion guide. This is in contrast to the data set from figure 6.2(a) in which the buffer gas was contaminated [87] and the formation of YO^+ and hydrate additions occurred in the guide.

The need for extreme gas purity is common to all existing and planned gas cell devices. Much effort has been put into cleaning up the gas down to the sub-ppb impurity level, however even at this low level the molecular formation still seems to be a problem in some cases. Partly because of these difficulties, cryogenic gas catchers are currently being developed [179]. At the IGISOL facility the development of a new cryogenic ion guide is underway and a first experiment is scheduled to test laser ionization in the cooled buffer gas cell. In this manner, similar to the present work, the evolution of the molecular sidebands on chemically reactive elements such as yttrium can be monitored as a function of the cooling temperature. It will be important though not only to develop and incorporate these cryogenic techniques further, but to ensure a clean environment through which the ions must pass once they are extracted from the gas cell.

6.2 Studies of the role of the beam-related plasma

The dynamics of the He and Ar plasma are of critical importance for the development of laser ionization in an ion guide. The plasma created mainly by the degrading of the primary beam in the gas leads to recombination and consequently provides a loss mechanism for the laser ionization process as has been experimentally shown by the LISOL group [180]. In this section different aspects of the processes induced by the presence of the plasma in the ion guide will be discussed.

The section starts with a small description of the theory of the creation and decay of a weakly-ionized plasma, i.e. a plasma with a high neutral fraction. The experimental

data, discussed in section 6.2.2, complements the off-line data for the yttrium system presented in section 6.1. Molecular formation is studied under the influence of a beam-produced plasma. The ratio of the yields obtained is compared to a simple rate equation model. The evolution of the buffer gas plasma itself is discussed in section 6.2.3 for helium and argon. Bismuth has been chosen to investigate the possibility of laser ionization on-line as it is chemically inert and consequently provides a good test case to study the recombination process for ions produced by knock-out from a target. The recombination dynamics of bismuth ions have been investigated for both argon and helium and are discussed in section 6.2.4.

6.2.1 Theory of a weakly-ionized plasma

The dynamics of the plasma density are described in [181]. The governing partial differential equation for the electron-ion pair density reads

$$\frac{dn_e}{dt} = Q - \alpha n_e^2 \tag{6.7}$$

where n_e denotes the density of electron-ion pairs and Q the ionization-rate density. The system is solved by

$$n_e(t) = n_0 \frac{e^{2t/t_{plasma}} - 1}{e^{2t/t_{plasma}} + 1} \tag{6.8a}$$

with

$$n_0 = \sqrt{Q/\alpha} \tag{6.8b}$$

and

$$t_{plasma} = \frac{1}{n_0 \alpha} = \frac{1}{\sqrt{Q\alpha}} \tag{6.8c}$$

where t_{plasma} is the time needed to reach an equilibrium density for $t \gg t_{plasma}$. The term α is the total recombination rate of the plasma in the gas.

For weak plasmas with a high neutral fraction such as in the case of IGISOL the atomic buffer gas ions A^+ immediately dimerize to diatomic ions A_2^+ [182]. The dissociation-recombination of the dimerized buffer gas

$$A_2^+ + e^- \rightarrow A^* + A \tag{6.9}$$

is predominant. A second-order process, the so-called "neutral-stabilized" or "three-body" recombination

$$A_2^+ + e^- + A \rightarrow A^* + 2A \tag{6.10}$$

was first discussed by Thomson [183] and Pitaevskii [184]. The theory was later refined by Bates and Khare [185, 186] and states that the coefficient for three-body recombination α_3 is proportional to $P/T^{5/2}$ where P is the pressure and T the temperature. As a consequence this term becomes the dominant contribution for high pressures and low temperatures. For both argon and helium, the rate coefficients have been determined experimentally [187, 188]

$$\begin{aligned} \alpha_{Ar} &= 1.07 \cdot 10^{-6} \mathrm{cm^3 s^{-1}} \quad \text{for argon and} \\ \alpha_{He} &= 1.12 \cdot 10^{-7} + 2.2 \cdot 10^{-27}\,[\mathrm{He}]\,\mathrm{cm^3 s^{-1}} \quad \text{for helium} \end{aligned} \tag{6.11}$$

where [He] is the number density of the helium gas. The production rate Q for the plasma is calculated using

$$\begin{aligned} Q &= \frac{I}{A}\frac{dE/dx}{W} \\ &= 6.25 \cdot 10^{12}\frac{I}{A}\frac{dE/dx}{W} \quad \text{ion-electron pairs cm}^3/\text{s} \end{aligned} \tag{6.12}$$

where I is the beam current in pμA, A the beam spot area in cm^2, (dE/dx) the linear energy loss of the ion in eV/cm and W the mean ionization energy in eV needed to produce one electron-ion pair. The formula is a good approximation if the beam is passing through the cell and consequently a constant energy dE/dx is deposited throughout the full stopping path. For a stopped beam the energy loss changes as a function of the residual beam energy during the stopping process. In this case dE/dx can be approximated by E/x where E is the degraded beam energy before entering the gas cell and x is the stopping range in the cell. The value for W

$$\begin{aligned} W_{Ar} &= 26.4 \text{ eV} \quad \text{for argon and} \\ W_{He} &= 41 \text{ eV} \quad \text{for helium.} \end{aligned} \tag{6.13}$$

is dependent on the buffer gas type [180,189]. If the primary beam is turned off or the plasma is transported away from the beam interaction zone the production parameter Q in equation (6.7) can be set to 0. The solution of the differential equation for the plasma decay then can be written

$$n_e(t) = \frac{n_0}{1 + t/t_{plasma}} \tag{6.14}$$

where $n_e(0) = n_0$ is the initial plasma density. A typical time-dependence of the electron density is shown in figure 6.4 for a pressure of 50 mbar in He and an initial plasma density of 10^{10} electron-ion pairs per cm^3. The figure states that for an ion guide with a long evacuation time such as the HIGISOL ion guide described in section 4.5 or the LISOL ion guide described in section 6.1 the plasma has decayed

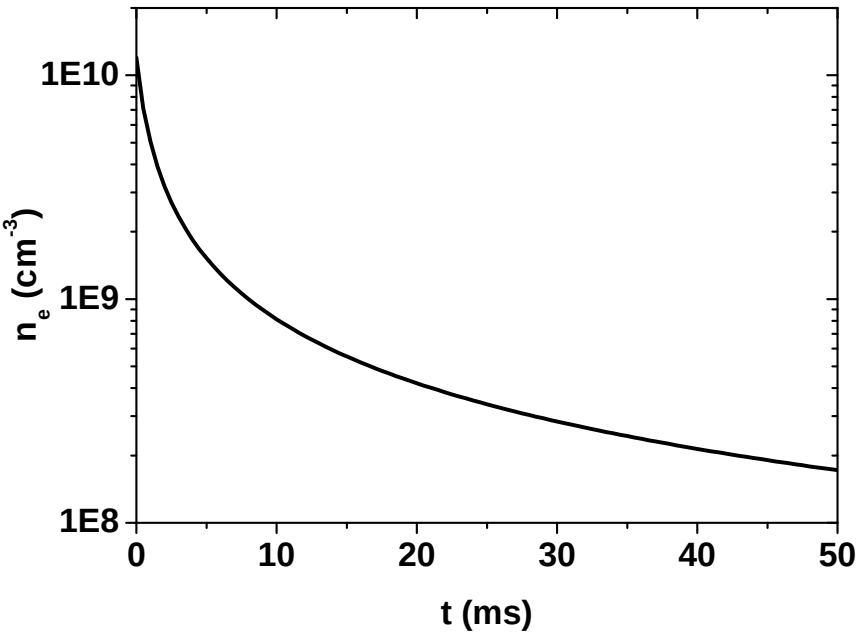

Figure 6.4: Decay of the electron density in helium at a pressure of 50 mbar.

by more than 1 order of magnitude when it reaches the nozzle. The equilibrium level is calculated by

$$n_e(t) \sim \frac{n_0}{t/t_{plasma}} = \frac{1}{\alpha t} \quad \forall\, t > t_{plasma}\ . \tag{6.15}$$

The motion of the plasma in a buffer gas is usually discussed in the framework of ambipolar diffusion. In this picture the neutrality of the plasma is preserved by the electric interaction of the ions and electrons. Consequently, the density of ions and electrons $n = n_I = n_e$ as well as the total flux $J = J_I = J_e$ of ions and electrons are equal. The flux J is written as

$$\begin{aligned} J = J_e &= -\mu_e n E - D_e \frac{\partial n}{\partial x} \\ &= J_I = \mu_I n E - D_I \frac{\partial n}{\partial x} \end{aligned} \tag{6.16}$$

and is split into a field-dependent part and a diffusion-dependent part, where μ and D are constants for the mobility and the diffusion of the electrons and ions respectively. The static field E created by the plasma can be calculated from (6.16) to be

$$E = \frac{D_I - D_e}{\mu_e + \mu_I} \frac{1}{n} \frac{\partial n}{\partial x}\ . \tag{6.17}$$

The mobility of electrons μ_e and the diffusion coefficient D_e are typically two to three orders of magnitude higher than those for ions [190] and consequently the expression for the field E can be simplified to

$$E \sim -\frac{D_e}{\mu_e} \frac{1}{n} \frac{\partial n}{\partial x}\ . \tag{6.18}$$

The Einstein relation

$$\frac{D}{\mu} = \frac{k_B T}{q} \tag{6.19}$$

where q is the electric charge, can be used to relate the diffusion process to the mobility. One obtains the final result

$$E \sim -\frac{k_B T}{q} \frac{1}{n} \frac{\partial n}{\partial x}\ . \tag{6.20}$$

If the plasma is assumed to decay according to equation (6.14) during its evacuation with a speed $v_{evac} = \partial x / \partial t$, the field can be calculated to be

$$\begin{aligned} E &\sim -\frac{k_B T}{q} \frac{1}{n} \frac{\partial n}{\partial t} \frac{\partial t}{\partial x} \\ &= \frac{k_B T}{q} \frac{\alpha}{v_{evac}} n(t(x))\ . \end{aligned} \tag{6.21}$$

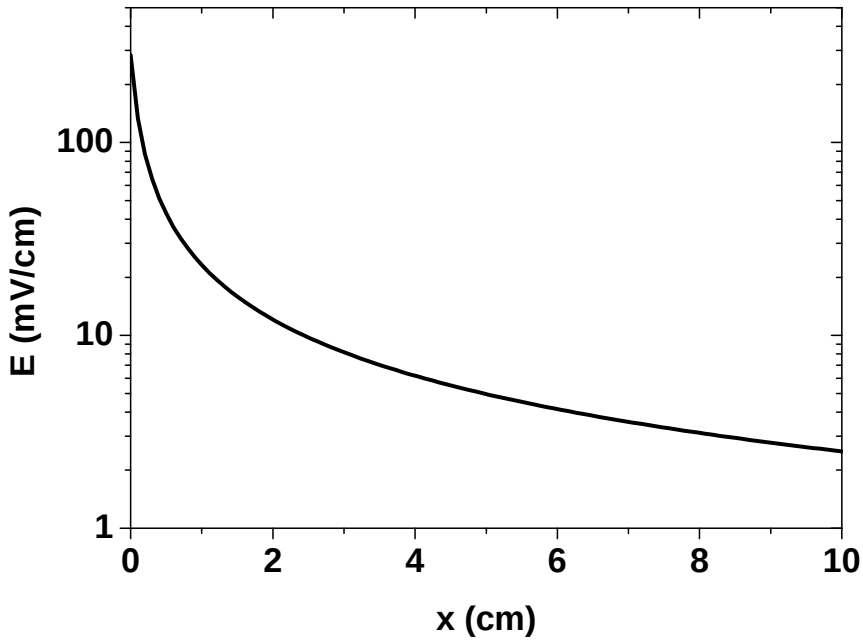

Figure 6.5: Electrostatic field E created by a weak plasma of 10^{10} electron ion pairs per cm^3.

The field strength estimated for a gas velocity of 1 m/s and an electron-ion density $n_0 = 10^{10}$ per cm^3 in He gas is shown in figure 6.5. A field strength of up to 280 mV/cm is reached in the beam interaction region.

To obtain an expression for the coupled motion of electrons and ions in the plasma the expression for the field E from equation (6.18) can be inserted into equation (6.16)

$$J = -D_a \frac{\partial n}{\partial x} \tag{6.22}$$

with

$$D_a = \frac{\mu_I D_e + \mu_e D_I}{\mu_e + \mu_I} \sim D_I + \frac{\mu_I}{\mu_e} D_e = D_I \left(1 + \frac{T_e}{T_I}\right) . \tag{6.23}$$

The expression for the so-called ambipolar diffusion constant D_a has been again simplified by making use of the different mobility of ions and electrons and the Einstein relation. In the ambipolar approximation the diffusion of both electrons and ions is described by the ambipolar diffusion constant D_a. In thermal equilibrium conditions

$T_e \sim T_I \sim T$ the ambipolar diffusion constant can be simplified to

$$D_a \sim 2D_I \tag{6.24}$$

and is governed by the diffusion constant D_I for ions.

6.2.2 Dynamics of molecular formation in the presence of a plasma

For the production of radioactive ion beams it is beneficial to study the dynamics of the recombination of ions in the gas in the presence of a plasma produced by the primary beam. In a first experiment at IGISOL of this type the impact of the plasma on yttrium ions created by direct beam ionization and laser ionization was studied. The general setup has been already described in section 6.1. This experiment was carried out under high impurity conditions. Neutral yttrium was provided by a resistively heated filament placed into the Leuven ion guide. The plasma was produced by a 10 nA α beam at an energy of 30 MeV. The dynamics were probed experimentally by applying pulsed primary beams from the cyclotron. The timing of the cyclotron pulsing, the laser radiation and the data acquisition system was performed by the JYFLTRAP control software [59].

Time spectra for yttrium and its molecular compounds are shown in figure 6.6. The beam was turned on from 1 to 2.5 s and the laser radiation from 1.5 to 3 and 3.5 to 4 s respectively, as indicated by the differently coloured shaded boxes. The behaviour in general is explained by the interplay between the different processes in the ion guide, i.e. ionization, molecular formation, recombination and evacuation. A quantitative model based on rate equations has been developed. The typical equations describing both chemical and recombination processes for Y and YO can be written as

$$\begin{aligned} \frac{d\mathrm{Y}}{dt} &= N_{\mathrm{Y}} - \lambda_{\mathrm{Y}}\mathrm{Y}(t) - \alpha n_e(t)\mathrm{Y}(t) \\ \frac{d\mathrm{YO}}{dt} &= \lambda_{\mathrm{Y}}\mathrm{Y}(t) - \lambda_{\mathrm{YO}}\mathrm{YO}(t) - \beta n_e(t)\mathrm{YO}(t) \\ \mathrm{Y}(0) &= \mathrm{Y}_0 \\ \mathrm{YO}(0) &= 0\,. \end{aligned} \tag{6.25}$$

The rate N_{Y} describes any ion production mechanism as for example laser ionization. The two loss rates λ_{Y} and λ_{YO} identify the molecular formation, the terms $\alpha n_e(t)\mathrm{Y}(t)$ and $\beta n_e(t)\mathrm{YO}(t)$ describe the recombination losses. The extended model described in detail in [191] is capable of reproducing the main features of the data, in particular the occurrence of spikes in the yield during the beam-on and beam-off period. A somewhat qualitative discussion will be given here.

A detailed view of the important characteristics of the data in figure 6.6 is shown in an overlayed plot in figure 6.7.

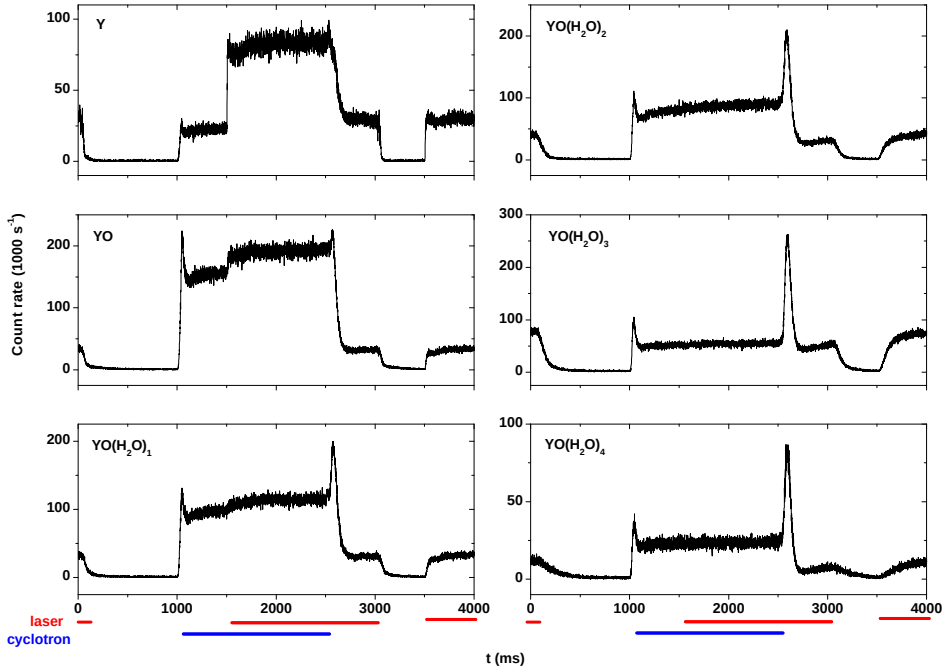

Figure 6.6: Dynamics of the yield of yttrium and its molecular compounds in a He plasma. The lines on the bottom of the figure indicate laser radiation (red) and beam irradiation (blue).

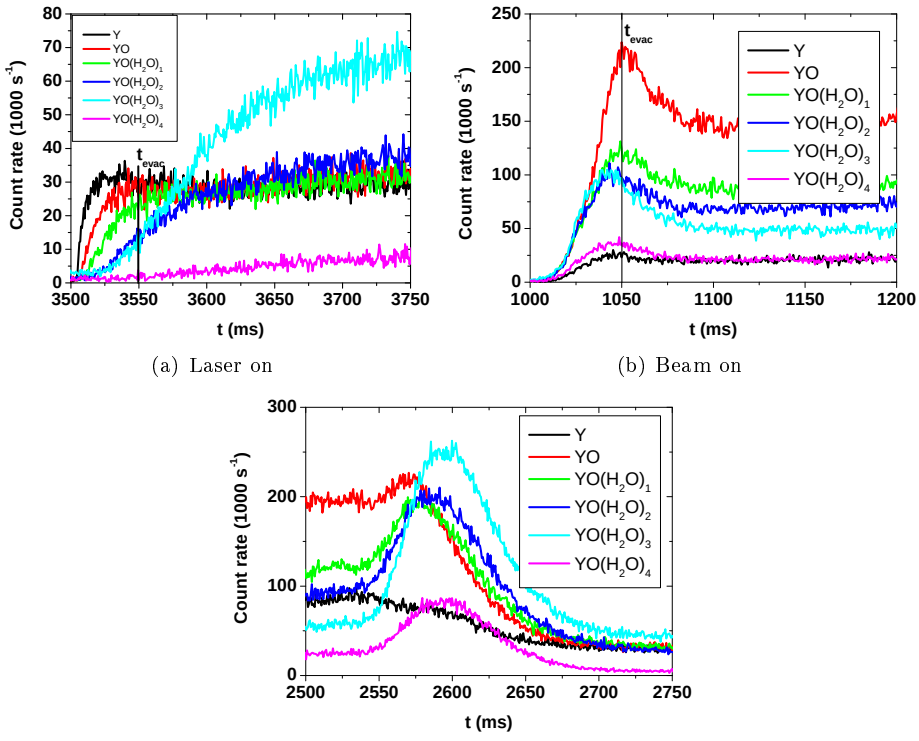

(a) Laser on

(b) Beam on

(c) Beam off

Figure 6.7: Details of figure 6.6 showing the laser-on period (a), the beam-on period (b) and the beam-off period (c).

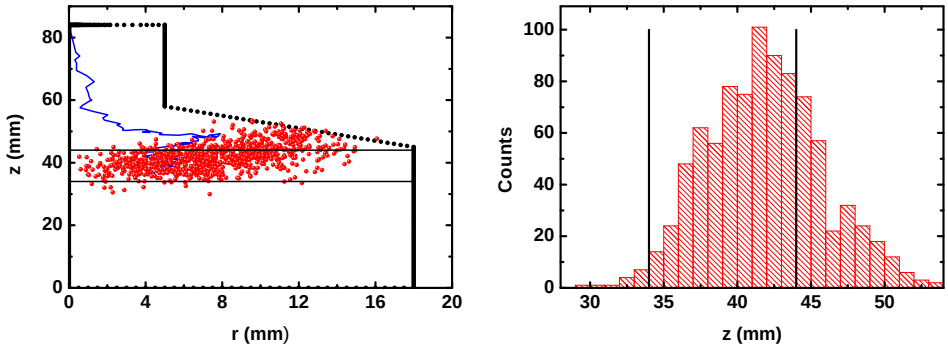

Figure 6.8: Simulation of a starting distribution of ions with an evacuation time of 50 ms.

Figure 6.7(a) shows the rise of the signal when the laser has been turned on without the presence of the beam-created plasma. The dataset provides the saturated yield of the laser signal in contrast to the data of figure 6.2(a) which shows the evacuation of a 50 ms laser pulse. The sum of all compounds gives the total laser ion signal from the guide and is governed by the evacuation of the ion guide as shown in figure 4.7. In principle, by linking the sequential build-up of molecules with the gas flow. From this data, the ionization probability and survival of ions located in different regions in the ion guide can be probed. Yttrium ions can only survive molecular formation if they are created close to the nozzle region, while laser ions created in the back of the guide most probably are extracted as hydrate molecules.

The "beam-on" period is detailed in figure 6.7(b). A spike appears for all species with a common delay of approximately 50 ms, most pronounced for YO which is the molecule with the highest abundance in on-line conditions. A gas flow simulation was carried out to reconstruct the production site of ions created during the spike. To identify the location of the ions the gas flow was inverted in the simulation, corresponding to a time-reversal according to equation (4.14). The ions were created within a random spot in the nozzle exit area. Their time-reversed tracks were followed for 50 ms into the ion guide and their final position was recorded. Ions hitting a wall were neglected. The result of a calculation with 1000 ions is shown in figure 6.8. Figure 6.8(a) shows the distribution of ions with an evacuation time of 50 ms in the cell. The two horizontal lines marking the position of the beam entrance windows show that these ions are indeed located in the beam interaction region. Figure 6.8(b) shows a histogram of the position of the ions in z-direction. The slight asymmetry towards the nozzle is caused by ions located at higher radii r. The spike in figure 6.7(b) arises

indeed from direct beam ionization. For comparison with the molecular formation under off-line conditions the evacuation time of 50 ms from the beam interaction zone is illustrated by a vertical line in figure 6.7(a), indicating that the majority of yttrium ions are converted to molecules once they reach the nozzle.

A different behaviour is observed for the beam-off period depicted in figure 6.7(c). Note that the laser radiation is continuously turned on during this period and consequently the time structure describes a transition from a regime dominated by direct beam ionization and recombination to off-line conditions dominated by laser ionization and molecular formation. During the "beam-on" period YO provides the highest count rate while during the beam-off period $YO(H_2O)_3$ is the most abundant molecule. The spikes are delayed but don't overlap in time. In contrast again the sequential build-up of molecules typical for off-line conditions such as in figure 6.2(a) is observed. Note the delay of the response of the ion signal to the "beam-off" time at 2500 ms by approximately 50 ms which can be attributed to the full evacuation of the plasma from the ion guide after the beam has been turned off. The increase in yield after the plasma has been evacuated can be attributed to the increased survival probability of ions.

The saturated ion yield of the different compounds of yttrium is illustrated in figure 6.9 for the different conditions in the ion guide. During the laser on condition yields similar to those described in section 6.1 are obtained with a maximum contribution of $YO(H_2O)_3$. Hydrates are preferably formed in the back of the ion guide and the increased yield can be attributed to the position of the filament which is located in the back of the guide. In contrast, if only the beam is turned on, the maximum is shifted towards YO and the yield falls off rapidly for the hydrogenic molecules. A similar shift can be observed in figure 6.9 for the case when both the beam and the laser radiation are turned on indicating the dominance of the ionization by direct beam impact over laser ionization for all compounds except for the bare yttrium ion. The possibility of laser ionization during the beam on period can be extracted by subtracting the yield obtained in a "laser+beam" condition from that of the "beam only" condition, represented by the black curve in figure 6.9. In the case of yttrium a clear increase can be observed when the laser is turned on during the beam-on period. This effect decreases monotonically for the molecules until the full signal is completely dominated by direct beam ionization in the case of $YO(H_2O)_4$.

Following the discussion so far, yttrium ions are produced in the beam region and are then evacuated from the ion guide in a time of 50 ms (see figure 6.8). A molecular rate equation model using the parameters of table 6.1 was run to estimate the abundances of ions created in the beam region. The result is shown in figure 6.10(a). After an evacuation time of 50 ms the maximum yield is expected around $YO(H_2O)_2$ and consequently molecular formation alone cannot explain the abundance distribution of the beam-created ions peaking at YO. The relatively high YO yield during on-line

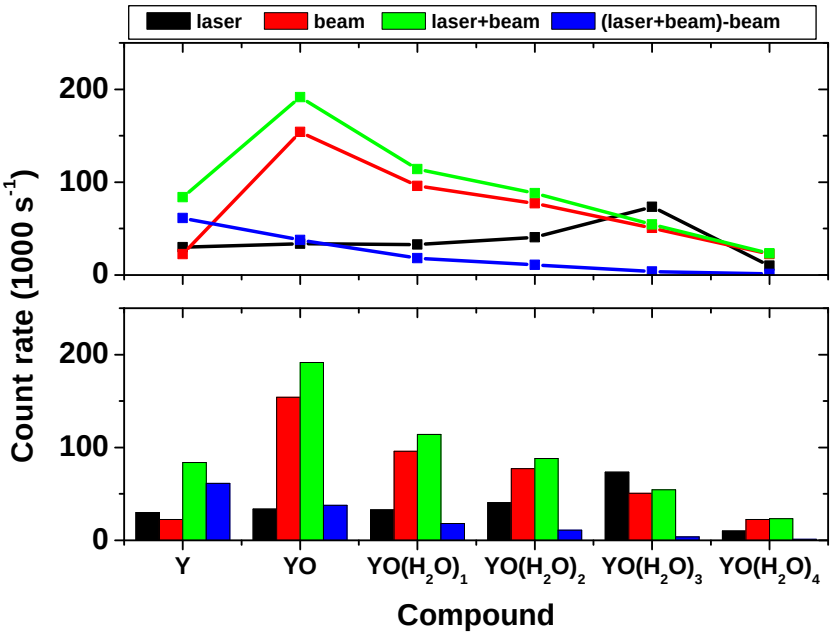

Figure 6.9: Comparison of the yields of yttrium for the different compounds.

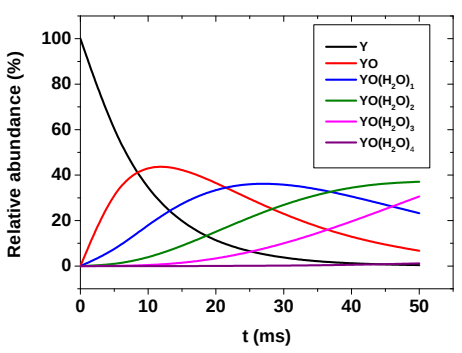

(a) Simulation of the expected abundance of beam-produced ions without recombination processes.

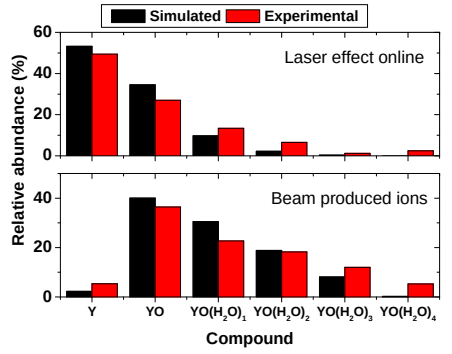

(b) Refined simulation with additional recombination terms.

Figure 6.10: Results of a simulation model to describe the abundance of laser-produced and beam-produced ions.

conditions as well as the decrease in the laser effect for heavier molecules can only be explained by additional recombination of ions and molecules in the evacuation volume. By simply adding recombination rates of 10 ms for Y and YO and 5 ms for the hydrates the yield of yttrium ions created in the beam region and by lasers are reproduced reasonably well, as illustrated in figure 6.10(b). For this simulation the abundance of beam-produced ions was calculated by stopping the simulation at 50 ms, while the laser ion abundance was calculated by integrating over the time-profile of each compound. The increased recombination rate $\tau = 1/n_e\alpha$ needed in the model to suppress the formation of hydrates can be explained by the higher recombination coefficient α [192] for complex molecules and the increased density experienced by ions starting from the back of the ion guide. From the recombination rates obtained by the model the average electron-ion density in the evacuation volume can be estimated to be

$$n_e \sim \frac{1}{\alpha_{He} t}|_{t\to 10\text{ ms}} \sim 8 \cdot 10^8 \text{ cm}^{-3} . \tag{6.26}$$

This value is in rather good agreement with the typical electron-ion density in this volume calculated by equation (6.14) and illustrated in figure 6.4.

Particular attention has to be given to the dynamics of laser-ionized Y, as the primary goal of the laser ion source is to extract an ionic beam without molecular sidebands. As the survival of yttrium is restricted to an evacuation time of approximately 5 ms, the ion signal probes the conditions in the direct vicinity of the nozzle. Figure 6.11(a) illustrates the rise of the laser ion signal under "beam on" and "beam off" conditions.

When the cyclotron beam is turned off, the rise time is governed by molecular formation, however during "beam-on" conditions the survival of yttrium ions is limited to a small region around the nozzle area, evacuated in a few milliseconds, corresponding to a fast saturation of the ion signal. The electron-density in the nozzle area can be estimated from the fast rise of the Y signal to 10^{10} cm^{-3} which contradicts the picture of the decay of the plasma in the beam region with a value of approximately 10^8 cm^{-3} after 50 ms of evacuation time to the nozzle area (see figure 6.4). An additional source for the creation of ion-electron pairs in the evacuation volume between the beam region and the exit nozzle may be excitation and subsequent relaxation of buffer gas atoms into metastable states by VUV photons emitted during the recombination in the beam region. The existence of an increased electron-ion density produced by photons or other mechanisms can be probed via its effect on laser-ionized yttrium during the "beam-on" period, as illustrated by figure 6.11(b). Only 10 ms after the cyclotron beam has been turned on, the yttrium signal is reduced. The speed of the process indicates fast build-up of electron density and can be explained for example by photon irradiation from the beam interaction region as discussed in more detail in section 6.2.3.

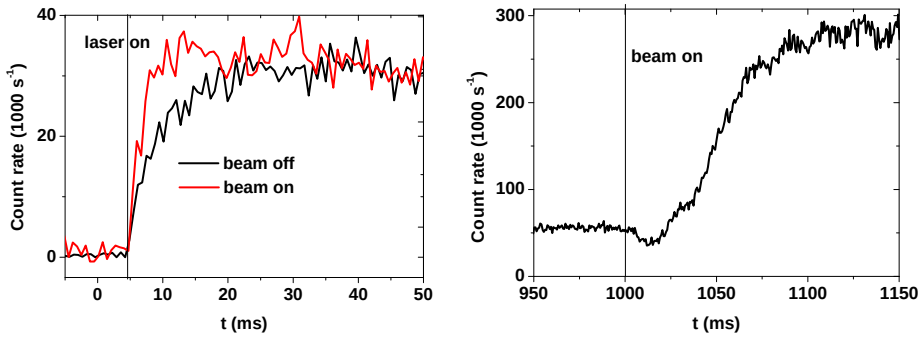

(a) (b)

Figure 6.11: Effects of the beam-produced plasma in the nozzle area. (a) Comparison between the rise time of the laser ion signal of yttrium with and without beam. (b) Recombination of laser produced ions when the cyclotron beam is turned on.

The dominance of recombination over laser ionization for hydrates can be illustrated by comparing time-profile data with and without laser ionization as shown in figure 6.12 for the case of $YO(H_2O)_3$. The laser effect shown in the upper panel is calculated by subtracting the two graphs shown in the lower panel. While the cyclotron beam is on, no laser effect can be observed. Approximately 50 ms after the beam has been turned off, the plasma is evacuated and the laser ion signal increases. The continued slow rise of the laser ion signal after the spike can be attributed to evacuation, only interrupted by the period between 3 and 3.5 seconds when the laser has been turned off.

In conclusion one can state that evacuation, molecular formation and recombination are the important processes in the gas cell which can seriously affect the extraction efficiency of atomic ions from the ion guide. While molecular formation is present for ions having a high chemical reactivity with impurities in the buffer gas, recombination can restrict efficient extraction of all laser ions from the cell to a region very close to the nozzle with an evacuation time of only a few ms.

6.2.3 Dynamics of the buffer gas plasma

In the previous section the importance of recombination evoked by free electrons produced by the primary beam in the buffer gas was discussed. The data presented in this section aims at describing the dynamics of the plasma produced by ionization of the buffer gas. The dynamics are probed by extracting the time-dependent mass-separated yield of the buffer gas ions produced by the impact of the primary beam. A

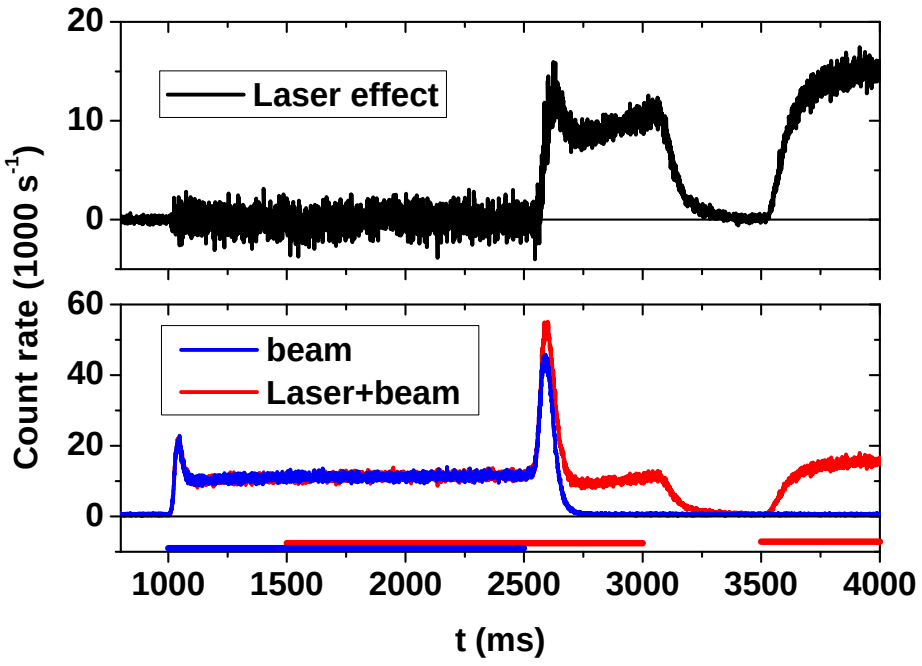

Figure 6.12: Laser ionization during the beam-off period. The lines on the bottom of the figure indicate the periods of laser radiation (red) and beam irradiation (blue).

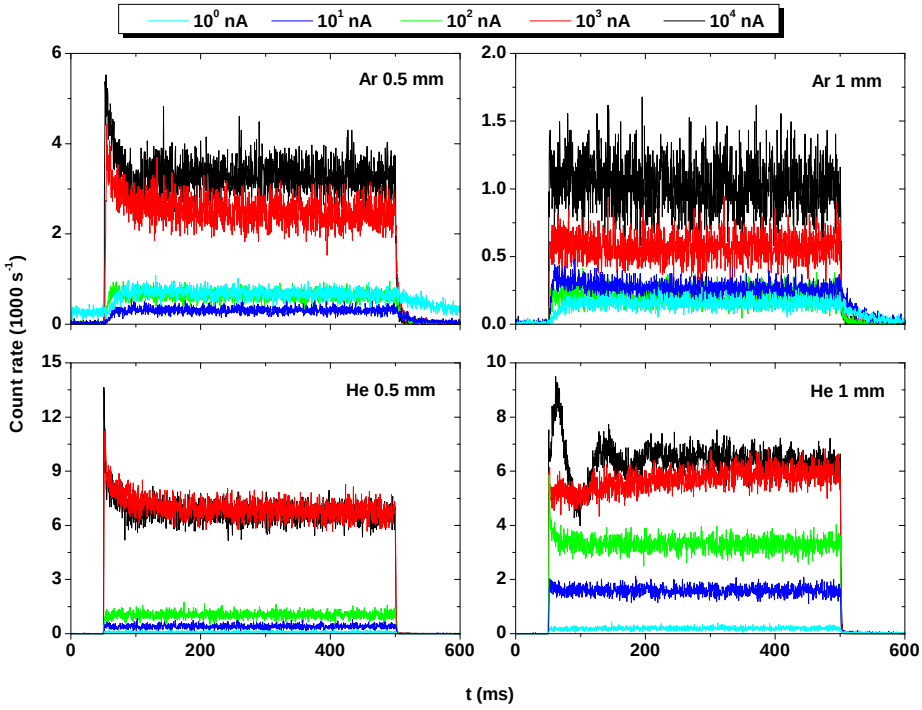

Figure 6.13: Dynamics of the plasma created by a 30 MeV proton beam in Ar and He for exit nozzles of 0.5 and 1 mm diameter.

series of measurements has been carried out using the HIGISOL ion guide described in detail in section 4.5, applying a 30 MeV proton beam to produce the plasma. Two different nozzles with a diameter of 0.5 and 1 mm were tested in order to vary the evacuation time. The buffer gas pressure was fixed at 200 mbar. For each cycle 2048 bins with a bin width of 0.32768 ms were recorded. The beam was turned on at 50 ms and turned off at 500 ms for each cycle. The datasets for both He and Ar buffer gases and beam intensities ranging from 1 nA to 10 μA are shown in figure 6.13.

The first general feature of the data after the beam has been turned on is a spike, appearing primarily at high primary beam current. The delay in the rise of the signal with reference to the beam gate ranges from 5 ms for low primary beam intensities $<$100 nA to $\ll$1 ms for high beam intensities. Consequently only a direct ionization mechanism can explain this phenomena.

One possibility to excite the buffer gas could be the interaction with photons produced by the beam impact in the interaction region and subsequent ionization of

gas	λ (nm)	A (s^{-1})	σ cm^2	dE/dx (eV/cm)
He	58.4334	$1.798 \cdot 10^9$	$3.7 \cdot 10^{-12}$	604
Ar	104.8220	$5.201 \cdot 10^8$	$3.4 \cdot 10^{-12}$	4263
gas	$(d\epsilon/dx)/(dE/dx)$	Photons per proton	J_γ ($cm^{-2}s^{-1}$)	$1/k_{\mathrm{pump}}$ (ms)
He	0.24	23	$6 \cdot 10^{12}$	42
Ar	0.29	345	$1 \cdot 10^{14}$	3

Table 6.3: Estimate of the excitation of the $^1S \rightarrow {}^1P$ transition via photon absorption for a 1 μA 30 MeV proton beam in 200 mbar buffer gas.

the metstable buffer gas by charge exchange processes. A more detailed discussion of the possible processes involved can be found in [191]. The photon spectrum of noble gases excited by direct beam impact has been studied for helium [193] and argon [194] and is dominated by the $^1P_1 \rightarrow {}^1S_0$ transition with a wavelength of 58.4334 nm ($A = 1.798 \cdot 10^9$/s) and 104.8220 nm ($A = 5.201 \cdot 10^8$/s), respectively. A rather large fraction (24% for helium and 29% for argon) of the total energy loss dE/dx of the primary beam is converted into photon radiation $d\epsilon/dx$ during the stopping process and approximately 50% of the photons arise from an excitation of the buffer gas into the $^1P_1$ state [195]. The probability rate k_{pump} for absorption can be estimated from the photon intensity emitted from the beam interaction region in the following manner;

$$\begin{aligned} k_{\mathrm{pump}} &= \frac{dP}{dt} = \sigma \times J_\gamma \\ &= \text{cross section} \times \text{Photons per proton} \times \text{beam intensity} \times \text{geometry} \times 1/\text{area} \\ &\sim \frac{3\lambda^2}{4}\frac{A}{2\pi\Delta\nu} \times \frac{1}{2}\frac{dE}{dx}\frac{d\epsilon/dx}{dE/dx}\frac{L}{h\nu} \times \frac{I}{q} \times \frac{1}{2} \times \frac{1}{\pi L^2/4} \end{aligned} \tag{6.27}$$

where L is the diameter of the ion guide and I the electrical current of the primary beam. The line broadening of the $^1P_1 \rightarrow {}^1S_0$ transition, $\Delta\nu$, is governed by pressure broadening and was estimated to be 10 MHz/mbar. 50% of the light is assumed to be emitted in the forward direction, taken into account by the geometry factor. Table 6.3 gives typical numbers calculated for the experimental setup in this work. The passage of a single proton through the buffer gas provides enough energy to produce 23 photons in helium and 345 in argon. For a 1 μA proton beam typical timescales $1/k_{pump}$ to efficiently pump into the metstable state can be estimated to 42 ms in helium and 3 ms in argon, respectively, indicating that pumping of the $^1S \rightarrow {}^1P$ transition might be possible. However, as the cross section for ionization is expected to be orders of magnitude smaller, direct photo ionization of the excited ^1P

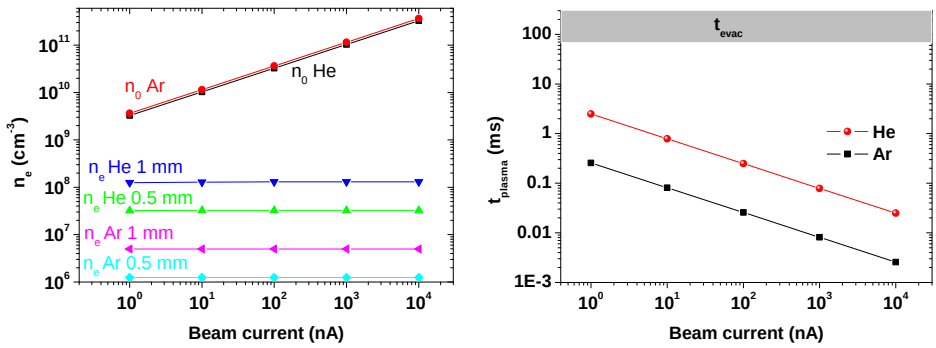

(a) Electron-ion density n_e

(b) Plasma decay time t_{plasma}

Figure 6.14: Electron-ion density n_e and plasma decay time t_{plasma} in the beam interaction region for Ar and He buffer gas.

state can be excluded. Ionization of the excited helium atom will most likely occur via collisions with other excited atoms or with energetic electrons. From the pressure dependence of the decay of the metastable buffer gas atom in the ^{1}P state [193, 194] it was concluded that at a pressure beyond 100 Torr, the excited state is most likely destroyed by two- and three-body collisions and not by the allowed transition to the metastable ^{1}S state.

To be able to discuss the survival of ions in the buffer gas as a function of primary beam current, the electron density was calculated in the beam region and in the nozzle area using equations (6.8) and (6.14), respectively. Figure 6.14(a) shows the electron-ion density. An electron-ion density n_0 of up to 10^{11} cm^{-3} is reached in the beam region leading to fast plasma decay times compared to the evacuation time according to equation (6.8c). The according decay times are illustrated in figure 6.14(b). Ions created in the ion guide can only survive if their evacuation time is smaller than the plasma decay time calculated via equation (6.8c). Consequently an ion leaving the beam-interaction area will recombine in the guide and cannot contribute to the ion signal. In contrast, ions created close to the nozzle have a small evacuation time and a high survival probability. The plasma density n_e in the nozzle area indicated in figure 6.14(a) was calculated for an evacuation time of 250 ms for He with a 0.5 mm exit nozzle, estimated from figure 4.9. The plasma densities at the exit of the ion guide are basically constant as a function of primary beam current as the plasma is in equilibrium and equation (6.15) is applicable. The plasma density $n_e(t_{evac})$ only depends on the evacuation time and the recombination coefficient α which is approximately a factor of 9 higher in argon compared to helium.

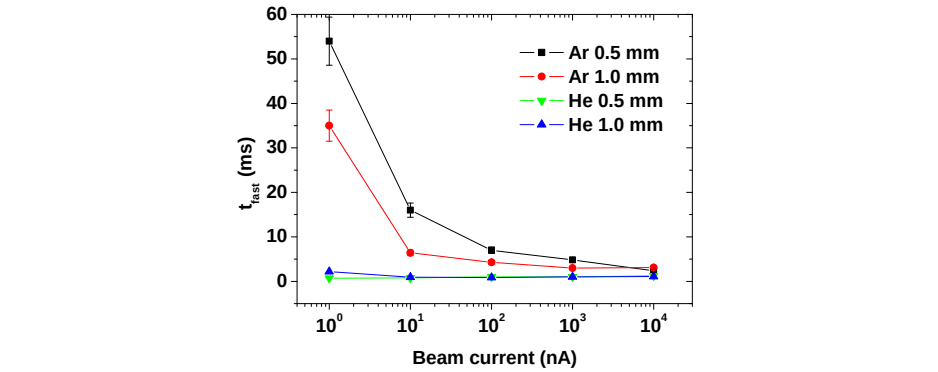

(a) Decay time of fast component

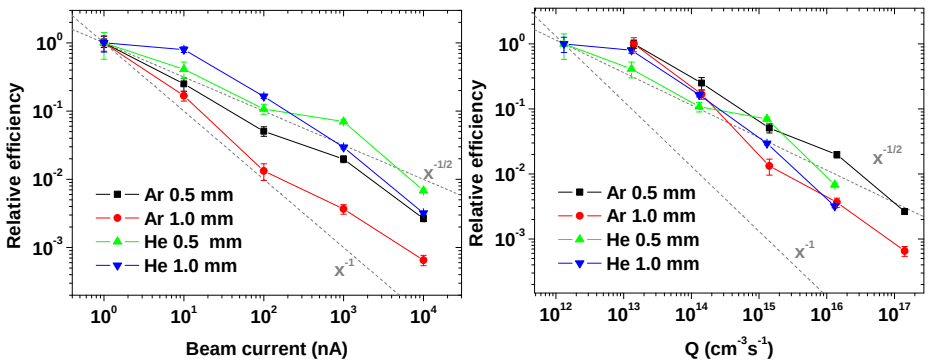

(b) Relative efficiency as function of beam intensity (left) and Q (right)

Figure 6.15: Decay times of the fast component and relative efficiency as a function of primary beam intensity.

Information about the survival probability of ions in the guide can be extracted from the falling edge profiles in figure 6.13. A plot of the fast component of the decay time is shown in figure 6.15(a). For helium the signal decays in ∼1 ms independent of the intensity of the primary beam and the nozzle diameter indicating the dominance of recombination close to the nozzle area. In contrast, in the case of argon a transition from a regime dominated by evacuation towards a regime where the plasma-recombination dominates can be observed, at a primary beam current of 10 to 100 nA. To disentangle the evacuation time from the recombination time, a double-exponential fit was applied to the falling edges. The slow component of the fit function was kept fixed at the low-intensity limit of 1 nA, where a single exponential fit gave an adequate agreement with the data. At this limit decay times of 54 ms (0.5

mm nozzle) and 35 ms (1 mm nozzle) were obtained reflecting the dominance of the evacuation process. The nozzle diameter has only a limited influence on the general trend observed, most apparent at a small beam current for argon. The difference in the decay times in argon and helium buffer gas can only be attributed to the difference in the recombination coefficient from equation (6.11).

The effect of the plasma density on the relative extraction efficiency is illustrated in figure 6.15(b). In the left graph, the efficiency is plotted as a function of primary beam current. A clear difference in behaviour can be observed for the different buffer gas types. In general, the higher relative efficiency of the ion guide for extraction of helium ions indicates a tolerance for higher primary beam intensities due to the difference in the recombination rate coefficients. The different evacuation time, caused by a change of the exit nozzle diameter only has a clear effect for a low beam intensity down to 10 nA. In this case the relative efficiency follows the calculated electron-density at the nozzle illustrated in figure 6.14(a) with a maximum for the shortest evacuation time (1mm diameter exit hole in helium). The difference in the plasma-production rate for the two buffer gases can be taken into account by plotting the relative efficiency as a function of the parameter Q as shown in the right graph of figure 6.15(b). The drop in efficiency can be rather well estimated by a $Q^{-1/2}$ power law, indicated in the graph, which is a typical scaling parameter for the description of various effects caused by a plasma such as the ambipolar electric field of equation (6.20), the build-up of space charge as for example observed in large buffer gas cells [196] and in the ion guide technique [197], dominated by recombination.

6.2.4 Comparison of ion survival in Argon and Helium buffer gas

A first experiment to investigate the possibility of laser ionization under on-line conditions has been carried out for the case of bismuth. A physics motivation lies in the investigation of the nuclear structure beyond the $N = 126$ shell closure, for example discussed in [198]. Additionally a number of short-lived multi-quasiparticle states exist in neutron-deficient bismuth wich may be ideally studied using resonance ionization spectroscopy in the gas cell [132]. The advantage of bismuth compared to yttrium lies in the negligible chemical reactivity with the buffer gas. Consequently, the dominating processes in the gas cell are evacuation and recombination. These two quantities affect the ion survival and are dependent on the type of buffer gas used (compare equations (4.7) and (6.11)). In this experiment the time profiles of bismuth ions in the plasma have been studied for both helium and argon.

To test the effect of the buffer gas the HIGISOL ion guide was prepared with a 6.4 mg/cm^2 bismuth target on a 7.4 mg/cm^2 tantalum backing foil. The target was irradiated by a 500 nA beam of 60 MeV protons. In this manner the stable isotope ^{209}Bi was produced on-line by knock-out of the target material, therefore providing

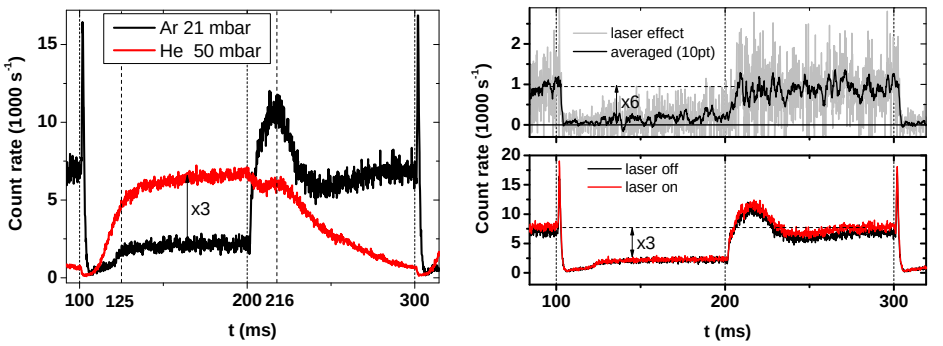

(a) Comparison of survival in He and Ar

(b) Laser effect in Ar

Figure 6.16: (a) Ion survival of ^{209}Bi in argon and helium. The cyclotron is turned on between 100 and 200 ms. The first on-line laser effect observed in IGISOL is shown in (b).

comparable conditions as in a run for the production of radioactive nuclei. To probe the evacuation time profiles the cyclotron was pulsed in a 100ms-off-100ms-on cycle. Pressures of 21 mbar and 50 mbar were applied for argon and helium, respectively. Figure 6.16(a) illustrates the data obtained in both cases.

The figure illustrates the complexity of the dynamics of the system. A number of processes are involved in the build-up and the decay of the plasma as for example discussed in [199–201]. When the cyclotron is turned on at 100 ms the remaining ions in the nozzle from the previous cycle are immediately neutralized. An important conclusion can be drawn that the presence of the plasma is not restricted to the beam region, in accordance with the data presented in section 6.2.3. In the case of argon a strong spike occurs prior to neutralization. At approximately t =125 ms the signal reaches saturation in both cases, indicating an equilibrium in recombination, production and evacuation. Note that under on-line conditions the signal obtained in helium is approximately 3 times higher, reflecting the faster evacuation and the smaller recombination rate in helium gas. When the beam is turned off at 200 ms the signal increases in the case of argon, yet simply decays in helium. However in both buffer gases, a local maximum is observed at 216 ms.

The strikingly different time profiles seen in figure 6.16(a) suggest a stronger recombination of the ion of interest in argon, followed by an increase in the ion survival rate after the primary beam has been turned off. A very long "afterglow" exists in argon. A theoretical understanding of pulsed discharge sources is still not complete and much effort has been put into the understanding of the so-called "afterpeak", described in [202, 203] and references therein. In general the enhanced ionization and

optical emission during the afterglow is attributed to an increased number of excited level populations caused by the recombination of the plasma by a capture-radiative-cascade (CRC) process. This process involves a three-body recombination into highly excited levels and a subsequent radiative decay cascade. The metastable population can relax via Penning ionization which is observed as an ion signal increase during the afterglow of the plasma. A more detailed description of possible ionization and recombination pathways in the ion guide is given in [191].

As in the case of yttrium, by introducing resonant laser light into the buffer gas cell the effect of laser ionization can be studied as illustrated in figure 6.16(b) in argon buffer gas. Note that this dataset illustrates the first on-line ionization signal obtained by the FURIOS laser ion source. As the effect is rather small compared to the direct ionization a 10 point adjacent averaging was applied to the data. Because of the low statistics the data has to be treated with care. A clear signal of laser ionization can only be observed during the beam-off period. The laser signal follows the overall trend observed in figure 6.16(a), exhibiting abrupt recombination when the beam is turned on and a smooth signal recovery when the beam is turned off. During the beam-on period a small laser signal of 145(100) counts per second can be observed, compared to 874(184) during the beam-off period, corresponding to an enhancement factor of $\sim$6. For ions created by the beam impact the yield is $\sim$3 times higher during the beam-off period compared to the beam-on period during saturation of the signal. In contrast to the beam-related ionization, the time profile of the laser effect does not show any complex structure during the beam-on and beam-off period. This indicates that the spikes observed do not arise from a sudden increase in survival but from an additional ionization process. Consequently the laser ionization process is only in competition with electron-ion recombination and evacuation.

7 Summary and Outlook

A variety of different experiments have been carried out following the installation of the FURIOS laser ion source at the IGISOL facility, Jyväskylä, Finland in 2005. The highlights were presented in this thesis.

A hybrid laser system, consisting of high-repetition rate dye and Ti:Sapphire lasers has been installed and is continuously being improved. Along with control software and a remotely controllable mechanical shutter system, an atomic beam unit has been installed.

A significant effort has been made during this thesis to develop an injection-seeded high-repetition rate Ti:Sapphire laser. With a linewidth of approximately 20 MHz this laser provides an excellent tool for high-resolution spectroscopy and trace analysis of rare isotopes. The system has been tested at the University of Mainz and has been recently transfered to Jyväskylä.

The development of the FURIOS laser ion source required the adaption of the IGISOL front-end. A new ion guide for heavy-ion fusion-evaporation reactions has been designed and built, incorporating the possibility of laser ionization. The ion guide has been tested under off-line and on-line conditions. An important sub-task was to test the possibility of laser ionization in the sextupole ion beam guide (SPIG) in the so-called LIST mode. To achieve an efficient transport of atoms from the ion guide into the SPIG structure gas jet studies have been carried out.

The gas jet has been visualized by creating a discharge in the buffer gas and subsequently photographing the metastable fluorescence, revealing the need to design a De Laval exit nozzle to match the conditions in the SPIG. More studies are required to optimize the coupling of the ion source to the SPIG. For this purpose an off-line testing unit is currently being built. A collaboration with the University of Warsaw has been established to support the optimization of the design via detailed gas jet simulations.

For the production of neutron-deficient silver beams a hot-cavity ion catcher has been built and adapted to IGISOL. A stable laser ion beam has been produced by evaporating an atomic sample placed inside the catcher. Both a high-resolution and a high-efficiency mode have been tested. A first on-line run is scheduled for the summer 2008.

A total of 14 different elements have been studied by resonant laser ionization spec-

troscopy during this thesis and some highlights were presented. Different ionization techniques have been applied, namely autoionization, Rydberg ionization and non-resonant ionization using a copper vapour laser in both hot cavity ion sources and in the IGISOL buffer gas. In-source spectroscopy has been studied in the gas cell for the case of bismuth and in a hot cavity for the case of aluminium. In the latter case the novel seeded high-repetition rate Ti:Sapphire laser was successfully tested for the first time in a RIS application. A new technique of collinear laser spectroscopy assisted by optical pumping in an rf cooler-buncher device has been successfully tested off-line and on-line. In this thesis the optical manipulation of niobium and yttrium have been discussed.

In a series of on-line runs involving laser ionization a detailed picture of the processes in the gas cell limiting the efficiency of the ion guide technique has been developed. The role of impurities has been studied for the ideal case of yttrium which is very sensitive to the most important molecules in the gas, namely oxygen and water. A model has been developed to distinguish between impurities in the buffer gas and in the surrounding vacuum chamber and the effect of both on the ion survival. A second important aspect investigated in this thesis was the dynamics of the plasma created by the passage of a primary beam and its impact on the recombination processes in the ion guide. From studies involving pulsed beams from the cyclotron it could be concluded that the plasma is not localized in the beam interaction region but also significantly influences the ion survival in the region close to the exit nozzle. It has been concluded that the survival of ions is limited to this region, creating a challenge for obtaining laser ionization in the IGISOL buffer gas cell.

The same effect has been illustrated for filament-produced atoms ionized by laser radiation in the buffer gas environment. Different approaches can be followed in the future to improve the selectivity of resonant laser ionization in IGISOL. The development of laser ionization in the buffer gas requires the separation of the ion guide into a zone with a high neutralization probability in the beam region and a subsequent extraction zone with a high ion survival probability, a so-called "shadow gas cell", as proposed by the LISOL group. A possible first design is shown in figure 7.1. An aperture of 5 mm diameter separates the two chambers. The evacuation time of the second chamber can be changed by adjusting the volume of the guide. The design shown in figure 7.1 exhibits a typical additional evacuation time of approximately 100 ms using an exit nozzle of 1 mm diameter and He buffer gas.

The conditions for laser ionization are completely different outside of the buffer gas cell. Electrons are immediately stripped from the gas by the electrostatic field of the SPIG electrodes, stopping the recombination process. In this environment the laser ionization process is not in competition with recombination and molecular recombination. In future studies, therefore, more weight will be attributed to laser ionization in high vacuum. Additional selectivity can be gained by operating the SPIG in the

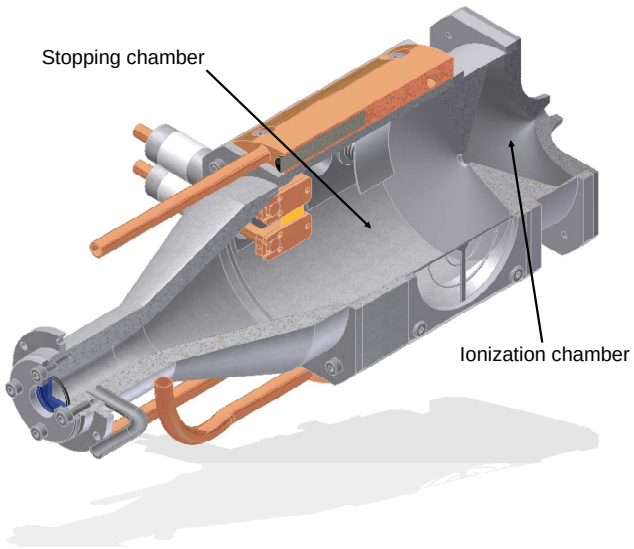

Figure 7.1: HIGISOL ion guide with two chambers for recombination and ionization.

LIST mode and repelling beam-produced ions. Unfortunately, the window in the mass separator needs to replaced to increase the laser ionization efficiency, which can only be achieved during the shutdown period for the IGISOL upgrade in late 2009.

Lately a new cryogenic ion guide has been tested for the first time at the IGISOL facility. The use of a cryogenically cooled buffer gas has several advantages over operation in room temperature. As the density of the buffer gas is proportional to $1/T$ at constant pressure, a higher energy loss dE/dx and consequently a higher stopping fraction of the recoil ions can be achieved. This allows for more compact buffer gas cells. The smaller evacuation time connected with the reduced volume is partially counteracted by a reduced conductance, proportional to $\sqrt{T}$. A higher gas flow rate scaling by $\sqrt{T}$ needs to be pumped by the vacuum system.

Additionally to the general change in the density and the evacuation of the gas cell, the conditions in the cell change drastically in a cryogenically-cooled environment. Impurities can be efficiently frozen out, therefore maximizing the survival of ions against molecular formation. Three-body recombination becomes the dominant process with a $P/T^{5/2}$ dependence on the pressure P and the temperature T. Therefore, for high beam intensities, efficient extraction of the 1^+ charge state from a cryogenic buffer gas cell can only be provided in combination with electric fields. The efficiency is

primarily limited by the build-up of space charge. To what extend laser ionization can provide a means to enhance the efficiency remains to be seen.

A Circuit diagrams for the locking electronics

Circuit diagram of the lock-in amplifier and PID module

In this appendix the circuit diagrams of the phase-sensitive light detection and feedback electronics for the seeded Ti:Sapphire laser (see section 3.1.3) is described. A sketch of the circuit is shown in figure A.1. The photodiode signal (Eingang Photodiode) is band-pass filtered and amplified by operational amplifiers IC1A, IC2A and IC3A. IC4 and IC6 act as phase-shifting devices for both the reference (Eingang Referenz) and the signal (Eingang Photodiode). A circuit of type AD633 was taken as a multiplier with a response function of

$$w = z + \frac{(x_1 - x_2)(y_1 - y_2)}{10} \tag{A.1}$$

L1, C4 and C5 serve as low-pass filter to cut off the modulation at the double input frequency of the reference. The PID control is constituated by R20 and R22 (proportional), R20 and C7 (integral) and R21 and C6 (differential). The signal can be monitored at different locations of the circuit. When the stabilization is turned off by opening switch S2 (Externe Modulation) an external modulation can be applied to directly modulate the output signal. When the stabilization is turned on the stabilization can be reset by shorting condensator C7 via the Reset button S1. S3 (Umschalter pos./neg.) can be switched to provide a positive or negative feedback to the system. The output signal is provided by X8 (Ausgang).

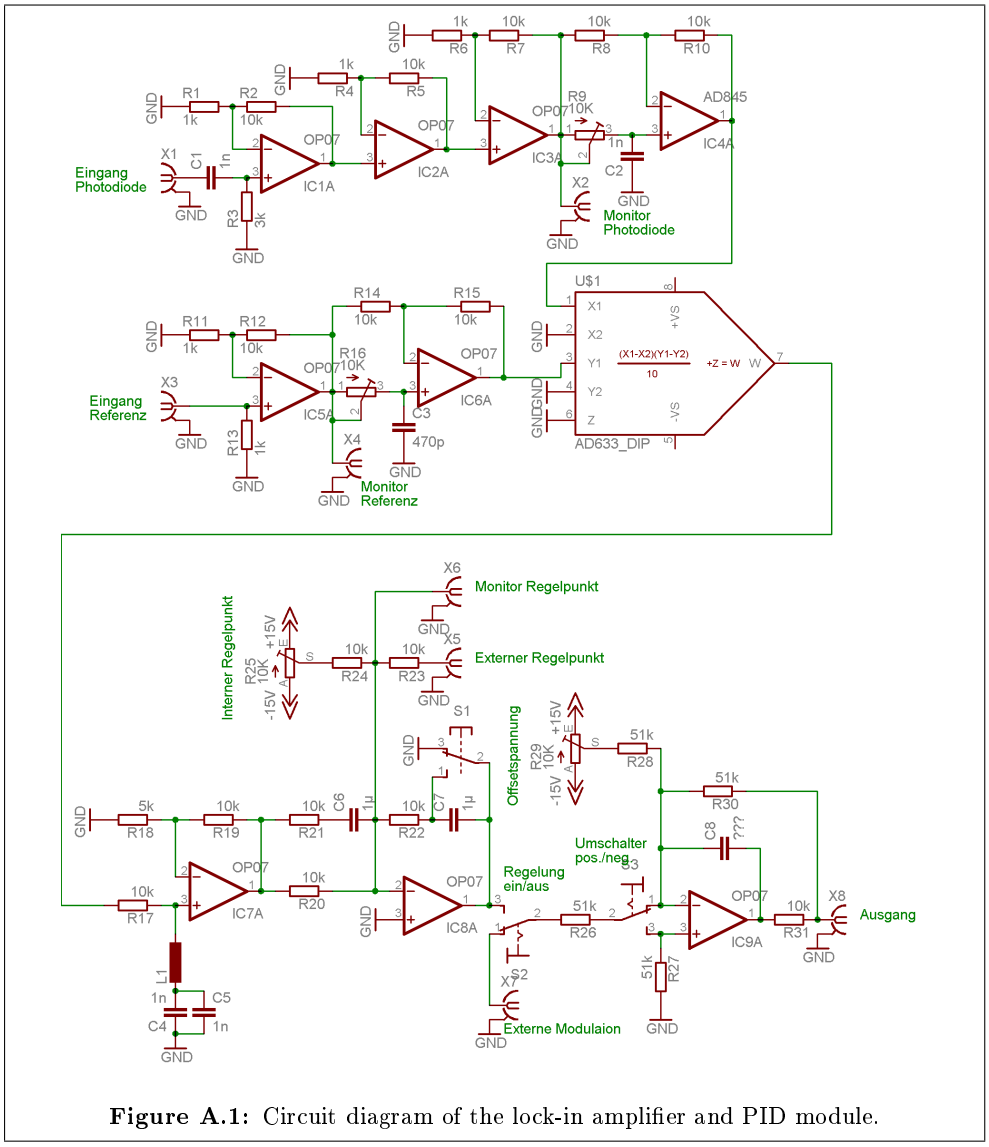

Figure A.1: Circuit diagram of the lock-in amplifier and PID module.

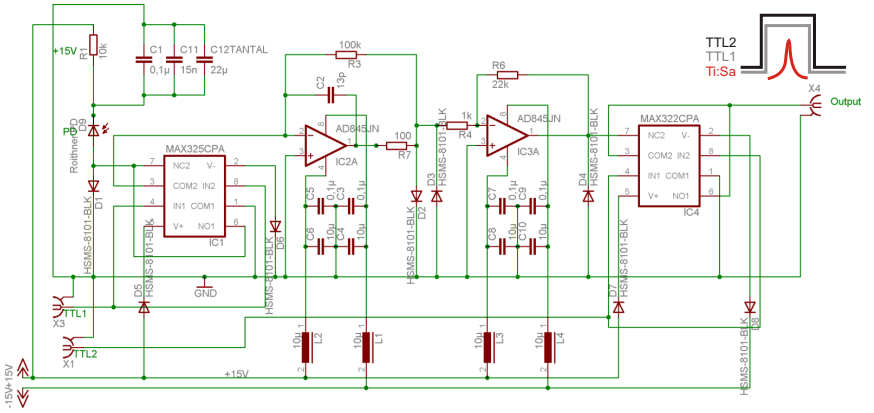

Figure A.2: Circuit diagram of the photodiode amplifier module.

Circuit diagram of the photodiode amplifier

A schematic of the circuit diagram of the photodiode amplifier is shown in figure A.2. The operational voltage of 15 V is supplied to a fast photodiode[1]. The signal of the photodiode is amplified by two operational amplifiers. The photodiode can be shorted to ground by applying a TTL pulse (TTL1) to the analogue switch IC1 of type MAX325CPA. The second switch interrupts the connection between the photodiode and the amplifiers, depending on the state of TTL2. A switching diagram is depicted in the top-right bottom of the figure. To avoid that the Ti:Sapphire laser pulses continuously saturate the photodiode, subsequently the amplifiers and the photodiode are shorted for the duration of a single laser pulse.

[1] Roithner Lasertechnik SSO-PD-Q-11.9-5-TO5

Bibliography

[1] W. Demtröder, *Laserspektroskopie*, 5. ed. (Springer-Verlag, Berlin, Heidelberg, New York, 2000).

[2] B. H. Bransden and C. J. Joachain, *Physics of atoms and molecules* (Addison Wesley Longman Limited, Edinburgh Gate, Harlow, Essex CM20 2JE, England, 1995).

[3] B. W. Shore, *The Theory of Coherent Atomic Excitation Vol. 1+2* (John Wiley & Sons, New York, 1990).

[4] K. Blum, *Density matrix theory and applications* (Springer, Berlin, Heidelberg, New York, 1996).

[5] W. Nörtershäuser, B. A. Bushaw, P. Müller, and K. Wendt, Appl. Opt. **39**, 403 (2000).

[6] T. Kessler, Diploma thesis, University of Mainz, 2004.

[7] R. C. Hilborn, Am. J. Phys. **50**, 982 (1982).

[8] T. F. Gallagher, *Rydberg atoms* (Cambridge University Press, Cambridge, 1994).

[9] B. Kaulakys, J. Phys. B **17**, 4485 (1984).

[10] K. D. Heber, P. J. West, and E. Matthias, Phys. Rev. A **37**, 1438 (1988).

[11] R. W. LaBahn and J. Callaway, Phys. Rev. **147**, 28 (1966).

[12] V. S. Letokhov, *Laser Photoionization Spectroscopy* (Academic Press Inc., Orlando, 1987).

[13] G. S. Hurst and M. G. Payne, *Principles and Application of Resonance Ionisation Spectroscopy*, 1. ed. (Adam Hilger, London, 1988).

[14] U. Köster, V. N. Fedoseyev, and V. I. Mishin, Spectrochim. Acta, Part B **58**, 1047 (2003).

[15] C. Mattolat, Manuscript in preparation.

[16] Y. Liu *et al.*, Nucl. Instrum. Methods Phys. Res., Sect. B **243**, 442 (2006).

[17] G. S. Hurst, M. G. Payne, S. D. Kramer, and J. P. Young, Rev. Mod. Phys. **51**, 767 (1979).

[18] R. P. Madden and K. Codling, Phys. Rev. Lett. **10**, 516 (1963).

[19] A. Temkin, *Autoionization: recent developments and applications* (Plenum Press, New York, 1985).

[20] U. Fano, Phys. Rev. **124**, 1866 (1961).

[21] G. I. Bekov, V. S. Letokhov, O. I. Matveev, and V. I. Mishin, Opt. Lett. **3**, 159 (1978).

[22] D. Kleppner, M. G. Littman, and M. L. Zimmerman, in *Rydberg States of Atoms and Molecules*, edited by R. Stebbings and F. Dunning (Cambridge University Press, Cambridge, 1983), Chap. 3, pp. 73–116.

[23] I. I. Sobel'man, *Atomic Spectra and Radiative Transitions* (Springer, Berlin, Heidelberg and New York, 1979).

[24] V. S. Lebedev, J. Phys. B **24**, 1977 (1991).

[25] V. S. Lebedev, J. Phys. B **24**, 1993 (1991).

[26] T. J. Wittaker and B. A. Bushaw, Chem. Phys. Lett. **79**, 506 (1981).

[27] K. Niemax, Appl. Phys. B **32**, 59 (1983).

[28] M. G. Payne *et al.*, Phys. Rev. Lett. **35**, 1154 (1975).

[29] I. D. Moore *et al.*, J. Phys. G **31**, S1499 (2005).

[30] R. Horn, Ph.D. thesis, Universität Mainz, 2003.

[31] C. Rauth, Diploma thesis, Universität Mainz, 2003.

[32] T. Kessler *et al.*, Hyperfine Interact. **171**, 121 (2006).

[33] F. Canova *et al.*, in *Laser-Induced Damage in Optical Materials: 2005. Proceedings of the SPIE*, edited by G. J. Exarhos *et al.* (SPIE, Boulder, CO, USA, 2005), No. 1, p. 599123.

[34] V. I. Mishin *et al.*, Nucl. Instrum. Methods Phys. Res., Sect. B **73**, 550 (1993).

[35] V. Fedosseev *et al.*, Hyperfine Interact. **162**, 15 (2006).

[36] L. Fraile, Eur. Phys. J. A **25**, 723 (2005).

[37] B. Tordoff, Ph.D. thesis, University of Manchester, 2006.

[38] F. Kneubühl and M. Sigrist, *Laser* (Teubner, Wiesbaden, 2005).

[39] R. Seiler, T. Paul, M. Andrist, and F. Merkt, Rev. Sci. Instrum. **76**, 103103 (2005).

[40] J. C. Barnes, N. P.and Barnes, IEEE J. Quantum. Electron. **29**, 2670 (1993).

[41] S. Hannemann, E. J. van Duijn, and W. Ubachs, Rev. Sci. Instrum. **78**, 103102 (2007).

[42] P. Dupre and T. A. Miller, Rev. Sci. Instrum. **78**, 033102 (2007).

[43] P. Brockman *et al.*, Opt. Lett. **11**, 712 (1986).

[44] G. A. Rines and P. F. Moulton, Opt. Lett. **15**, 434 (1990).

[45] T. D. Raymond and A. V. Smith, Opt. Lett. **16**, 33 (1991).

[46] T. Kessler *et al.*, Las. Phys. **18**, 842 (2008).

[47] A. E. Siegman, *Lasers* (University Science Books, Hampshire, UK, 1986).

[48] Wolfram Research, Inc., *Mathematica 6*, Champaign, Illinois, 2007.

[49] L. Ricci *et al.*, Opt. Commun. **117**, 541 (1995).

[50] A. Kasapi, G. Y. Yin, and M. Jain, Appl. Opt. **35**, 1999 (1996).

[51] B. A. Bushaw, B. D. Cannon, G. K. Gerke, and T. J. Whitaker, Opt. Lett. **11**, 422 (1986).

[52] J. Lettry *et al.*, Nucl. Instrum. Methods Phys. Res., Sect. B **204**, 363 (2003).

[53] Y. Liu, Resonant ionization of Cu in a hot-cavity laser ion source with Ti:Sapphire lasers, Manuscript in preparation.

[54] M. Facina, Ph.D. thesis, IKS Leuven, 2004.

[55] Y. Kudryavtsev *et al.*, Nucl. Instrum. Methods Phys. Res., Sect. B **179**, 412 (2001).

[56] J. F. McCann, J. Pezy, and P. Wilsen, J. Phys. E: Sci. Instrum. **15**, 322 (1982).

[57] K. Singer *et al.*, Rev. Sci. Instrum. **73**, 4402 (2002).

[58] P. Müller *et al.*, Radiochim. Acta **88**, 487 (2000).

[59] J. Hakala *et al.*, Nucl. Instrum. Methods Phys. Res., Sect. B **In Press, Accepted Manuscript**, doi:10.1016/j.nimb.2008.05.086 (2008).

[60] COMSOL AB, *COMSOL Multiphysics 3.4*, Stockholm, Sweden, 2007.

[61] J. Äystö, Nucl. Phys. A **693**, 477 (2001).

[62] J. Huikari *et al.*, Nucl. Instrum. Methods Phys. Res., Sect. B **222**, 632 (2004).

[63] P. Karvonen *et al.*, Eur. Phys. J. - Special Topics **150**, 283 (2007).

[64] P. Van Duppen, Nucl. Instrum. Methods Phys. Res., Sect. B **126**, 66 (1997).

[65] Y. Kudryavtsev *et al.*, Nucl. Phys. A **701**, 465 (2002).

[66] Y. Kudryavtsev *et al.*, Nucl. Instrum. Methods Phys. Res., Sect. B **204**, 336 (2003).

[67] L. Vermeeren *et al.*, Phys. Rev. Lett. **73**, 1935 (1994).

[68] P. Van Duppen *et al.*, Hyperfine Interact. **127**, 401 (2000).

[69] I. D. Moore *et al.*, in *Frontiers in Nuclear Structure, Astrophysics, and Reactions*, No. 1 in *American Institute of Physics Conference Series*, edited by S. V. Harissopulos, P. Demetriou, and R. Julin (AIP, Isle of Kos (Greece), 2006), pp. 511–513.

[70] K. Blaum *et al.*, Nucl. Instrum. Methods Phys. Res., Sect. B **204**, 331 (2003).

[71] J. F. Ziegler, J. Appl. Phys. **85**, 1249 (1999).

[72] H. Bethe, Ann. Phys. **397**, 325 (1930).

[73] F. Bloch, Z. Phys. A. **81**, 363 (1933).

[74] L. C. Northcliffe, Annu. Rev. Nuc. Sci. **13**, 67 (1963).

[75] C. Scheidenberger *et al.*, Nucl. Instrum. Methods Phys. Res., Sect. B **142**, 441 (1998).

[76] O. Tarasov, D. Bazin, M. Lewitowicz, and O. Sorlin, Nucl. Phys. A **701**, 661 (2002).

[77] J. F. Ziegler, *The Stopping Range of Ions in Solids* (Pergamon Pr, Oxford, 1985).

[78] L. P. Ekström and R. B. Firestone, WWW Table of Radioactive Isotopes, database version 2/28/99, 2008.

[79] J. D. Anderson, *Modern compressible flow: With historical perspective* (McGraw-Hill Professional, New York, 2002), Vol. 3.

[80] O. Reynolds, P. Roy. Soc. Lond. (1854-1905) **35**, 84 (1883).

[81] G. P. Flynn, R. V. Hanks, N. A. Lemaire, and J. Ross, J. Chem. Phys. **38**, 15 (1963).

[82] J. Kestin *et al.*, J. Phys. Chem. Ref. Data **13**, 229 (1984).

[83] A. A. Pavelyev, A. I. Reshmin, S. K. Teplovodskii, and S. G. Fedoseev, Fluid Dyn. **38**, 545 (2003).

[84] K. Peräjärvi *et al.*, Nucl. Instrum. Methods Phys. Res., Sect. A **449**, 427 (2000).

[85] K. Peräjärvi, Ph.D. thesis, University of Jyväskylä, 2001.

[86] M. Winter, Webelements.com, `http://www.webelements.com/webelements/elements/text/K/heat.html`, access on 28.08.2007.

[87] T. Kessler *et al.*, Nucl. Instrum. Methods Phys. Res., Sect. B **266**, 681 (2008).

[88] R. Béraud *et al.*, Nucl. Instrum. Methods Phys. Res., Sect. A **346**, 196 (1994).

[89] P. Dendooven *et al.*, Nucl. Instrum. Methods Phys. Res., Sect. A **408**, 530 (1998).

[90] J. B. Neumayr *et al.*, Nucl. Instrum. Methods Phys. Res., Sect. B **244**, 489 (2006).

[91] B. Marsh, Ph.D. thesis, University of Manchester, 2007.

[92] P. Karvonen *et al.*, Nucl. Instrum. Methods Phys. Res., Sect. B **In Press, Accepted Manuscript**, doi:10.1016/j.nimb.2008.07.022 (2008).

[93] R. Courant and K. O. Friedrichs, *Supersonic Flow and Shock Waves*, Vol. 21 of *Applied Mathematical Sciences* (Springer, Berlin, New York, 1999).

[94] M. Rasi, R. Saintola, and K. Valli, Nucl. Instrum. Methods Phys. Res., Sect. A **378**, 251 (1996).

[95] A. Vogler, Research on freely expanding gasjets from ion guide nozzles, 2006, internal Report.

[96] The MathWorks, Inc., *MatLab R2007b*, Natick, MA 01760-2098, USA, 2007.

[97] J. A. Inman, P. M. Danehy, R. J. Nowak, and D. W. Alderfer, Technical report, American institue of Aeronautics and Astronautics (unpublished).

[98] F. Paschen, Ann. Phys. **273**, 69 (1889).

[99] K. T. A. L. Burm, Contrib. Plasma Phys. **47**, 177 (2007).

[100] J. D. Cobine, *Gaseous conductors: Theory and engineering applications* (Dover Publications, New York, 1958).

[101] M. A. Hassouba, F. F. Elakshar, and A. A. Garamoon, FIZIKA A **11**, 81 (2002).

[102] H. Okubo *et al.*, IEEE T. Dielect. El. In. **4**, 450 (Aug 1997).

[103] M. L. Norman and K. H. Winkler, Los Alamos Science **12**, 46 (1985).

[104] A. Iivonen *et al.*, Nucl. Instrum. Methods Phys. Res., Sect. A **307**, 69 (1991).

[105] J. Rienitz, Nature **254**, 293 (1975).

[106] V. Gopal *et al.*, Eur. J. Phys. **29**, 607 (2008).

[107] P. L. Eggins and D. A. Jackson, J. Phys. D **7**, 1894 (1974).

[108] M. Bylina, Master's thesis, Warsaw University, 2007.

[109] J. Kurpeta, private communication.

[110] I. Mukha *et al.*, Eur. Phys. J. A **25**, 131 (2005).

[111] M. La Commara et al., Nucl. Phys. A **708**, 167 (2002).

[112] I. Mukha *et al.*, Phys. Rev. Lett. **95**, 022501 (2005).

[113] L. Batist et al., Nucl. Phys. A **720**, 245 (2003).

[114] I. Mukha *et al.*, Phys. Rev. C: Nucl. Phys. **70**, 044311 (2004).

[115] I. Mukha *et al.*, Nature **439**, 298 (2006).

[116] J. Äystö, Nature **439**, 279 (2006).

[117] U. Koster, V. N. Fedoseyev, and V. I. Mishin, Spectrochim. Acta, Part B **58**, 1047 (2003).

[118] R. Kirchner, K. H. Burkard, W. Huller, and O. Klepper, Nucl. Instrum. Methods **186**, 295 (1981).

[119] R. Kirchner and E. Roeckl, Nucl. Instrum. Methods **127**, 307 (1975).

[120] R. Kirchner, Nucl. Instrum. Methods Phys. Res., Sect. B **26**, 204 (1987).

[121] R. Kirchner *et al.*, Nucl. Instrum. Methods Phys. Res., Sect. A **247**, 265 (1986).

[122] R. Kirchner, Nucl. Instrum. Methods Phys. Res., Sect. B **70**, 186 (1992).

[123] T. Kessler *et al.*, Nucl. Instrum. Methods Phys. Res., Sect. B **In Press, Accepted Manuscript**, doi:10.1016/j.nimb.2008.05.030 (2008).

[124] T. Kessler *et al.*, J. Phys. B **40**, 4413 (2007).

[125] T. Gottwald *et al.*, Nucl. Instrum. Methods Phys. Res., Sect. B **In Press, Accepted Manuscript**, doi:10.1016/j.nimb.2008.05.059 (2008).

[126] Y. Liu, Rev. Sci. Instrum. **Accepted Manuscript**, (2008).

[127] K. Wies, Ph.D. thesis, University of Mainz, 2006.

[128] J. Barth, Diploma thesis, University of Mainz, 2005.

[129] R. L. Kurucz, P. L. Smith, C. Heise, and J. R. Esmond, Kurucz Atomic spectral line database, `http://www.pmp.uni-hannover.de/cgi-bin/ssi/test/kurucz/sekur.html`, access on 28.08.2007.

[130] Y. Ralchenko, A. E. Kramida, and J. Reader, `http://physics.nist.gov/PhysRefData/ASD/index.html`, access on 28.08.2007.

[131] F. Scheerer, F. Albus, F. Ames, and H. J. Kluge, Spectrochim. Acta, Part B **47**, 793 (1992).

[132] I. D. Moore *et al.*, Hyperfine Interact. **171**, 135 (2006).

[133] B. Bühler, C. Cremer, and G. Gerber, Z. Phys. A: Hadrons Nucl. **320**, 71 (1985).

[134] B. Tordoff *et al.*, Hyperfine Interact. **171**, 197 (2006).

[135] B. Tordoff *et al.*, Nucl. Instrum. Methods Phys. Res., Sect. B **252**, 347 (2006).

[136] S. G. Johnson, B. L. Fearey, C. M. Miller, and N. S. Nogar, Spectrochim. Acta, Part B **47**, 633 (1992).

[137] J. C. Hardy and I. S. Towner, Phys. Rev. C **71**, 055501 (2005).

[138] I. S. Towner and J. C. Hardy, Phys. Rev. C **77**, 025501 (2008).

[139] T. Eronen *et al.*, Phys. Rev. Lett. **100**, 132502 (2008).

[140] S. Rahaman *et al.*, Phys. Lett. B **662**, 111 (2008).

[141] N. Trautmann and H. Folger, Nucl. Instrum. Methods Phys. Res., Sect. A **282**, 102 (1989).

[142] B. N. L. National Nuclear Data Center, Nuclear Wallet Cards 7th edition, `http://www.nndc.bnl.gov/wallet/wccurrent.html`, 2008.

[143] C. E. Moore, in *Atomic Energy Levels*, edited by Natl. Bur. Stand. (U.S.), Circ. 467 (U.S. Government Printing Office, Washington, DC, 1958), Vol. 3.

[144] P. Palmeri and J. F. Wyart, J. Quant. Spectrosc. Radiat. Transfer **61**, 603 (1999).

[145] U. Hager *et al.*, Phys. Rev. Lett. **96**, 042504 (2006).

[146] P. Campbell *et al.*, Phys. Rev. Lett. **89**, 082501 (2002).

[147] A. Kankainen *et al.*, Eur. Phys. J. A **29**, 271 (2006).

[148] T. H. R. Hirata, Hirata Atomic Spectral Line List, `http://cdsweb.u-strasbg.fr/viz-bin/VizieR?-source=VI/69`, 2007.

[149] J. Nolen, Nucl. Phys. A **734**, 661 (2004).

[150] Y. Liu *et al.*, Particle Accelerator Conference, 2005. PAC 2005. Proceedings of the 1640 (2005).

[151] T. Ishikawa, J. Appl. Phys. **87**, 7617 (2000).

[152] W. Ritz, Phys. Z. **4**, 406 (1903).

[153] R. Jastrow, Phys. Rev. **73**, 60 (1948).

[154] D. Hartree, Proc. Camb. Phil. Soc. **24**, 426 (1928).

[155] D. T. Rooney and J. Chaiken, J. Chem. Phys. **93**, 466 (1990).

[156] P. S. Epstein, Ann. Phys. **355**, 489 (1916).

[157] E. Schrödinger, Ann. Phys. **385**, 437 (1926).

[158] J. A. C. Gallas, H. Walther, and E. Werner, Phys. Rev. A **26**, 1775 (1982).

[159] M. L. Zimmerman, M. G. Littman, M. M. Kash, and D. Kleppner, Phys. Rev. A **20**, 2251 (1979).

[160] M. L. Zimmerman, T. W. Ducas, M. G. Littman, and D. Kleppner, J. Phys. B **11**, L11 (1978).

[161] A. König, J. Neukammer, H. Hieronymus, and H. Rinneberg, Phys. Rev. A **43**, 2402 (1991).

[162] T. W. Ducas and M. L. Zimmerman, Phys. Rev. A **15**, 1523 (1977).

[163] G. S. Agarwal, J. Cooper, S. L. Haan, and P. L. Knight, Phys. Rev. Lett. **56**, 2586 (1986).

[164] C. E. Theodosiou, Phys. Rev. A **30**, 2881 (1984).

[165] S. Kunze *et al.*, Z. Phys. D: Atom. Mol. Cl. **27**, 111 (1993).

[166] L. Weissman *et al.*, Phys. Rev. C **65**, 024315 (2002).

[167] T. G. Cooper, J. Billowes, P. Campbell, and M. R. Pearson, J. Phys. G **22**, 99 (1996).

[168] H. B. G. Casimir, *On the interaction between atomic nuclei and electrons* (W. H. Freeman and Company, Haarlem, 1963).

[169] J. Billowes and P. Campbell, J. Phys. G **21**, 707 (1995).

[170] E. Otten, in *Treatise on Heavy-Ion science*, edited by D. Bromley (Plenum Press, New York, 1989), Vol. 8, p. 517.

[171] B. Cheal *et al.*, Phys. Lett. B **645**, 133 (2007).

[172] A. Nieminen *et al.*, Phys. Rev. Lett. **88**, 094801 (2002).

[173] P. Campbell *et al.*, Phys. Rev. Lett. **89**, 082501 (2002).

[174] P. Campbell, Hyperfine Interact. **171**, 143 (2006).

[175] University of Jyväskylä, JYFL Annual Report, 2007.

[176] G. K. Koyanagi, D. Caraiman, V. Blagojevic, and D. K. Bohme, J. Phys. Chem. A **106**, 4581 (2002).

[177] V. G. Anicich, Jet Propulsion Laboratory Publication **03**, 1 (2003).

[178] D. K. Bohme, private communication.

[179] P. Dendooven, S. Purushothaman, and K. Gloos, Nucl. Instrum. Methods Phys. Res., Sect. A **558**, 580 (2006).

[180] M. Facina *et al.*, Nucl. Instrum. Methods Phys. Res., Sect. B **226**, 401 (2004).

[181] E. W. McDaniel, *Collision phenomena in ionized gases* (John Wiley & Sons, New York, 1964).

[182] B. H. Mahan, J. Chem. Phys. **43**, 3080 (1965).

[183] J. J. Thomson, Phil. Mag. **47**, 337 (1924).

[184] L. P. Pitaevskii, Soviet Physics-JETP **15**, 919 (1962).

[185] D. R. Bates and S. P. Khare, Proc. Phys. Soc. **85**, 231 (1965).

[186] D. R. Bates, J. Phys. B **17**, 2363 (1984).

[187] R. J. van Sonsbeek, R. Cooper, and R. N. Bhave, J. Chem. Phys. **97**, 1800 (1992).

[188] R. Cooper, R. J. van Sonsbeek, and R. N. Bhave, J. Chem. Phys. **98**, 383 (1993).

[189] F. Sauli, in *Experimental Techniques in High-Energy Nuclear and Particle Physics*, edited by T. Ferbel (World Scientific, Singapore, 1991).

[190] H. S. W. Massey, *Atomic and Molecular Collisions* (Taylor & Francis Ltd, London, 1979).

[191] I. D. Moore *et al.*, Nucl. Instrum. Methods Phys. Res., Sect. B **Manuscript in preparation**, (2008).

[192] Y. Kudryavstev, private communication.

[193] D. M. Bartell, G. S. Hurst, and E. B. Wagner, Phys. Rev. A **7**, 1068 (1973).

[194] N. Thonnard and G. S. Hurst, Phys. Rev. A **5**, 1110 (1972).

[195] G. S. Hurst, T. E. Stewart, and J. E. Parks, Phys. Rev. A **2**, 1717 (1970).

[196] A. Takamine *et al.*, Rev. Sci. Instrum. **76**, 103503 (2005).

[197] I. D. Moore, Nucl. Instrum. Methods Phys. Res., Sect. B **In Press, Accepted Manuscript**, doi:10.1016/j.nimb.2008.05.054 (2008).

[198] J. Billowes and P. Campbell, Hyperfine Interactions **129**, 289 (2000).

[199] A. Bogaerts and R. Gijbels, J. Appl. Phys. **92**, 6408 (2002).

[200] N. Baguer, A. Bogaerts, and R. Gijbels, J. Appl. Phys. **93**, 47 (2003).

[201] A. Bogaerts and R. Gijbels, Phys. Rev. A **52**, 3743 (1995).

[202] A. Bogaerts, R. Gilbels, and G. Jackson, J. Anal. At. Spectrom. **18**, 533 (2003).

[203] A. Bogaerts, J. Anal. At. Spectrom. **22**, 502 (2007).

List of publications

[1] T. Kessler, H. Tomita, C. Mattolat, S. Raeder, and K. Wendt. An injection seeded high repetition rate Ti:sapphire laser for high-resolution spectroscopy and trace analysis of rare isotopes. *Las. Phys.*, 18(7):842–849, July 2008.

[2] T. Kessler, I. D. Moore, H. Penttilä, F. Quinquis, and J. Äystö. Towards on-line production of $N = Z$ ^{94}Ag at IGISOL. *Nucl. Instrum. Methods Phys. Res., Sect. B*, In Press, Accepted Manuscript:doi:10.1016/j.nimb.2008.05.030, 2008.

[3] T. Kessler, T. Eronen, C. Mattolat, I. D. Moore, K. Peräjärvi, P. Ronkanen, P. Thörle, B. Tordoff, N. Trautmann, K. Wendt, K. Wies, and J. Äystö. Upgrade to the IGISOL laser ion source towards spectroscopy on Tc. *Hyperfine Interact.*, 171(1):121–126, July 2006.

[4] T. Kessler, K. Brück, C. Baktash, J. R. Beene, Ch. Geppert, C. C. Havener, H. F. Krause, Y. Liu, D. R. Schultz, D. W. Stracener, C. R. Vane, and K.Wendt. Three-step resonant photoionization spectroscopy of Ni and Ge: ionization potential and odd-parity Rydberg levels. *J. Phys. B*, 40(23):4413–4432, 2007.

[5] T. Kessler, I. D. Moore, Y. Kudryavtsev, K. Peräjärvi, A. Popov, P. Ronkanen, T. Sonoda, B. Tordoff, K. D. A. Wendt, and J. Äystö. Off-line studies of the laser ionization of yttrium at the IGISOL facility. *Nucl. Instrum. Methods Phys. Res., Sect. B*, 266(4):681–700, February 2008.

[6] I. D. Moore, T. Kessler, Yu. Kudryavstev, K. Peräjärvi, A. Popov, P. Ronkanen, T. Sonoda, B. Tordoff, K. D. A. Wendt, and J. Äystö. On-line studies with laser ionization and the first stopped primary beams at IGISOL. *Nucl. Instrum. Methods Phys. Res., Sect. B*, Manuscript in preparation, 2008.

[7] P. Karvonen, T. Sonoda, I. D. Moore, J. Billowes, A. Jokinen, T. Kessler, B. Marsh, H. Penttilä, A Popov, B. Tordoff, and J. Äystö. A sextupole ion beam guide to improve the efficiency and beam quality at IGISOL. *Nucl. Instrum. Methods Phys. Res., Sect. B*, In Press, Accepted Manuscript:doi:10.1016/j.nimb.2008.07.022, 2008.

[8] B. Cheal, K. Baczynska, J. Billowes, P. Campbell, T. Eronen, D. Forest, T. Kessler, I. D. Moore, M. Rüffer, B. Tordoff, G. Tungate, and J. Äystö. Laser pumping of ions in a cooler buncher. *Hyperfine Interact.*, In Press, Accepted Manuscript:doi:10.1007/s10751–008–9629–5, 2008.

[9] B. Cheal, J. Billowes, P. Campbell, B. Tordoff, T. Eronen, A. Jokinen, T. Kessler, I. D. Moore, H. Penttilä, J. Äystö, K. Baczynska, M. L. Bissell, D. H. Forest, M. D. Gardner, M. Rüffer, and G. Tungate. Laser spectroscopy and the nature of the shape transition at $N = 60$. *Proceedings of the Fourth International Conference on Fission and Properties of Neutron-Rich Nuclei, Sanibel Island 2007*, In Press, Accepted Manuscript, 2008.

[10] T. Gottwald, C. Geppert, F. Schwellnus, K. Wies, K. Wendt, Y. Liu, C. Baktash, J. R. Beene, C. C. Havener, H. F. Krause, D. R. Schultz, D. W. Stracener, C. R. Vane, T. Kessler, and B. Tordoff. Optical spectroscopy and performance tests with a solid state laser ion source at HRIBF. *Nucl. Instrum. Methods Phys. Res., Sect. B*, In Press, Accepted Manuscript:doi:10.1016/j.nimb.2008.05.059, 2008.

[11] V. V. Elomaa, T. Eronen, U. Hager, A. Jokinen, T. Kessler, I. D. Moore, S. Rahaman, C. Weber, and J. Äystö. Development of a carbon-cluster ion source for JYFLTRAP. *Nucl. Instrum. Methods Phys. Res., Sect. B*, In Press, Accepted Manuscript:doi:10.1016/j.nimb.2008.05.029, 2008.

[12] Y. Liu. Emittance Characterization of a Hot-Cavity Laser Ion Source at HRIBF. *Rev. Sci. Instrum.*, Accepted Manuscript, 2008.

[13] Y. Liu. Resonant ionization of Cu in a hot-cavity laser ion source with Ti:Sapphire lasers. Manuscript in preparation.

[14] H. Tomita, C. Mattolat, T. Kessler, F. Schwellnus, S. Raeder, K. D. A. Wendt, N. Trautmann, K. Watanaba, and T. Iguichi. Ultra Trace Determination Scheme for ^{26}Al by High-Resolution Resonance Ionization Mass Spectrometry using a Pulsed Ti:Sapphire Laser. *J. Nucl. Sci. Tech.*, In Press, Accepted Manuscript, 2008.

[15] K. Post and H. Mach. Precise lifetime measurement of the 192.3-keV state in ^{104}Mo. *Phys. Rev. C*, Accepted Manuscript, 2008.

[16] D. L. Smith, H. Mach, H. Penttila, H. Bradley, J. Aysto, V.-V. Elomaa, T. Eronen, D. G. Ghita, J. Hakala, M. Hauth, A. Jokinen, P. Karvonen, T. Kessler, W. Kurcewicz, H. Lehmann, I. D. Moore, J. Nyberg, S. Rahaman, J. Rissanen, J. Ronkainen, P. Ronkanen, A. Saastamoinen, T. Sonoda, O. Steczkiewicz, and C. Weber. Lifetime Measurements of the negative parity 7^- and 8^- states in ^{122}Cd. *Phys. Rev. C*, 77(1):014309, 2008.

[17] H. Penttilä, J. Äystö, V. V. Elomaa, T. Eronen, D. Gorelov, U. Hager, J. Hakala, A. Jokinen, A. Kankainen, P. Karvonen, T. Kessler, I. D. Moore, S. Rahaman, S. Rinta-Antila, V. Rubchenya, and T. Sonoda. Independent fission yields with JYFLTRAP. *Eur. Phys. J. - Special Topics*, 150(1):317–318, November 2007.

[18] P. Karvonen, T. Sonoda, I. D. Moore, J. Billowes, A. Jokinen, T. Kessler, H. Penttilä, A. Popov, B. Tordoff, and J. Äystö. LIST developments at IGISOL. *Eur. Phys. J. - Special Topics*, 150(1):283–284, November 2007.

[19] B. Tordoff, T. Eronen, V. V. Elomaa, S. Gulick, U. Hager, P. Karvonen, T. Kessler, J. Lee, I. D. Moore, A. Popov, S. Rahaman, S. Rinta-Antila, T. Sonoda, and J. Äystö. An ion guide for the production of a low energy ion beam of daughter products of α-emitters. *Nucl. Instrum. Methods Phys. Res., Sect. B*, 252(2):347–353, November 2006.

[20] B. Tordoff, J. Billowes, P. Campbell, B. Cheal, D. Forest, T. Kessler, J. Lee, I. D. Moore, A. Popov, G. Tungate, and J. Äystö. Investigation of the low-lying isomer in ^{229}Th by collinear laser spectroscopy. *Hyperfine Interact.*, 171(1):197–201, July 2006.

[21] I. D. Moore, T. Kessler, J. Äystö, J. Billowes, P. Campbell, B. Cheal, B. Tordoff, M. Bissel, and G. Tungate. Resonance ionization spectroscopy of bismuth at the IGISOL facility. *Hyperfine Interact.*, 171(1):135–141, July 2006.

[22] I. D. Moore, J. Billowes, P. Campbell, T. Eronen, C. Geppert, A. Jokinen, P. Karvonen, T. Kessler, B. Marsh, A. Nieminen, H. Penttilä, S. Rinta-Antila, T. Sonoda, B. Tordoff, K. Wendt, and J. Äystö. Laser Ion Source Development at IGISOL. In S. V. Harissopulos, P. Demetriou, and R. Julin, editors, *Frontiers in Nuclear Structure, Astrophysics, and Reactions*, volume 831 of *American Institute of Physics Conference Series*, pages 511–513, Isle of Kos (Greece), April 2006. AIP.

[23] Y. Liu, C. Baktash, J. R. Beene, H. Z. Bilheux, C. C. Havener, H. F. Krause, D. R. Schultz, D. W. Stracener, C. R. Vane, K. Brück, Ch. Geppert, T. Kessler, and K. Wendt. Laser ion source tests at the HRIBF on stable Sn, Ge and Ni isotopes. *Nucl. Instrum. Methods Phys. Res., Sect. B*, 243(2):442–452, February 2006.

[24] Y. Liu, C. Baktash, J. R. Beene, H.Z. Bilheux, C. C. Havener, H. F. Krause, D. R. Schultz, D. W. Stracener, C. R. Vane, K. Wendt, Ch. Geppert, T. Kessler, and K. Brück. Laser Ion Source Development for ISOL Systems at RIA. *Particle Accelerator Conference, 2005. PAC 2005. Proceedings of the*, pages 1640–1642, May 2005.

[25] I. D. Moore, A. Nieminen, J. Billowes, P. Campbell, Ch. Geppert, A. Jokinen, T. Kessler, B. Marsh, H. Penttilä, S. Rinta-Antila, B. Tordoff, K. D. A. Wendt, and J. Äystö. Development of a laser ion source at IGISOL. *J. Phys. G*, 31(10):S1499–S1502, 2005.

[26] A. Nieminen, I. D. Moore, J. Billowes, P. Campbell, K. Flanagan, Ch. Geppert, J. Huikari, A. Jokinen, T. Kessler, B. Marsh, H. Penttilä, S. Rinta-Antila, B. Tordoff, K. Wendt, and J. Äystö. Laser Ion Source Project at IGISOL. *Hyperfine Interact.*, 162(1):39–43, April 2005.

[27] T. Kessler. Optimierung eines Ti:Saphir-Lasersystems für den Einsatz an einer On-line-Ionenquelle - Spektroskopie an Zinn. Diploma thesis, University of Mainz, 2004.

ISSN 1054-660X, Laser Physics, 2008, Vol. 18, No. 7, pp. 1–8.

An Injection-Seeded High-Repetition Rate Ti:Sapphire Laser for High-Resolution Spectroscopy and Trace Analysis of Rare Isotopes

T. Kessler[a, b], H. Tomita[a, c], C. Mattolat[a], S. Raeder[a], and K. Wendt[a]

[a] *AG Larissa/Quantum, Institut für Physik, Johannes Gutenberg Universität, Staudinger Weg 7, D-55128 Mainz, Germany*
[b] *Department of Physics, University of Jyvaskyla, Survontie 9, Fi-40500 Jyväskylä, Finland*
[c] *Department of Quantum Engineering, Graduate School of Engineering, Nagoya University, Nagoya, Aichi 464-8603, Japan*
e-mail: thomas.kessler@phys.jyu.fi; tomita@avocet.nucl.nagoya-u.ac.jp; mattolat@uni-mainz.de;
sraeder@students.uni-mainz.de; kwendt@uni-mainz.de
Received January 20, 2008

Abstract—An injection-seeded high-repetition rate (~10 kHz) Ti:sapphire laser with a spectral bandwidth of ~20 MHz and an average output power of above 1.5 W has been developed. We report on its demonstration and characteristics with respect to the spectral, temporal, and spatial properties as well as the output energy. In crossed-beam resonance ionization on a well-collimated thermal atomic beam, the ~200 MHz hyperfine structure of the D_2 transition at 308 nm of ^{27}Al has been well resolved. Applications of the system in the field of in-source laser spectroscopy for on-line produced short-lived radioactive isotopes as well as for selective-trace isotope determination are discussed.

PACS numbers: 42.60.By, 42.62.Fi, 32.80.Fb, 82.80.d

DOI: 10.1134/S1054660X0807@@@@

INTRODUCTION

The well-established technique of resonance ionization spectroscopy (RIS) on atomic species using precisely tuned powerful laser radiation in a multistep excitation and the ionization process has entered various fields of physics in recent decades [1, 2]. Combined with a mass selective separation in the technique of the resonance ionization mass spectroscopy (RIMS), resonance ionization has been widely and successfully used for analytical applications, for example, for the trace analysis of very long-lived rare radioactive isotopes [3]. A second, more recent application of RIMS has been found in the development of elemental selective ion sources for on-line facilities for the production and investigation of exotic radioactive ions with the highest purity [4, 5].

In both fields, the choice of the appropriate laser system and its operational characteristics is crucial and strictly depends on the individual experimental setup. For the majority of analytical studies, in addition to the elemental selectivity, a high isotopic selectivity is also required. For this purpose, narrow bandwidth (~1 MHz) continuous-wave (cw) laser systems must be used, delivering only a low power yet permitting the resolution of isotope shifts and a hyperfine structure in high-resolution spectroscopy. To ensure a highest sensitivity in trace detection, or, alternatively, a high efficiency of an on-line resonance ionization laser ion source (RILIS), a sufficiently high laser power is imperative to ensure the saturation of each individual excitation step. Therefore, powerfully pulsed laser systems, usually operating in a high-repetition rate mode (~kHz regime) with small duty cycle losses, are most suitable to minimize the ionization efficiency losses. The spectral line width of these laser systems is typically on the order of a few GHz. On the one hand, this is by far sufficient to select an element; however, on the other hand, this value most often does not permit the resolution of isotope shifts or a hyperfine structure in optical transitions. In pulsed-laser RIMS, isotope selection is thus usually only provided through the different isotopic masses within the subsequent mass-selective ion detection system, e.g., a magnetic sector field of a high-transmission mass separator or a quadrupole-mass spectrometer in an analytical device.

Direct laser spectroscopy in an on-line ion source has recently been demonstrated at ISOLDE, CERN, where the different transition frequencies of individual hyperfine structure components of the nuclear ground (g) and isomeric (m) states in $^{68g,\,m}$Cu and $^{70g,\,m1,\,m2}$Cu could be used to determine the magnetic moments of both nuclei [6]. In this case, conventional pulsed-dye lasers were used for the selection and to separate the lines with a spectral resolution of about 4 GHz. For higher spectral resolution, usually pulsed-dye amplifiers (PDA) are in use as, for example, discussed in [7]. Their rather simple design comprises a single-pass amplification of a narrow bandwidth continuous-wave laser radiation in a series of dye cells, which have been inverted by an intense-pump laser pulse. The spectral bandwidth reduction of pulsed Ti:sapphire lasers would be of similar importance. Seeded Ti:sapphire multipass

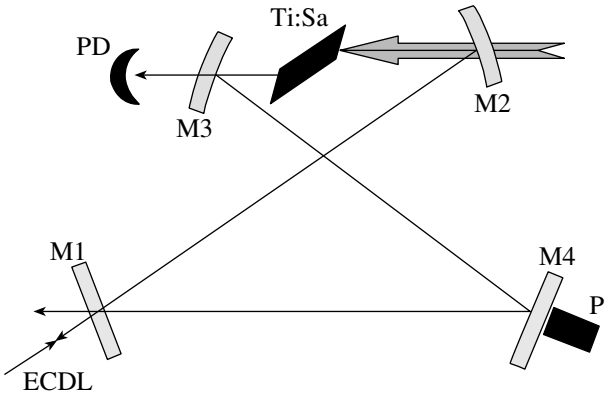

Fig. 1. Schematic diagram of the cavity geometry. Explanations and abbreviations are given in the text.

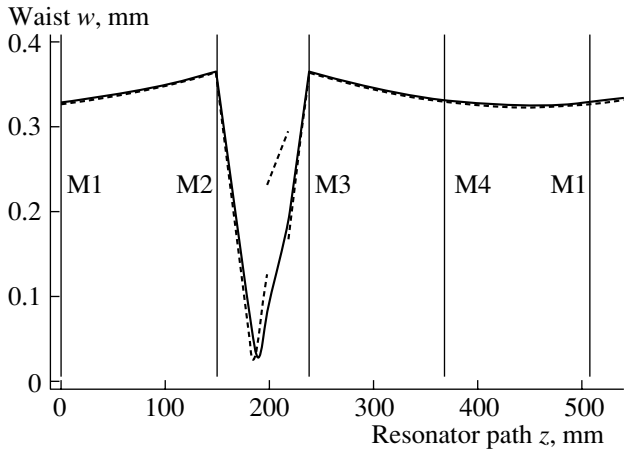

Fig. 2. ABCD calculation of the mode in the bow-tie cavity. The vertical lines mark the positions of the mirrors along one resonator roundtrip. The dashed and solid lines represent the waist of the laser mode in the tangential and sagittal planes, respectively. The former exhibits a discontinuity at the entrance and exit of the Ti:sapphire crystal due to the Brewster cut.

amplifiers, similar in design to the standard PDA layout, have been developed [8]. However, due to the long lifetime of the Ti:sapphire excited-laser level and the resulting comparably low optical cross section for the stimulated emission, this method is not well suited for the high-repetition rate operation in the 10-kHz range. In contrast, the injection seeding of a pulsed Ti:sapphire laser with a narrow bandwidth radiation from a continuous-wave laser can be applied. This approach has been demonstrated in various publications [9–13], again generally concerning low-repetition rate systems below 1 kHz. The higher harmonic generation of a seeded Ti:sapphire laser radiation is reported in [14] and is vital, e.g., for the RIS applications by extension of the wavelength coverage of the Ti:sapphire laser towards the blue, ultraviolet, and vacuum ultraviolet region of the electromagnetic spectrum.

In this work, we report on the injection seeding of a high-repetition rate Ti:sapphire laser system by a continuous-wave diode laser. At a repetition rate of 7 kHz, a spectral bandwidth of 20 MHz and an average output power of 1.5 W was achieved, satisfying the need for both the ionization efficiency, and the required resolution for spectroscopic applications on continuously evaporated thermal atomic beams. In our setup, the accessible wavelength range was extended by the third-harmonic generation from a fundamental wavelength of 924 nm, using nonlinear crystals for frequency doublings towards 462 nm and the subsequent frequency mixing with the fundamental towards 308 nm. For the characterization of the performance of the injection-seeding process, high-resolution laser spectroscopy on the hyperfine structure of 27A1 using the strong D2 line at 308 nm was performed in a Doppler-reduced crossed-beam setup. Photo ions were detected following the nonresonant ionization using frequency-doubled Ti:sapphire light.

EXPERIMENTAL SETUP

In this section, the basic design of the injection-seeded pulsed Ti:sapphire (slave) laser resonator and the coupling to the continuous-wave diode (master) laser is presented. First, development steps were carried out using a conventional z-shaped linear standing-wave resonator design [15]. Due to the spatial hole burning in the standing-wave cavity, the complete suppression of neighboring longitudinal modes appearing at a distance of ±300 MHz, determined by the reciprocal resonator roundtrip time, is not possible. To avoid this effect, a standard bow-tie ring resonator design was chosen as the slave cavity. The geometry of this traveling wave resonator cavity is shown in Fig. 1. The cavity is formed by two curved mirrors (radius of curvature 75 mm) M2 and M3, and two flat mirrors, M1 and M4. M1 serves as the output coupler with a reflectivity of 80%. The mirror set is coated for a wavelength range from 890 to 1050 nm. A 20-mm-long Ti:sapphire laser crystal with an optical density of $\alpha = 1.5$ cm^{-1}, positioned between the two curved mirrors, was pumped through M2 by the second harmonic at 532 nm of a high-repetition rate Nd:YAG laser. The pump beam with an average input power of 15 W and a temporal pulse duration of 300 ns was focused onto the crystal by a $f = 85$ mm lens. Due to the lack of a sufficient pump power, the repetition rate was reduced from the typically used 10 to 7 kHz, which correspondingly increases the pulse energy by a factor of about 1.4. The mode of the resonator cavity was simulated and optimized using the ABCD formalism [16]. The resulting mode envelope is depicted in Fig. 2 along the resonator roundtrip. The total cavity length amounts to roughly 50 cm resulting in a roundtrip time of 1.7 ns. The total dimensions of the

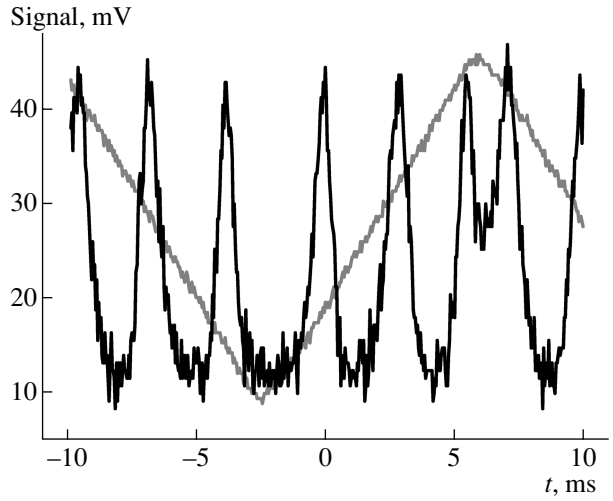

Fig. 3. Fringe pattern of the Ti:sapphire cavity during the resonator scan. The triangular grey line illustrates the applied ramp voltage to the piezoactuator.

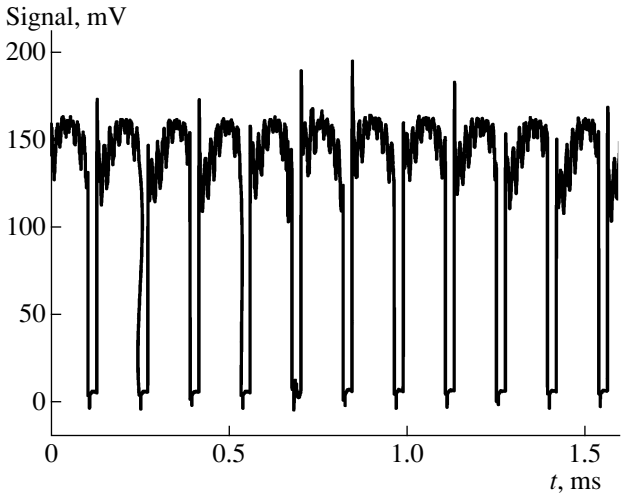

Fig. 4. Photodiode signal for the Ti:sapphire cavity in the mode-locked operation.

compact cavity design are approximately 100 × 140 mm.

The external-cavity diode laser (ECDL) beam is injected via the output coupler (M1) into the slave cavity and is protected from the optical feedback by three consecutive optical isolators with a total suppression of 160 dB in the reverse direction.

The diode laser is locked to a commercial frequency stabilized helium-neon laser via the fringe-offset lock technique with a precision of typically 1 MHz limited by an acoustic jitter [17]. The Ti:sapphire cavity is locked to the diode-laser frequency via a standard dither lock system operating at 60 kHz [18]. This provides a negative feedback loop from a photodiode signal (PD) to a piezoactuator (P), which moves the flat mirror M4 accordingly. The quality factor of the cavity was determined by applying a ramp voltage to the piezoactuator and monitoring the photodiode voltage on an oscilloscope as shown in Fig. 3. The finesse of the cavity, defined as the ratio of its free spectral range divided by the FWHM of the cavity resonance, was determined to be $F \approx 6(1)$, corresponding to losses of ~40(5)% in the cavity, i.e., twice the transmission of the output coupler. The lock was set to the top of the fringe to hold the cavity length in resonance with the diode laser frequency as shown in Fig. 4.

Upon the arrival of the Ti:sapphire pulse, the photodiode and amplifier were electronically shortened for a duration of ~10 μs to avoid a charge buildup and a corresponding saturation by the intense Ti:sapphire laser light leaking through mirror M3. During that time, no photo signal was detected for the locking, which is visible in Fig. 4 as the baseline drops from ~150 to ~0 mV for about 20 each 140 μs. However, these regular 7-kHz dropout signals do not affect the error signal. For a more detailed description of the locking system, the reader is referred to [15].

CHARACTERIZATION OF THE LASER SYSTEM

The temporal structure of a laser pulse emitted by the free-running cavity was monitored on a fast photodiode as shown in Fig. 5. In addition, the pump laser pulse with a length of 300 ns is shown for comparison. The temporal pulse length of the ring laser is typically about 50 ns. The spatial profile was monitored by a commercial beam-profiler CCD camera (Ophir Beamstar-V-PCI) at a distance of 20 cm from the output coupler. A cut through the intensity pattern in the y and x direction is shown in Fig. 6 revealing a rather perfect TEM_{00} profile. Consequently, Gaussian fits give excellent agreement with the data. From the fit, the FWHM

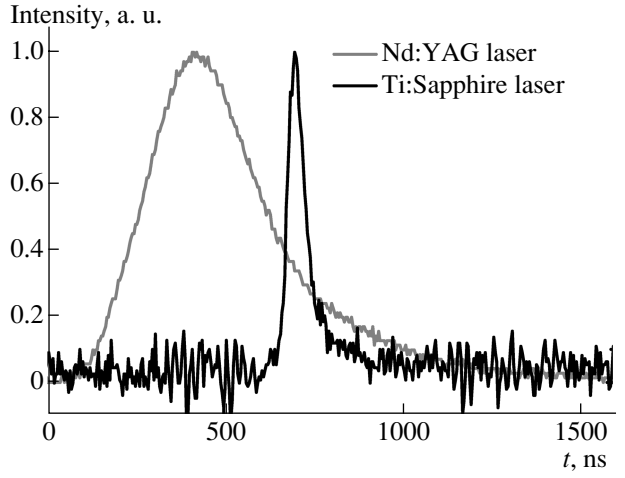

Fig. 5. Temporal pulse profile of the pump laser (FWHM ~ 300 ns) and seeded Ti:sapphire laser (FWHM ~50 ns).

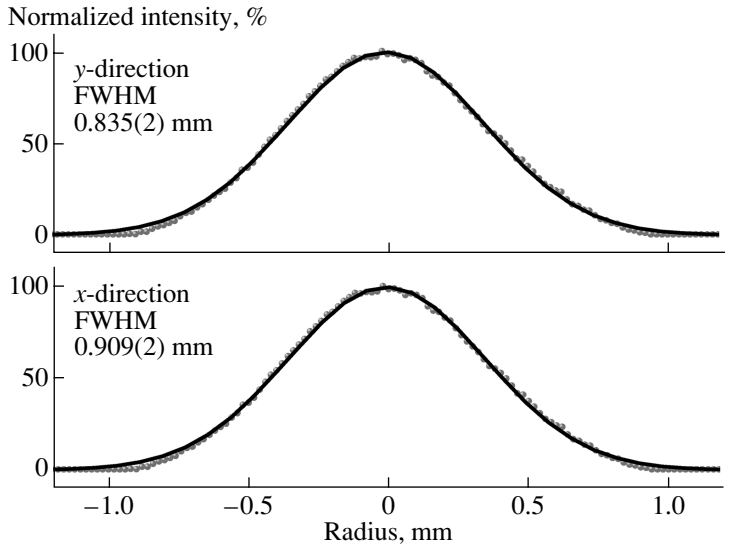

Fig. 6. Spatial profile of the Ti:sapphire laser together with Gaussian fits to the data.

beam waists are 0.835(2) and 0.909(2) mm in the y and x axes, respectively, exhibiting only a slight ellipticity due to the imperfect compensation of the astigmatism. As expected, the spatial profile is not affected by seeding the cavity.

The conversion efficiency of the Ti:sapphire laser is estimated from the gradient of the output power compared to the input Nd:YAG power as shown in Fig. 7. The conversion efficiency of the free-running laser is 9(2)% per the lasing direction, while 18(2)% is obtained unidirectionally during the injection seeding.

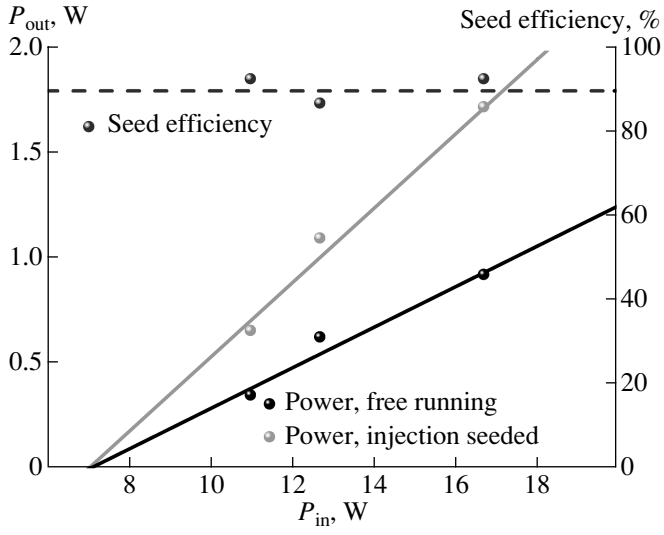

Fig. 7. Output power versus pump power of the Ti:sapphire laser in seeded and free-running operation mode and extracted-seed efficiency.

The absolute Ti:sapphire laser output power values (one-sided) for the input pump laser powers of 11, 13, and 17 W are given in Fig. 7, both for the free-running and seeded operation. The lasing threshold extracted from a linear fit is not affected in a measurable way by the seeding process. An average seed efficiency of $\varepsilon \approx 90\%$ is extracted from the data using the simple expression

$$\varepsilon = \frac{P_{\text{seed}}}{2P_{\text{unseed}}}. \quad (1)$$

Due to the well-adapted mode matching, the seed efficiency was saturated at a very low seeding power from the diode laser of about 0.5 mW.

In order to investigate the spectral bandwidth of the seeded Ti:sapphire, the laser was coupled into a confocal Fabry–Perot interferometer (FPI) with a free spectral range of ~300 MHz. The oscilloscope trace of the fringe pattern as well as the ramping voltage for the piezoactuator moving one of the FPI mirrors is shown in Fig. 8. From the resolved spectrum and the precisely known free spectral range of the FPI of 298, 111(12) MHz, the spectral bandwidth of the laser is determined to be 20(5) MHz. Figure 9 shows a detailed view of a single fringe. Due to the 7-kHz pulsed structure of the laser light and the slow ramping of the FPI (25 ms), the peak reveals a regular substructure determined by the temporal occurrence of the individual short laser pulses during the slow ramping of the FPI length. The individual pulses are clearly resolved by the fast photodiode, their envelope determines the spectral width.

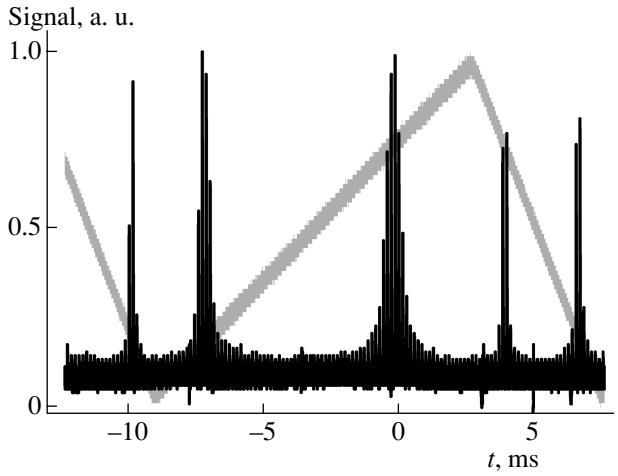

Fig. 8. Fringe pattern of the Ti:sapphire laser in the seeded-operation mode in a 300-MHz FPI. The ramping voltage of the FPI mirror is shown.

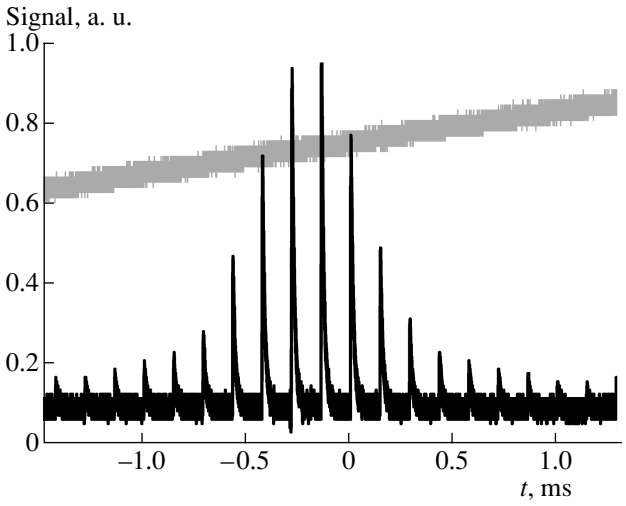

Fig. 9. Detailed view of a single FPI fringe exhibiting the occurrence of individual laser pulses during the slow FPI ramping.

SPECTROSCOPIC INVESTIGATION OF THE HYPERFINE STRUCTURE OF ^{27}Al

To demonstrate the suitability of the seeded Ti:sapphire laser for high-resolution spectroscopic applications, the well-known hyperfine structure of the only stable isotope of aluminum, ^{27}Al with nuclear spin I = 5/2, was investigated [19]. The strong D_2 transition from the $3s^2 3p\ ^2P_{3/2}$ atomic ground state to the $3s^2 3d\ ^2D_{3/2}$ excited level at 32 435.45 cm^{-1} was chosen as a benchmark test case, exhibiting a relatively small hyperfine structure splitting in the range of 300 MHz. Nonresonant laser ionization was performed using the residual frequency-doubled blue laser light at 462 nm from the frequency-tripling process for the ionization step. For the spectroscopy, the seeded Ti:sapphire laser was scanned over the hyperfine structure and photoions were detected as a function of the laser wavelength.

The required laser radiation at 308 nm was achieved by the sequential frequency doubling and tripling of the fundamental light (~924 nm) of the seeded Ti:sapphire laser using standard nonlinear optics. With an output power of approximately 1.5 W in the fundamental, ~150 mW of second-harmonic light was produced and ~10 mW in the third harmonic was available for the spectroscopy. To minimize the saturation and the resulting power broadening of the strong resonance transition, the power of the UV radiation was reduced to very low values of around ~0.3 mW. Thus, the trade-off between the signal strength, enhancing statistics, and resolution, determined by the experimental line width was optimized towards the latter to optimally prove the laser performance. Remaining nonconverted, the second-harmonic laser radiation was by far sufficient for the efficient nonresonant ionization from the excited state above the ionization potential (I.P.) at 48278.38 cm^{-1}. The scheme and the hfs structure are shown in Fig. 10.

Measurements were performed in a crossed-beam geometry as illustrated in Fig. 11. A graphite furnace atomic-beam oven was filled with metallic aluminum and heated electrothermally by a current of ~80 A to a temperature of about 2500 K. The metallic sample was produced by extraction from an aluminum solution in HNO_3, wrapped in a titanium foil serving as a reductive and loaded into the furnace. A typical sample size was 3×10^{17} atoms. The oven was optimized to form a well-collimated atomic beam with the dimensions of 40-mm length and 2.4-mm inner diameter. At a distance of 146 mm from the oven, an electrode with a 1-mm aperture was placed on an axis to reduce the transversal Doppler broadening of the atomic beam. From the geometry, a residual transversal Doppler width in the order of ~100 MHz is expected. To suppress the surface ions evaporated from the oven, the collimating electrode was set to a positive potential (+11 V). The atoms passing through the aperture were excited shortly after by the resonant laser radiation in a transversal geometry and ionized by the nonresonant laser radiation entering into an anticollinear direction to the atomic beam. The resonant ions were then focused by ion-optical elements and deflected by a static transversal quadrupole deflector into a commercial quadrupole mass filter (qmf) for the background reduction and the ion detection using a channeltron detector. The laser scanning and data readout were performed via a computer-controlled data acquisition system.

A frequency scan of the resonant excitation is shown in Fig. 12, clearly exhibiting the fact that the six individual hfs components are well resolved by excitation with the injection seeded Ti:sapphire laser. From the fit

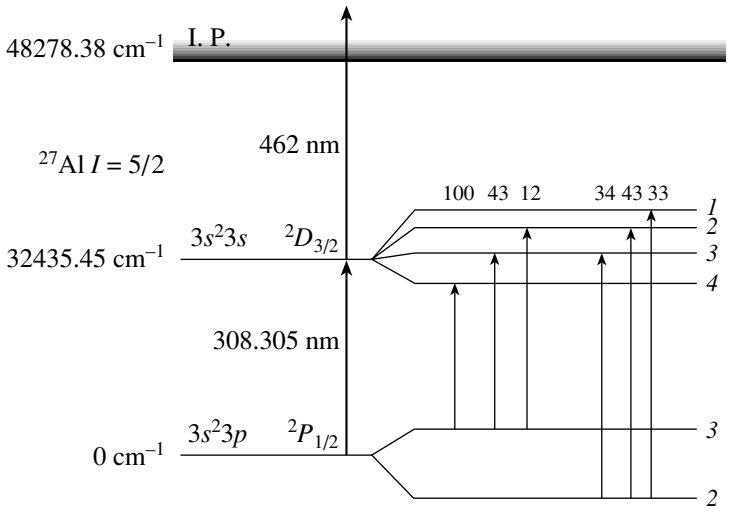

Fig. 10. Resonant ionization scheme for ^{27}Al together with the hyperfine splitting of the ground and excited-atomic states, J levels, and relative intensities of individual hfs components are given on the right-hand side and above the diagram, respectively.

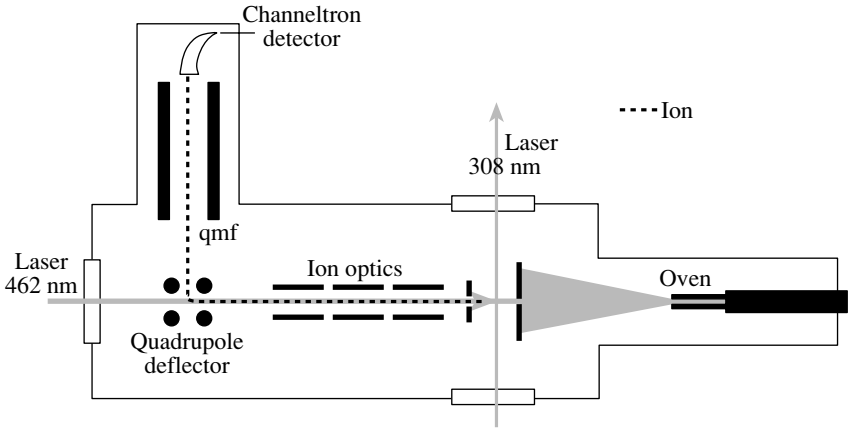

Fig. 11. Spectroscopic setup for high resolution RIS in aluminum.

routine discussed below, an experimental line width of 145(1) MHz FWHM was determined. This value is fairly identical for all hyperfine components and only slightly above the expectation for the experimental situation. The minor increase is ascribed to combined contributions from the power broadening and a laser bandwidth of 20 MHz in total by far surpassing the natural line width of ~12 MHz of the transition [19]. Due to the vast dominance of the Doppler broadening against all other contributions, i.e., from the saturation broadening, the laser line width or natural width, the use of a Voigt profile was disapproved and all components are well represented by a simple Gaussian shape. Thus, for the analysis, a standard χ^2 minimization routine was applied to the data using the sum of six Gaussian functions of identical width w as a fitting function according to the expression

$$y_{(\nu)} = y_0 + A\sum_{i=1}^{6} A_i e^{-\left(\frac{(\nu-\nu_0-\nu_i)}{w/(2\sqrt{\ln(2)})}\right)^2}. \qquad (2)$$

Concerning the spectrometric parameters of interest in this study, i.e., the accuracy and linearity of the scan as well as the intensity stability during the scan for the narrow bandwidth seeded-pulsed laser, a full fit of the hfs with all free parameters was not appropriate. As the most significant test to demonstrate and prove the laser characteristics, a direct comparison of the experimental spectrum with the known literature values was attempted. For this purpose, a fit was carried out with the data inserting all relevant parameters as the known

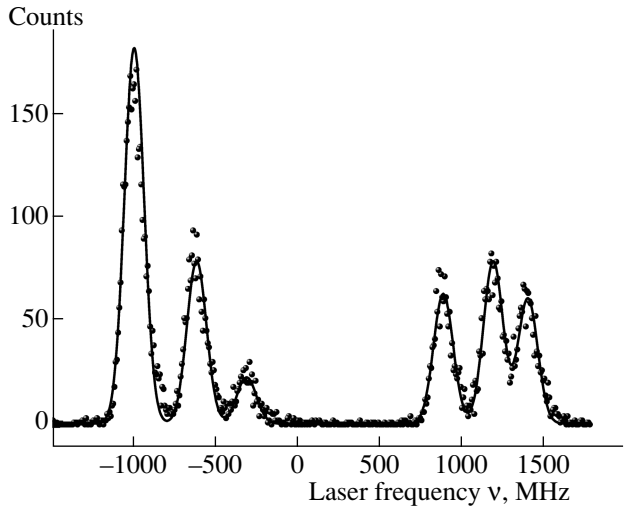

Fig. 12. Frequency scan across the hfs of the resonance transition at 308 nm for ^{27}Al, experimental data, and Gaussian curves fit. The latter uses the fixed hyperfine component splittings and amplitudes from [19].

fixed-input data. Relative intensities A_i of each individual hfs component were calculated by the 6*j* symbols of the transition. The expected frequency positions ν_i of each hyperfine component relative to the center of gravity were determined from the *A* and *B* hyperfine factors as measured by Cooper et al. [19]. These include, for the $^2P_{1/2}$ ground state, the value of A = 502.0336(5) MHz and, for the $^2D_{3/2}$ excited state, A = –98.87(12) MHz and B = 17.5(8) MHz. A compilation of the corresponding input data for our spectra is given in the table. Only four remaining fit parameters of the lowest relevance remain, all acting only on the whole spectrum and not on the individual peaks: the insignificant background level y_0, the similarly insignificant absolute frequency position of the center of gravity ν_0, the total scaling amplitude A, and the identically chosen full width at half maximum (FWHM) w of all transitions. Remarkably, the fit of the experimental spectrum with this widely fixed set of data gives a value of χ^2 = 1.1 and, thus, corresponds to a perfect reproduction of the theory by our experimental data. The almost ideal agreement is visible in Fig. 12, demonstrating the good performance and high specifications of our seeded laser. As a quantitative result for the laser-scanning procedure, we can extract that a scan range of 2.5 GHz can be addressed with a precision and linearity of at least 10 MHz per step or better. The intensity variations, pulse-to-pulse fluctuations, or steering contributes by only about 10% to the peak intensity during scans. We ascribe these good results to the fact that the frequency tuning is carried out under the permanent control of the stabilization system.

Relative position and intensity of the hyperfine-structure components in the $3s^23p\ ^2P_{1/2} \longrightarrow -3s^23d\ ^2D_{3/2}$ transition in ^{27}Al [19] used as the fixed input data for the comparison

ν_i, MHz	A_i/%
–993.9(5)	81/81
–612.4(4)	35/81
–308.0(4)	10/81
893.7(4)	28/81
1198.1(4)	35/81
1409.9(8)	27/81

CONCLUSIONS

A high-repetition rate (7 kHz) injection-seeded Ti:sapphire laser system with a spectral band width of 20 MHz and an average output power of 1.5 W has been developed and was systematically investigated for characterization. As a performance test, crossed-beam spectroscopy was performed on the hyperfine structure of ^{27}Al to demonstrate the suitability of the system for high-resolution applications. Through the perfect reproduction of the known data, the linearity and intensity stability along a scan range of at least 2.5 GHz could be demonstrated.

As a part of the ongoing development of laser-ion sources for the efficient and selective production of the widest range of radioactive ion beams, direct laser spectroscopy within the ion source today is a topic of highest interest. In this context, we plan to use this narrow bandwidth, high power, and high-repetition rate laser in the near future for on-line studies of isotope shifts and hyperfine structures of short-lived radioactive nuclei, e.g., at the IGISOL radioactive ion-beam facility at the University of Jyväskylä, Finland [20]. A corresponding program of research has recently commenced for high-resolution in-source laser spectroscopy using seeded-dye lasers combined with Ti:sapphire lasers. One element of particular relevance is bismuth, where three isomers of interest are to be studied representing different nuclear multiquasiparticle states of near-spherical shape, namely, ^{207m}Bi (21/2$^+$, 182 μs), ^{204m}Bi (10$^-$, 13 ms), and ^{204m}Bi (17$^+$, 1.07 ms) [20]. A measurement of the isomer shifts would provide a direct comparison of the mean-square charge radii between the isomeric and the nuclear-ground states in each case. The short lifetimes of these isomers pose extreme challenges to standard laser spectroscopic techniques, such as collinear laser spectroscopy, due to the decay of the excited states during the release and transport to the experiment. The possibility of in-source high-resolution laser spectroscopy on such short-lived species opens up a wealth of new physics opportunities. It could also be applied to the bismuth atomic system, where, in recent tests, the power of the seeded-dye laser was too low for efficient ionization [7]. Here, again, the injection-seeded Ti:sapphire characterized in this work will be an ideal tool to use in future studies.

A second nuclear structure physics motivation is the search for the predicted exceptionally low-lying (7.6(5) eV) isomeric state in ^{229}Th [21]. One method to directly infer the existence of such an isomer is to study its effect on the hyperfine structure. The creation of a low-energy (~30 kV) ion beam of thorium has been developed at the IGISOL facility; however, at present, the ion yield is by far not sufficient to perform a conventional collinear laser experiment [22], Thus, we foresee the use of the seeded Ti:sapphire laser system to probe the existence of the spectacular isomer directly within the ion source/ion guide combination by in-source high-resolution resonance ionization spectroscopy.

In addition to its application for on-line in-source laser spectroscopy for the fundamental research of the nuclear structure and phenomena, the injection-seeded Ti:sapphire laser as presented here will also find access to the broad field of rather similar laser-based techniques for the ultratrace isotope determination in analytics. So far, this research area has relied dominantly on the use of continuous-wave lasers and very often suffers from both the inaccessibility of spectral ranges, e.g., in the blue to ultraviolet spectral region or the low-laser power available. Through the advent of narrow-bandwidth high-repetition rate powerfully pulsed laser radiation, which can easily be converted into higher harmonics, we expect a significant simplification of the laser systems for those analytical instruments as well as access to new isotopes of interest. Such activities have already been started and will be discussed in detail by H. Tomita in [15].

ACKNOWLEDGMENTS

This work has been supported by the European Commission within the 6th Framework Program "Integrating Infrastructure Initiative—Transnational Access," (contract no. 506065 (EURONS)), by the Academy of Finland under the Finnish Center of Excellence Program 2006–2011 (Nuclear and Accelerator-Based Physics Program at JYFL), and by BMBF 06Mz197.

REFERENCES

1. V. S. Lethokov, Laser photoionization spectroscopy. (Academic, Orlando 3, 1987).
2. G. S. Hurst and M. G. Payne, *Principles and Application of Resonance Ionisation Spectroscopy* (Adam Hilger, Bristol, 1988).
3. P. Müller, B. A. Bushaw, K. Blaum, et al., Fresenius J. Anal. Chem. **370**, 508 (2001).
4. V. I. Mishin, V. Fedoseyev, H. J. Kluge, et al. (ISOLDE Collab.), Nucl. Instrum. Methods Phys. Res. B **73**, 550 (1993).
5. P. Van Duppen, P. Dendooven, M. Huyse, et al., Hyperfine Interact. **74**, 193–204 (1992).
6. L. Weissman, U. Koster, R. Catherall, et al., Phys. Rev. C **65**, 024315 (2002).
7. I. D. Moore, T. Kessler, J. Aysto, et al., Hyperfine Interact. **171**, 135 (2006).
8. R. Seiler, T. Paul, M. Andrist, and F. Merkt, Rev. Sci. Instrum. **76**, 103103 (2005).
9. S. Hannemann, E. J. van Duijn, and W. Ubachs, Rev. Sci. Instrum. **78**, 103102 (2007).
10. P. Dupré and T. A. Miller, Rev. Sci. Instrum. **78**, 033102 (2007).
11. P. Brockman, C. H. Bair, J. C. Barnes, et al., Opt. Lett. **11**, 712 (1986).
12. G. A. Rines and P. F. Moulton, Opt. Lett. **15**, 434 (1990).
13. T. D. Raymond and V. A. Smith, Opt. Lett. **16**, 33 (1991).
14. F. Brandi, D. Neshev, and W. Ubachs, Phys. Rev. Lett. **91**, 163901 (2003).
15. H. Tomita, C. Mattolat, T. Kessler, et al., "Development of High-Repetition Rate Ti:Sapphire Narrow-band Laser for Trace Analysis of ^{26}Al by Resonance Ionization Mass Spectroscopy" (in press).
16. A. E. Siegman, *Lasers* (Univ. Sci. Books, Sausalito, 1986).
17. B. A. Bushaw, B. D. Cannon, G. K. Gerke, and T. J. Whitaker, Opt. Lett. **11**, 422 (1986)
18. A. Kasapi, G. Y. Yin, and M. Jain, Appl. Opt. **35**, 1999 (1996)
19. T. G. Cooper, J. Billowes, P. Campbell, and M. R. Pearson, J. Phys. G **22**, 99 (1996).
20. J. Äystö, Nucl. Phys. A **693**, 477 (2001).
21. B. R. Beck, J. A. Becker, P. Beiersdorfer, et al., Phys. Rev. Lett. **98**, 142501 (2007).
22. B. Tordoff, T. Eronen, V. V. Elomaa, et al., Nucl. Instrum. Methods Phys. Res. B **252**, 347 (2006).

SPELL: OK

Available online at www.sciencedirect.com
ScienceDirect
Nuclear Instruments and Methods in Physics Research B xxx (2008) xxx–xxx
NIM B
Beam Interactions with Materials & Atoms
www.elsevier.com/locate/nimb

Towards on-line production of $N = Z$ ^{94}Ag at IGISOL

T. Kessler [a,*], I.D. Moore [a], H. Penttilä [a], F. Quinquis [b], J. Äystö [a]

[a] University of Jyväskylä, JYFL, PL 35 (YFL), Survontie 9, 40014 Jyväskylä, Finland
[b] ENSICAEN – 6, Boulevard Maréchal Juin, 14050 Caen Cedex, France

Available online

Abstract

A future study of the ground state and low-lying isomeric states of ^{94}Ag and ^{96}Ag at the Ion Guide Isotope Separator On-Line (IGISOL) facility, University of Jyväskylä, requires the development of a low-energy beam of neutron-deficient silver. In order to attain the highest possible extraction efficiencies the coupling of a hot cavity graphite catcher device to the IGISOL mass-separator is planned. A heavy-ion fusion-evaporation reaction will produce the silver recoils which will be captured in the graphite catcher. Resonant laser ionization techniques will be applied to efficiently and selectively ionize the evaporated silver atoms. A simulation program has been written to study the energy and emittance of the recoils in order to optimize the capture geometry. The off-line development of a laser ionization scheme is discussed and the first results of a performance test of the hot cavity with beam on target are given.

PACS: 21.10.−k; 23.40.−s; 27.60.+j; 29.25.Rm

Keywords: Laser ion source; Silver; IGISOL

1. Introduction

The study of radioactive neutron-deficient silver isotopes in the region of the $N = Z$ line has been of considerable interest within the nuclear physics community for several years. In particular the isotopes of ^{94}Ag [1–3] and ^{96}Ag [4] have been extensively studied. The recently observed (21^+) isomeric state with a half-life of 0.39(4) s in the odd–odd $N = Z$ nucleus ^{94}Ag [5] has been identified as a nuclear spin trap having the highest spin ever observed for β-decaying nuclei. The properties of this isomer are unprecedented in the entire known Segre chart. Its decay can proceed via five pathways, β-delayed γ-ray, proton and two-proton emission as well as direct proton and two-proton radioactivity. In particular, the direct emission of one-proton and two-protons from the same long-lived nuclear state is a unique phenomenon, with the hindered rate of the former and the enhanced probability of the latter decay mode as well as the indication of a strong deformation of the parent state needing verification [6,7]. It is a challenge to future experiments to obtain proton–proton correlations with high resolution and better statistics, and furthermore to directly determine the shape of the (21^+) isomer via measurements of the nuclear quadrupole moment.

In order to obtain a better understanding of both the ground states and isomeric states of these exotic nuclei a program of development was recently launched at the ion guide isotope separator on-line (IGISOL) facility, Jyväskylä, Finland. By efficiently and selectively producing low-energy ion beams of the isotopes/isomers of interest we firstly aim to perform high-precision mass measurements of the ground and isomeric states. This information will afford a unique determination of the energy of these states. It should be noted that the ground state of ^{94}Ag has in fact never previously been studied. In the future we intend to perform in-source resonance ionization spectroscopy on both ^{94}Ag and ^{96}Ag which will provide model-independent information on the change of the mean-square charge radii and, furthermore, by measuring

* Corresponding author. Tel.: +358 14 2602440; fax: +358 14 2602351.
E-mail address: thomas.kessler@phys.jyu.fi (T. Kessler).

0168-583X/$ - see front matter © 2008 Elsevier B.V. All rights reserved.
doi:10.1016/j.nimb.2008.05.030

the hyperfine structure of the isomeric states the spectroscopic quadrupole moment and thus the shape of the isomers will be determined. The use of resonance ionization spectroscopy in the ion source has been recently demonstrated at the ISOLDE facility, CERN, to determine the nuclear charge radii of neutron-deficient lead isotopes beyond the $N = 104$ midshell [8]. The method with which such ion beams are to be produced at the IGISOL facility will be explained in the following section.

2. Development of a ^{94}Ag beam at IGISOL

Development work for the production of a radioactive ion beam of ^{94}Ag is currently ongoing at the IGISOL facility. We aim for a primary beam intensity of at least 300 pnA of ^{40}Ca at approximately 5 MeV/u impinging on a 4 μm thick ^{58}Ni target to drive the fusion-evaporation reaction of ^{58}Ni(^{40}Ca,p3n)^{94}Ag. In the earlier work at the ISOL facility of GSI, Darmstadt, the beam intensity was 75 pnA and with a separator efficiency of 30% the ^{94}Ag isomers were produced with an intensity of 2 atoms/s [6]. The nickel target, segmented into four pieces, is mounted on a rotating wheel which is placed in front of a catcher device.

To efficiently stop the fusion-evaporation recoils two approaches are being investigated. On the one hand the standard heavy-ion IGISOL (HIGISOL) approach will be applied using a gas catcher device similar to the one described in [9]. On the other hand a graphite catcher device similar to that proposed in [10] has been built at Jyväskylä and first on-line tests have been performed using the primary beam to heat the catcher. The advantages of the latter method lie in the fast release time of several ms and high extraction efficiencies of close to 50% [11]. The details of this approach will be discussed in these proceedings.

A schematic drawing of the graphite catcher device is shown in Fig. 1. The catcher material used in this work is sintered graphite.[1] Two graphite foils of thickness 10 μm are inserted into a tantalum cavity with an inner diameter of 9.5 mm. The cavity is sealed by a 2 mg/cm^2 tantalum shield with additional layers of heat shield wrapped around the device. An exit hole in the cavity of 1 mm in diameter is placed between the two graphite catchers in the direction of the IGISOL extraction electrode (see Fig. 1). The ion source is placed on a high voltage potential of 30 kV and the extraction electrode, at a distance of about 30 mm from the source, serves as an intermediate acceleration stage at a potential of ~20 kV.

The use of resonant laser ionization is forseen in the near future as a means with which selective and efficient ionization of the silver atoms evaporated from the hot catcher device may be achieved. Off-line tests have been carried out to develop an efficient ionization scheme for Ag using the FURIOS laser ion source [12]. An ionization efficiency of 14% has been reported by the ISOLDE RILIS

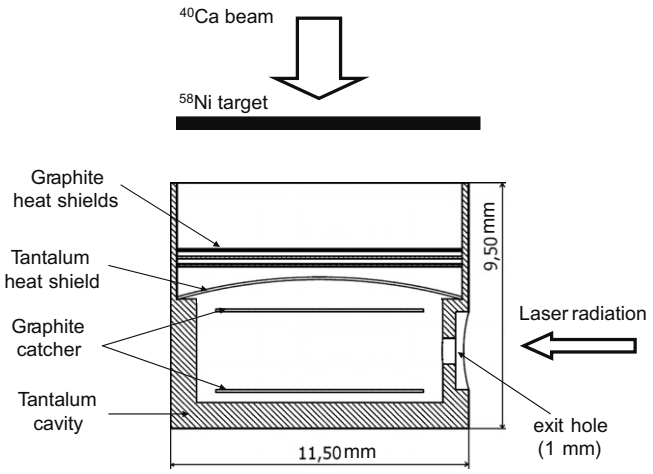

Fig. 1. Schematic drawing of the graphite ion catcher at JYFL.

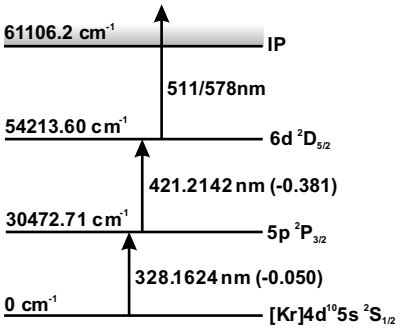

Fig. 2. Ionization scheme for silver [15,16].

laser ion source facility [13] using non-resonant post-ionization. The proposed ionization scheme shown in Fig. 2 can be realized by a combination of a frequency-doubled dye laser for the first excitation step and a frequency-doubled Ti:Sapphire laser for the second excitation step. An atomic beam unit, described in [14], was used to test the resonant ionization scheme shown in Fig. 2 using photons from the first two excitation steps also for the final non-resonant ionization step. Metallic silver was loaded into a joule-heated oven and a low pressure silver vapour (~ 0.01 mbar) was produced with an oven temperature of approximately 2000 °C. In this work ~ 80 mW of 421 nm laser light from the Ti:Sapphire was used. The fundamental laser power from the dye laser was measured to be ~600 mW, however the frequency-doubled 328 nm was too low in power to be measured. A frequency scan of the first and second excitation steps is shown in Fig. 3. Alternatively, the first step can as well be produced by a frequency-quadrupled Ti:Sapphire laser as done by the on-line RIS facility TRILIS at TRIUMF, Vancouver, Canada [17]. This releases up the high-power pump laser needed for the dye laser system[2] for non-resonant post-ionization.

[1] Grade 5890PT by Le Carbone-Lorraine.

[2] CVL, (Oxford Lasers LM100X(KE)).

Please cite this article in press as: T. Kessler et al., Towards on-line production of $N = Z$ ^{94}Ag at IGISOL, Nucl. Instr. and Meth. B (2008), doi:10.1016/j.nimb.2008.05.030

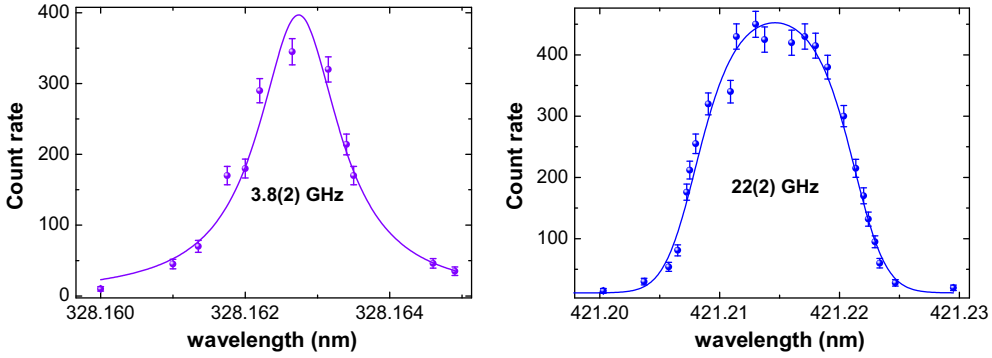

(a) First excitation step (b) Second excitation step

Fig. 3. Laser frequency scans of the first and second excitation steps of the ionization scheme proposed in Fig. 2.

3. Theoretical description of the recoil distribution

In the standard HIGISOL approach thin targets of a few micrometer thickness are used. To construct an efficient catcher device the angle spread and energy of the recoils out of the target needs to be estimated beforehand. This is particularly important for the graphite catcher as the typical maximum diameter is around 1 cm to ensure good thermal containment. Therefore a Monte-Carlo simulation program was written to describe the fusion-evaporation process and the degrading of the beam and the recoils in the target.

The stopping power dE/dx of the nickel foil is estimated to be $\sim$13.5 MeV/(mg/cm^2) [18]. Therefore the energy of the ^{40}Ca beam in the target ranges from 180 MeV to about 120 MeV. The cross section for the reaction is assumed to be constant for this energy range and therefore the probability for a reaction to occur is assumed to be uniform throughout the target.

The first step of the program comprises the selection of a random starting point of the primary ^{40}Ca ions on the front surface of the target foil within an estimated beam diameter of 3 mm. The path that the ^{40}Ca ions follow in the target up to a randomly chosen thickness is calculated by the SRIM code [18].

The fusion-evaporation reaction is calculated in a single step,

$$^{40}\mathrm{Ca} + {}^{58}\mathrm{Ni} \rightarrow {}^{94}\mathrm{Ag} + (3n + p). \quad (1)$$

where only the extreme case in which the three evaporated particles (three neutrons and a proton) are emitted in the same direction is taken into account. Therefore the maximum recoil momentum is achieved for the ^{94}Ag product. The kinematics of the fusion-evaporation process are calculated in the center-of-mass frame. A random angle is chosen for the outgoing momentum of the ^{94}Ag recoil and the path the recoils follow from the site of the fusion-evaporation process to the end of the target is calculated again by using SRIM.

The target thickness was optimized to cover the excitation curve around the maximum cross-section energy. In the simulation more than 99% of the ^{94}Ag ions leave the target. The recoil energies of these ions are illustrated in Fig. 4. Rather low energies ranging from 0 to 60 MeV were obtained from the simulation and therefore the same geometry can be used in a HIGISOL ion guide where gas is used as a stopping material exhibiting a lower stopping power than the graphite catcher.

The phase space of the recoils after the target is extrapolated linearly to a distance d, where the catcher device is situated. For the graphite catcher used in this work with a maximum acceptance diameter of 9.5 mm, the fraction of ions stopped was calculated as a function of d. The results of such a calculation are illustrated in Fig. 5. Fig. 5(a) shows the transversal recoil distribution 20 mm downstream from the target. At this typical distance for our experimental setup approximately 81% of the recoils are stopped. Fig. 5(b) illustrates the captured fraction of recoils as a function of distance d from the target. Additionally for each distance the average transversal radius of the recoils was calculated. At a distance of about 30 mm from the target the average diameter reaches the diameter of the catcher. At this distance approximately 65% of the recoils can be stopped.

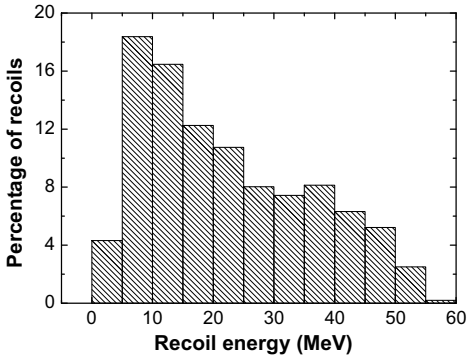

Fig. 4. Energy distribution of the ^{94}Ag recoils after the target.

Please cite this article in press as: T. Kessler et al., Towards on-line production of $N = Z$ ^{94}Ag at IGISOL, Nucl. Instr. and Meth. B (2008), doi:10.1016/j.nimb.2008.05.030

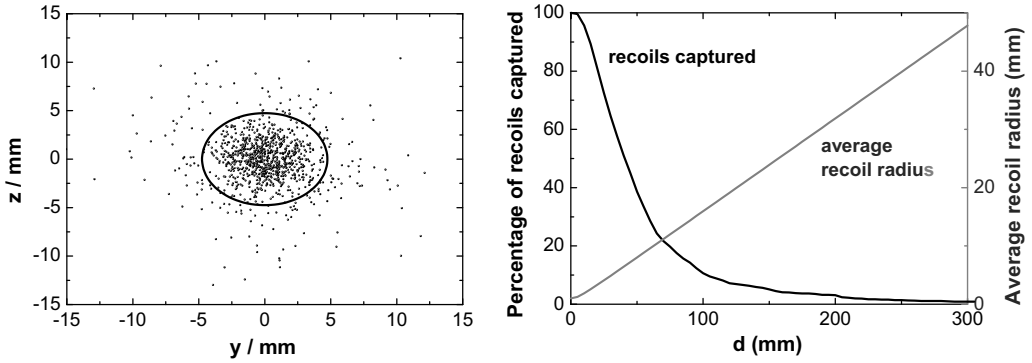

(a) Recoil distribution 20 mm after the target. The solid line defines the entrance to the graphite catcher.

(b) Number of ions captured as a function of distance d to the target.

Fig. 5. Results of the simulation.

4. First test of the catcher device

In a first test experiment the heating capability of the ion catcher by the primary beam and the stability were tested at a range of beam intensities. The catcher device was placed at a distance of 2 cm downstream from the nickel target wheel. A micro-channel plate (MCP) detector situated after the focal plane of the IGISOL mass-separator was used to count the ions. A maximum beam current of 1 eμA $^{40}Ca^{8+}$ ions at an energy of 183 MeV was delivered from the JYFL cyclotron. By scanning the dipole magnet $^{39}K^{+}$ could be identified as a product of surface ionization from the hot cavity. The cyclotron beam was subsequently pulsed to gain information on the time structure of the surface ions, shown in Fig. 6(a). The fast evacuation of the order of several microseconds is not typical for the intrinsic delay of a hot cavity. From the kinetic gas theory the following formula for the intrinsic delay time $t_{1/2,\mathrm{ID}}$ can be derived:

$$t_{1/2,\mathrm{ID}} = 4\ln(2)\frac{V}{A}\sqrt{\frac{\pi m}{8k_{\mathrm{B}}T}}, \tag{2}$$

where V indicates the volume (213 mm^3), A the exit hole area (0.79 mm^2) and T the temperature of the cavity. For the given dimensions of our cavity and assuming a temperature of 1000 K an intrinsic delay time $t_{1/2,\mathrm{ID}} \sim 1$ ms is obtained for the evaporation of $m = 39$ ions in agreement with typical release times given in [11]. Delay times of microseconds are more typical for a direct release from a surface probed by the extraction field [19]. Therefore we conclude that the surface ions are most probably evaporated from the shielding material surrounding the cavity.

For the release of potassium a minimal evaporation temperature of 759 °C [20] is required. No other surface

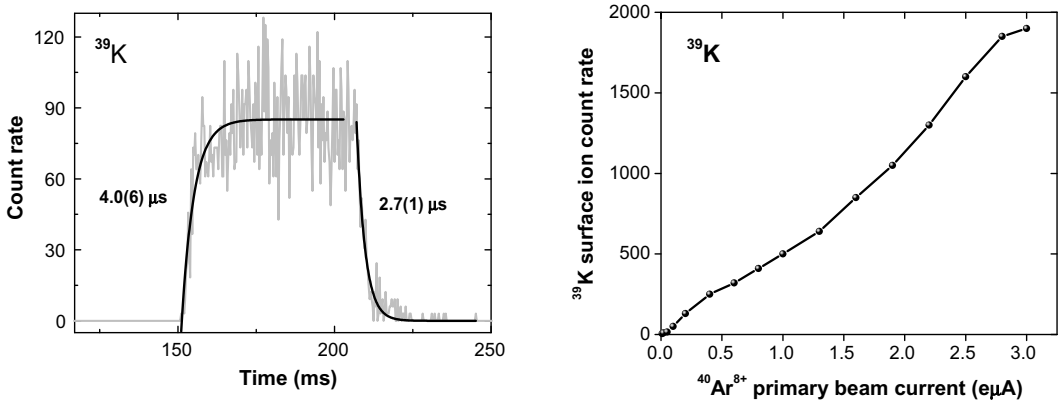

(a) Time structure of $^{39}K^{+}$ surface ions.

(b) Dependence of the $^{39}K^{+}$ yield on the $^{40}Ar^{8+}$ primary beam current.

Fig. 6. Experimental results.

Please cite this article in press as: T. Kessler et al., Towards on-line production of $N = Z$ ^{94}Ag at IGISOL, Nucl. Instr. and Meth. B (2008), doi:10.1016/j.nimb.2008.05.030

ionized species (for example rubidium) was seen, which would suggest insufficient heating of the catcher by the primary beam. As an interesting test, the lasers were tuned to ionize calcium atoms to see if the temperature required to evaporate the implanted primary beam (1484 °C) was reached at the maximum available intensities. This test was unsuccessful which either indicates that the cavity temperature must be somewhere in between the temperature needed to surface ionize potassium and evaporate calcium, or that calcium has a very low efficiency of release from graphite. Taking into account the degrading of the energy of the Ca^{8+} beam by the nickel target to 150 MeV and a beam intensity of 125 pnA a maximum heating power on the first catcher of ~19 W was provided. This value is about one order of magnitude lower compared to electron-bombardment heating by a cathode as in [21], where a power of up to 400 W can be achieved. With an external heating of the catcher the required temperature to evaporate silver of 2000 °C can easily be achieved [10].

Finally the beam was switched to $^{40}Ar^{8+}$ at 180 MeV where an increased maximum beam current of 3 eμA was provided by the cyclotron. The dependence of the ^{39}K yield as a function of primary beam intensity is illustrated in Fig. 6(b). An approximately linear dependence on the primary beam intensity was observed indicating a direct relationship with the temperature of the cavity.

5. Conclusion and outlook

The development of a beam of radioactive neutron-deficient silver isotopes is underway at the IGISOL facility of the University of Jyväskylä, Finland. The aim of this work is to study the nuclear structure of ground and isomeric states in ^{94}Ag and ^{96}Ag. Besides the well-established HIGISOL approach a hot cavity graphite ion catcher is under development. A simulation program has been written to estimate the angular spread of the recoils from the target and therefore the geometric capture efficiency of the catcher device. Additionally, the simulation model can be used to estimate and optimize the efficiency of the HIGISOL ion guide. A first test of the catcher has revealed that external heating is required to provide the necessary temperature of $\geqslant$2000 °C to efficiently release the silver recoils from the graphite material. In order to meet this requirement an external electron-bombardment heating system has been borrowed from GSI, Darmstadt, Germany and is currently being implemented into the front end of the IGISOL system. A first on-line experiment utilizing this new heating source is forseen towards the end of 2008.

Acknowledgements

We are indebted to Heikki Kettunen for technical support in assembling the graphite catcher.

This work has been supported by the LASER Joint Research Activity project under the EU 6th Framework program "Integrating Infrastructure Initiative – Transnational Access", Contract No. 506065 (EURONS) and by the Academy of Finland under the Finnish centre of Excellence Program 2006-2011 (Nuclear and Accelerator Based Physics Program at JYFL).

References

[1] I. Mukha et al., Eur. Phys. J. A 25 (0) (2005) 131.
[2] M. La Commara et al., Nucl. Phys. A 708 (3–4) (2002) 167.
[3] I. Mukha et al., Phys. Rev. Lett. 95 (2) (2005) 022501.
[4] L. Batist et al., Nucl. Phys. A 720 (3-4) (2003) 245.
[5] I. Mukha et al., Phys. Rev. C: Nucl. Phys. 70 (4) (2004) 044311.
[6] I. Mukha et al., Nature 439 (7074) (2006) 298.
[7] J. Äystö, Nature 439 (7074) (2006) 279.
[8] H. De Witte et al., Phys. Rev. Lett. 98 (11) (2007) 112502.
[9] P. Dendooven et al., Nucl. Instr. and Meth. A 408 (2-3) (1998) 530.
[10] R. Kirchner, K.H. Burkhard, W. Huller, O. Klepper, Nucl. Instr. and Meth. 186 (1–2) (1981) 295.
[11] R. Kirchner, Nucl. Instr. and Meth. B 70 (1-4) (1992) 186.
[12] I.D. Moore et al., J. Phys. G: Nucl. Part. Phys. 31 (10) (2005) S1499.
[13] U. Koster, V.N. Fedoseyev, V.I. Mishin, Spectrochim. Acta, Part B 58 (6) (2003) 1047.
[14] B. Tordoff, PhD Thesis, University of Manchester, 2006.
[15] R.L. Kurucz, P.L. Smith, C. Heise, J.R. Esmond, Kurucz Atomic spectral line database, <http://www.pmp.uni-hannover.de/cgi-bin/ssi/test/kurucz/sekur.html>, (accessed 28.08.07).
[16] Y. Ralchenko, A. Kramida, J. Reader, <http://physics.nist.gov/PhysRefData/ASD/index.html>, (accessed 28.08.07).
[17] J. Lassen, private communication.
[18] J. Ziegler, The Stopping Range of Ions in Solids, Pergamon Press, 1985.
[19] J. Lettry, R. Catherall, U. Koster, U. Georg, O. Jonsson, S. Marzari, V. Fedosseev, Nucl. Instr. and Meth. B 204 (2003) 363.
[20] M. Winter, Webelements.com, <http://www.webelements.com/webelements/elements/text/K/heat.html>, (accessed 28.08.07).
[21] R. Kirchner, E. Roeckl, Nucl. Instr. and Meth. 127 (2) (1975) 307.

Please cite this article in press as: T. Kessler et al., Towards on-line production of $N = Z$ ^{94}Ag at IGISOL, Nucl. Instr. and Meth. B (2008), doi:10.1016/j.nimb.2008.05.030

Hyperfine Interact
DOI 10.1007/s10751-006-9496-x

Upgrade to the IGISOL laser ion source towards spectroscopy on Tc

T. Kessler · T. Eronen · C. Mattolat · I. D. Moore · K. Peräjärvi · P. Ronkanen · P. Thörle · B. Tordoff · N. Trautmann · K. Wendt · K. Wies · J. Äystö

Abstract A new method of optical pumping has been applied to increase the power of the Ti:Sapphire laser system of the FURIOS laser ion source, Jyväskylä. This upgrade has led to a factor of two improvement in the output power, and has been directly employed in the first off-line laser ionisation tests on the long-lived refractory isotope ^{99}Tc. In the future further studies will be done to determine the efficiency of this ionisation scheme and to employ it for on-line experiments.

Keywords Laser ion source · Technetium · IGISOL

1 Introduction

The IGISOL (Ion-Guide Isotope Separator On-Line) technique has been in use for the past 20 years. During this time there has been a number of technical advances to improve the performance of the technique [1]. Due to the production mechanism the ion guide method is not dependent on target chemistry and therefore

T. Kessler (✉) · T. Eronen · I. D. Moore · K. Peräjärvi · P. Ronkanen · J. Äystö
Department of Physics, University of Jyväskylä, Survontie 9, PL 35 (YFL),
40014 Jyväskylä, Finland
e-mail: thomas.kessler@phys.jyu.fi

C. Mattolat · K. Wendt · K. Wies
AG Larissa/Quantum, Inst. f. Physik, Johannes Gutenberg Universität, Staudinger Weg 7,
55128 Mainz, Germany

P. Thörle · N. Trautmann
Inst. f. Kernchemie, Johannes Gutenberg Universität, Fritz-Straßmann-Weg 2,
55128 Mainz, Germany

B. Tordoff
Nuclear Physics Group, Schuster Laboratory, University of Manchester, Brunswick Street,
Manchester M13 9PL, UK

is the ISOL system of choice for the production of refractory short-lived nuclei [2]. Despite the attractive features of a universal production of exotic nuclei and the fast (submillisecond) release, two drawbacks remain. The IGISOL is rather unselective, a problem in particular for proton-induced fission reactions, and in some cases inefficient. To overcome these deficiencies a laser ion source has been installed at the University of Jyväskylä consisting of both solid-state Ti:Sapphire lasers and dye lasers [3].

One of the elements of interest for study at the IGISOL facility is technetium. From a physics point of view, there is a three-fold motivation: nuclear astrophysics, weak interaction physics and nuclear structure physics. For example, according to the conserved vector current hypothesis (CVC), the matrix elements of the superallowed Fermi transitions between the 0^+ isobaric analog states (IAS) should all be equal, independent of nuclear structure apart from small radiative and isospin-symmetry breaking terms. These latter terms become increasingly important with increasing Z of the nucleus, and uncertainties between different theoretical calculations dominate the uncertainty of the isospin correction [4]. A measurement of the Q-value and half-life of the $N = Z$ superallowed beta emitter, ^{86}Tc, would provide important experimental input to this field.

In addition, nuclei close to the $N = Z$ line play a special role in nuclear astrophysics since the rapid-proton (rp) capture process passes right through them. On the neutron-rich side of the valley of stability, extending the ability to produce even more exotic Tc isotopes will benefit for the studies of nuclear structure in this region, and also provide input for calculations dealing with the astrophysical *r*-process.

The ability to perform spectroscopy on exotic Tc isotopes relies on the need to produce intense and pure beams of these nuclei. By combining the IGISOL technique with the efficiency and selectivity of a laser ion source this requirement will be achieved.

2 Experimental setup

In order to selectively ionise Tc, an efficient resonance ionisation scheme must first be developed. Due to the refractory nature, particular attention to the production of an atomic vapour must be addressed. High temperatures and a stable operating condition are required, developments which go hand in hand with the continuous improvement of the laser system in use. In this section the experimental setup used for the preparatory experiments for the laser ionisation of Tc is described. After a short introduction to the ion guide and IGISOL technique, the modification to the laser system will be explained.

2.1 The ion guide technique

The ion guide used for the laser ionisation of Tc is described in detail in [5]. It is equipped with a mount for an electrothermally heated filament. The filament was prepared at the nuclear chemistry department of the University of Mainz using an electrodeposition technique as described in [6]. The filament substrate is made from rhenium and is cut into a 20×4 mm^2 foil, with a thickness of 25 μm. A sample of 10^{14} atoms of ^{99}Tc with a half-life, $T_{1/2} = 2.111 \cdot 10^5$ years [7], is deposited onto the foil

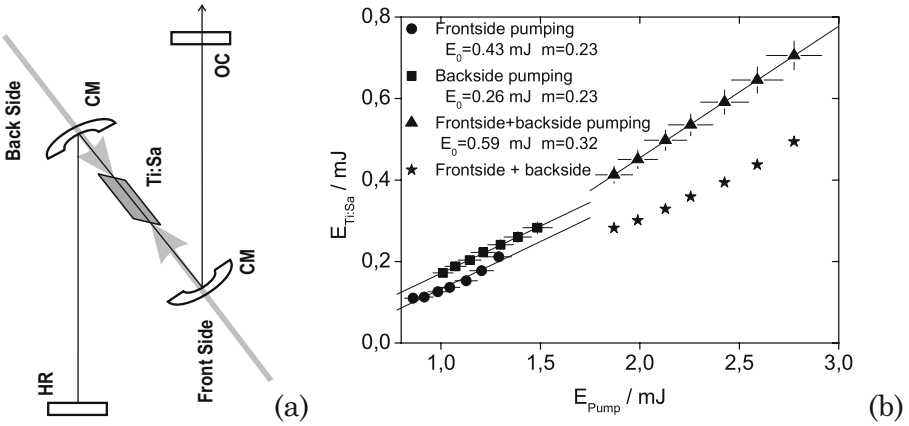

Fig. 1 **a** The double-sided Ti:Sapphire laser. *HR = high reflector*, *CM = curved mirror*, Ti:Sa = Ti:Sapphire crystal, *OC = output coupler*. **b** Conversion efficiencies for the double-sided Ti:Sapphire laser

and can be evaporated with temperatures of up to 1,500 °C under vacuum. The laser radiation enters the ion guide on-axis via an entrance window in the rear. A helium gas flow at a pressure of 60 mbar extracts the resonant ions through the exit nozzle of the ion guide. The ions are subsequently guided through a radio-frequency sextupole device before being accelerated to 30 kV and mass separated. The final detection is done with a set of microchannel plates (MCP) downstream from the IGISOL focal plane.

2.2 Laser system and new developments

The FURIOS laser system was designed to operate as a twin laser system. One setup consists of two commercial dye lasers pumped by a Copper Vapour Laser (CVL) operating at 12 kHz. In this work an all solid-state system was used consisting of three Ti:Sapphire lasers pumped by a commercial 12 kHz Nd:YAG laser.

Of crucial importance in developing a laser ion source is the ability to efficiently ionise the element of interest. The bottle neck of the ionisation process is often the final step, either non-resonant or resonant, due to the low absorption cross sections. In order to provide the laser power required for achieving an efficient ionisation of Tc, a modified version of the Ti:Sapphire lasers in use has been developed. This involves pumping of the Ti:Sapphire crystal on both sides in order to achieve a higher population inversion in the active medium. Figure 1a shows a schematic of the double-pumping principle. The crystal is positioned between the two curved mirrors (CM) within the z-shaped cavity. The Nd:YAG pump laser is focussed onto the crystal through the rear of these mirrors. Figure 1b illustrates the conversion efficiency for the double-sided pumping cavity compared to that of a standard single-sided laser. The energy of the pump laser was varied by adjusting the repetition rate from 7 to 10 kHz in steps of 0.5 kHz. The circles and squares correspond to the output energy obtained by pumping the crystal from the front and rear side respectively. The

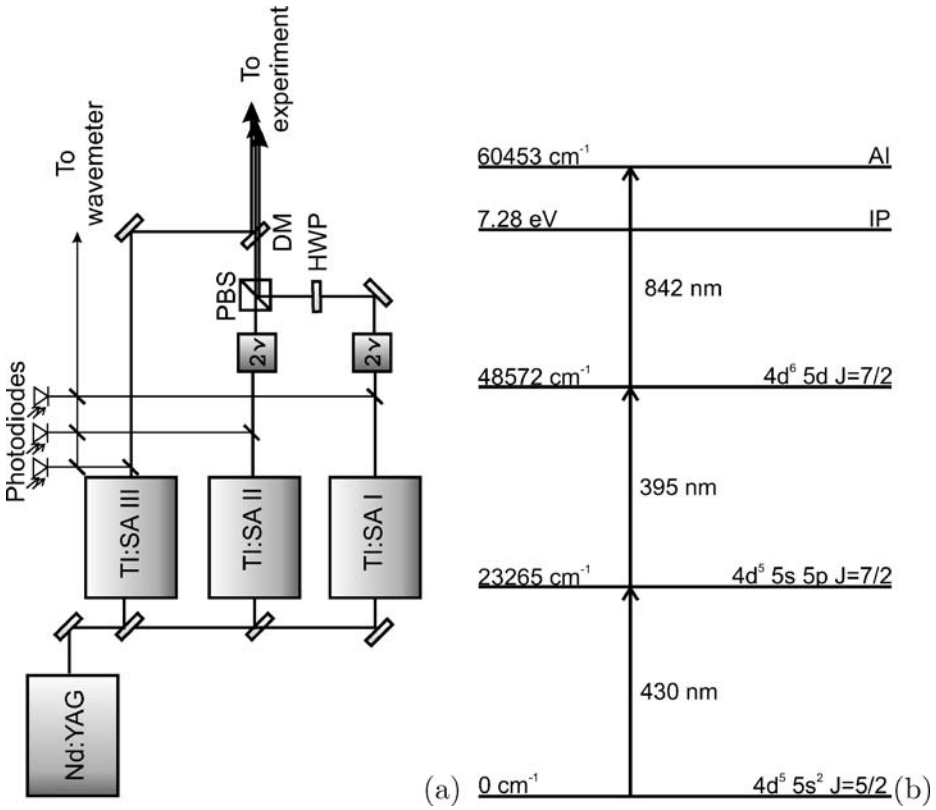

Fig. 2 **a** Laser system used for resonance ionisation of Tc. **b** Relevant atomic energy levels in Tc and the transitions used in this work

triangles correspond to the output pulse energy obtained when pumping both sides at the same time. A linear fit of the form

$$E_{out} = (E_{in} - E_0) \cdot m \tag{1}$$

was applied to the data, where m is denoted as the slope efficiency and E_0 the lasing threshold. The extracted coefficients are shown in the figure.

The result of the fitting shows an increase in the slope efficiency for the double-sided pumping with a maximum value for the output energy of 0.7 mJ/pulse. This value can not be obtained with single-sided pumping due to the damage threshold of the Ti:Sapphire crystal. The slope-efficiency for the front-side is higher than for the back-side since the overlap of the pump-beam with the laser-mode is optimized for this side.

A comparison between the double-sided pumped cavity with the sum of the two single-sided cavities (indicated by stars in Fig. 1b) suggests that the double-sided Ti:Sapphire laser is more efficient [8]. This can be explained by the fact that the same threshold has to be surpassed for both the single-sided and the double-sided cavities. Consequently the inversion gain due to back-side pumping directly contributes to the

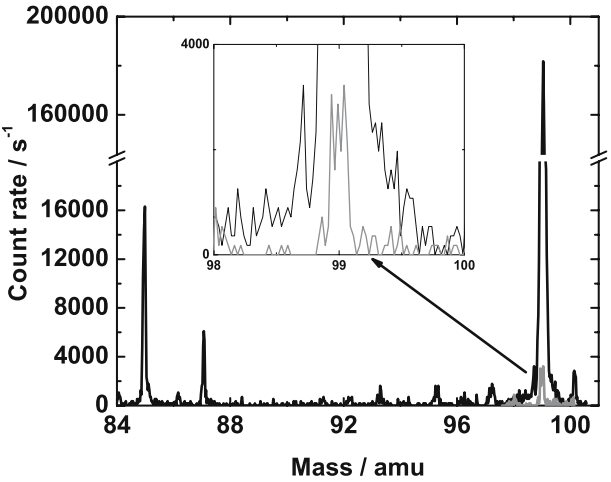

Fig. 3 Mass scan from 84 to 100 amu. The surface ionised isotopes ^{85}Rb and ^{87}Rb as well as the laser ionised ^{99}Tc appear in the spectrum. The insert shows the mass scan in the region of 99 amu with lasers off. Note the *y*-axis break

laser process. During a high power test up to 5 W output power was obtained with a total input power of 28 W at a typical repetition rate of 10 kHz.

2.3 Laser setup for Tc

A schematic of the laser system used for the resonant ionisation of Tc is shown in Fig. 2a, while Fig. 2b shows the ionisation scheme developed by the University of Mainz.

The excitation of the first and second steps at 429.8 and 395.2 nm, respectively, was achieved using two BBO crystals (2ν) to generate the second harmonic frequency. Both laser beams were overlapped spatially using a polarizing beamsplitter cube (PBS) combined with a half-wave plate (HWP). The final ionisation step of 841.7 nm was realised using the fundamental wavelength of the double-sided Ti:Sapphire laser. The infrared light is then combined with the second harmonic light using a dichroic mirror (DM). Temporal synchronisation of all lasers was achieved using Pockels cells serving as q-switches in the laser cavities. The laser powers measured at the entrance window of the ion guide were as follows: 70 mW for the first step; 130 mW for the second step; 1.4 W for the ionisation step. The power available for the first two steps exceeds that needed to saturate the transitions (Wies, personal communication). As no spectroscopic investigations have been carried out for the third step it is unknown as to whether this step is saturated.

3 First laser ions of ^{99}Tc

Following the alignment of the lasers into the ion guide the filament was continuously heated to provide an atomic vapour of Tc. At a current of 18 A corresponding to a filament temperature of $\approx$ 1,400 °C, a first Tc laser ion signal was observed. A maximum count rate of 180,000 counts/s was obtained after optimizing the laser wavelengths, spatial overlap and IGISOL ion beam tuning. Figure 3 shows a mass scan in the range of 84 to 100 amu. A key parameter for a laser ion source is the

selectivity, determined by measuring the ratio of laser ions to non-resonant ions. In this work a selectivity of ≈ 56 was observed. Non-resonant surface ions were observed in the mass scan due to the high temperature needed to evaporate the Tc sample from the Re substrate. As expected, the alkali metal isotopes ^{23}Na, ^{39}K, ^{41}K, ^{85}Rb and ^{87}Rb were all observed. The non-resonant signals observed at positions of 92–101 amu most likely arise from molecular contaminants formed from impurities in the buffer gas.

4 Conclusion and outlook

An ion guide has been built for efficient and selective laser ionisation of exotic refractory radioisotopes at the IGISOL facility, Jyväskylä, using the FURIOS laser system. To provide a more efficient laser ionisation, the solid-state Ti:Sapphire lasers have been upgraded to enable a double-sided pumping technique. This has resulted in a significant increase in the total output power and therefore a more readily achievable ability to saturate resonant transitions. The first off-line laser ion signal of the long-lived ^{99}Tc isotope has been observed at IGISOL using a three step excitation scheme.

In the near future laser ionisation of ^{99}Tc will be attempted within the sextupole ion guide, incorporating the so-called LIST principle [9]. Furthermore an efficiency measurement for the laser ionisation process will be carried out, with a view towards a first on-line test towards the end of the year.

Acknowledgements The work has been supported by the EU within the 6th framework programme Integrating Infrastructure Initiative – Transnational Access, Content Number: 506065 (EURONS). We also acknowledge support from the Academy of Finland under the Finish Centre of Excellence from 2000–2005 (Project no 44875), Nuclear and Condensed Matter Physics Program at JYFL). BT acknowledges the Marie Curie Foundation (EC).

References

1. Penttilä, H., et al.: Eur. Phys. J. **25**, 745 (2005)
2. Äystö, J.: Nucl. Phys. **A693**, 477 (2001)
3. Moore, I.D., et al.: J. Phys. G: Nucl. Part. Phys. **31**, 1499 (2005)
4. Towner, I.S., Hardy, J.C.: Phys. Rev. **C71**, 035501 (2005)
5. Kessler, T., Moore, I.D.: A study of the laser ionization of Yttrium at the IGISOL facility. (in press)
6. Trautmann, N., Folger, H.: NIM B **A282**, 102 (1989)
7. National Nuclear Data Center, Brookhaven National Laboratory: Nuclear Wallet Cards 7th edition. http://www.nndc.bnl.gov/wallet/wccurrent.html. Cited 24 May 2006 (2006)
8. Kessler, T.: Diploma Thesis. University of Mainz, Germany (2004)
9. Blaum, K., et al.: NIM B **204**, 331 (2003)

IOP Publishing Journal of Physics B: Atomic, Molecular and Optical Physics

J. Phys. B: At. Mol. Opt. Phys. **40** (2007) 4413–4432 doi:10.1088/0953-4075/40/23/002

Three-step resonant photoionization spectroscopy of Ni and Ge: ionization potential and odd-parity Rydberg levels

T Kessler[1], K Brück[1], C Baktash[2], J R Beene[2], Ch Geppert[1], C C Havener[2], H F Krause[2], Y Liu[2], D R Schultz[2], D W Stracener[2], C R Vane[2] and K Wendt[1]

[1] Johannes-Gutenberg-Universität Mainz, Staudinger Weg 7, D-55099 Mainz, Germany
[2] Physics Division, Oak Ridge National Lab, Oak Ridge, TN 37831, USA

E-mail: klaus.wendt@uni-mainz.de

Received 31 May 2007, in final form 6 October 2007
Published 13 November 2007
Online at stacks.iop.org/JPhysB/40/4413

Abstract

In preparation of a laser ion source, we have investigated multi-step laser ionization via Rydberg and autoionizing states for atomic Ni and Ge using a mass separator with an ion beam energy of 20 keV. For both elements resonant three-step excitation schemes suitable for modern Ti:sapphire laser systems were developed. Rydberg series in the range of principal quantum numbers $20 \leqslant n \leqslant 80$ were localized, assigned and quantum numbers were allocated to the individual resonances. Ionization potentials (IP) were extracted from fits of the individual series and quantum defects of individual levels were analysed for confirmation of series assignment. For Ni the ionization potential could be extracted with significantly increased precision compared to literature with a value of E_{IP} (Ni) $= 61\,619.77(14)$ cm^{-1}. Also, at least one notable autoionizing state above the first IP was discovered for both elements, and the different ionization schemes via Rydberg or autoionizing states were compared with respect to line shape, ionization efficiency and selectivity.

1. Introduction

Laser-based resonance ionization spectroscopy (RIS) of atomic species, usually combined with ion mass selection (RIMS), is widely developed today and serves well as an efficient and highly selective ionization tool. RIMS is particularly useful in those cases where mass separation of an elemental or isotopic species from an initial sample is insufficient, e.g. due to strong isobaric contaminations, and additional selection is desirable. In the RIMS approach, neutral atoms (or molecules, which we shall not address further here) are usually ionized by

a stepwise resonant multi-photon absorption process, accelerated in a static electric field, and afterwards undergo conventional mass separation. This combination results in an ion beam of the highest isobaric and isotopic purities that can be used in further experimental investigations. Typical applications include laser isotope enrichment, analytical ultra-trace isotope analysis and online preparation of purified exotic radioactive species, produced in dedicated nuclear reactions.

About 20 years after the first proposal [1] and demonstration [2], resonance ionization laser ion sources (RILIS) have now become the most commonly applied ionization technique at the major online radioactive ion beam facilities, e.g. ISOLDE (CERN/Geneva) [3–5]. Due to its high efficiency and selectivity, RILIS is in use for more than 50% of the experimental program at ISOLDE and its overall operation period [6]. The basic prerequisite for successful use of RILIS for a desired element is the precise knowledge of the major parameters of an appropriate resonant multi-step ionization scheme. To ensure high ionization probability, the excitation steps must involve strong resonance transitions. Thus optical transition strengths and easy accessibility of individual transition wavelengths for each individual optical excitation step are of major concern and must be verified for the lasers in use. Therefore detailed spectroscopic studies are needed for each element of interest prior to any RIS application [7].

In particular, the final ionizing step is of crucial importance for both the efficiency and selectivity of the process because the optical absorption cross section is generally much lower for bound–free transitions than for dipole-allowed transitions between bound atomic levels. Thus, especially for direct non-resonant ionization into the continuum, relatively high laser power is required, that is also likely to decrease isotopic selectivity because of non-resonant processes. A preferable alternative that increases selectivity is to employ a final resonant step (i.e. excitation into a high-lying Rydberg state), which can be efficiently ionized via atomic collisions, blackbody radiation or electric fields. Optical pumping into an autoionizing state located above the ionization limit in the continuum is even more desirable. These resonant excitation processes significantly increase the ionization efficiency and reduce the laser power needed for saturation of the transition, but on the other hand significantly increase the complexity of the technique. Specifically, an additional powerful, tuneable laser is needed and a proper choice of a possible electric field in the atom–laser interaction region must be made, avoiding resonance line disturbances but enabling field ionization if required. A spectroscopic investigation of high-lying levels and/or the continuum structure of the element of interest is required. Such investigations for Ni and Ge are the topic of this paper.

While the aforementioned ISOLDE RILIS is based on dye lasers pumped by a powerful copper vapour laser, the use of high-repetition-rate Ti:sapphire laser systems has been successfully demonstrated in offline RILIS tests in recent years [8, 9]. The latter are now accepted as reasonable alternatives to the more widely used but maintenance intensive dye-laser systems. Both the Canadian online facility ISAC at TRIUMF [10], as well as the Finnish online facility JYFL/IGISOL at Jyväskylä [11] installed such laser systems for their RILIS activities very recently. These all-solid-state lasers provide radiation within a somewhat limited infrared-to-red wavelength region between about 700 and 950 nm, but this range is significantly extended by the generation of higher harmonics, namely in the ranges of 360–470 nm (second harmonic), 240–310 nm (third harmonic) and 200–230 nm (fourth harmonic), using nonlinear crystals. To establish the full range of applicability of the Ti:sapphire laser systems for RIMS investigations, extensive spectroscopic investigations on numerous elements are presently being carried out. These concern development and characterization of appropriate excitation schemes, analysis of level structures and completion of atomic level schemes for highly excited states around the ionization limit.

The work on Ni and Ge reported here was motivated by a proposed next-generation online rare isotope facility. In response, the development of a state-of-the-art RILIS system, exclusively using Ti:sapphire lasers, for the preparation of ultra-pure and high intensity beams of short-lived exotic species was initiated. This activity was carried out at the Holifield Radioactive Ion Beam Facility (HRIBF) at Oak Ridge National Laboratory (ORNL) in the USA. Fundamental studies for our RILIS layout and operation were performed at the Ion Source Test Facility (ISTF-2) at ORNL using the Mainz University Ti:sapphire laser system. RILIS investigations on stable isotopes of the elements Ni, Ga, Ge and Sn were performed in preparation of future applications to short-lived radioisotopes of these elements, which are of high interest to nuclear and/or astrophysical investigations. For example, the doubly magic nuclei ^{100}Sn and ^{78}Ni are of special importance for the understanding of nuclear structure [12], while ^{84}Ge isotopes serve to verify theoretical predictions about the *r*-process path of nucleosynthesis [13]. The nuclear level structure of the $0^+ \rightarrow 0^+$ beta-emitter ^{62}Ga was investigated recently at ISAC/TRIUMF as the first application of their Ti:sapphire RILIS to analyse the V_{ud}-element part of the CKM-matrix [14, 15] motivating further RILIS applications and investigations.

Results from the ORNL RILIS preparatory studies, which focus on ion source design and development, have been given elsewhere [9]. They include efficiency measurements for the resonant excitation process as well as saturation curves of the optical transitions used. In this paper we present detailed analysis of spectroscopic aspects of the Ti:sapphire laser RIMS measurements, obtained in the resonant ionization of the elements Ni and Ge. Here extensive investigations of Rydberg series were carried out, ionization potentials and quantum defects were extracted, and comparison to autoionization was made.

2. Experimental setup

2.1. Laser setup

The laser setup consists of three dedicated, pulsed Ti:sapphire lasers developed and built at the University of Mainz, which provide powerful tuneable laser light at a high repetition rate and well-adapted spectral profiles for optical spectroscopy in hot vapour or gas cells. A detailed description of the system is given in [16–18]. At ORNL, the three Ti:sapphire lasers are jointly pumped by a single commercial high-repetition-rate (10 kHz) Nd:YAG laser that provides 60 W of pump power at 532 nm. A Pockels cell is installed in each Ti:sapphire laser cavity to serve as a Q-switch and ensure proper temporal synchronization of individual Ti:sapphire laser pulses with a precision of about 5 ns. Wavelength selection is provided by a Lyot filter and an etalon in each laser that is controlled remotely via actuators. The laser frequencies are measured and read out by a commercial wavemeter. The spectral and temporal behaviour for the three lasers is controlled by a personal computer (PC). Spectral line widths of about 5 GHz and pulse durations of about 50 ns are typical. The small size of the lasers ($\sim$30 $\times$ 40 cm) makes the laser system very portable.

For universal RILIS use, the fundamental Ti:sapphire laser wavelength range must be extended by generation of higher harmonics of the laser frequency. A corresponding unit for frequency doubling, tripling and quadrupling was set up at and provided by Mainz University. The second harmonic is generated in a simple single-pass arrangement using a nonlinear BBO crystal. Fundamental and second harmonic frequencies can be mixed afterwards in a second BBO crystal for efficient generation of the third harmonic. Alternatively, the second harmonic can be doubled again for frequency quadrupling. Typical output powers achieved are $\sim$2 W

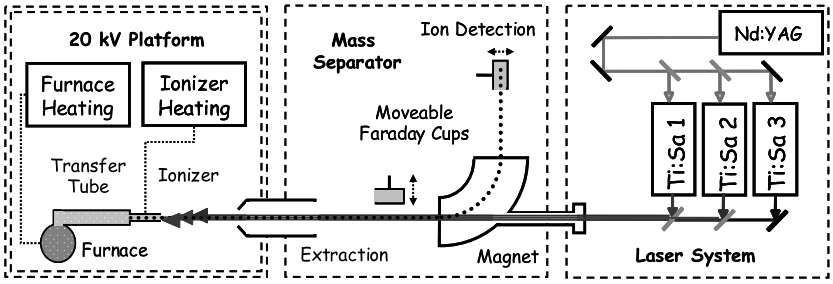

Figure 1. Sketch of the ISTF-2 ion source test facility and mass separator used for the present RIS/RILIS measurements.

in the fundamental, ∼200 mW in the doubled and about 40 mW both in the frequency tripled and quadrupled range.

Telescopes are used for laser beam transport and focusing over the distance of about 4 m towards the ISTF-2 ion source, while spatial overlapping of the individual lasers beams is done using polarizing beam splitters and dichroic mirrors. The laser beams enter the vacuum chamber of the mass separator through a window installed in line with the ion source-ionizer axis using a view port located behind the separator magnet. The (inaccessible) laser beam path from the window to the atomic vapour source inside the vacuum is about 4 m. With the telescopes, all laser beams are focussed down to a beam diameter of typically ∼3 mm to match the size of the transfer tube and ionizer funnel of the actual RILIS construction.

2.2. Ion source test facility

A schematic illustration of the ISTF-2 ion source and mass separator at ORNL, including the Mainz laser system, is shown in figure 1. The neutral atom and ion source assembly are mounted on a high-voltage platform that is typically operated at a potential of 20 kV. The extracted ion beam is directed towards a 90° sector dipole magnet for mass separation (radius ∼0.61 m). The separated ion beam travels another 2 m in vacuum before reaching various ion beam diagnostics. The overall ion beam path has a length of about 6 m.

Various ion sources are installed and operated at ISTF-2 for test and optimization. For this RILIS development, a standard high-temperature surface ionization ion source equipped with a target material reservoir (furnace) was adapted for optimum neutral atom production. The species of interest is introduced into the heated furnace in a solid form and evaporated at temperatures around 1000 °C. The atomic vapour effuses into an independently heated transfer tube and ionizer assembly, both made of tantalum. The latter is operated at a temperature that is a trade-off between acceptably low-surface ionization yield and reasonably short wall residence time for the vapour, thus acting predominantly as a heated atomizer instead of an ionizer. The dimensions of the transfer tube are 8.5 mm inner diameter and ∼100 mm length, while the ionizer tube is 30 mm long and 3 mm in diameter. A technical drawing of this source and details of its operation and performance are given in [9]. After ion creation, dominantly inside the tubular ionizer, either by surface or laser ionization, the ions are pushed forward towards the extraction hole by the small gradient of the electric potential resulting from the direct current heating of the transfer tube and ionizer. When exiting into the high-voltage section, the ions are accelerated to an energy of 20 keV by a spatially adjustable extractor electrode at ground potential. The optimized extraction geometry, Einzel lens and electrostatic steering together produce a well-collimated, well-centred ion beam for mass dispersion in the sector

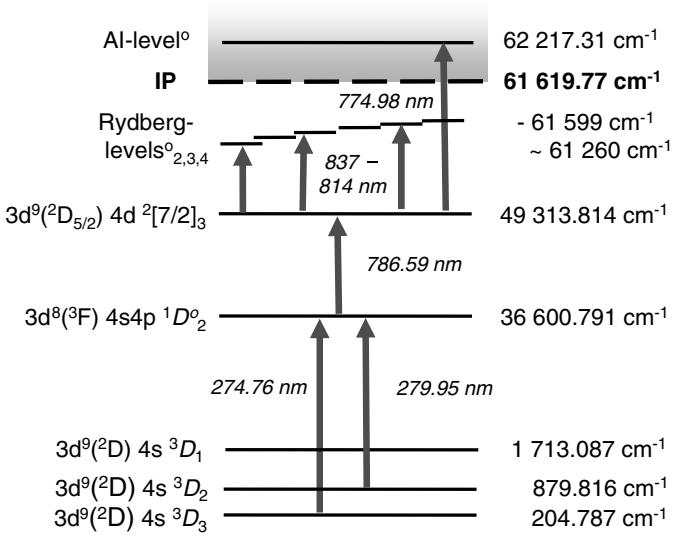

Figure 2. Scheme used for three-step resonance excitation into odd-parity high-lying Rydberg states or autoionizing states of Ni. For high-lying levels the J_1 K coupling notation from [20] has been adopted.

field magnet. The latter is operated with a moderate resolving power of $\Re = m/\Delta m \approx 200$ that ensures a high transmission of around 90%. Faraday cups, a channeltron detector as well as an emittance metre installed along the beam line, are used for ion beam diagnostics. The measurements presented here use only a simple Faraday cup installed after the magnet for mass-selective ion current measurement by a commercial electrometer with sensitivity in the low pA range. The output signal is monitored and saved by a data acquisition PC equipped with a 16-bit ADC card.

3. Results

3.1. Spectroscopy of the Rydberg series in nickel

Three-step resonance excitation and ionization of Ni via a Rydberg state was demonstrated earlier by Ishikawa using dye lasers [19]. For the Ti:sapphire laser system used here, an alternative excitation scheme had to be established which is shown in figure 2. The level assignments were taken from the NIST tables [20]. The first excitation step, in the ultraviolet spectral range around 276 nm, starts either from the low-lying $J = 3$ (204.787 cm^{-1}) or $J = 2$ (879.816 cm^{-1}) fine structure sublevels of the $3d^9$ (^{2}D) 4s ^3D_J multiplet. At a typical ionizer temperature of 1700 °C these sublevels have populations of ∼27% and ∼12% respectively. A transition at 786.59 nm was used in the second excitation step. For the third step, we investigated different ionization pathways that involve the population of either high-lying Rydberg levels or autoionizing levels, located slightly above the first ionization potential (IP). The highest ionization rate was obtained at a wavelength of 822.0 nm leading to a Rydberg state with a principal quantum number of $n = 30$, as discussed in detail below. Therefore, this transition was used to investigate the line shapes of the lower two excited levels in this excitation scheme. All investigations were performed using the most abundant even isotope

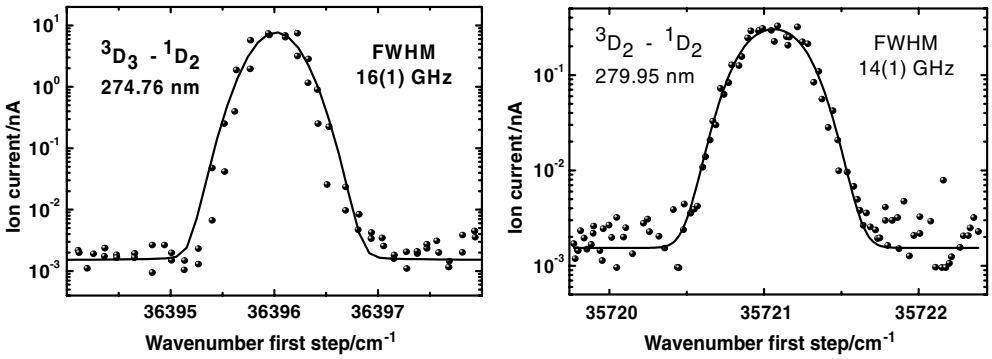

Figure 3. Scans of the two alternative first excitation steps at 274.76 nm or 279.95 nm in Ni.

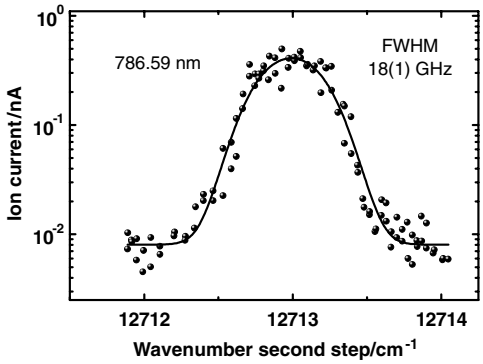

Figure 4. Frequency scan of the second excitation step of at 786.59 nm in Ni.

^{58}Ni to increase the signal strength and avoid effects from the hyperfine structure or hyperfine-induced-level mixing occurring for odd-A isotopes.

Frequency scans of the two alternative first excitation steps are shown in figure 3. Photoion currents measured versus wavenumbers are plotted on a logarithmic scale with the second and third steps fixed on resonance. Voigt profile fits to the measurements are displayed in the figure. Despite more than three times higher transition strength (5.768×10^6 Hz) for the 279.95 nm line ($J = 2 \rightarrow J = 2$) than that (1.649×10^6 Hz) of the 274.76 nm line ($J = 3 \rightarrow J = 2$) [21], the photoion current observed for the ($J = 2 \rightarrow J = 2$) transition was about ten times smaller. This must be related to different experimental conditions and cannot be explained by just considering the population difference in the $J = 2$ state. Although the available laser power of about 40 mW was insufficient for full saturation and thus only a minor contribution from power broadening was expected, broadened line widths of 16(1) GHz full width at half maximum (FWHM) and 14(1) GHz FWHM, respectively, were observed for these two first-step transitions. Figure 4 shows a frequency scan of the second excitation step at 786.59 nm. Due to the high laser power (∼1 W) available here, this step is fully saturated, resulting also in a broad resonance structure similar to that in the first excitation step with a width of 18(1) GHz FWHM. The total line width of both the first and the second steps can be explained by a composition of the Doppler broadening (∼1–5 GHz), the laser line width (∼5 GHz) and additional power broadening with a saturation parameter S_0 not too far from 1.

The former two contributions are typically described by a Gaussian line shape. To model the line shape of the saturated profile a fit of the following form has proven to be most suitable for the experimental geometry considered here:

$$y(\nu) = y_0 + A_0 \cdot \frac{S(\nu)}{S(\nu)+1}. \tag{1}$$

Here y_0 denotes the offset and A_0 is the amplitude of the fit. The experimental line shape of the transition $S(\nu)$ is dominated by laser width and Doppler broadening and thus has been approximated by the Gaussian function

$$S(\nu) = S_0 \cdot \mathrm{e}^{-0.5((\nu-\nu_c)/w)^2}. \tag{2}$$

Note that for $S_0 \ll 1$ the functional dependence $y(\nu)$ indeed converges towards a standard Gaussian. The fitting routine in all cases yielded saturation parameters S_0 in the range of 0.5–0.8, which does not yet indicate a high level of saturation and should be improved in the future.

Ionization of the different members of the Ni Rydberg series was recorded by scanning the third excitation step in the frequency range of 11 950–12 290 cm^{-1}. This produces a total excitation energy slightly above 61 264 cm^{-1}, which is only 0.03 eV below the ionization limit of Ni tabulated at 7.6398 eV = 61 619 cm^{-1} [22]. These states were then efficiently ionized inside or during the exit of the hot 'ionizer' tube. The dominant ionization mechanism cannot be identified easily. Separation of contributions from black-body radiation or collisions inside the 1700 °C hot ionizer tube as well as field ionization in the ion source–extractor region is somewhat possible. The absence of significant contributions of the latter will be discussed below. Discrimination of contributions from black-body radiation induced or collisional ionization of the high-lying states would require, e.g., a well-controlled pressure variation inside the ionizer funnel, which could not be accomplished during these measurements. Nevertheless, the signal strengths for ionization through Rydberg levels or an autoionizing level are not significantly different, which suggest that at least a major part of the Rydberg ionization must occur inside the ionizer funnel, e.g. by black-body photon impact. The assumption of a strong contribution of black-body radiation is also supported by comparing the thermal energy of about 0.25 eV at 1700 °C to the energy gap between level position and ionization limit.

An overview of the measured Rydberg resonances, which are observed for total excitation energy between 61 260 and 61 599 cm^{-1} (i.e., states located between ∼360 cm^{-1} and ∼20 cm^{-1} below the IP), is given in figure 5. The total excitation energy, indicated on top of both spectra, was obtained by adding the known excitation energy of the second excited state (49 313.814 cm^{-1}) to the measured wavenumber of the third laser. Due to experimental limitations, the measurements were interrupted in two ranges between 61 490 $\mathrm{cm}^{-1} < E_{\mathrm{Ryd}} <$ 61 497 cm^{-1} and 61 548 $\mathrm{cm}^{-1} < E_{\mathrm{Ryd}} <$ 61 574 cm^{-1} resulting in a few Rydberg levels not detected. Two levels located at 61 566 cm^{-1} and 61 568 cm^{-1} were measured on a different day with higher laser power and therefore have been rescaled, which also slightly affect their background level in the graph. An enlargement of the energy range 61 574 $\mathrm{cm}^{-1} < E_{\mathrm{Ryd}} <$ 61 599 cm^{-1} is shown in figure 6, demonstrating the high resolution of each individual peak even for these highly excited levels.

A first tentative assignment of the quantum numbers n was done in accordance with the earlier spectroscopic work of Ishikawa [19], where excitation into the Rydberg levels $n = 17$–32 was reported starting from the same second excited state as reported here. Unfortunately, due to low resolution and apparently no proper wavelength calibration in that earlier study, the published data therein are only given in a somewhat qualitative figure. As no quantitative

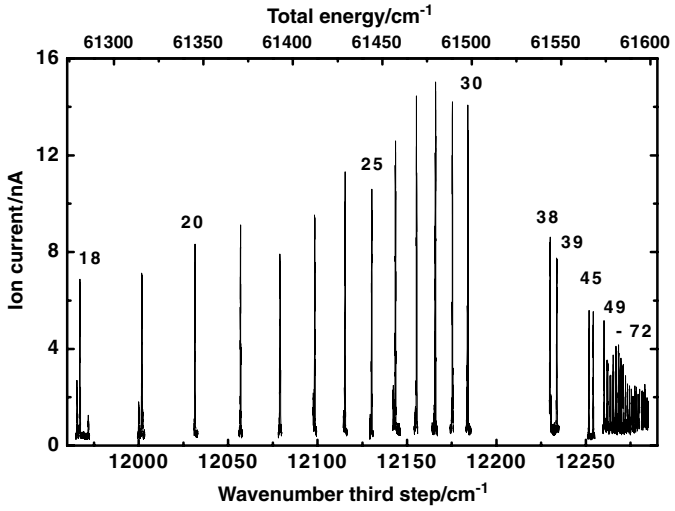

Figure 5. Ni Rydberg series as a function of the third excitation step wavenumber. Total excitation energies are given on the top of the graph and some tentative quantum numbers n are indicated as described in the text.

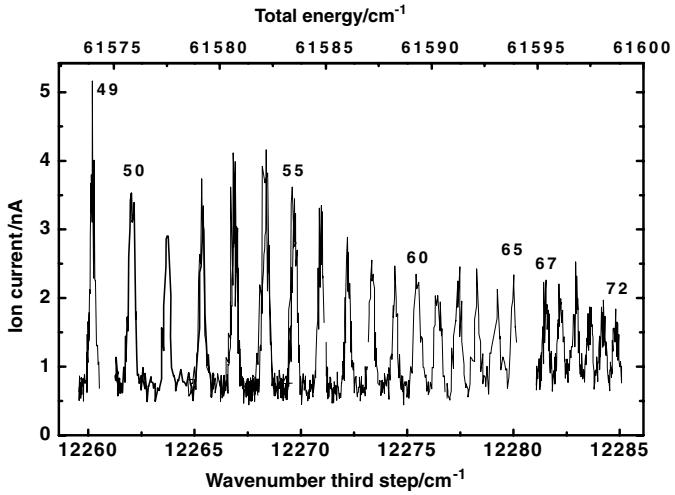

Figure 6. Zoom of the well-resolved spectrum of higher n Rydberg levels in Ni, demonstrating the high resolution of the measurement. Upper and lower horizontal scales are stretched by about a factor of 10 with respect to figure 5.

analysis of level positions or series assignment was attempted there, only a qualitative calibration of the quantum numbers of $n = 18$–30 with a precision in the level positions of about 3 cm^{-1} could be obtained. Thus, an independent verification of this n assignment was attempted by linking our measured data to known lower lying levels, i.e. the series heads, from literature through a Rydberg fit. This extrapolation provides semi-empirical theoretical level positions for all observed states up to $n = 72$, and the extension of the series towards higher states allows determination of the ionization potential with high accuracy.

For a proper assignment of the individual series the following approach was used, again using the J_1 K coupling according to [20]. Starting with the excitation from the even parity level $3d^9$ ($^2D_{5/2}$) 4d $^2[7/2]_3$, we assume that most of the odd-parity Rydberg levels populated via dipole radiation dominantly belong to either the $3d^9$ ($^2D_{5/2}$) nf $^2[7/2]^\circ_{3,4}$ or $^2[9/2]^\circ_4$ series or alternatively to the $3d^9$ ($^2D_{5/2}$) np $^2[7/2]^\circ_{3,4}$ series. Alternatively, the rearrangement of the core to $3d^8$ 4s, which is commonly observed in the Ni spectrum, might lead to a variety of additional accessible terms of odd parity with $J = 2$, 3 or 4. Nevertheless, we expect from comparison to other atomic systems that this rearrangement will significantly reduce the transition probability and that at least all strong levels observed here belong to one of the three series involving $3d^9$ mentioned above. For the case of the $3d^9$ ($^2D_{5/2}$) nf $^2[7/2]^\circ_{3,4}$ series, or alternatively, the $^2[9/2]^\circ_{4,5}$ series, quasi-degeneracy in energy is observed for similar n already for the two lowest candidates of $n = 4$ and 5. Also for the $3d^9$ ($^2D_{5/2}$) np $^2[7/2]^\circ_{3,4}$ series, the lowest levels with $J = 3$ and 4, respectively, are very close to energy for each individual n level $n = 4$, 5 and 6. For both p- and f-series no more levels have been identified so far.

The fit of level positions used a Rydberg formula of type

$$E_n = E_{\mathrm{IP}} - \frac{R_{\mathrm{M}}}{(n - \delta(n))^2}, \tag{3}$$

where the reduced-mass Rydberg constant is given by

$$R_{\mathrm{M}} = \frac{M}{m + M} \cdot R_\infty \tag{4}$$

and $\delta(n)$ is the quantum defect. Here, m and M are the electron and nuclear masses, respectively. $\delta(n)$ is approximated in second order in $1/(n - A)$ using the well-established Ritz expansion [23, 24]

$$\delta(n) = A + \frac{B}{(n - A)^2}, \tag{5}$$

where A is a constant offset and B is the n-dependent slope in the form of an inverse parabola. Both terms account for the shielding of the Coulomb potential of the nucleus by the core electrons. Note that $\delta(n)$ is determined by an appropriate choice of n modulo 1. Thus proper assignment of the absolute value of n is only obtained from additional information, i.e. from the known series head positions.

An additional additive term to equation (3) could be used to account for the Stark effect caused by the electrostatic extraction field of the mass separator. As discussed in detail, e.g., by Fabre and Haroche [26], this takes the form

$$E_{\mathrm{field}} = c_{\mathrm{S}} \cdot (n - \delta(n))^7, \tag{6}$$

where c_{S} is a constant. While this electric field term could have large influence on the IP position, significantly shifting it to lower values, its contribution to individual level positions, especially well below $n = 72$, is much smaller. The electric field strength at the location of ionization in our experiment is neither constant nor precisely known, and a considerable contribution from the strong acceleration field of the mass separator of up to $\sim$1 kV cm^{-1} was suspected. Thus this additional Stark term was tentatively considered in corresponding fits to the data with c_{s} being treated as a free parameter. The resulting change in the fitted energy positions as well as the resulting IP determined via Rydberg convergence amounted in no case to more than $\Delta(E_{\mathrm{IP}})_{\mathrm{Rydberg}} \approx 0.01$ cm^{-1}. This is more than one order of magnitude smaller than the experimental precision of our measurements. This negative finding of a sizeable field shift was backed up by an analysis of the ion pulse shape and according simulation

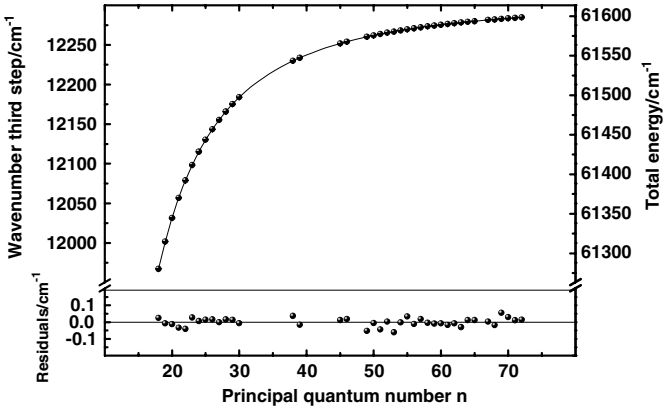

Figure 7. Experimentally determined energetic positions of Ni Rydberg levels, the fit uses the Rydberg formula discussed in the text. Experimental errors are well below the size of the data points. Residuals are shown at the bottom; note the scaling change on the vertical axis.

calculations, which will be published in a forthcoming article. Considerable field ionization in the extraction field would result in a significant, short prepeak in the photoion pulse structure, as has been observed, e.g., by Lettry *et al* in time-resolved analysis of laser ionization in the ISOLDE RILIS [27]. Contributing less than 1% to the overall photoion current, this temporal prepeak had no importance in our measurement. From the data, we could conclude that in our experiment ionization is almost exclusively taking place inside the extended transfer tube-ionizer assembly where the residual electric field is well below 1 V cm^{-1}. The ions then travel into the extraction electric field. Thus, ionization via field-induced tunnelling or any other sizeable perturbation of the atomic energy levels or polarization of the atom by Stark effect has been excluded for our experimental conditions.

For preparation of the Rydberg analysis, each resonance peak observed in the third excitation step scans was fitted individually. As this third step was not fully saturated, a Lorentzian line shape was used as a sufficiently good representation simplifying the numerical expense. The individual energy positions were fitted afterwards jointly using equation (3) with the ionization potential E_{IP} and both quantities A and B of the quantum defect (equation (5)) as free fit parameters. A χ^2 value of 1.17 was obtained, which confirms the correctness of level positions determined as well as error size. Absolute energetic positions of the Rydberg levels were calculated by adding the energy of the second excited state of 49 313.814 cm^{-1}. Results for excitation wavenumbers and total energy are shown in figure 7 together with the Rydberg fit curve (3) versus the tentatively assigned principal quantum number n. Experimental errors as well as the fit errors are well below the size of the data points, and thus residuals are given at the bottom of the graph in a strongly enhanced scale. For a detailed discussion of errors we refer to the following section.

For an attempt of a conclusive assignment of the measured levels to either the p- or the f-series, the two possible series heads and the lowest members as given in table 1 were inserted into our analysis and quantum defects were analysed in corresponding fits. In general, the development of the quantum defect $\delta(n)$ is well investigated and understood for numerous series and in various spectra, as discussed e.g. in detail in [23] for the clear spectrum of neutral caesium.

Quantum defects extracted from our data and three different fits to the data are given in figure 8. There the data are given as a function of $n^* = n - \delta(n)$, to enable presentation of both

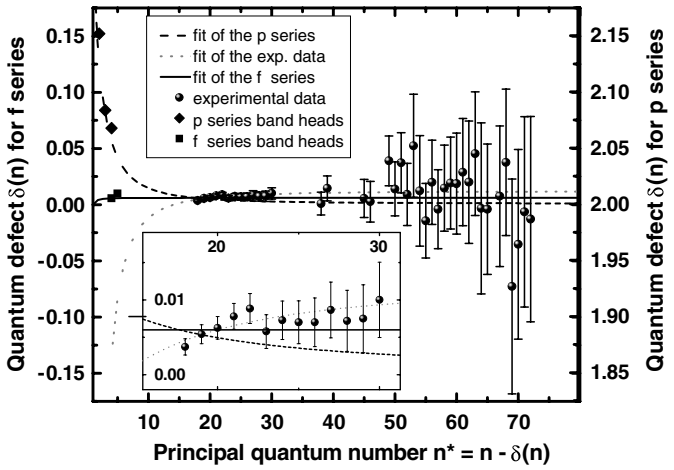

Figure 8. Quantum defects $\delta(n)$ for the measured Rydberg levels obtained from the Rydberg fit to the level positions. For series assignment band heads and low-lying known members for the p- and f-series, respectively, are considered and corresponding additional fit curves are given. Left-hand vertical scaling is for the f-series, right-hand scaling for the p-series. Fit parameters and inlay as discussed in the text.

Table 1. Energetic positions and quantum defects of level heads and other known members for the p- and f-series in question [20].

Spectroscopic notation	Level position [20]	Quantum defect
$3d^9\,(^2D_{5/2})\,4p\,{}^3F^\circ_4$	29 480.989 cm^{-1}	2.152
$3d^9\,(^2D_{5/2})\,5p\,{}^3F^\circ_4$	48 715.586 cm^{-1}	2.084
$3d^9\,(^2D_{5/2})\,6p\,{}^2[7/2]^\circ_4$	54 544.313 cm^{-1}	2.068
–	–	–
$3d^9\,(^2D_{5/2})\,4f\,{}^2[7/2]^\circ_4$	54 741.636 cm^{-1}	0.0056
$3d^9\,(^2D_{5/2})\,5f\,{}^2[7/2]^\circ_4$	57 213.433 cm^{-1}	0.0099

series in the same diagram. Note the different vertical scaling for the f and p-series quantum defect, given on the left-hand side and right-hand side axes of the graph, respectively.

The figure clearly shows through the large-error bars that extraction of $\delta(n)$ values from energetic positions of individual levels is very sensitive to the experimental precision. This is particularly true for the higher n states, where the $1/n^2$ dependence in equation (5) rapidly increases the uncertainty in the $\delta(n)$ values calculated from the experimental level positions. The experimental data thus are most meaningful for the mid-range quantum numbers $n =$ 18–30, for which an enlarged view is given in the inlay. Both diagrams show three different fits. The grey dotted line marks the fit used for the extraction of the quantum defect $\delta(n)$ considering only the experimental data. This leads to the fit parameters $A = 0.012(2)$ and a negative value of $B =$ –2.4(6), corresponding to a weakly increasing trend of $\delta(n)$ with n. An additional fit to the experimental data including the f-series head and lowest states from the literature is represented by the black solid line, while the experimental data including the p-series head and one additional level are fitted by the black dashed line. The quantum defect of the f-series is basically constant around $\delta(n) = 0$, represented by the almost vanishing fit parameters $A = 0.006(1)$ and $B = -0.006(9)$, again being slightly negative. As expected, the

p series shows a well-pronounced effect of shielding for low n, which leads to fit parameters of $A = 2.001(6)$ and a large and significantly positive $B = 2.20(2)$). Thus the trend observed in the experimental data towards increasing $\delta(n)$ contradicts the p-series development, while the f-series fit shows quite acceptable agreement in trend and size. The inlay expresses this fact clearly. Furthermore, this assignment confirms the choice of the principal quantum numbers n in accordance with Ishikawa [19]. Thus we conclude that the Rydberg levels discussed here most likely can be identified as members of the degenerate $3d^9\,(^2D_{5/2})\,nf\,^2[7/2]^\circ_{3,4}$ or $^2[9/2]^\circ_4$ series, and we have adopted the principal quantum numbers accordingly. In the present work, we thus have newly and precisely determined the energy positions of 38 of these Rydberg levels in the range of $n = 18$–72 with only a few missing candidates in the range of $n = 30$–37, $n = 40$–44 and $n = 47$, 48 and $n = 66$. Energetic positions of all levels are given as a function of the quantum number in table 2. The experimental error is dominated by the precision in the calculation of the total energy, given as the sum of the three individual excitation steps. We compared the energetic positions extracted from the measured data for the first two excitation steps to the literature values of the first and second excited states of 36 600.791 cm^{-1} and 49 313.814 cm^{-1}, respectively, from [20]. In all measurements a precision and correctness of better than 0.1 cm^{-1} is found for each step. This value even corresponds to a conservative estimation of the fit precision of about 10% of the peak FWHM in figures 3 and 4, which we assumed to account for the occasionally limited statistics. The uncertainty in the calibration of the third step wavenumbers is again determined by the accuracy of the wavemeter. This has again been estimated conservatively to amount to 0.1 cm^{-1}, including the much smaller uncertainties from the fit of each resonance, which in all cases are well below 0.01 cm^{-1}. Summing these error contributions leads to an overall uncertainty of 0.14 cm^{-1} for the total energy of each Rydberg level. As discussed below, this value must also be considered for the resulting ionization potential from the fitting procedure.

3.2. Determination of the ionization potential of nickel

The Rydberg series $3d^9\,(^2D_{5/2})\,nf\,^2[7/2]^\circ_{3,4}$ or $^2[9/2]^\circ_4$ discussed so far, both converge towards the same, lowest series limit. Thus the fit to the Rydberg–Ritz formula yields a rather precise value for the first ionization potential of Ni. For this determination, careful consideration of experimental errors is also necessary. Errors arise in the precision of individual peak positions of Rydberg states extracted from the Voigt fits as discussed above as well as in the fitting routine of the Rydberg–Ritz formula. In addition, a possible slight detuning of the first two optical excitation steps from resonance during the measurement could lead to a shift in the third step excitation wavenumbers and thus must be taken into account. To ensure highest precision, and to disentangle these individual error contributions, the fit of the series limit of the third excitation step was carried out by directly using the experimental values and errors of the third step excitation. This fit results in a value of $E_{3\text{rd step}}(n \to \infty) = 12\,305.96(2)$ cm^{-1} for the series limit for excitation from the second excited state, only considering error contributions from the width of the individual resonances and from the fitting routine but disregarding any systematic error in the wavelength. The ionization potential is finally determined by adding the known level energy of the second excited state of 49 313.814 cm^{-1}. Again, both additional calibration errors concerning the excitation of the first two steps and the correctness of the third step wavenumber must be considered, corresponding to a quadratically summed error of 0.14 cm^{-1} for the precision of an absolute value of the ionization potential by this experiment. We obtain E_{IP} (Ni) = 61 619.77(14) cm^{-1}, which is about a factor of 7 more precise than, but in good agreement with, the earlier value of $E_{IP} = 61\,619.1(10)$ cm^{-1}, determined by Page and Gudemann [22].

Table 2. Level positions of the measured members of the degenerate $3d^9$ ($^2D_{5/2}$) nf $^2[7/2]^\circ_{3,4}$ or $^2[9/2]^\circ_4$ series in Ni, giving the total excitation energy versus the principal quantum number n. Errors of the peak fits are given, indicating the much higher relative precision of the data.

Quantum number n ($3d^9$ ($^2D_{5/2}$) nf $^2[7/2]^\circ_{3,4}$ or $^2[9/2]^\circ_4$ series)	Energetic position (this work) (cm^{-1})
18	61 280.95(14)
19	61 315.63(14)
20	61 345.27(14)
21	61 370.76(14)
22	61 392.87(14)
23	61 412.24(14)
24	61 429.15(14)
25	61 444.11(14)
26	61 457.36(14)
27	61 469.16(14)
28	61 479.74(14)
29	61 489.23(14)
30	61 497.77(14)
–	–
38	61 543.79(14)
39	61 547.58(14)
–	–
45	61 565.58(14)
46	61 567.92(14)
–	–
49	61 574.01(14)
50	61 575.86(14)
51	61 577.53(14)
52	61 579.19(14)
53	61 580.64(14)
54	61 582.13(14)
55	61 583.53(14)
56	61 584.77(14)
57	61 586.01(14)
58	61 587.15(14)
59	61 588.24(14)
60	61 589.28(14)
61	61 590.26(14)
62	61 591.22(14)
63	61 592.10(14)
64	61 593.00(14)
65	61 593.81(14)
–	–
67	61 595.33(14)
68	61 596.03(14)
69	61 596.78(14)
70	61 597.41(14)
71	61 598.02(14)
72	61 598,62(14)

3.3. Comparison of ionization via Rydberg and autoionizing states

Besides excitation of high-lying Rydberg levels, we searched for autoionizing levels in the vicinity of the ionization limit to optimize the ionization yield. Notwithstanding the complex

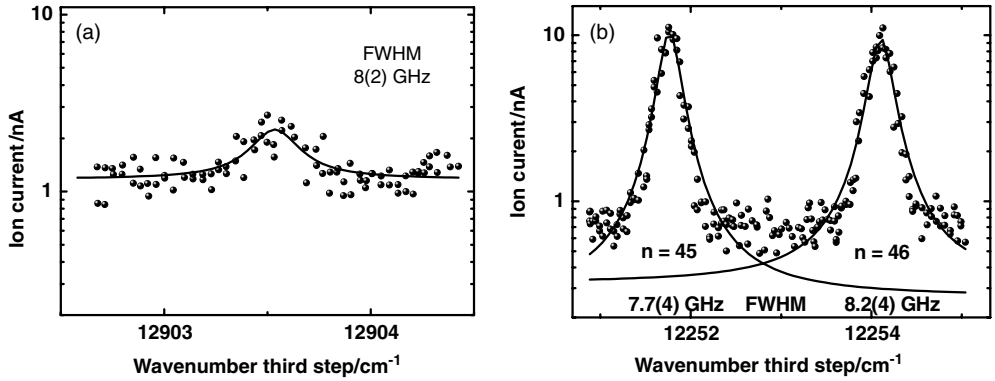

Figure 9. (*a*) Autoionizing level at 62 217.31 cm^{-1} compared to (*b*) the $n = 45$ and 46 Rydberg levels, both given versus the excitation wavenumber in the third step.

spectrum of Ni, we found only one weak indication for an autoionizing state of odd parity in the spectral region investigated up to more than 500 cm^{-1} above the ionization limit. This potential autoionizing resonance at 62 217.31(14) cm^{-1} is shown in figure 9(*a*); it exhibits a low-resonance enhancement of only about a factor of 2. Quite unexpectedly, also a rather narrow bandwidth of only 8(2) GHz, corresponding to a width typically observed for a bound state resonance, was found. Thus we suspected that this resonance could possibly be ascribed to an alternative excitation scheme in the second excitation step and corresponding ionization enhancement. Nevertheless, such a level, which could provide proof of this assumption, has not been identified previously in literature [20]. For a comparison of the ionization enhancement using this resonance to the values obtained through Rydberg excitations, the $n = 45$ and 46 Rydberg levels are shown in figure 9(*b*). The spectra were measured under essentially identical experimental conditions with respect to ionizer temperature, atomic vapour density at the location of ionization, laser intensities and mass separator transmission.

These Rydberg states are about a factor of 2 weaker than the strongest ones observed around $n \approx 27$. Showing a rather similar line width, they exhibit resonance enhancements of about a factor of 15 with a slightly lower background. Thus ionization of Ni via the autoionizing level in our experiment is at least a factor of ∼10 less efficient than by Rydberg ionization. The autoionizing level might nevertheless be of importance for experimental conditions, where ionization of the Rydberg levels is not possible. This consideration applies, for example, when laser excitation/ionization is taking place inside a cold surrounding, i.e. an ion trap structure used for cooling and bunching in the laser ion source trap approach LIST [28].

3.4. Spectroscopy of the Rydberg series in germanium

Spectroscopic investigations similar to those for nickel were also carried out on germanium, using the most abundant isotope ^{74}Ge. The three-step excitation scheme used there is sketched in figure 10. This scheme, starting in the $J = 2$ level of the $4s^2\ 4p^2\ ^3P_{0,1,2}$ ground state configuration, leads to a spectrum that is much simpler than that of Ni. In addition, odd-parity Rydberg series has been extensively studied earlier, resulting in the knowledge of the $4s^2\ 4p$ *n*s, *n*d and *n*g states for principal quantum numbers up to $n_s \rightarrow 43$, $n_d \rightarrow 70$ and $n_g \rightarrow 15$, and a very precise literature value for the first ionization potential Ge II ($^2P^\circ_{1/2}$) of $E_{IP} =$ 63 713.24(10) cm^{-1} [29]. Our laser scans for the first and second excitation steps are shown in

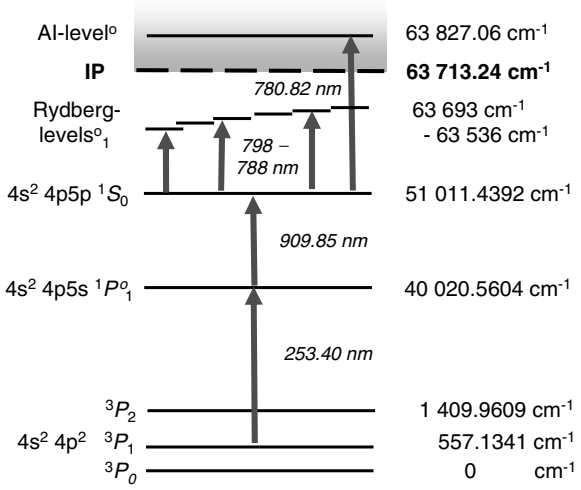

Figure 10. Scheme used for three-step resonance excitation of Ge.

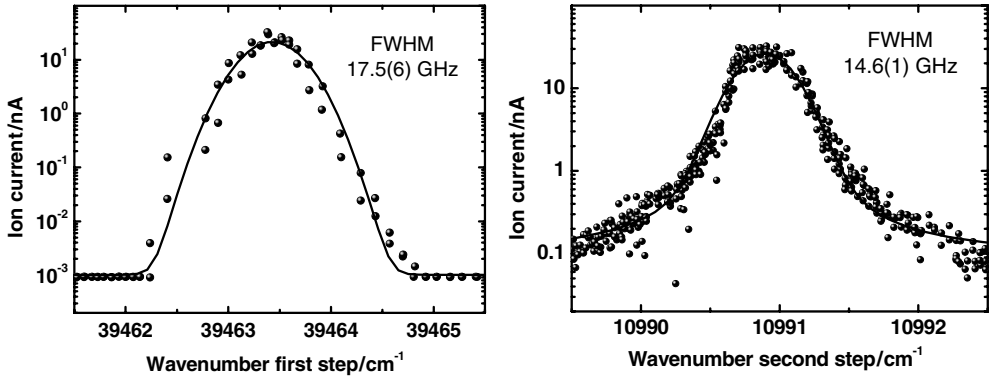

Figure 11. Scan of the first and second excitation step in Ge.

figure 11, again plotted using a logarithmic scale and fitted with a Voigt profile. Line widths of about 15 GHz were obtained again governed by the Gaussian contribution.

The third laser step was scanned over a 170 cm^{-1} spectral range with only minor gaps during a search for Rydberg states and an efficient ionization scheme. Altogether 40 strong Rydberg states were measured and most of them could easily be identified by comparison with the literature [20]. Starting from the second excited $4s^2$ 4p 5p $^1S_0$ level, seven members of the Rydberg series $4s^2$ 4p ns $(1/2, 1/2)_1^\circ$ for $n = 32$–35 and $n = 47$–49 and 33 members of $4s^2$ 4p nd $(1/2, 3/2)_1^\circ$ in the range of $n = 26$–78 were recorded. For both series, the principal quantum number n of each resonance could easily be assigned using identifications in the literature. Figure 12 shows the measured and assigned spectrum for the region around 63 580–63 610 cm^{-1}, where members of the s- and d-series are well resolved. The variation in the line intensities is ascribed to strong-level mixing in this n-region.

A plot of spectra taken close to the ionization potential is given in figure 13, again showing the third step excitation wavenumber at the lower and the total energy at the upper horizontal axes. Two large gaps in the measurements result from experimental limitations in the laser

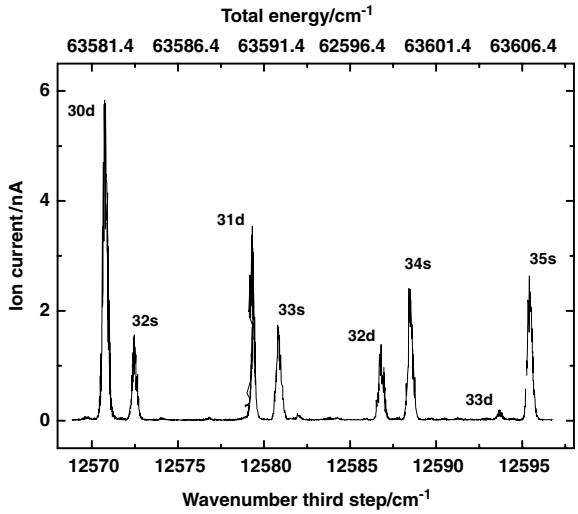

Figure 12. $J = 1$ spectrum of the third excitation step in the spectral region around 12 570–12 600 cm^{-1} (lower scale), corresponding to overall excitation energy of 63 580–63 610 cm^{-1} (upper scale). Members of the s- and d-series are well resolved and assigned according to [20].

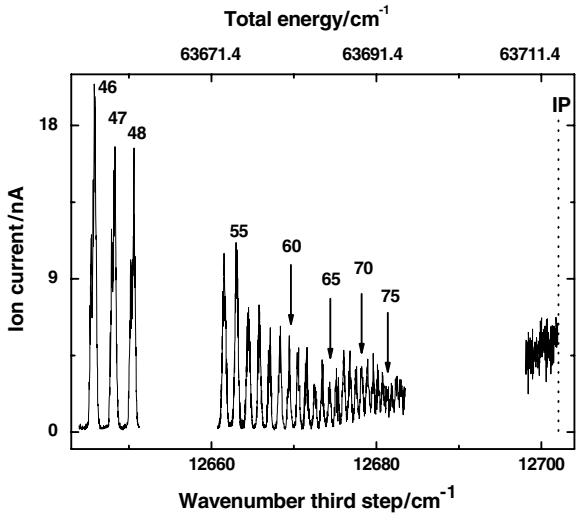

Figure 13. $J = 1$ spectrum of the third excitation step in the region around 12 540–12 720 cm^{-1} close to the ionization potential IP, which is indicated. The range corresponds to an overall excitation energy of 6 3650–63 730 cm^{-1}. Members of the d-series are well resolved and assigned according to [20].

scan range. For $J = 1$ only the d-series is listed in literature for this spectral range, and level assignments were made as indicated. The three peaks assigned to $n = 46$–48 clearly exhibit double-peak structures. From the Rydberg fits the left-hand side peaks could be clearly identified as the $n = 47$–49 members of the s-series.

An overview on the level energies of both the $4s^2\,4p\,ns\,(1/2,\,1/2)^\circ_1$ and $4s^2\,4p\,nd\,(1/2,\,3/2)^\circ_1$ series members investigated is shown in figure 14, including corresponding Rydberg fits

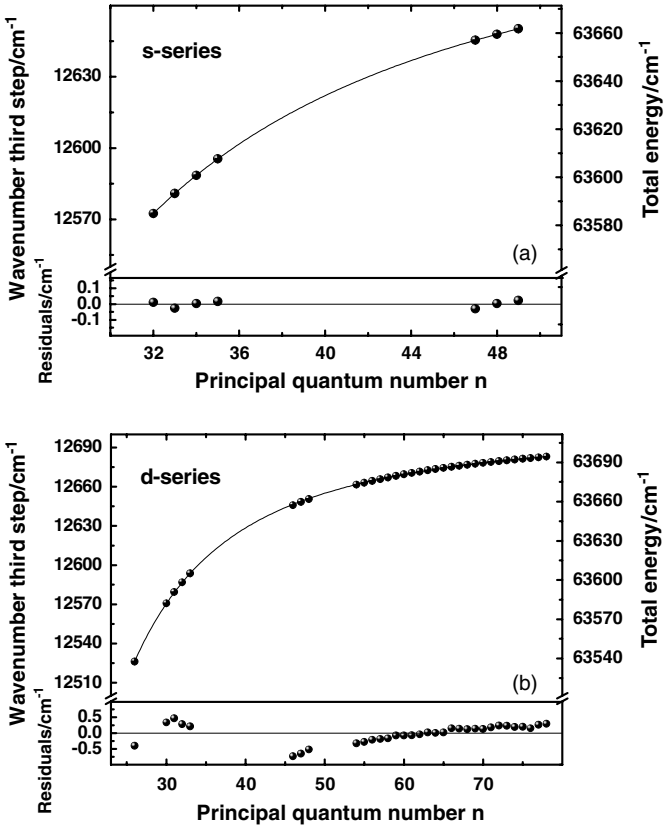

Figure 14. Measured level positions of (a) the $4s^2$ 4p ns (1/2, 1/2)$^\circ_1$ and (b) the $4s^2$ 4p nd (1/2, 3/2)$^\circ_1$ Rydberg series in Ge, wavenumber of third excitation step (left) and total excitation energy (right) versus principal quantum number n. The residuals between data and fit are given at the bottom; note the change in the scaling of the axis.

Table 3. Level positions of the $4s^2$ 4p ns (1/2, 1/2)$^\circ_1$ Rydberg series in Ge, giving the total excitation energy versus the principal quantum number n. Literature values and deviations from our data are given for comparison where available.

Principal quantum number n ($4s^2$4p ns (1/2, 1/2)$^\circ_1$ -series)	Energy (this work) (cm^{-1})	Energy (NIST) [20] (cm^{-1})	Deviation (cm^{-1})
32	63 583.91(14)	63 583.80	0.11
33	63 592.29(14)	63 592.40	−0.11
34	63 599.94(14)	63 600.03	−0.09
35	63 606.88(14)	63 607.02	−0.17
–			
47	63 656.83(14)	–	
48	63 659.33(14)	–	
49	63 661.67(14)	–	

and the residuals. Quantitative level energies are given in tables 3 and 4 including a comparison to earlier literature values, where available. This gave confidence in our measurements and evaluations, as in all cases this intercomparison provided a perfect agreement between our

Table 4. Level positions of the $4s^2\ 4p\ nd\ (1/2,\ 3/2)^\circ_1$ Rydberg series in Ge, giving the total excitation energy versus the principal quantum number n. Where available, literature values and deviations from our data are given for comparison.

Principal quantum number n ($4s^2\ 4p\ nd\ (1/2,\ 3/2)^\circ_1$ -series	Energy (this work) (cm^{-1})	Energy (NIST) [20] (cm^{-1})	Deviation (cm^{-1})
26	63 537.72(14)	63 537.76	−0.04
–			
30	63 582.21(14)	63 582.23	−0.02
31	63 590.77(14)	63 590.62	0.15
32	63 598.23(14)	63 598.15	0.08
33	63 605.13(14)	63 605.06	0.07
–			
46	63 657.28(14)	63 657.22	0.06
47	63 659.72(14)	63 659.69	0.03
48	63 662.06(14)	63 661.94	0.12
–			
54	63 672.99(14)	63 673.04	−0.05
55	63 674.48(14)	63 674.47	0.01
56	63 675.92(14)	63 675.93	−0.01
57	63 677.24(14)	63 677.24	0.00
58	63 678.49(14)	63 678.56	−0.07
59	63 679.75(14)	63 679.74	0.01
60	63 680.86(14)	63 680.84	0.02
61	63 681.92(14)	63 682.03	−0.10
62	63 682.96(14)	63 683.10	−0.14
63	63 683.97(14)	63 684.03	−0.05
64	63 684.86(14)	63 684.87	−0.01
65	63 685.75(14)	63 685.70	0.05
66	63 686.71(14)	63 686.70	0.01
67	63 687.49(14)	63 687.40	0.09
68	63 688.23(14)	–	
69	63 688.97(14)	–	
70	63 689.64(14)	–	
71	63 690.36(14)	–	
72	63 691.05(14)	–	
73	63 691.65(14)	–	
74	63 692.19(14)	–	
75	63 692.76(14)	–	
76	63 693.25(14)	–	
77	63 693.87(14)	–	
78	63 694.40(14)	–	

data and the literature values with statistically distributed discrepancies of about 0.1 cm^{-1} well within the size of our experimental errors. Thus any systematic deviation of our wavelength calibration could be excluded and the proper estimation of the error size was confirmed independently.

The Rydberg fit according to (3) and (5) to the seven members of the $4s^2\ 4p\ ns\ (1/2,\ 1/2)^\circ_1$ Rydberg series, including the three novel ones of $n = 47$–49, yields an ionization potential for Ge of 63 713.30(14) cm^{-1} with slightly lower precision but in full agreement with the literature value of 63 713.24(10) cm^{-1} [20]. The precision of the fit is demonstrated by the small residuals as given in figure 14(*a*). In contrast, a similar fit to the 33 members of the $4s^2\ 4p\ nd\ (1/2,\ 3/2)^\circ_1$ series measured, including the 11 newly measured levels of $n = 68$–78 does

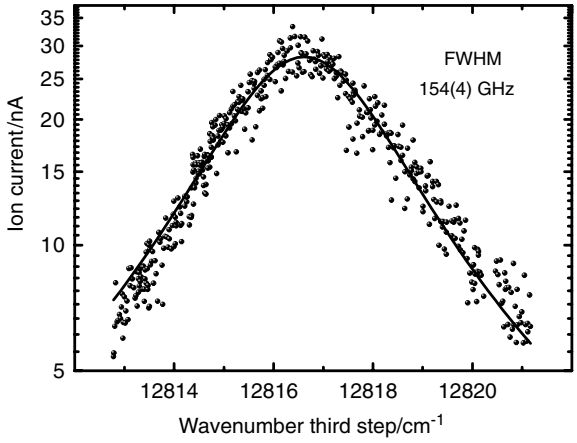

Figure 15. Laser scan of the third excitation step across the autoionizing resonance at 63 827.06 cm^{-1} in Ge.

not lead to satisfying results. It delivers a value of the ionization potential for the d-series equal to 63 712.77(14) cm^{-1}, which is slightly but significantly below the expectation. The value is achieved with unrealistic parameters of $A = 1.34$ but $B = –260$ in equation (5). Also the residuals show an unexplained systematic trend and an unexpected large size with deviations up to 0.8 cm^{-1}, well above the experimental error, especially in the region of n around 47. This discrepancy is by far exceeding the precision in the reproduction of the literature values for the series members with $n < 67$. Thus the d-series generally excludes the application of the Rydberg formula in its simple form of equations (3) and (5), which is ascribed to the occurrence of strong-level mixing but not further studied in this work. Nevertheless, in both cases of the s- and d-series the expected general trend of the quantum defect is verified at least qualitatively: for the s-series the quantum defect decreases with increasing n due to the decreasing penetration of the electronic core by the valence electron, while for the d-series, a weak increase of its quantum defect represents the positive trend of polarization of the core by the valence electron for larger n.

Finally, the third laser excitation was again scanned across and above the ionization potential to search for autoionizing resonances. A particularly strong resonance was identified at 12 816.62(2) cm^{-1}, corresponding to an overall excitation energy of 63 827.06(14) cm^{-1} located about 125 cm^{-1} above the ionization limit. The resonance is shown in figure 15. The broad Lorentzian line shape of this autoionizing structure (154 GHz) indicates a strong coupling of the state to the continuum. A photoion current of approximately 30 nA was obtained, which was considerably higher than the maximum current of about 20 nA obtained via Rydberg levels. We conclude that contrary to the case of Ni, the multi-step resonance ionization in Ge is most easily and efficiently performed through this autoionizing state.

4. Conclusion and outlook

Together with [9], this work completes the description of a first experiment directed towards the development of a laser ion source for future rare isotope facilities at ORNL. Efficient ionization schemes for the elements Ni and Ge were established and investigated spectroscopically. Special attention was given to the ionizing step. Rydberg states and autoionizing states were considered for both the elements. Only for Ge an autoionizing level with reasonable resonance

enhancement could be observed. Rydberg series were recorded for both the elements and quantum-defects as well as precise ionization potentials were calculated. Individual series was identified and principal quantum numbers could be assigned to each resonance and confirmed by interrelation to known low-lying levels. In the case of Ni, spectroscopic studies to search for a strong autoionizing resonance suitable for Ti:sapphire laser systems will be carried out in the near future.

Acknowledgment

This research has been sponsored by the US Department of Energy, under contract DE-AC05–00OR22725 with UT-Battelle, LLC, as well as the German Bundesministerium für Bildung und Forschung under contract 06Mz197.

References

[1] Kluge H J, Ames F, Ruster W and Wallmeroth K 1985 *Proc. Acc. Radioact. Beams, WS, TRI* vol 85 p 119
[2] Ames F, Brumm T, Jäger K, Kluge H J, Suri B M, Rimke H, Trautmann N and Kirchner R 1990 *Appl. Phys.* B **51** 200
[3] Köster U 2002 *Nucl. Phys.* A **701** 441
[4] Köster U, Fedoseyev V N and Mishin V I 2003 *Spectrochim. Acta* B **58** 1047
[5] Catherall R, Fedoseyev V N, Köster U, Lettry J, Suberlucq G, Marsh B A and Tengborn E 2004 *Rev. Sci. Instrum.* **75** 1614
[6] Fedoseyev V N, Köster U, Weisman L, Mishin V I, Horn R, Huber G, Lassen J, Wendt K, Fedorov D V and (ISOLDE Collaboration) 2003 *Nucl. Instrum. Methods Phys. Res.* **204** C 353
[7] Fedoseyev V N, Marsh B A, Fedorov D V, Köster U and Tengborn E 2005 *Hyperfine Interact.* **162** 15
[8] Rauth C, Geppert Ch, Horn R, Lassen J, Bricault P and Wendt K 2004 *Nucl. Instrum. Methods Phys. Res.* B **215** 268
[9] Liu Y *et al* 2006 *Nucl. Instrum. Methods Phys. Res.* B **243** 442
[10] Geppert Ch, Bricault P, Horn R, Lassen J, Rauth C and Wendt K 2004 *Nucl. Phys.* A **746** 631
[11] Moore I D *et al* 2005 *J. Phys. G: Nucl. Part. Phys.* **31** 1499
[12] Stolz A *et al* 2004 *Nucl. Phys. A* **746** 54
[13] Pfeiffer B, Kratz K L, Thielemann F K and Walters W B 2001 *Nucl. Phys.* A **693** 282
[14] Ball G C *et al* 2005 *J. Phys. G: Nucl. Part. Phys.* **31** S1491
[15] Hyland B *et al* 2006 *Phys. Rev. Lett.* **97** 102501
[16] Gruening C, Huber G, Kratz J V, Passler G, Trautmann N, Waldek A and Wendt K 2001 Resonance ionization spectroscopy 2000 *AIP Conf. Proc.* **584** 255
[17] Yi J, Geppert Ch, Horn R and Wendt K 2003 *Japan. J. Appl. Phys.* **42** 5066
[18] Horn R, Geppert Ch, Kratz J V, Passler G, Rauth Ch, Trautmann N and Wendt K *Preprint*, University of Mainz at press
[19] Ishikawa T 2000 *J. Appl. Phys.* **87** 7617
[20] Ralchenko Yu, Jou F-C, Kelleher D E, Kramida A E, Musgrove A, Reader J, Wiese W L and Olsen K 2007 *NIST Atomic Spectra Database (version 3.1.2)*, http://physics.nist.gov/asd3 (National Institute of Standards and Technology, Gaithersburg, MD)
[21] Kurucz R L and Bell B 1995 *Atomic Line Data Kurucz CD-ROM No. 23* (Cambridge, MA: Smithsonian Astrophysical Observatory)
[22] Page R H and Gudeman C S 1990 *J. Opt. Soc. Am.* B **7** 1761
[23] Ritz W 1903 *Phys. Z.* **4** 406
[24] Hartree D 1928 *Proc. Camb. Phil. Soc.* **24** 426
[25] Fabre C and Haroche S 1983 *Rydberg States of Atoms and Molecules* ed RF Stebbings and FBD Dunning (Cambridge: Cambridge University Press) p 132
[26] Weber K H and Sansonetti C J 1987 *Phys. Rev.* **35** 11
[27] Lettry J, Catherall R, Köster U, Georg U, Jonsson O, Marzari S, Fedosseev V and and the ISOLDE Collaboration 2003 *Nucl. Instrum. Methods Phys. Res.* B **204** 363
[28] Wendt K, Blaum K, Brueck K, Geppert Ch, Kluge K H, Mukherjee M, Schwarz S and Wies K 2004 *Nucl. Phys.* A **746** 47
[29] Sugar J and Musgrove A 1993 *J. Phys. Chem. Ref. Data* **22** 1213

Available online at www.sciencedirect.com
ScienceDirect
Nuclear Instruments and Methods in Physics Research B 266 (2008) 681–700
NIM B
Beam Interactions with Materials & Atoms
www.elsevier.com/locate/nimb

Off-line studies of the laser ionization of yttrium at the IGISOL facility

T. Kessler [a,*], I.D. Moore [a], Y. Kudryavtsev [b], K. Peräjärvi [a,c], A. Popov [d], P. Ronkanen [a], T. Sonoda [a,1], B. Tordoff [e], K.D.A. Wendt [f], J. Äystö [a]

[a] Department of Physics, University of Jyväskylä, P.O. Box 35 (YFL), FI-40014 Jyväskylä, Finland
[b] Instituut voor Kern-en Stralingsfysika, University of Leuven, Celestijnenlaan 200 D, B-3001 Leuven, Belgium
[c] STUK – Radiation and Nuclear Safety Authority, P.O. Box 14, FI-00881 Helsinki, Finland
[d] Petersburg Nuclear Physics Institute, Gatchina, St-Petersburg 188350, Russia
[e] Nuclear Physics Group, Schuster Laboratory, Brunswick Street, University of Manchester, Manchester M13 9PL, UK
[f] Institut für Physik, Johannes Gutenberg-Universität, 55099 Mainz, Germany

Received 27 September 2007; received in revised form 8 November 2007
Available online 23 December 2007

Abstract

A laser ion source is under development at the IGISOL facility, Jyväskylä, in order to address deficiencies in the ion guide technique. The key elements of interest are those of a refractory nature, whose isotopes and isomers are widely studied using both laser spectroscopic and high precision mass measurement techniques. Yttrium has been the first element of choice for the new laser ion source. In this work, we present a new coupled dye–Ti:Sapphire laser scheme and give a detailed discussion of the results obtained from laser ionization of yttrium atoms produced in an ion guide via resistive heating of a filament. The importance of not only gas purity, but indeed the baseline vacuum pressure in the environment outside the ion guide is discussed in light of the fast gas phase chemistry seen in the yttrium system. A single laser shot model is introduced and is compared to the experimental data in order to extract the level of impurities within the gas cell.

PACS: 29.25.Ni; 32.80.Fb; 34.50.Lf; 41.85.Ar

Keywords: Laser resonance ionization; Yttrium; Molecular formation; Ion guide

1. Introduction

In the early 1980s the ion guide technique was developed in Jyväskylä in order to overcome limitations related to the standard ISOL technique, namely the inability to produce refractory elements and a need for complicated ion source-target combinations. A full description of the IGISOL technique may be found in [1,2] and references therein, however it will be briefly described here. A projectile beam impinges on a thin target and the reaction product nuclei recoil out into a chamber filled with a buffer gas, usually helium. The highly-charged ions slow down, thermalize in the gas and continuously change their charge state until a significant fraction, 1–10% reach a 1^+ charge state. This fraction is transported out of the ion guide with the gas flow and is guided through a radio frequency sextupole ion guide (SPIG) before being injected into the mass separator. The key advantage of the IGISOL technique is the short evacuation time of radioactive nuclei (≈ms timescales) resulting in a chemical insensitivity of the ion guide.

However, for certain reactions, there are two inherent deficiencies in this ISOL method, namely the lack of Z-selectivity and a poor efficiency. These drawbacks become more important in fission reactions involving the light-ion

* Corresponding author. Tel.: +358 14 2602440; fax: +358 14 2602351.
E-mail address: thomas.kessler@phys.jyu.fi (T. Kessler).
[1] Present address: Instituut voor Kern-en Stralingsfysika, University of Leuven, Celestijnenlaan 200 D, B-3001 Leuven, Belgium.

0168-583X/$ - see front matter © 2007 Elsevier B.V. All rights reserved.
doi:10.1016/j.nimb.2007.11.076

bombardment of heavy actinide targets. The plasma generated from the passing of the fission fragments through the stopping gas can lead to severe recombination losses. This deteriorates the ion guide efficiency.

In order to overcome the deficiencies arising from the plasma effect and to provide Z-selectivity an alternative approach to the IGISOL technique has been pioneered by the LISOL group at the University of Leuven [3,4]. By allowing the recoiling product nuclei to neutralize a selective re-ionization process is achieved using lasers. This work has demonstrated the feasibility of combining high-power low-duty cycle lasers with the ion storage capability of a high pressure gas cell. By employing a pulsed primary beam with a time structure that is optimized for the evacuation time of the ion guide highly efficient ionization has been reached for Ni [5,6] and several other refractory elements, such as Co, Rh and Ru [7]. The presence of only weakly ionized plasma means that the gas flow rates to transport ions out of the ion guide can be significantly lower than in the standard IGISOL system. This permits heavier stopping gases to be used such as Ar, leading to a better stopping efficiency for recoiling nuclei. In comparison to the standard IGISOL however, the laser ion guides suffer from longer delay times. It was demonstrated in these studies that the gas impurity plays a significant role down to the level of 1 ppb.

At the IGISOL facility, a similar project is underway to combine the selectivity and efficiency of a laser ion source with the fast (sub-millisecond) evacuation and chemical non-selectivity of the ion guide technique [8]. The fast evacuation, extreme purity and substantially improved intensities will push existing spectroscopic experiments further from stability than is presently possible. Several techniques are being developed. One is similar to that pioneered by the Leuven group as discussed above. A second technique, developed in order to provide the highest selectivity, will ionize the neutral atoms after extraction from the gas cell, within the SPIG [9]. This latter technique will not be discussed. In this paper we concentrate on issues leading to the development of the "standard" ion guide laser ion source.

The first element for study with the new laser ion source is yttrium. This is a very challenging element due to the chemical reactivity of yttrium ions and atoms to any impurities within the gas cell. It has been chosen as a first case based on a need to extend a rich programme at the IGISOL facility of ground state nuclear structure studies in the refractory region [10–12]. From a physics point of view there is a threefold motivation to study yttrium: nuclear astrophysics interests, weak interaction physics (the super-allowed beta decay of the $N = Z$ nucleus, ^{78}Y) and nuclear structure physics.

In order to probe the properties of nuclei on either side of the valley of beta stability different reaction mechanisms are used to populate the isotopes of interest. Heavy-ion reactions can be used to produce nuclei close to the $N = Z$ line in regions that play a special role in nuclear astrophysics since the rapid-proton (rp) capture process passes right through them. The properties of these neutron-deficient nuclei, in particular the masses and beta decay half-lives, are needed to perform rp-process nuclear reaction network calculations. Due to the relatively low production yields using heavy-ion reactions at IGISOL the laser ion source aims to improve the yield of the nuclei of interest. Light-ion induced fission reactions are used in order to probe exotic nuclei on the neutron-rich side of the valley of stability. The resultant problem in this reaction is not the efficiency of producing the nuclei, rather the often overwhelming background from more abundantly produced isobars. In this case the laser ion source aims to provide a means of being more selective.

2. Experimental set-up

In order to selectively ionize yttrium, resonance ionization schemes were developed involving two experimental components, the laser system of choice and an atomic beam source. Resonance ionization spectroscopy was performed off-line using a compact atomic beam unit, discussed in Section 2.2. For a realistic study of laser ionization of yttrium a laser ion guide was loaned from the LISOL group at Leuven. The details of this ion guide will be discussed in Section 2.3. In order to control the arrival time of the lasers such that evacuation and molecular formation within the ion guide may be studied, a mechanical shutter mechanism developed for this purpose is described in Section 2.4.

2.1. Laser system

The laser ion source facility at Jyväskylä employs a novel twin laser system, based on a combination of high-resolution titanium sapphire lasers and dye lasers, each with independent pump lasers. A more detailed description of the laser facility may be found in [8], however will be briefly described with emphasis on the lasers used specifically for the laser ionization of yttrium. Fig. 1 shows the optical layout of the laser system used in this work. In the configuration shown in Fig. 1, the primary (master)

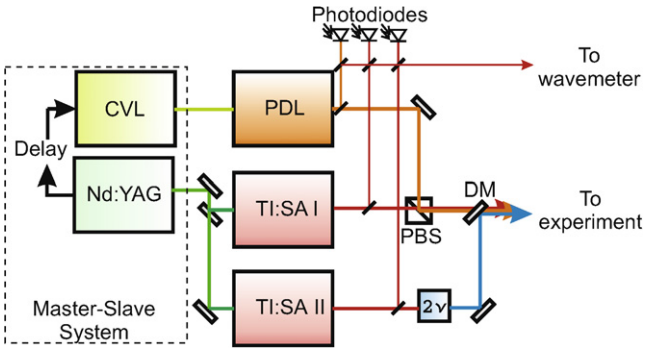

Fig. 1. Laser system used for the resonant ionization of yttrium. PBS, polarising beamsplitter cube and DM, dichroic mirror.

laser system, an all-solid-state system, consists of a high repetition rate (12 kHz) diode-pumped Nd:YAG laser (Lee Laser, LDP-200MQG) with up to 100 W average laser power in the second harmonic, pumping two tunable titanium sapphire (Ti:Sa) lasers. The average output power of Ti:Sa I was 1.5 W, while that of Ti:Sa II was 3 W. This increase in laser power for the second Ti:Sa is attributed to a double-sided pumping technique, described in detail in [13]. Each laser contains a Lyot filter and etalon for generation of narrow bandwidth laser radiation (≈5 GHz). The temporal synchronization of the 30–50 ns pulses from the two lasers was achieved using remote-controlled Q-switches installed into each individual resonator. In order to access a variety of first excited states in yttrium, second harmonic generation with a beta-barium borate (BBO) crystal extended the fundamental IR range of the Ti:Sapphire laser into the blue region of the electromagnetic spectrum. With approximately 3 W fundamental power from Ti:Sa II a typical frequency doubled power of ≈400 mW was achieved.

The second laser system (slave) consists of a high repetition rate copper vapour pump laser (Oxford Lasers LM100X(KE)) with up to 45 W average laser power. Two fundamental lasing wavelengths are attainable with this laser, 511 nm (green) and 578 nm (yellow), with an approximate power ratio of 2:1. The 511 nm laser light is used to pump a pulsed dye laser (Spectra Physics PDL-3) running with a DCM dye dissolved in methanol, enabling an output wavelength range of 610–660 nm. The typical output power during this work was 400 mW at around 640 nm. This is lower than expected based on the typical powers achieved at ISOLDE using a copper vapour laser pumped dye laser, however the speed of the JYFL dye circulators was optimized for low repetition rate pumping only [14]. As of the time of writing, the circulators have been upgraded and the typical pulsed dye laser power is now close to 1 W at 640 nm. The linewidth and temporal pulse length of the dye laser are 1 GHz and 20 ns, respectively.

Fast silicon photodiodes (Roithner LaserTechnik SSO-PD-Q-0.25-5-SMD) are used to monitor the temporal overlap of the individual lasers. Fig. 2 shows the temporal profiles of the Nd:YAG, the copper vapour laser, a single Ti:Sapphire laser and the dye laser. In the case of a free-running system the lasers do not fire synchronously due to the different build-up times needed to attain a population inversion within the two types of gain media. This would result in the inability to achieve a stepwise resonant excitation (lifetimes of typical atomic excited states are a few ns). While the Q-switches are used to attain a temporal overlap between the Ti:Sapphire lasers, the copper vapour laser can be triggered by the master clock of the Nd:YAG laser via a delay such that the dye laser pulse is synchronized with the Ti:Sa pulses.

Approximately 1% of the output power from each laser is used for monitoring the temporal overlap and wavelength. An optical fibre couples the individual lasers into

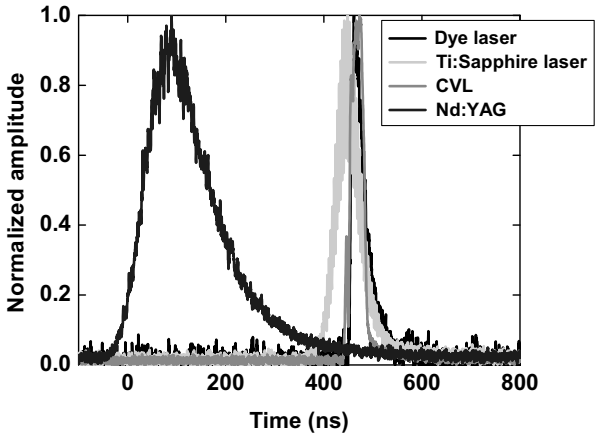

Fig. 2. Temporal profiles of the two pump lasers, a single Ti:Sapphire laser and a pulsed dye laser.

a commercial wavemeter (High Finesse, WS-6) for wavelength determination. The main beams from the dye laser and Ti:Sa I are coupled together spatially using a polarizing beamsplitter cube (PBS, see Fig. 1) and are then overlapped with the frequency doubled laser light of Ti:Sa II using a dichroic mirror (DM). The laser beams are sent overlapped both temporally and spatially either to an atomic beam unit, described in the following section, or to the IGISOL as described in Section 3 for experiments.

2.2. Atomic beam unit

An atomic beam unit (ABU) was used to test the relative efficiency of several ionization schemes for atomic yttrium. A schematic diagram of the ABU is shown in Fig. 3. The operational principle is based on a crossed-beams technique. A sample of yttrium was loaded into a tubular tantalum furnace with a length of 50 mm, an outer diameter of 2 mm and a thickness of 0.5 mm. The sample is vaporized

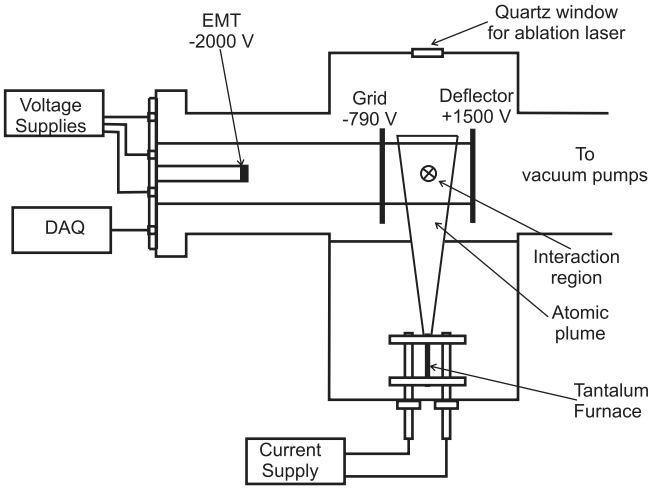

Fig. 3. Schematic diagram of the atomic beam unit used for testing resonant ionization schemes. The principle is described in the text. The applied voltages have been optimized experimentally to provide the maximum ion counting rate on the EMT.

under vacuum ($\approx 1 \times 10^{-5}$ mbar) using a resistive heating current of approximately 50 A. An atomic plume of yttrium passes through the laser interaction region and is stepwise resonantly excited and ionized. An electrostatic field, generated by a deflector-grid system using the potentials as shown in Fig. 3, is used to extract the ions towards an electron multiplier tube (EMT) (ETP Electron Multipliers, Model AF150H). At an operating potential of −2 kV the multiplier gain is specified to approximately 3×10^7. Fast negative ion signals from the EMT are amplified, discriminated from the background noise and shaped for counting using a PC counter card. A labview-based computer control program is used to scan the laser wavelengths while simultaneously recording the ion signal. In order to reduce background counts from the fast edges of the Q-switches and the thyratron of the CVL laser, the signal is gated on the arrival time of the ions after the lasers fire.

In order to study more refractory elements that cannot be extracted from the oven via resistive heating, the experimental setup can be modified in order to produce a pulsed atomic plume of the species of interest. In this case the tantalum oven is removed in favour of a metallic "boat" mounted on an electric motor with a variable rotation speed. A quartz window on the top of the ABU enables the delivery of a low repetition rate (20 Hz) 1064 nm Nd:YAG laser operating with a typical pulse energy of 25 mJ, to be used for laser ablation [15]. In this running mode the ion signal is additionally gated on the trigger pulse of the ablation laser.

2.3. Laser ion guide

In this work a laser ion guide loaned by the LISOL group at Leuven was used and is shown in Fig. 4. The body of the ion guide is made from brass and all parts are sealed with indium enabling heating of the whole guide up to 120 °C. The volume of the gas cell is split into two parts, the main volume into which a primary beam enters and where a filament can be mounted and a channel of 10 mm in diameter and 26 mm in length, termed the ionization channel. The conductance of the exit hole of 0.5 mm diameter in helium gas is equal to 0.112 l/s. An evacuation time for the whole guide of 480 ms can be estimated by dividing the stopping chamber volume by the exit-hole conductance. The evacuation time of the ionization channel is similarly calculated and is 18 ms. Compared to the ion guides used in JYFL these extraction times are considerably longer due to the smaller exit hole, however an increase in time is necessary in order to achieve neutralization of the recoiling nuclei. Atoms of different elements can be produced inside the cell by the resistive heating of a corresponding filament, either made directly from the chosen element, or with material evaporated onto the surface of a filament. In this work, an yttrium filament of thickness 3.75 mg/cm^2 cut into a bowtie configuration with a diameter of 3 mm at the narrowest part was mounted within the guide towards the rear (not shown in Fig. 4). Laser light

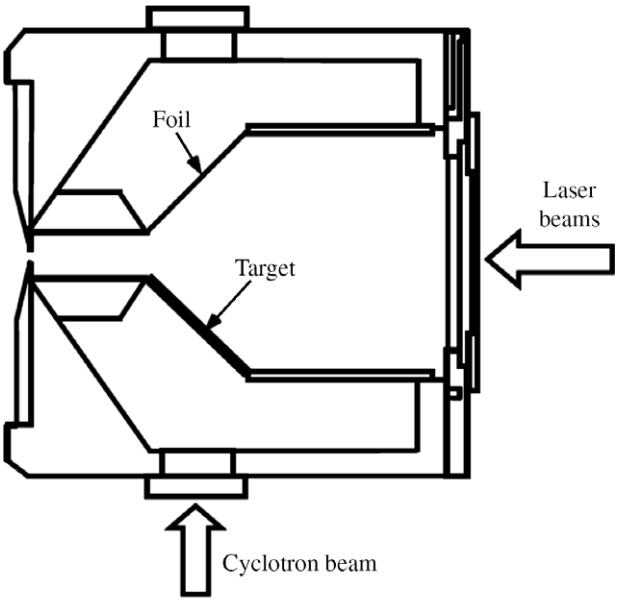

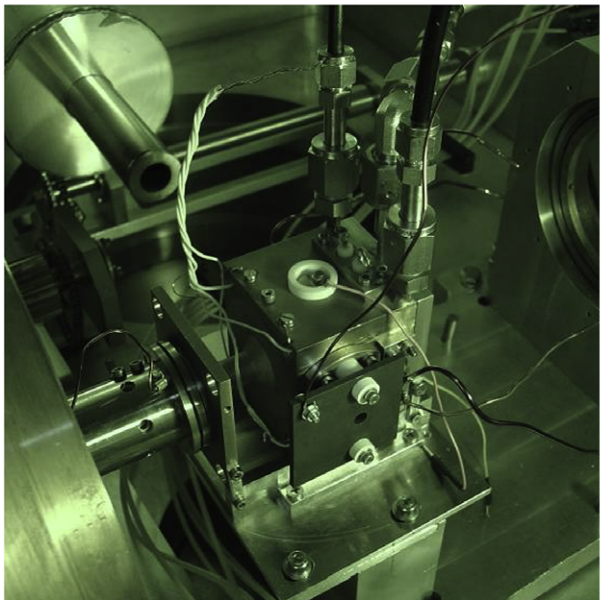

Fig. 4. Schematic view of the laser ion source loaned by the LISOL group at Leuven (top) and a picture of it installed in the IGISOL chamber (bottom). In the picture the lasers enter from the right, and the SPIG is seen directly in front of the ion guide exit hole. The beam pipe towards the beam dump can be seen in the top of the picture.

enters the cell longitudinally through a sapphire window in the rear, ionizing neutral atoms along the axis. The diameter of the laser beam is brought to a gradual focus of approximately 3 mm near the exit hole.

2.4. Control of the laser to ion guide arrival time

The temporal control of the spatially overlapped lasers is mandatory for the investigation of the evacuation time and the timescales of any subsequent molecular formation within the ion guide. For low repetition rate laser systems with a duty cycle lower than the evacuation time of the

ion guide a DAQ trigger can be used. However, this is not possible for high repetition rate systems such as that used in this work and therefore a fast shutter mechanism was designed to provide the required timing information. As the required time resolution is restricted by the bin width of the data readout system (≈0.5 ms) a mechanical solution is still feasible and preferred over a fast (ns) but rather expensive light switch in a typical polarizer/analyzer setup in combination with a Pockels cell as proposed in [16]. In this experiment a modified version of the mechanical shutter design detailed in [17] was used. A conventional broken hard-drive disk was dismantled and the readout arm of the disk was connected to an electrical switching circuit providing a shutter current of roughly 500 mA. The shutter arm was extended with a thin aluminium plate to decrease the shutter time (Fig. 5).

The direction of the feeding current could be switched by using standard TTL logic. The performance of the shutter was tested using a continuous wave helium–neon laser beam focused in the same manner as that of the Ti:Sapphire laser beams. The light was detected by a fast photodiode behind the shutter. A typical delay time of 5–14 ms between the TTL signal and the shutter mechanism was observed depending on the alignment of the shutter with the laser beam, with an overall jitter of 50 μs. A shutter time of roughly 20 μs was achieved. The long delay of the shutter does not allow for laser "on" timescales of less than 15 ms. Therefore, to reach the single laser shot level for a high repetition rate laser system (each laser pulse is separated by 100 μs in a 10 kHz system) a double shutter system was recently designed. In this approach two shutters were put in series into the laser beam so that shutter 1 opens the laser path and shutter 2 blocks the path. The damping of the movement of the shutters was improved to reduce the jitter of the shutter mechanism. By choosing an appropriate TTL logic a pulse of laser radiation of 100 μs was achieved as illustrated in Fig. 6.

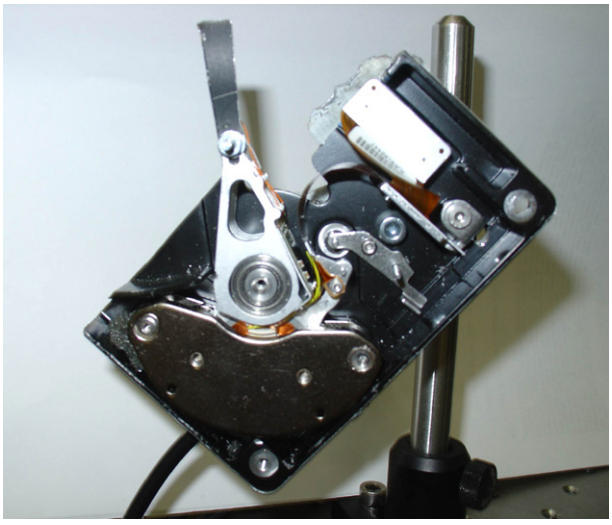

Fig. 5. A photograph of the modified hard disk with extended readout arm used for mechanical control of the laser arrival time at the ion guide.

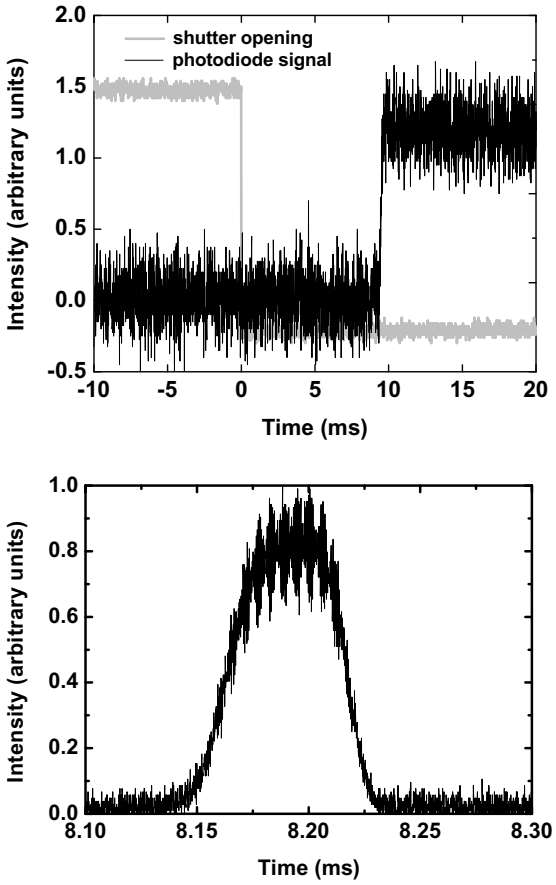

Fig. 6. The delay between the TTL for the single-arm shutter and the detection of the helium–neon laser (top). With the double shutter system in place the control of the temporal overlap is of the order of 100 μs (bottom).

3. Results and discussion

The off-line development described in this paper has led to a number of results which will be discussed within the following individual subsections. Section 3.1 details the work carried out within the atomic beam unit on yttrium using the mixed dye–Ti:Sapphire laser system to provide a suitable resonance ionization scheme to be tested in the laser ion guide. The initial work done in the LISOL gas cell is detailed in Section 3.2, including first studies on the gas phase chemistry performed in March 2006. In these studies the buffer gas was contaminated due to a leak in the gas feeding line. Therefore the experiment was repeated in March 2007. Section 3.3 highlights the results obtained from this second experiment, and furthermore discusses the effect of introducing impurities into the IGISOL chamber via a controlled leak valve.

3.1. Development of a laser ionization scheme for yttrium

The search for an appropriate resonant ionization scheme is of crucial importance prior to working with a laser ion source. Ideally, as in the case of the work dis-

cussed in this article, off-line searches for new schemes can be done without the need for an ISOL facility. The most important priority is the comparison of the efficiencies of the ionization schemes. For details on the theory behind resonance ionization and related experiments involving this technique the reader is referred to [18,19]. An atomic energy level scheme showing the transitions investigated in this work is shown in Fig. 7.

The atomic excitation energy of the levels labeled on the right of Fig. 7 is given in units of cm^{-1}. The energy levels are identified on the left side and are given in the Russel–Saunders-coupling notation with the atomic structure labeled as $^{2S+1}L_J$, where S is the total spin, L the total orbital angular momentum and J the quantum number of the spin–orbit interaction. The wavelengths of the transitions between the levels are denoted in units of nm and are given as wavelength in vacuum. Next to the wavelength, the log-gf (transition strength) is listed if known from the literature [20,21].

The first resonant transition step was realized using a frequency-doubled Ti:Sapphire laser, while the second resonant step was driven by the fundamental output of a second Ti:Sapphire laser. A non-resonant ionization step was achieved by exciting the atoms across the ionization potential (IP), 50,144.275 cm^{-1}, with the frequency doubled light from the first transition. The dye laser was used to scan across the IP to search for the existence of possible auto-ionizing levels. These levels can then be used in a third resonant ionizing step and provide an enhancement in the cross section probability for ionization compared to that achieved for a simple non-resonant step.

A comparison between four different Ti:Sapphire ionization schemes tested in the atomic beam unit are shown in Table 1. A constant current of ≈53 A was supplied to the oven for the duration of the tests. In all cases the fundamental Ti:Sapphire laser power prior to frequency doubling for the first step was 2.1 W, leading to 300 mW in the second harmonic. This was high enough to achieve saturation for all first step transitions. The maximum power of the second steps varied between 1.1 W and 1.9 W. The count rate detected on the electron multiplier tube is shown in column 4 of Table 1. It is unlikely that the second step transition is being saturated and therefore it is more informative to show the ratio of the observed count rate to the power of the second step. This is calculated in the final column. Even though the laser power in the second step was lower for the $\lambda_2 = 813.71$ nm transition compared to the 813.01 nm transition, a higher ratio of count rate to second step power was achieved. This infers a larger transition strength of the 813.71 nm transition. A fifth scheme, $\lambda_1 = 404.877$ nm and $\lambda_2 = 853.114$ nm, was tested in the ion guide however showed no improvement and therefore will not be discussed further.

Table 1
Comparison of RIS schemes performed in the atomic beam unit

λ_1 (nm)	λ_2 (nm)	P_2 (W)	Count rate (s^{-1})	Count rate/P_2
407.85	839.46	1.9	4000	2105
407.85	840.21	1.4	2700	1929
414.40	813.71	1.1	4000	3636
414.40	813.01	1.4	4200	3000

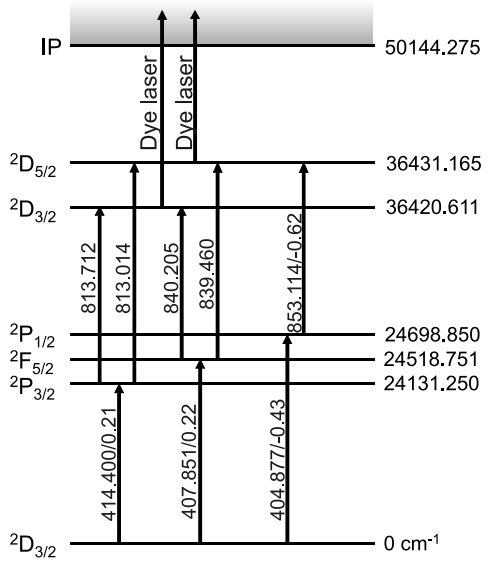

Fig. 7. Relevant atomic energy levels in yttrium and the transitions investigated in this work.

A graph showing the laser wavelength scans of the two resonant transitions from the optimum scheme of Table 1 is shown in Fig. 8. A fit of the form:

$$y(\nu) = y_0 + A_0 \cdot \frac{S(\nu)}{2(S(\nu)+1)} \tag{1}$$

with

$$S(\nu) = S_0 \cdot e^{-0.5((\nu-\nu_0)/w)^2} \tag{2}$$

was applied for the first step transition acknowledging a saturated lineshape profile dominated by the Gaussian spectral profile of the laser radiation. $S(\nu)$ denotes the frequency dependent saturation parameter, y_0 a signal offset and A_0 the signal amplitude. The factor S_0 describes the resonant saturation magnitude for a two-level system. This provides a good approximation due to the high level of saturation of the first transition compared to the second and final transitions. Fitting of the data yields a value of 49(15) for S_0, supporting the conclusion that the first step is indeed saturated. The second step was fitted with a non-saturated Gaussian function corresponding to $S_0 \ll 1$ in Eq. (2).

The pulsed dye laser (PDL) was used to search for auto-ionizing levels. Two wavelength scans were made over the range of the available dye (DCM, 610–660 nm) starting from the excitation levels populated by the two second step Ti:Sapphire transitions at 36,420.611 cm^{-1} and 36,431.165 cm^{-1}. A summary of the lasers used for the different transitions and the laser powers measured at the entrance to the atomic beam unit is shown in Table 2. Fig. 9 shows the

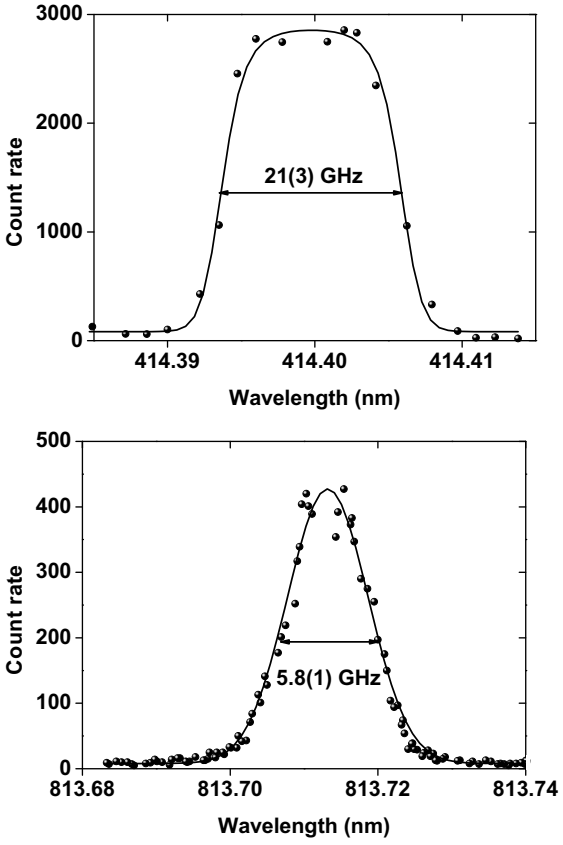

Fig. 8. Resonant laser wavelength scans of the most efficient first (top) and second (bottom) step transitions. The full-width at half-maximum (FWHM) value is shown.

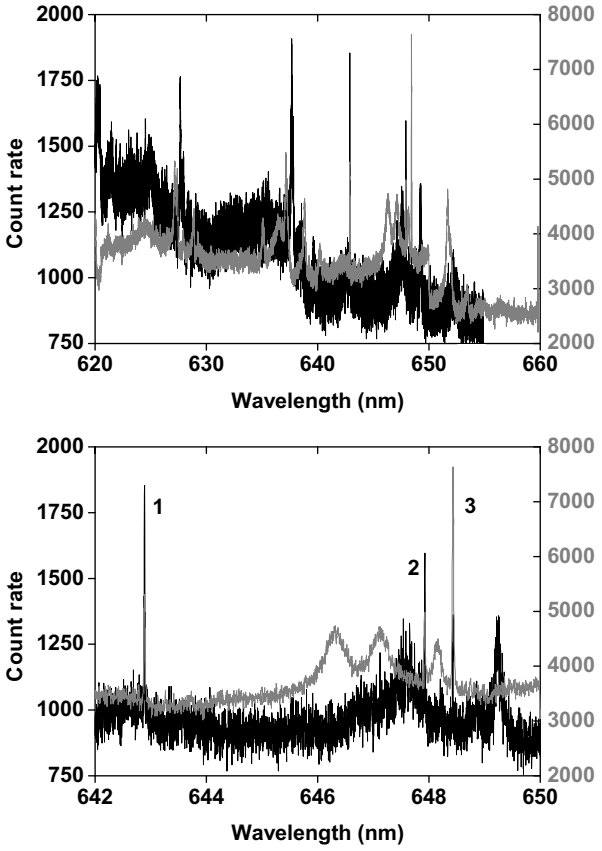

Fig. 9. Dye laser spectrum starting from excitation levels of 36,431.165 cm^{-1} (black line, left scale) and 36,420.611 cm^{-1} (grey line, right scale), respectively. The top figure shows the full dye laser scan, while the spectrum on the bottom is a magnified part highlighting the three narrow resonances of interest (see text for discussion).

Table 2
The mixed Ti:Sapphire–dye transitions and laser powers obtained at the entrance to the atomic beam unit

Step	λ (nm)	Power at ABU (mW)	Laser
1	414.40	240	Ti:Sa 2nd harmonic
2	813.71	750	Ti:Sa
2	813.01	1050	Ti:Sa
3	619–655	200–400	Dye (DCM)

resultant dye laser spectrum starting from excitation levels of 36,431.165 cm^{-1} (black line, left scale) and 36,420.611 cm^{-1} (grey line, right scale), respectively. A spectrum of resonances of differing intensities and widths was observed. The numerous broad structures were identified as auto-ionizing states. This was confirmed by blocking the second excitation step. If the signal drops to the background level then the second step is needed to perform the triple resonant ionization process. Three narrow resonances were also identified in both third step dye laser scans overlapping at exactly the same wavelength. These are labeled as 1, 2 and 3 in the more detailed view of the dye laser spectrum shown in the bottom figure of Fig. 9. It was concluded after further investigation that these resonances correspond to the dye laser driving a second step transition from 24,131.250 cm^{-1} to levels at 39,686.0 cm^{-1}, 39,565.1 cm^{-1} and 39,553.0 cm^{-1} (resonances 1, 2 and 3, respectively) not shown in Fig. 7. The atomic levels at 39,686.0 cm^{-1} and 39,565.1 cm^{-1} are previously known, while the level at 39,553.0 cm^{-1} is newly discovered.

The difference in linewidth between the second step excitation driven by the dye laser and that of a standard auto-ionizing resonance is shown in Fig. 10. Due to the non-saturated transitions both resonances were fitted by a Lorentzian lineshape profile on a linear background of the form:

$$y(v) = y_0 + b(v - v_c) + A \cdot \frac{w}{4(v - v_c)^2 + w^2}. \quad (3)$$

The linear background has a slope b and a constant offset y_0 at the centroid frequency v_c, while the last term is a Lorentzian with a full-width at half-maximum (FWHM) of w and amplitude A. The auto-ionizing resonance has a FWHM of 184(10) GHz. This can be compared to a FWHM of 11.3(7) GHz in the second scan, more typical of a bound state resonance.

Table 3 details the effects of blocking the different laser transitions, using the dye laser driving the new second step transition from the atomic level at 24,131.250 cm^{-1} to the level at 39,553.0 cm^{-1}. It is clear that the first step in the

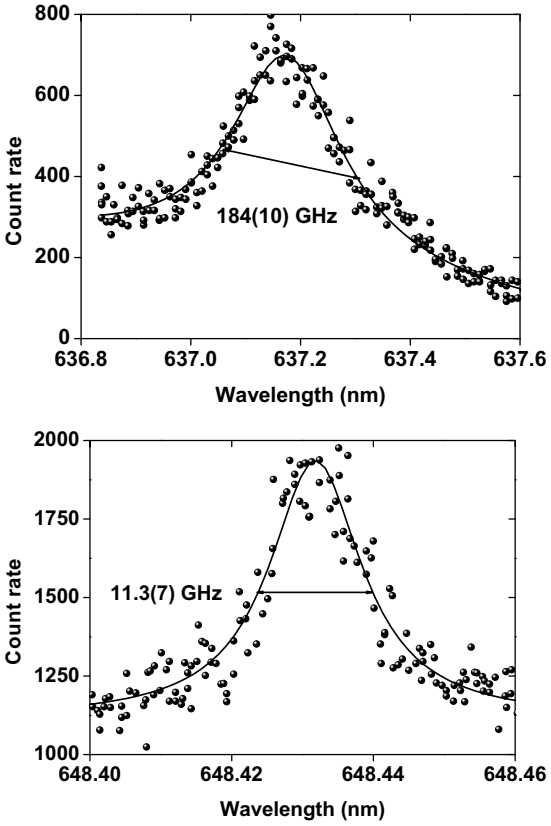

Fig. 10. The top figure shows a dye wavelength scan and the corresponding lineshape profile of a typical auto-ionizing state in yttrium, while the resonance on the bottom corresponds to a scan and lineshape fit of the bound state resonance peak 3 in Fig. 9.

Table 3
The effect of blocking Ti:Sa I (414.40 nm), Ti:Sa II (813.71 nm) and the dye laser (648.43 nm) on the ion count rate

	Ti:Sa I 1st step blocked	Ti:Sa I 1st step only	Ti:Sa II 2nd step blocked	Dye 2nd step blocked	All lasers available
Count rate (ions/s)	0	10	600	1200	1800

scheme is pivotal. When this transition is blocked the ion signal disappears. If only the blue transition is used it is possible to have a double-blue non-resonant transition after the first step, though this is very weak, only 0.5% of the total count rate. By reducing the temperature of the oven this signal disappears and so these ions are indeed created via interaction with the laser beam. By including the second resonant Ti:Sapphire transition approximately 2/3 of the total ion signal is achieved. The main ionization pathway used in this case is then blue–IR–blue, where the final blue step is non-resonant. If the dye laser is used alone to drive a second step transition then approximately 1/3 of the total signal, 600 ions/s, is reached. In this scenario the possible ionization schemes are blue–red–blue and blue–red–red. When all three lasers are allowed to interact with the yttrium atoms, additional blue–IR–red and blue–red–IR pathways are possible, resulting in a total ion signal of 1800 ions/s.

The reason for the different rates depending on which second step laser is blocked may be due to different transition strengths, or to any efficiency differences in pumping using a dye or Ti:Sapphire laser. Future investigations on the latter possibility are needed and an atomic system will have to be found that enables the same transition wavelength to be used. In this manner the intrinsic differences between the laser systems, such as the pulse length (10 ns for a dye laser and 50 ns for a Ti:Sapphire laser) may be studied as a function of the ionization efficiency. However, for the purpose of a laser ion source, the high peak ion count rate achieved with this mixed dye–Ti:Sapphire scheme has led to the use of the twin laser system for the majority of the following studies in this article. Indeed, to our knowledge this is the first time that two second step transitions have been used for a laser ionization scheme. The spectroscopic capability of the combined laser system enables a maximal wavelength coverage representing a unique tool for on-line laser ion source facilities.

3.2. Ion guide laser ionization of filament-produced yttrium atoms – March 2006

Under off-line conditions yttrium laser ions are formed through the resonant excitation and ionization process of atoms evaporated from an yttrium filament, as described in Section 2.3. The ions are evacuated from the laser ion guide, transported through a radio frequency sextupole device and injected into the mass separator via stages of differential pumping. After acceleration to 30 kV the beam is mass separated by a dipole magnet, allowing separation of nuclei and contaminants with a typical mass resolving power of the order of 300–600 depending on the operational parameters of the guide and the front-end of the separator. Finally, the ions are detected on a set of multichannel plates, downstream from the separator focal plane. During transport through the ion guide there are many loss mechanisms for ions produced by laser ionization. As the atom or ion moves through the guide towards the exit nozzle it collides many times with buffer gas atoms and impurity molecules. This can result in chemical bond formation or trapping in a metastable state which both lead to losses as the laser scheme excites only from the atomic ground state.

The main loss mechanism in off-line conditions is the formation of molecules via reactions between an atom X or ion X^+ with a ligand molecule M in the presence of the buffer gas (in this case helium),

$$X^{(+)} + M \leftrightarrow X^{(+)}M^*, \tag{4}$$

$$X^{(+)}M^* + He \rightarrow XM^{(+)} + He. \tag{5}$$

The time evolution of the process of atoms or ions converting to molecules may be described by a reaction rate coefficient k ($cm^3\ s^{-1}$) and the rate equation:

$$\frac{dn}{dt} = -nk[M], \tag{6}$$

where n is the number of atoms or ions and $[M]$ the ligand molecular concentration. A corresponding time constant for the formation of the molecular ion can be defined as

$$\tau = 1/k[M]. \tag{7}$$

It is known that yttrium ions have a strong affinity towards binding with oxygen [22]. The main residual impurity in the buffer gas is water therefore the formation of YO^+ can either happen directly or via the dehydrogenation reaction:

$$Y^+ + H\text{–}O\text{–}H \rightarrow H\text{–}Y^+\text{–}O\text{–}H \rightarrow H_2Y\text{–}O^+ \rightarrow YO^+ + H_2. \tag{8}$$

This has been discussed more thoroughly in [23] for the case of titanium. Within the literature one may find a reaction rate constant $k = 4.1 \times 10^{-10}\,cm^3\,s^{-1}$ [22] for the reaction

$$Y^+ + O_2 \rightarrow YO^+ + O. \tag{9}$$

With an impurity level of 1 ppm, which corresponds to a concentration $[M]$ of $\approx 4 \times 10^{12}$ atoms/cm^3 at a helium gas pressure of 150 mbar, the reaction time τ for the formation of molecular YO^+ is 612 μs. This is a very short time in comparison to the bulk ion guide evacuation time of 480 ms and therefore it is imperative to study the effects of impurities on the yttrium laser ions and to have control over the gas purity to a level close to a ppb.

In this work, high-purity helium gas (grade 6.0, 99.9999%) supplied by Linde Gas AG, Germany, has been used. The tubes of the gas feeding lines are made of stainless steel and were baked to ≈150 °C. The gas passes through a cold trap made of activated carbon, cooled with liquid nitrogen, to remove impurities. Additional purification was provided by a getter-based purifier (Saes MonoTorr PS4-MT15-R-2). According to [23] these cleaning steps should take the gas down to the sub-ppb impurity level. The yttrium filament was continuously heated throughout the measurements and therefore atoms were continually available for laser ionization during the laser "on" period. A helium pressure of 150 mbar was used throughout the off-line studies. The ion signal from the channel plates was fed into a multi-channel analyzer (MCA), triggered by the JYFLTRAP labview control program [24] in order to study the evacuation time of the ions and corresponding molecules, with a time resolution of 655.36 μs per bin. The first evacuation time profiles showing the evolution of the yttrium laser ions and molecular formation were taken in March 2006, and are shown in Fig. 11.

The laser radiation was pulsed on for the first 90 ms of a full cycle of about 4 s. This was accomplished using the "single-arm" mechanical shutter device discussed in Section 2.4, triggered by a delayed TTL signal from the JYFLTRAP control program. A delay of ≈5 ms occurs before the first ions were detected. This was caused by a time delay in the shutter and is not related to the time-of-flight of the

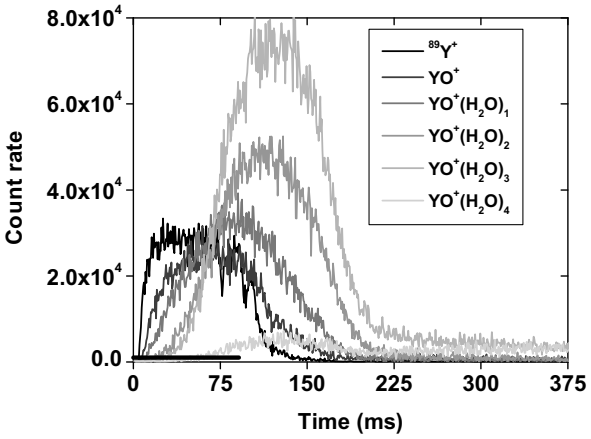

Fig. 11. Time-of-flight profiles of yttrium laser ions and corresponding molecules. The black horizontal bar along the time axis represents the period the lasers were on.

ions. It can be seen from Fig. 11 that the laser-produced Y^+ ions reach a saturation level before the lasers are turned off. The structure seen in the falling edge of the yttrium time profile is related to a "ringing" of the shutter arm which was addressed in the March 2007 data (Section 3.3) with the addition of the double-shutter device. The characteristic time to reach saturation can be related to a combination of the survival time of Y^+ via Eq. (7) against losses due to molecular formation and evacuation from the ion guide. It should be noted that the ion guide had a constant source of yttrium atoms produced from the heated filament prior to the moment of laser ionization and this level is in saturation with both evacuation from the guide and losses due to neutral atom–molecule formation. Fig. 12 shows an exponential growth curve fitted to the $^{89}Y^+$ data resulting in a value of $\tau = 5.1(4)$ ms. As the evacuation time from the ion guide as a whole is far longer than this timescale, this saturation time is indicative of the survival time of yttrium ions during evacuation against molecular formation. Using the known conductance of the exit hole (112 cm^3 s^{-1}) this saturation time translates into a corresponding effective volume for laser ionization of

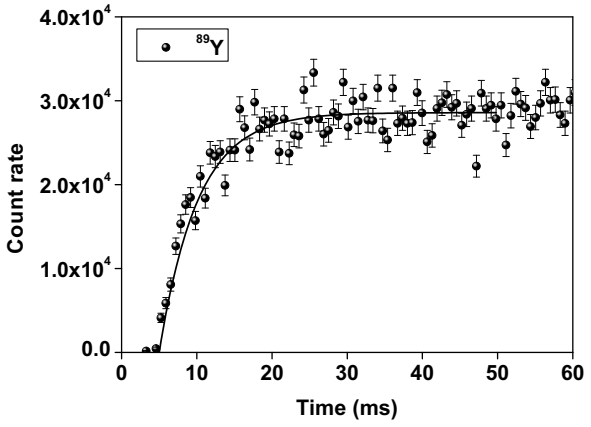

Fig. 12. An exponential fit of the count rate towards saturation of laser ionized $^{89}Y^+$.

$\approx 0.57\ \mathrm{cm}^3$. The laser ions which survive molecular formation are created close to the exit hole in a volume only 28% of the total volume of the ionization channel of the LISOL ion guide (Fig. 4). Ions created deeper within the gas cell have a high probability of forming molecules and thus reduce the Y^+ signal.

It can be seen from Fig. 11 that the formation of YO^+ ions is delayed with respect to the Y^+ ions, and each subsequent addition of a hydrate to the YO^+ molecule is delayed even further. The time behaviour indicates the following sequence of hydration of YO^+ ions:

$$YO^+ + H_2O \rightarrow YO^+(H_2O) \quad (A = 123), \tag{10}$$

$$YO^+(H_2O) + H_2O \rightarrow YO^+(H_2O)_2 \quad (A = 141), \tag{11}$$

$$YO^+(H_2O)_2 + H_2O \rightarrow YO^+(H_2O)_3 \quad (A = 159), \tag{12}$$

$$YO^+(H_2O)_3 + H_2O \rightarrow YO^+(H_2O)_4 \quad (A = 177). \tag{13}$$

The relative intensities, the saturation time of the Y^+ signal and the delay times of the subsequent molecules illustrated in Fig. 11 can provide information about specific impurity concentrations in an environment where the impurity level can be controlled. Although this is not the case in this work, the saturation time extracted from the experimental results can be combined with Eq. (7) to estimate an impurity level. Under the assumption that the time scale for the dehydrogenation reaction of Eq. (8) is similar to that of Eq. (9) then, with an ion guide pressure of 150 mbar helium, the impurity level is ≈ 0.1 ppm. This result was rather surprising due to the careful treatment of the gas purity, suggesting that the system was not as clean as we had expected. The bare atomic fraction of yttrium amounted to 10% of the sum of all the species shown in Fig. 11. This figure can be compared to Fig. 14 of [23] in which the gas was purified to the expected ppb level. In this figure the Ti^+ signal was scaled down by a factor of 50 to show it on the same scale as the subsequent molecules. The reaction coefficient k for Ti^+ with oxygen is $4.6 \times 10^{-10}\ \mathrm{cm}^3\ \mathrm{s}^{-1}$ [22] which is the same order of magnitude as for yttrium.

It is of interest to get a deeper understanding of the time scales of formation of individual molecules from the experimental data. One important difference between the laser system used in this work and that of the LISOL system is the repetition rate of the lasers. It is possible to study the evolution of laser ions created in the LISOL system from a single laser shot, i.e. at a repetition rate of effectively 1 Hz, in which the time between laser pulses is longer than the evacuation time of the cell. In this case a fresh portion of atoms is available before the next pulse arrives. In this work a high repetition rate laser system is used. The double-shutter mechanism discussed in Section 2.4 was used to reduce the 10 kHz laser system to 2–3 individual laser pulses, each 30–50 ns wide and separated by 100 μs. However, due to the reduced energy per pulse of the high repetition rate system the ionization efficiency was most likely too low to detect any laser ions and therefore a different treatment of the data is needed in order to study the molecular formation on single shot time scales.

The reaction rate $k[M]$ reflects the probability that a single ion will be converted into a molecule during its evacuation from the ion guide. In a 10 kHz laser system each shot provides a new sample of yttrium ions which has a probability of molecular formation. The time-of-flight profiles seen in Fig. 11 are therefore a convolution of all single-shot events, refreshed with every subsequent laser shot. The procedure to obtain the molecular reaction rates from the data is performed by applying the following four steps:

- Data from Fig. 11 are summed up to obtain an overall Y^+ signal. In this manner the sum can be thought of as the total current extracted from the ion guide before mass separation.
- A single laser shot ion evacuation profile is extracted from the summed data by taking the derivative of the overall time distribution.
- The molecular formation process is applied to the yttrium ions evacuated from a single shot.
- The single-shot data for the different molecular compounds are reintegrated to the summed data and compared with the experimental data.

In this approach it is assumed that the molecular formation process is a closed system and losses due to, for example, diffusion and neutralization with electrons caused by the passage of the laser beam are not taken into account in this simple model. One can therefore write

$$Y^+ + YO^+ + YO^+(H_2O) + YO^+(H_2O)_2 + YO^+(H_2O)_3 + YO^+(H_2O)_4 = \mathrm{const.} \tag{14}$$

According to this assumption the total sum of the data represents the Y^+ signal after evacuation from the ion guide without any molecular formation. In the second step a relationship between the summed signal, total(t) and a single laser shot, shot(t) is established. It is assumed that the atomic yttrium vapour recovers during the time t between two consecutive laser shots. This is a reasonable conclusion for two reasons: firstly, the filament is heated continuously and secondly, the product of ionization efficiency for an individual laser shot with the number of laser shots that the irradiated volume sees during the evacuation time is $\ll 1$. The total signal is therefore the integral of individual shots shifted in time

$$\mathrm{total}(t) = \int_0^{t_{\mathrm{off}}} \mathrm{shot}(t-s)\,\mathrm{d}s, \tag{15}$$

where t_{off} denotes the time when the laser radiation is turned off. This is the case in which the laser duty cycle is much smaller than the response time of the system. A single laser shot evacuation profile can be reproduced by taking the derivative of the total signal (15),

$$\begin{aligned} \tfrac{\mathrm{d}}{\mathrm{d}t}\mathrm{total}(t) &= \tfrac{\mathrm{d}}{\mathrm{d}t}\int_0^{t_{\mathrm{off}}} \mathrm{shot}(t-s)\,\mathrm{d}s \\ &= \mathrm{shot}(t) - \mathrm{shot}(t-t_{\mathrm{off}}) \\ \rightarrow \mathrm{shot}(t) &= \tfrac{\mathrm{d}}{\mathrm{d}t}\mathrm{total}(t) + \mathrm{shot}(t-t_{\mathrm{off}}). \end{aligned} \tag{16}$$

Note that the last expression in the formula, shot($t - t_{off}$), gives zero for $t < t_{off}$ as shot($t < 0$) = 0. Therefore for $t < t_{off}$ the single shot distribution is simply the derivative of the total signal total(t), while for $t > t_{off}$ the contribution of shot($t - t_{off}$) has to be taken into account. Fig. 13 illustrates the summed time-of-flight profile of yttrium and the molecular compounds individually shown in Fig. 11, and the corresponding derivative of the sum signal. Note that the sum data start at $t = 0$ s, unlike the data in Fig. 11 which have an initial delay of ≈5 ms. In Fig. 13 the delay has been removed as it does not originate from the gas cell evacuation. The single shot time profile was processed with an adjacent averaging smoothing filter taking into account the closest 100 neighbouring points. The sum profile clearly has some structure within it which is directly related to the intensity balance of the individual molecules and is reflected in the differentiated signal which can be used to illustrate the evacuation time profile of a single laser shot. The single shot profile is not a smooth distribution in time rather there is a fast decay in the first few milliseconds followed by a long tail, extending beyond 300 ms, which is not surprising as the total evacuation time of the ion guide based on the volume and conductance of the exit hole is 480 ms.

Assuming that the molecular formation follows the evolution process of Eqs. (10)–(13) one can use Eq. (6) to formulate a set of rate equations of the form:

$$\begin{aligned}
\frac{d[Y^+]}{dt} &= -k_1[M][Y^+],\\
\frac{d[YO^+]}{dt} &= k_1[M][Y^+] - k_2[M'][YO^+],\\
\frac{d[YO^+(H_2O)]}{dt} &= k_2[M'][YO^+] - k_3[M'][YO^+(H_2O)],\\
\frac{d[YO^+(H_2O)_2]}{dt} &= k_3[M'][YO^+(H_2O)] - k_4[M'][YO^+(H_2O)_2],\\
\frac{d[YO^+(H_2O)_3]}{dt} &= k_4[M'][YO^+(H_2O)_2] - k_5[M'][YO^+(H_2O)_3],\\
\frac{d[YO^+(H_2O)_4]}{dt} &= k_5[M'][YO^+(H_2O)_3],
\end{aligned} \tag{17}$$

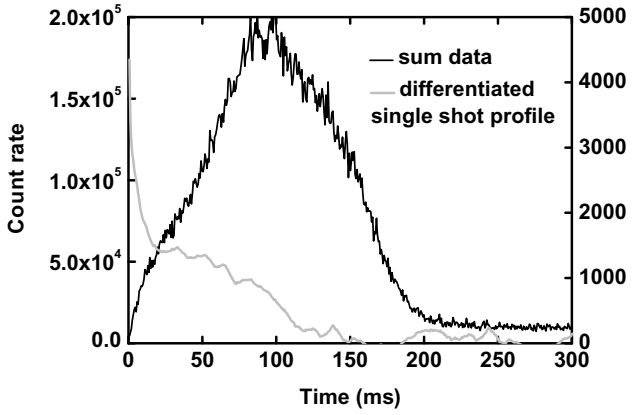

Fig. 13. The summed data from Fig. 11 and the corresponding differentiated single shot evacuation time profile, calculated according to Eq. (16) with $t_{off} = 90$ ms.

where $[M]$ is the sum of the impurity water and oxygen atom concentrations and $[M']$ is the water impurity concentration alone. The reaction rate coefficient k_1 is known from the literature [22], while k_2 to k_5 are rate coefficients for the subsequent molecular formation reactions. These are expected to be within the same order of magnitude as k_1 [25]. In this closed system of rate equations in which the condition of total current conservation is fulfilled (Eq. (14)) the initial starting condition is that $[Y^+](t = 0) = 1$. The five reaction rates $k_n[M \text{ or} M']$ form the free parameters within this model.

A single yttrium atom in the ion guide is ionized by the laser at $t = 0$. The probability for molecular formation can be determined when the ion has finally reached the exit hole and is evacuated. Applying the rate equation model of Eq. (17) to the differentiated single shot profile of Fig. 13 results in a typical single shot evacuation time profile for each ionic compound in the gas cell. These individual profiles are then reintegrated using Eq. (15). The five reaction rate parameters are adjusted to optimize the agreement of the simulation to the ratios of the different molecules observed in the experimental data. Fig. 14 shows the individual experimental time-of-flight profiles of Fig. 11 compared with the reintegrated single shot profiles. In order to illustrate the sensitivity of the reaction rate parameter to the comparison with experimental data, Fig. 15 shows how the simulated time profile of $[Y^+]$ varies as a function of $k_1[M]$. Recall that the model should reproduce the signal amplitudes as the total sum is conserved. The relative error in the fitting procedure is approximated to 10%. The time constants for molecular formation extracted from the reaction rate parameters that provide the optimum fits in Fig. 14 are given in Table 4.

It can be seen from τ_1 that the model overestimates the experimental saturation time of $[Y^+]$ (Fig. 12) by ≈4 ms. The discrepancy appears to be related to the fast falling edge of the single shot profile rather than missing physics in the model. The long formation time τ_5 is due to poor statistics and so had an uncertainty of 50% associated with the fit. This fourth hydrate addition is laser-related and has a very long evacuation time profile, even though the count rate is considerably smaller than the other molecules (Fig. 11). To a first approximation, the single shot treatment presented in this work appears to reproduce the experimental evacuation time profiles reasonably well. In ideal conditions this model, along with the experimental time profiles, could be used to extract individual impurity concentrations within the gas cell. The source of the impurities would not be an issue only the relative concentrations that are reflected in the experimental data.

In this work the problem to extract definite values for the concentrations of oxygen and water lies in the mechanism used to form YO^+, which is either through a direct reaction of yttrium with oxygen, or with water via Eq. (8). However, if we naively assume that YO^+ is formed directly from Eq. (9) then we can estimate an impurity level of oxygen in the ion guide using the results obtained in

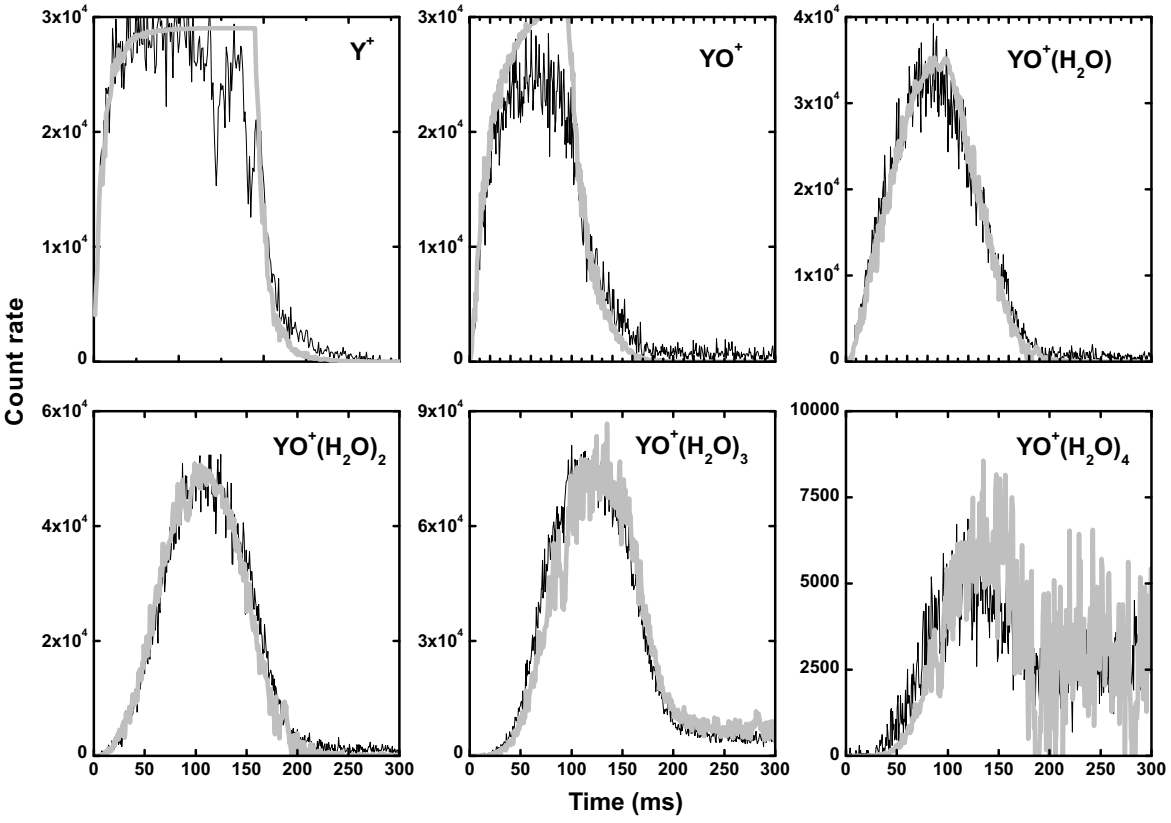

Fig. 14. Comparison between the simulated single-shot profiles (grey line) and the experimental data (black line).

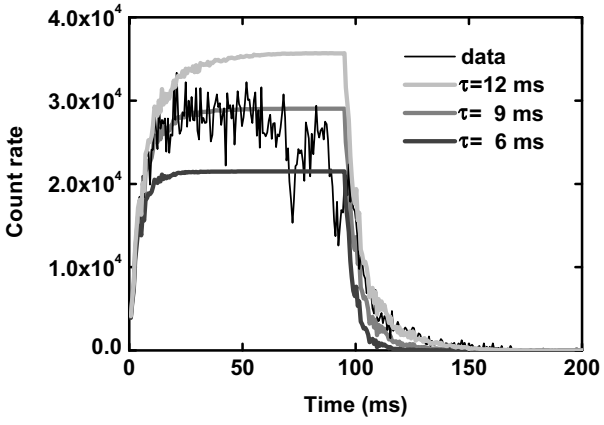

Fig. 15. The sensitivity of the simulated time profile for $[Y^+]$ as a function of different reaction rate parameters k_1 [M].

Table 4
The molecular formation time (ms) extracted from the fitted reaction rates

$\tau_1 = 1/k_1[M]$	$\tau_2 = 1/k_2[M']$	$\tau_3 = 1/k_3[M']$	$\tau_4 = 1/k_4[M']$	$\tau_5 = 1/k_5[M']$
9	14	19	31	400

Table 4. The number density of helium atoms in 150 mbar pressure is 3.71×10^{18} atoms/cm^3. Using a value of 9 ms for τ_1 the impurity concentration $[M]$ is equal to 2.71×10^{11} atoms/cm^3. Although earlier it was stressed that $[M]$ defined the sum of water and oxygen impurities, here we assume that as the reaction rate k_1 is that of Eq. (9) $[M]$ therefore refers to the level of oxygen. The subsequent impurity level is therefore 73 ppb assuming that the source of impurities is from the gas rather than the walls of the ion guide or other sources. Furthermore, a value of k_2 of 1.9×10^{-10} cm^3 s^{-1} has been measured for the reaction $YO^+ + D_2O \rightarrow YO^+(D_2O)$ [25]. Using the value τ_2 obtained in Table 4 the impurity concentration $[M']$ within the gas cell is calculated to be 3.76×10^{11} atoms/cm^3. Again, assuming that $[M']$ is from the gas then the impurity of water is at a level of 101 ppb. These numbers can be compared to the impurity level of $\approx$0.1 ppm obtained from the exponential growth fitted to the yttrium data in Fig. 12.

The first set of measurements described here was taken under rather unfavourable conditions in March 2006. Experimentally only the rise time of yttrium could be compared to the molecular formation model as all other molecules did not reach a saturation level. With hindsight a more meaningful comparison of the reaction rates extracted from the single-shot time profiles with the experimental data could have been made provided all molecules reached saturation. Importantly, as discussed briefly earlier, the extracted impurity level of $\approx$0.1 ppm was two orders of magnitude higher than expected following the careful treatment of the gas purity. Indeed, following this work two problems were discovered. The first was a possi-

ble leak in the final part of the gas line going directly to the ion guide, while the second was a leak in the venting valve attached directly to the IGISOL chamber which led to a pressure of $\approx 10^{-2}$ mbar (measured directly on the chamber) without helium gas flowing through the ion guide. Typically the pressure without buffer gas should be in the range of a few 10^{-5} mbar to low 10^{-4} mbar depending on how soon after opening the vacuum chamber the pressure is measured. The experiment was therefore repeated in March 2007 along with a study of the effect of introducing a leak into the vacuum chamber while the ion guide is running at typical operating pressures. This work will be discussed in the following section.

3.3. Ion guide laser ionization of filament-produced yttrium atoms – March 2007

The same procedure as described in the previous section was followed in order to prepare the ion guide and to ensure clean gas purity conditions. At the beginning of the experiment a base line pressure of 1.3×10^{-4} mbar was measured in the IGISOL chamber without helium gas. These background conditions were approximately two orders of magnitude better than in the March 2006 experimental run. The chamber pressure was then monitored as a function of ion guide pressure, shown in Fig. 16. At an operating pressure of 150 mbar, the chamber pressure was $\approx 8.4 \times 10^{-4}$ mbar. These numbers should not be taken as absolute values as the cold cathode gauge (model TPR 020) measurements have a dependence on the type of gas and it is calibrated for air. Additionally, the vacuum gauges are mounted on the opposite wall of the IGISOL chamber to that of the exit nozzle of the ion guide and therefore background measurements in the presence of flowing helium gas do not reflect the immediate surroundings of the expanding gas jet.

The double-arm mechanical shutter was used to ensure a better control over the laser arrival time and also to reduce

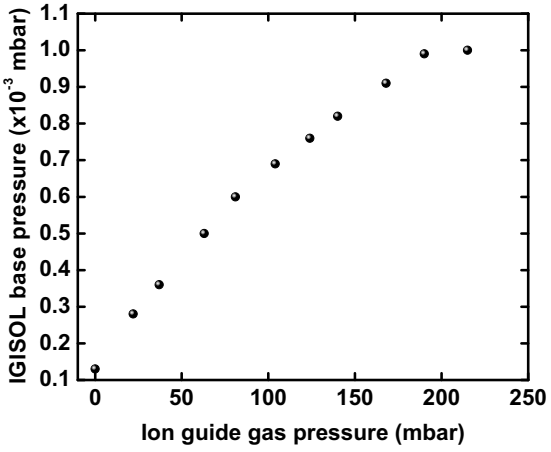

Fig. 16. IGISOL vacuum chamber pressure as a function of ion guide pressure.

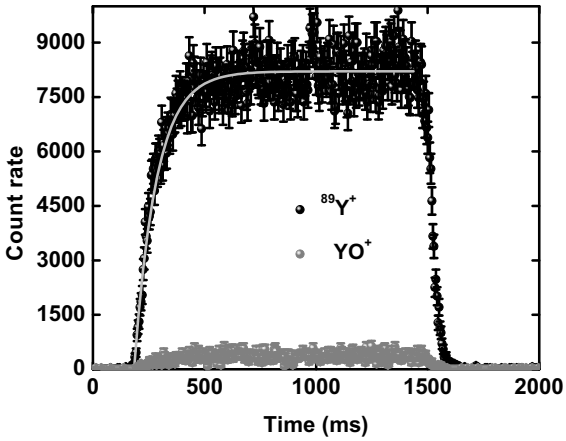

Fig. 17. Evacuation time profiles of Y^+ and YO^+. The laser was on from 100 ms to 1.4 s. The grey line shows an exponential fit to the yttrium data.

any effects related to "ringing" which is clearly visible on the falling slope of the yttrium time profile in Fig. 15. The laser was turned on after 100 ms and then at a time of 1.4 s was turned off, allowing a complete saturation of any molecules. The evacuation time profiles of the data taken under these new conditions are shown in Fig. 17.

The most striking difference between these data and that of Fig. 11 is that yttrium is now the dominant species over the next most abundant molecule extracted from the ion guide, yttrium oxide, by a factor of ≈20. No subsequent addition of hydrates could be observed at the expected mass numbers. Exponential fits to the rise time of the yttrium and the yttrium oxide data yielded values of 96(10) ms and 135(7) ms, respectively. The errors on the fits arise from a deviation from an exponential behaviour at the beginning of the rising edge, and therefore are conservatively increased to account for this effect. The rise time for yttrium, 96(10) ms can be directly compared with the rise time fitted in the March 2006 data, 5.1(4) ms (Fig. 12). With this new rise time and the ratio between yttrium and yttrium oxide, the primary effect on the time scale is now the evacuation time. By combining the rise time from these new data with the exit hole conductance, the effective volume for ion survival is ≈11 cm^3, approximately 20 times larger than in the earlier data.

One interesting detail seen in Fig. 17 is that the fall time of the yttrium signal is shorter than the rise time. This may be an indication of another effect that is not attributed to evacuation or molecular formation (which is minimal here). One possibility is a loss mechanism investigated and discussed in [23], that of recombination in the presence of ion–electron pairs created by the laser ionization process. Under the assumption that there are no losses of the laser ions through diffusion and molecular formation within the ion guide, and transport through the mass separator, a lower limit of the density of ion–electron pairs can be estimated from the total count rate of ^{89}Y seen in Fig. 17 and the ionization volume within the ion guide. With a total count rate of ≈8000 ions/s and a volume of

0.6 cm^3 (a cylinder of length 87 mm and diameter 3 mm) the ionization-density rate $Q \approx 10^4$ ion–electron pairs/cm^3 s. The time scale τ for the production of ion–electron pairs reaching an equilibrium with three-body recombination is given by

$$\tau = \frac{1}{\sqrt{Q \cdot \alpha}}, \tag{18}$$

where α is the pressure-dependent recombination coefficient. In 150 mbar helium gas, α is calculated to be 1.18×10^{-7} cm^3 s^{-1} [26]. A time scale τ of ≈25 s can be deduced, indicating that the number of electrons is not likely to be high enough to significantly reduce the fall-time of the signal. Therefore the explanation of the effect is still subject to speculation.

In this instance it is not clear whether the rise time can be used to extract an impurity level as in the case of the March 2006 data. This is because the new data reveal that the evacuation is playing a more dominant role and therefore the effect of impurities need to be deconvoluted from the time profile. However, an upper limit can be determined in the same way as in Section 3.2 and so with a helium pressure of 150 mbar in the ion guide, the impurity level can be estimated to be ≈7 ppb. This is a considerable improvement to the previous data and is more realistic based on the gas purity control discussed in detail in [23].

The same procedure as in Section 3.2 is then applied to extract a single laser shot evacuation profile from the summed data. The saturation of the data in this case means that the single shot can be derived simply from the derivative of the summed data according to Eq. (16). The simulation only takes into account the rising edge of the experimental data leading to saturation, corresponding to a length of the single shot of 500 ms. Following the differentiation of the summed signal and applying the rate equations for the known molecular formation the single shot profiles are reintegrated and compared with the experimental evacuation profiles. The summed experimental data and the differentiated signal are shown on the top in Fig. 18. It is clear that as the yttrium signal dominates, the summed profile closely follows that of the yttrium profile unlike the experimental data in Section 3.2. An exponential fit to the data yields a rise time of 99(10) ms, in agreement with the yttrium rise time of 96(10) ms. The saturation of the data is clearly helpful in extracting a reliable single shot profile which is seen to peak at approximately 50 ms before decreasing steadily to longer evacuation times. The peak of the rise time corresponds well with gas flow simulations that show the atomic vapour density is highest where the gas flow starts to converge towards the ionization channel of the ion guide.

For comparison, a true single shot evacuation time profile obtained using the low repetition rate laser system at the LISOL facility is shown on the bottom in Fig. 18 [27]. The data were taken using the same ion guide geometry and buffer gas as in the present work, using the lasers to ionize nickel atoms from a heated filament. In Fig. 18 the fast rise of the LISOL single shot profile, peaking at approximately 10 ms, arises from the evacuation of the ionization channel. The long tail of the distribution can be explained by the evacuation of the main body of the ion guide. While there is a rather good agreement between the two single shot evacuation profiles in terms of the time scale of the full evacuation of the ion guide (≈400 ms) the shapes of the profiles look rather different. A probable reason can be found in the difference between the laser-atom spatial overlap. In the LISOL system the laser beams are unfocussed and the laser fills the ionization channel (10 mm diameter). In the case of the IGISOL system the lasers enter the ion guide and are focused to a beam waist of ≈3 mm at the nozzle in order to provide sufficient laser intensity to saturate the required atomic transitions. The single shot profile in the latter case reflects the situation in which the lasers are not only probing a smaller volume of the ion guide but are more sensitive to any misalignment of the laser beam on the symmetry axis, which translates into a higher sensitivity to different regions of the gas flow. More experiments have to be performed to study the dependence of the evacuation profile on the geometry of

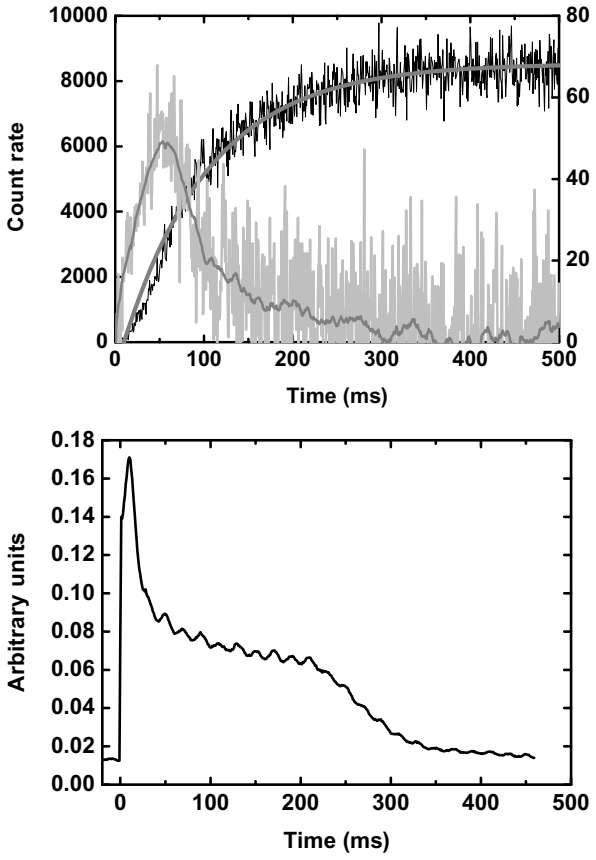

Fig. 18. Summed data from Fig. 17 and the corresponding differentiated single shot evacuation time profile (top). An exponential fit to the summed profile is shown and an adjacent averaging technique using 50 bins has been applied to the differentiated data in order to smooth out the fluctuations. On the bottom a true single laser shot evacuation time profile of ions produced by laser ionization with the LISOL low-repetition rate laser system is illustrated for comparison.

the ion guide, the laser ionization region and filament position in detail.

After applying the rate equation model of Eq. (17), Fig. 19 shows the individual ionic time profiles of the yttrium and yttrium oxide after evacuation from the gas cell. In this simulation the higher order reaction rate coefficients are assumed to be zero, reflecting the experimental data. The simulated time profiles have been created using an optimum τ_1 of 2.3 s. This fit parameter can be compared to τ_1 from Table 4 (9 ms) and reflects the fact that the evacuation time completely dominates the saturation profile. The ratio of yttrium to yttrium oxide has a very strong dependence on the value of τ_1. One may question why the experimentally fitted rise time of 96(10) ms is so much shorter than 2.3 s, and whether the simulation could reproduce the data with a shorter τ_1. The evacuation time, however, is not the same as the optimized value of the reaction rate coefficient used to correctly fit the ratios of Y^+ to YO^+. This observation illustrates that the single shot model is a powerful tool to directly probe the level of impurities in a system dominated by the evacuation time, where simply fitting the rise time of the atomic species can only provide an upper limit. Therefore, following the same assumptions used in Section 3.2 an oxygen impurity concentration $[M]$ of 1.06×10^9 atoms/cm^3 can be extracted, which can be translated into an impurity level of 0.29 ppb if the source of the impurity is in the helium gas. This is a factor of 20 lower than the upper limit estimated from fitting the rise time of the data.

In Fig. 19 the simulation clearly reproduces the rising edge and amplitude of the time profiles, however unlike Fig. 14 a striking deviation exists between the experimental falling edges and that of the simulation, which overestimates the decay time. This feature cannot be explained by the model as by definition the slope of the rising and falling edges is dominated by the time scale of the single shot event, and therefore should be the same. As mentioned previously, the reason for this discrepancy is not fully understood.

Finally the sensitivity of the model towards the shape of the single shot evacuation profile was investigated. The experimentally determined laser shot profile from the LISOL data, illustrated in Fig. 18, were used as an input for the simulation taking the same time scale τ_1 for molecular formation (2.3 s) extracted from the optimum fit of the differential profile to the yttrium experimental data. The results using the LISOL single shot are shown in Fig. 20. A constant scaling factor for both Y^+ and YO^+ was applied to take into account the arbitrary y-axis scale of the LISOL single shot profile. The simulated ratio of Y^+ to YO^+ is affected only slightly by the change of the profile, however compared with the fits in Fig. 19 it is noticeable

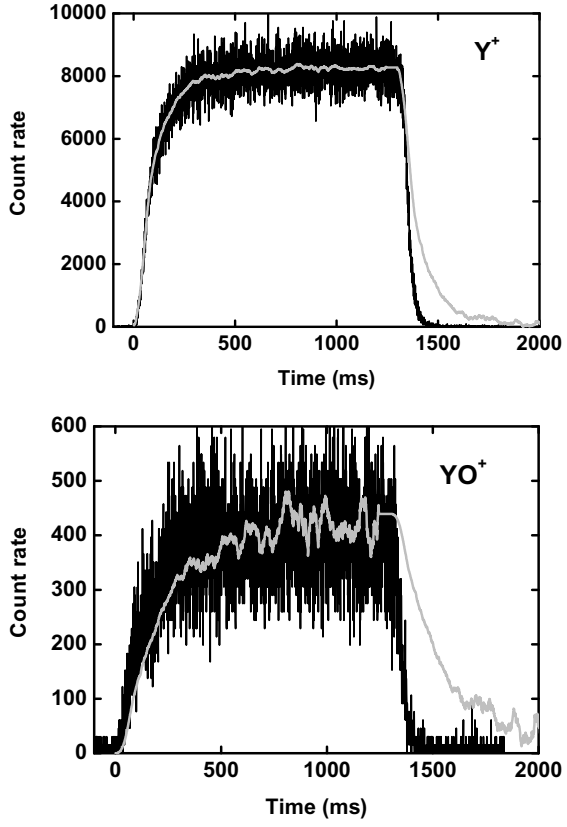

Fig. 19. Comparison between the simulated single shot profiles (grey line) and the experimental data (black line) using an optimum τ_1 of 2.3 s for the differentiated single shot.

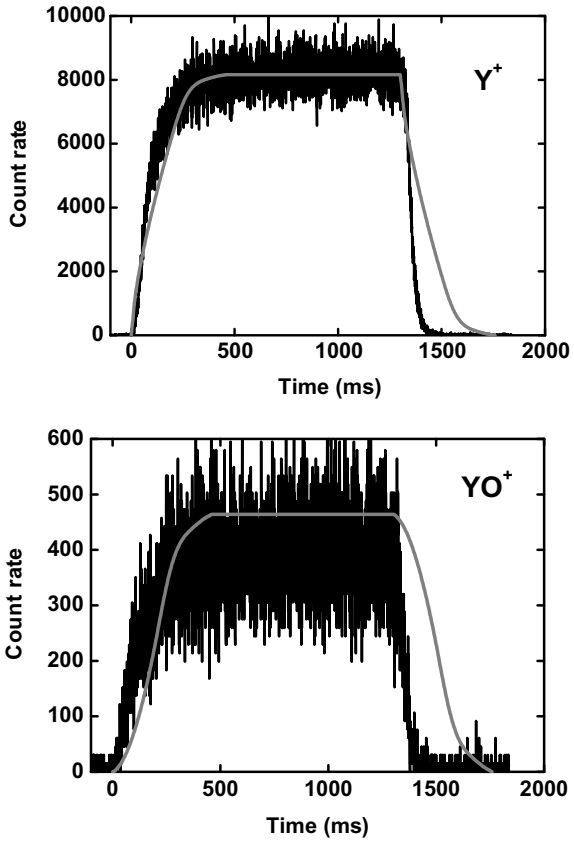

Fig. 20. Comparison between the simulated LISOL single shot profiles (grey line) and the experimental data (black line) using a τ_1 of 2.3 s.

that the rising edge of the data is not as well described. The difference in the simulated rising edges simply reflects the different shapes of the two single shot profiles, and in turn the differing laser-atom overlap geometries and thus laser ion evacuation times. Unsurprisingly, the choice of profile does not solve the discrepancy between the simulated falling edge and the experimental data.

In order to understand the importance of the baseline vacuum chamber pressure in a controlled fashion, a needle valve was attached directly to the IGISOL vacuum chamber. The motivation for this study arose from the poor conditions experienced in the 2006 experiment. The work of the LISOL group has shown that the vacuum chamber can be opened with no detrimental effects to the purity conditions as long as a gas flow is maintained within the ion guide [27]. During the following tests it is important to note that a helium gas pressure of 150 mbar was maintained in the ion guide throughout the measurements, and the IGISOL vacuum chamber pressure was measured at this gas pressure. Initially, when the needle valve was closed, the yttrium and yttrium oxide ion count rate was monitored starting from high purity conditions, and then subsequently worse conditions as the getter was bypassed, the liquid nitrogen cooled cold trap was bypassed and the helium gas bottle was changed from a grade 6.0 (99.9999% purity) to grade 4.6 (99.996% purity). It is interesting to note that these changes did not have any significant effect on the count rates or ratios. In previous studies at the IGISOL it had been noticed that grade 6.0 helium and/or use of the Saes MonoTorr purifier have seldom affected the performance of the device. A similar remark has been recently made in the studies of the extraction efficiency and extraction time of the SHIPTRAP gas-filled stopping cell [28]. In that work ordinary helium 4.6 was used without any significant degradation of the gas cell performance compared to helium 6.0.

A leak was introduced into the vacuum chamber and the count rates were monitored as a function of chamber pressure. Without a leak the chamber pressure was measured to be 8×10^{-4} mbar with an operating ion guide pressure of 150 mbar. The chamber pressure was steadily increased until at a level of 1×10^{-2} mbar a complete redistribution in the mass separated yields was identified. At higher pressures, measurements could not be reliably made as discharge within the SPIG started to occur. The distribution of molecules as a function of chamber pressure is illustrated as a histogram chart in Fig. 21. The bin width of the histogram has no meaning and this figure is simply used to illustrate the relative changes in the yields. The specific pressures measured are listed in the figure caption. It should be noted that these values do not indicate the pressure in the immediate vicinity of the gas jet, and therefore should be taken as relative measurements.

A fourth hydrate addition was also found to have a laser-related effect, however the masses above $YO^+(H_2O)_2$ had very poor mass resolution which indicated that an increase in the chamber pressure effects the pressure in the acceleration region of the SPIG. At a chamber pressure of 1×10^{-2} mbar evacuation time profiles were measured and are illustrated in Fig. 22. Only the lighter of the two hydrates are shown as these still had reasonable mass resolution. Yttrium is no longer the dominant ionic species detected and the yield has been considerably reduced. The most dominant molecules are now those of the two lightest hydrates, $YO^+(H_2O)$ and $YO^+(H_2O)_2$. Exponential growth fits to the data in Fig. 22 yield the values listed in Table 5.

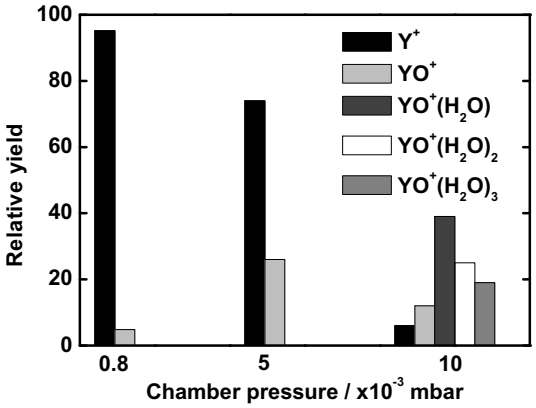

Fig. 21. Relative yields of Y^+ and related molecules as a function of IGISOL chamber pressure. The measured pressures were 8.6×10^{-4}, 5×10^{-3} and 1×10^{-2} mbar, respectively.

The trend of the saturation time for yttrium and yttrium oxide can be understood as the concentration of impurities is increasing, therefore via Eq. (7), τ is expected to decrease. Although the yttrium signal is now suppressed to a level

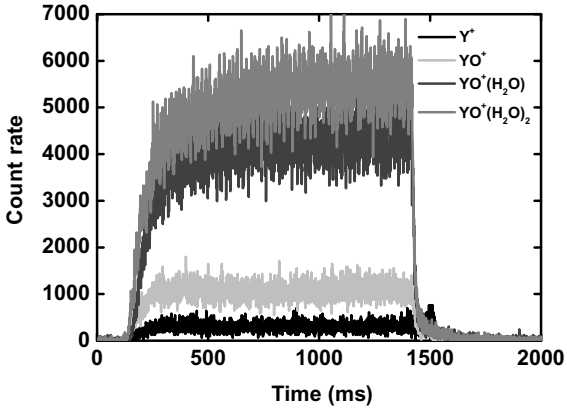

+fl

Fig. 22. Evacuation time profiles of Y^+ and subsequent molecules detected after a leak increased the vacuum chamber pressure to 1×10^{-2} mbar while the ion guide pressure was maintained at 150 mbar.

Table 5
Exponential growth times in ms extracted from the data in Fig. 22

$\tau_1 = 1/k_1[M]$	$\tau_2 = 1/k_2[M']$	$\tau_3 = 1/k_3[M']$	$\tau_4 = 1/k_4[M']$
55(5)	55(5)	106(4)	97(7)

less than 10% of the sum of all molecules, the time to reach saturation is still a factor of 10 larger than in the March 2006 data. One could imagine that close to the exit nozzle of the ion guide, before the leak is introduced, the dominant species is yttrium. This would have a time distribution profile effectively of the evacuation from the ion guide (≈100 ms as seen in Fig. 17). With a poor vacuum chamber pressure the evacuated ions may then be converted into molecules at the exit nozzle of the guide, or within the gas jet as the ions enter and pass through the SPIG. A transportation time of ≈200 μs through the SPIG for $A = 100$ ions has been estimated from simulations, using typical DC voltages on the SPIG and extractor electrode and assuming a pressure within the ion guide of 150 mbar. In this simulation the pressure within the SPIG was estimated based on the modeling of the gas flow (see [29] for details). Two of the more sensitive parameters to the time-of-flight appear to be the background pressure within the SPIG and the buffer gas velocity. At present experiments are being planned to demonstrate these effects directly. Although this transportation time is fast compared to the saturation time scales of Table 5, if the molecular impurity level in the SPIG region is high then molecular formation can rapidly occur via collisions within the gas jet.

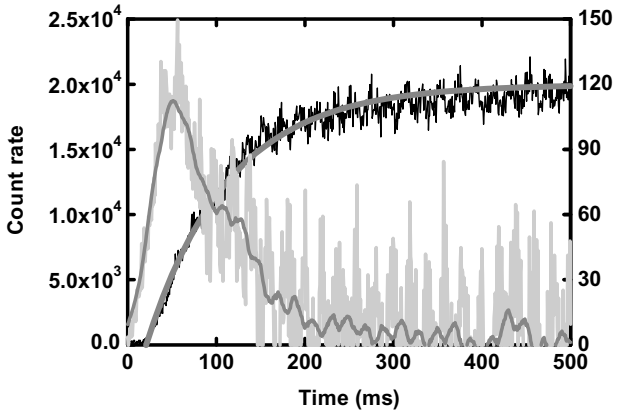

Fig. 23. Summed data from Fig. 22 and the corresponding differentiated single shot evacuation time profile. An exponential fit to the summed profile is shown yielding a rise time of 99(4) ms and an adjacent averaging technique using 50 bins has been applied to the differentiated data in order to smooth out the fluctuations.

In order to determine whether the single shot model is still valid under these conditions, Fig. 23 shows the summation of the molecular components of Fig. 22, and the subsequent single shot derivative. An exponential fit to the summed "leak data" gives a rise time value of 99(4) ms. Recall that the rise time of the summed data without the leak (Fig. 18) yielded a value of 99(10) ms. This is rather interesting as these two values are exactly the same, despite the fact that the summed data with no leak in the chamber is dominated by yttrium with a rise time of 96(10) ms and under poor vacuum conditions not only is the yttrium rise time reduced to 55(5) ms but it is no longer the dominant species. By worsening the vacuum conditions in the immediate chamber surrounding the ion guide the increase in impurity level reduces not only the saturation time of the

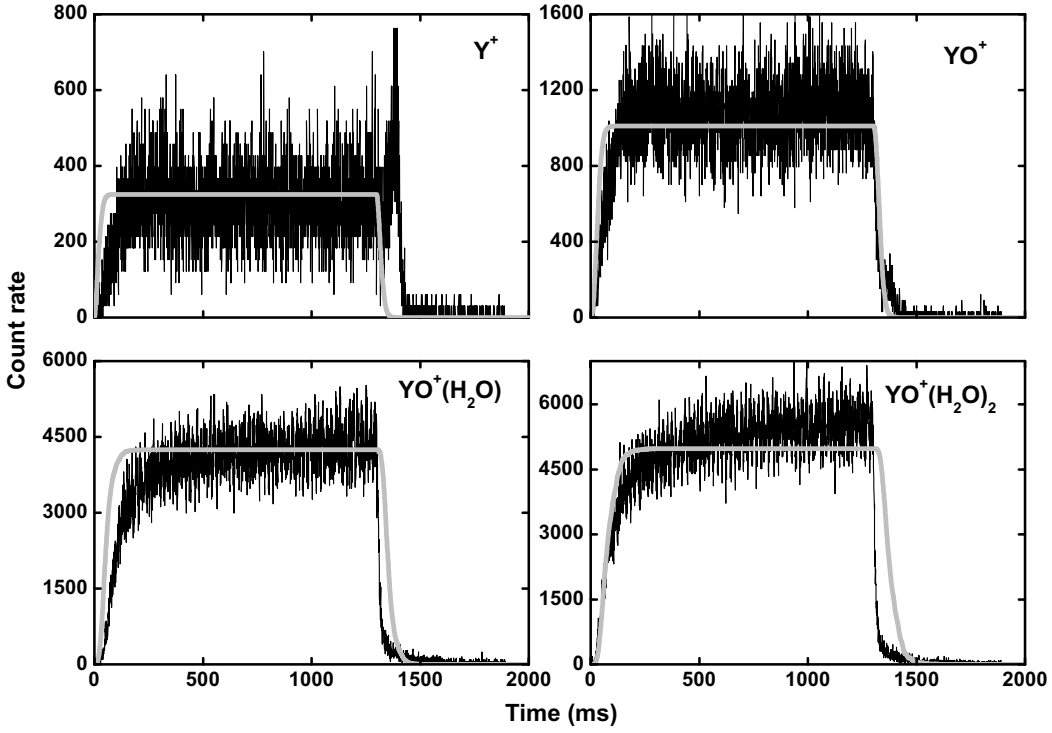

Fig. 24. Comparison between the simulated single shot profiles (grey line) and the experimental data (black line).

yttrium time distribution profile, but also radically changes the distribution of the intensities of yttrium and subsequent molecules. What is important to note, however, is that the sum profiles which give an indication of the total yield prior to mass separation are identical, and they reflect the evacuation time profile within the ion guide. It appears that ions are not "lost" after the introduction of a leak into the vacuum chamber rather they are simply redistributed into other molecular forms after leaving the exit nozzle of the gas cell.

After applying the rate equations of Eq. (17) for molecular formation, the single shot evacuation time profiles are illustrated in Fig. 24 for the data taken with poor vacuum pressure in the IGISOL chamber. Recall that in Fig. 19 the rising edge and amplitude were well-reproduced however the falling edge was over-estimated. As in Section 3.2 the relative error in the fitting procedure has been estimated to be ≈10%. The time constants for molecular formation extracted from the reaction rate parameters that provide the optimum fits to reproduce the correct ratios in Fig. 24 are given in Table 6. Although the simulated ratios of the molecules appear to be in a reasonable agreement with the data, the rise times of the re-integrated single shot profiles are consistently too fast. Due to the saturation of all experimental profiles the simulated time constants can be compared with the rise times directly fitted to the data (Table 5). The single shot model suggests that the level of impurities within the gas cell is higher than that reflected by the experimental data. This is another indication that by introducing a leak into the chamber there are molecular processes occurring after the nozzle on fast time scales that do not affect the overall evacuation time profile extracted from the gas cell.

Table 6
The molecular formation time (ms) extracted from the fitted reaction rates after optimization of the ratios of the molecules

$\tau_1 = 1/k_1[M]$	$\tau_2 = 1/k_2[M']$	$\tau_3 = 1/k_3[M']$
10	13	35

More supporting evidence for the suggestion that the presence of impurities in the environment outside the nozzle area only shifts the mass distribution of yttrium towards heavier molecules yet does not affect the total signal current or the general shape of the evacuation profile is given in Fig. 25. In this figure the free reaction rate parameters have been fixed to the experimental rise times given in Table 5. The increase of the time constants compared to those extracted from fitting the optimum molecular ratios listed in Table 6, lead to an increase in the expected rate of Y^+ and YO^+ and a decrease for the higher hydrated compounds. This is unsurprising because a longer time constant for the molecular formation infers the situation in which the resultant molecular rates should be lower for the same evacuation time of the gas cell. It should be noted that the sum of the simulation profiles appears to be very much larger than the sum of the experimental profiles. This is because there are higher mass hydrate molecules in the

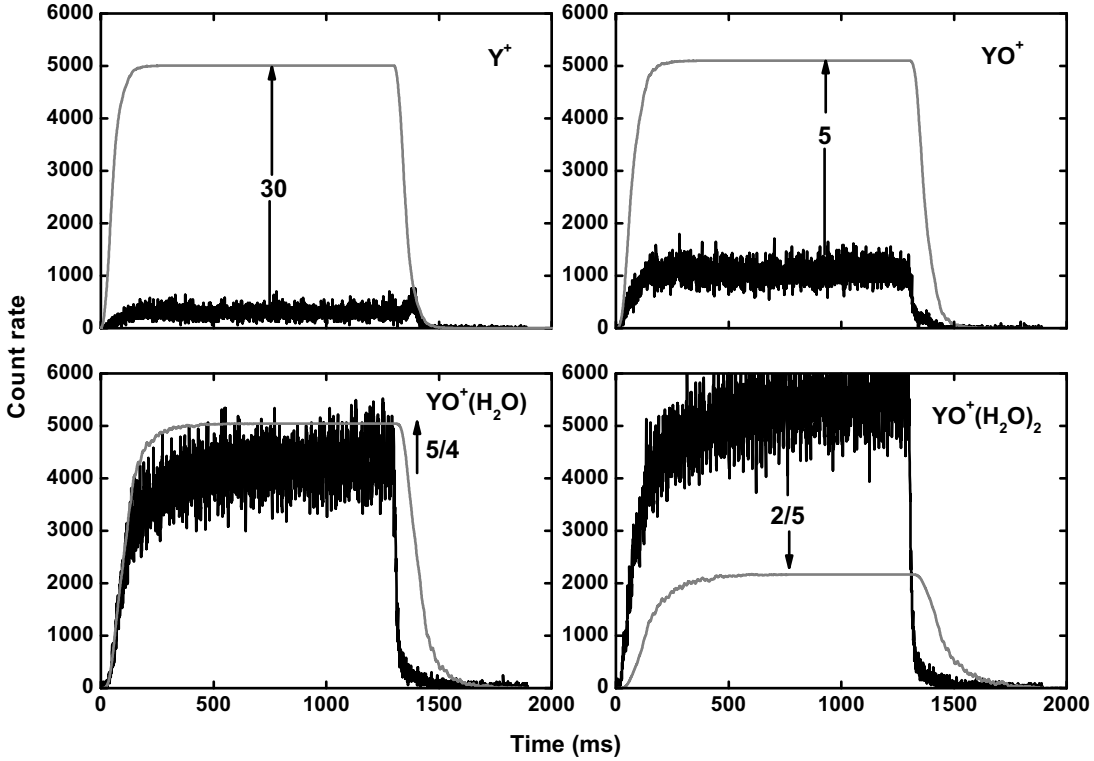

Fig. 25. The experimental data (black line) of Fig. 24 fitted using the single shot model (grey line) with reaction rate parameters fixed to the time constants of Table 5.

data (and detected with laser effects) however as they had no mass resolution it was decided to only discuss the lower mass molecules.

Finally, we note that the higher mass hydrate additions to YO^+ in the 2006 data had a reasonable mass resolution. Although the baseline pressure was found to be of the same order of magnitude as that used in the measurements of Fig. 22, the leak in the gas line appears to have been the dominant effect on the impurity level. This conclusion is supported not only by the good mass resolution of the molecules, but also by the clear difference in the time distribution of the hydrate additions (Fig. 11).

Interestingly, very little information is available about the importance of base pressure of the vacuum chamber to the operation of an ion guide/gas catcher system. The experimental work shown here, in combination with the use of our single shot model has implications for all gas catchers and discussions of the required impurity levels of the gas. The gas itself can be purified to a level of less than a ppb as shown in this work, however if the baseline pressure of the vacuum chamber surrounding the ion guide/gas catcher device is poor then a significant redistribution of the atomic ions into heavier molecular species on fast time scales can result. In fact, as highlighted in Fig. 21, even at a baseline vacuum pressure of 5×10^{-3} mbar (measured at 150 mbar ion guide pressure) one starts to redistribute the ions.

4. Summary and conclusions

The purpose of this work was to initiate a programme of research designed to lead to the successful implementation of a laser ion source for the efficient and selective production of exotic, short-lived refractory nuclei that are uniquely available at the IGISOL facility. The capabilities and flexibility of having a twin laser system running in parallel has been demonstrated with the development of a new laser ionization scheme for yttrium, in which both a dye laser and Ti:Sapphire laser were used for a second step transition providing the optimal choice of ionization scheme. In this work the laser ionization efficiency has not been explicitly discussed and is rather difficult to measure in off-line conditions. This will be addressed in a follow-up paper which discusses the role of beam ionization on the evacuation time profiles of yttrium and related molecules [30].

An ion guide was borrowed from the LISOL group at Leuven in order to make the first off-line measurements of laser produced yttrium ions from a heated filament. A detailed study was performed to understand the effects of gas purity on an element that exhibits strong molecular formation in the presence of impurities within the gas. Results obtained from the data taken in March 2006, illustrated in the form of time-of-flight profiles, indicated that the resultant impurity level was some two orders of magnitude worse than expected from similar studies discussed in [23]. This highlighted the importance of careful control of the gas-handling system. In order to gain a more detailed understanding of the competition between the molecular formation process and evacuation from the ion guide, the experimental data was analyzed in the framework of a series of molecular rate equations in order to extract time profiles of single laser shots.

A repeat of the experiment was performed in March 2007 in which the lasers ionized the yttrium atoms for a time period such that a clear saturation level could be achieved. With a better control over the gas purification a clear reduction in the level of impurities to sub-ppb could be achieved. The importance of the vacuum pressure in the immediate vicinity of the ion guide was apparent after a controlled leak was added directly to the vacuum chamber. What is rather astonishing is that although the increase in the number of impurities reduces the time needed to reach a saturation level in yttrium, by summing the individual yttrium and associated molecular time-of-flight profiles the total evacuation profile with and without the added leak has the same overall shape. This time profile reflects the evacuation time of the laser ions from within the ion guide. It appears that ions are not "lost" after the introduction of a leak into the vacuum chamber rather they are simply redistributed into other molecular forms after leaving the exit nozzle of the gas cell.

The development of the single shot model provides a new tool with which to extract from the data direct information of the level of impurities within the gas cell. This removes the need for complicated gas flow simulations which would be required if the evacuation time of the ions within the laser path was to be accurately described and then deconvoluted from the experimental time-of-flight profile in order to separate the effect due to chemistry. The issue of where the molecular formation is happening has been successfully addressed in this work and has led to the need for a better knowledge of the time-of-flight of ions through the sextupole ion guide, and the parameters which can most influence this time scale. In parallel, simulations are now underway both in Jyväskylä and at the NSCL facility, Michigan State University, in order to study the drift time of ions through the SPIG used in this work. This effort reflects not only the interest but concern of the gas catcher community as long drift times can result in losses of the ion of interest through molecular formation and possibly charge exchange.

In studies performed at Leuven with a cobalt filament and a 30 MeV cyclotron proton beam passing through a gas cell filled with 500 mbar argon, the final conclusion was that in order to explain the resulting molecular sidebands either the impurity of the buffer gas was higher than 1 ppb, or the molecular ions are formed close to the exit hole of the gas cell or in the gas jet leaving the ion source [31]. The present work provides a unique method with which to separate these two scenarios in the development of the single shot model. The need for extreme gas purity is common to all existing and planned gas cell devices. Much effort has been put into cleaning up the gas down

to the sub-ppb impurity level, however even at this low level the molecular formation still seems to be a problem in some cases. Partly because of these difficulties, cryogenic gas catchers are currently being developed [32]. In these devices it is hoped that the impurities can be frozen out by cooling the gas and the gas catcher/ion guide system to liquid nitrogen temperature. Future plans exist at the IGISOL facility to combine the new laser ion source with a cryogenic ion guide. In this manner, similar to the present work, the evolution of the molecular sidebands on chemically reactive elements such as yttrium can be monitored as a function of the cooling temperature. It will be important though not only to develop and incorporate these cryogenic techniques further, but to ensure a clean environment through which the ions must pass once they are extracted from the gas cell.

Acknowledgements

This work has been supported by the LASER Joint Research Activity Project under the EU 6th Framework program "Integrating Infrastructure Initiative-Transnational Access", Contract number: 506065 (EURONS) and by the Academy of Finland under the Finnish centre of Excellence Program 2006-2011 (Nuclear and Accelerator Based Physics Program at JYFL).

References

[1] J. Äystö, Development and applications of the IGISOL technique, Nucl. Phys. A 693 (1–2) (2001) 477.
[2] J. Huikari, P. Dendooven, A. Jokinen, A. Nieminen, H. Penttilä, K. Peräjärvi, A. Popov, S. Rinta-Antila, J. Äystö, Production of neutron deficient rare isotope beams at IGISOL; on-line and off-line studies, Nucl. Instr. and Meth. B 222 (3–4) (2004) 632.
[3] P. Van Duppen, Laser ion sources for on-line isotope separators, Nucl. Instr. and Meth. B 126 (1–4) (1997) 66.
[4] Y. Kudryavtsev, B. Bruyneel, S. Franchoo, M. Huyse, J. Gentens, K. Kruglov, W.F. Mueller, N.V.S.V. Prasad, R. Raabe, I. Reusen, P. Van den Bergh, P. Van Duppen, J. Van Roosbroeck, L. Vermeeren, L. Weissman, The Leuven isotope separator on-line laser ion source, Nucl. Phys. A 701 (1–4) (2002) 465.
[5] Y. Kudryavtsev, M. Facina, M. Huyse, J. Gentens, P. Van den Bergh, P. Van Duppen, Beams of isotopes produced at LISOL by laser ionization after thermalization of energetic ions in a gas cell, Nucl. Instr. and Meth. B 204 (2003) 336.
[6] L. Vermeeren, N. Bijnens, M. Huyse, Y.A. Kudryavtsev, P. Van Duppen, J. Wauters, Z.N. Qamhieh, P. Thoen, E. Vandeweert, R.E. Silverans, An on-line laser ion source based on resonance photoionization in a gas cell, Phys. Rev. Lett. 73 (14) (1994) 1935.
[7] P. Van Duppen, B. Bruyneel, M. Huyse, Y. Kudryavtsev, P. Van Den Bergh, L. Vermeeren, Beams of short lived nuclei by selective laser ionization in a gas cell, Hyperfine Interact. 127 (1) (2000) 401.
[8] I.D. Moore, A. Nieminen, J. Billowes, P. Campbell, C. Geppert, A. Jokinen, T. Kessler, B. Marsh, H. Penttilä, S. Rinta-Antila, B. Tordoff, K.D.A. Wendt, J. Äystö, Development of a laser ion source at IGISOL, J. Phys. G: Nucl. Part. Phys. 31 (10) (2005) S1499.
[9] I.D. Moore, J. Billowes, P. Campbell, T. Eronen, C. Geppert, A. Jokinen, P. Karvonen, T. Kessler, B. Marsh, A. Nieminen, H. Penttilä, S. Rinta-Antila, T. Sonoda, B. Tordoff, K. Wendt, J. Äystö, Laser ion source development at IGISOL, in: AIP Conf. Proc., Vol. 831, AIP, Isle of Kos, Greece, 2006, p. 511.
[10] U. Hager, T. Eronen, J. Hakala, A. Jokinen, V.S. Kolhinen, S. Kopecky, I. Moore, A. Nieminen, M. Oinonen, S. Rinta-Antila, J. Szerypo, J. Äystö, First precision mass measurements of refractory fission fragments, Phys. Rev. Lett. 96 (4) (2006) 042504.
[11] P. Campbell, H.L. Thayer, J. Billowes, P. Dendooven, K.T. Flanagan, D.H. Forest, J.A.R. Griffith, J. Huikari, A. Jokinen, R. Moore, A. Nieminen, G. Tungate, S. Zemlyanoi, J. Äystö, Laser spectroscopy of cooled zirconium fission fragments, Phys. Rev. Lett. 89 (8) (2002) 082501.
[12] A. Kankainen, L. Batist, S.A. Eliseev, V.V. Elomaa, T. Eronen, U. Hager, J. Hakala, A. Jokinen, I. Moore, Y.N. Novikov, H. Penttilä, K. Peräjärvi, A.V. Popov, S. Rahaman, S. Rinta-Antila, P. Ronkanen, A. Saastamoinen, D.M. Seliverstov, T. Sonoda, G.K. Vorobjev, J. Äystö, Mass measurements of neutron-deficient nuclides close to $A = 80$ with a Penning trap, Eur. Phys. J. A 29 (3) (2006) 271.
[13] T. Kessler, T. Eronen, C. Mattolat, I. Moore, K. Peräjärvi, P. Ronkanen, P. Thörle, B. Tordoff, N. Trautmann, K. Wendt, K. Wies, J. Äystö, Upgrade to the IGISOL laser ion source towards spectroscopy on Tc, Hyperfine Interact. 171 (1) (2006) 121.
[14] B. Tordoff, Development of resonance ionization techniques at the Jyväskylä IGISOL, PhD Thesis, University of Manchester, 2006.
[15] B. Tordoff, J. Billowes, P. Campbell, B. Cheal, D. Forest, T. Kessler, J. Lee, I. Moore, A. Popov, G. Tungate, J. Äystö, Investigation of the low-lying isomer in ^{229}Th by collinear laser spectroscopy, Hyperfine Interact. 171 (1) (2006) 197.
[16] J.F. McCann, J. Pezy, P. Wilsen, A versatile electronic light shutter composed of a high speed switching circuit coupled with a lithium niobate Pockels cell, J. Phys. E: Sci. Instr. 15 (3) (1982) 322.
[17] K. Singer, S. Jochim, M. Mudrich, A. Mosk, M. Weidemüller, Low-cost mechanical shutter for light beams, Rev. Sci. Instr. 73 (12) (2002) 4402.
[18] V.S. Letokhov, Laser Photoionization Spectroscopy, Academic Press Inc., US, 1987.
[19] G.S. Hurst, M.G. Payne, Principles and Applications of Resonance Ionization Spectroscopy, Institute of Physics Publishing, 1988.
[20] R.L. Kurucz, P.L. Smith, C. Heise, J.R. Esmond, Atomic spectral line database, http://www.pmp.uni-hannover.de/cgi-bin/ssi/test/kurucz/sekur.html, 2007.
[21] T. Hirata, Hirata Atomic Spectral Line List, http://cdsweb.u-strasbg.fr/viz-bin/VizieR?-source=VI/69, 2007.
[22] G.K. Koyanagi, D. Caraiman, V. Blagojevic, D.K. Bohme, Gas-phase reactions of transition-metal ions with molecular oxygen: room-temperature kinetics and periodicities in reactivity, J. Phys. Chem. A 106 (18) (2002) 4581.
[23] Y. Kudryavtsev, B. Bruyneel, M. Huyse, J. Gentens, P. Van den Bergh, P. Van Duppen, L. Vermeeren, A gas cell for thermalizing, storing and transporting radioactive ions and atoms. Part I: off-line studies with a laser ion source, Nucl. Instr. and Meth. B 179 (3) (2001) 412.
[24] J. Hakala, V.-V. Elomaa, T. Eronen, U. Hager, A. Jokinen, J. Aystö, The JYFLTRAP control and measurement system, Nucl. Instr. and Meth. B, submitted for publication.
[25] D. Bohme, Private communication.
[26] R.J. van Sonsbeek, R. Cooper, R.N. Bhave, Pulse radiolysis studies of ion–electron recombination in helium. Pressure and temperature effects, J. Chem. Phys. 97 (3) (1992) 1800.
[27] Y. Kudryavstev, Private communication.
[28] S. Eliseev, M. Block, A. Chaudhuri, Z. Di, D. Habs, F. Herfurth, H.-J. Kluge, J. Neumayr, W. Plaß, C. Rauth, P. Thirolf, G. Vorobjev, Z. Wang, Extraction efficiency and extraction time of the SHIPTRAP gas-filled stopping cell, Nucl. Instr. and Meth. B 258 (2) (2007) 479.
[29] P. Karvonen, in preparation.
[30] I. Moore, in preparation.
[31] M. Facina, A gas catcher for the selective production of radioactive beam through laser ionization, Ph.D. Thesis, IKS Leuven, 2004.
[32] P. Dendooven, S. Purushothaman, K. Gloos, On a cryogenic noble gas ion catcher, Nucl. Instr. and Meth. A 558 (2) (2006) 580.